



HAL
open science

Numerical and experimental study at the pilot scale of the hydrogen injection into liquid sodium by permeation through nickel membrane

Pietro Brazzale

► **To cite this version:**

Pietro Brazzale. Numerical and experimental study at the pilot scale of the hydrogen injection into liquid sodium by permeation through nickel membrane. Chemical and Process Engineering. Institut National Polytechnique de Toulouse - INPT, 2020. English. NNT : 2020INPT0101 . tel-04171499

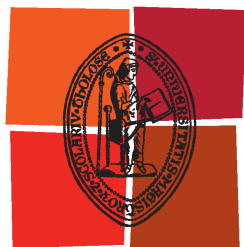
HAL Id: tel-04171499

<https://theses.hal.science/tel-04171499>

Submitted on 26 Jul 2023

HAL is a multi-disciplinary open access archive for the deposit and dissemination of scientific research documents, whether they are published or not. The documents may come from teaching and research institutions in France or abroad, or from public or private research centers.

L'archive ouverte pluridisciplinaire **HAL**, est destinée au dépôt et à la diffusion de documents scientifiques de niveau recherche, publiés ou non, émanant des établissements d'enseignement et de recherche français ou étrangers, des laboratoires publics ou privés.



Université
de Toulouse

THÈSE

En vue de l'obtention du

DOCTORAT DE L'UNIVERSITÉ DE TOULOUSE

Délivré par :

Institut National Polytechnique de Toulouse (Toulouse INP)

Discipline ou spécialité :

Génie des Procédés et de l'Environnement

Présentée et soutenue par :

M. PIETRO BRAZZALE

le jeudi 12 novembre 2020

Titre :

Numerical and experimental study at the pilot scale of the hydrogen injection into liquid sodium by permeation through nickel membrane

Ecole doctorale :

Mécanique, Energétique, Génie civil, Procédés (MEGeP)

Unité de recherche :

Laboratoire de Génie Chimique (LGC)

Directeur(s) de Thèse :

MME XUAN MI MEYER

M. XAVIER JOULIA

Rapporteurs :

M. ERIC FAVRE, UNIVERSITÉ LORRAINE
Mme GIULIA BOZZANO, POLITECNICO DE MILAN

Membre(s) du jury :

Mme PIERRETTE GUICHARDON, ECOLE CENTRALE DE MARSEILLE, Président
M. AURELIEN CHASSERY, CEA CADARACHE, Invité
M. CHRISTIAN LATGE, CEA CADARACHE, Membre
Mme XUAN MI MEYER, TOULOUSE INP, Membre
M. REMY DUPRAZ, FRAMATOME, Membre
M. THIERRY GILARDI, CEA CADARACHE, Membre
M. XAVIER JOULIA, TOULOUSE INP, Membre

A Giuseppe

Remerciements

Tout d'abord, je voudrais remercier la Prof. Giulia Bozzano et le Prof. Eric Favre, qui ont accepté d'être les rapporteurs de cette thèse.

Un grand remerciement va à Pierrette Guichardon et Remy Dupraz, qui se sont rendus disponibles pour évaluer mon travail en tant que membres externes du jury.

Merci à ma directrice de thèse Xuan Meyer et au co-directeur Xavier Joulia de l'INP de Toulouse; malgré la distance, vous avez pu me suivre régulièrement et avec beaucoup de dévouement. Nos échanges ont toujours été très fructueux et m'ont permis d'avancer dans les travaux d'un point de vue scientifique avec grande qualité. J'ai beaucoup apprécié votre soutien et le temps que vous m'avez consacré et j'espère avoir accompli un travail digne de votre rigueur scientifique.

Merci à l'équipe encadrante du CEA, qui m'a accompagné pendant ces trois années: Aurélien Chassery, Thierry Gilardi et Christian Latgé.

Merci au laboratoire LMCT qui m'a accueilli et m'a permis de réaliser cette thèse. Merci à l'ancien chef de projet TECNA Lionel Cachon qui a financé mon activité expérimentale en faisant confiance en mes capacités. Malgré tout, j'espère que les résultats obtenus avec ces travaux pourront un jour être utiles pour le développement de réacteurs RNR-Na.

Ce travail est le fruit d'une collaboration de longue date entre le CEA et le Laboratoire de Génie Chimique de l'INP de Toulouse, et il n'aurait pas pu s'achever sans la contribution fondamentale de certaines personnes, appartenant aux deux institutions, que je tiens particulièrement à remercier ci-dessous.

Laurent Ayrault et le laboratoire LETS qui m'ont accueilli sur la boucle Superfennec et m'ont permis de réaliser toute la campagne expérimentale. Merci en particulier à Gwendal Blevin, Bruno Morassano, Pierre Charvet et Caroline Bomy pour le support technique.

Pierre Lamagnère qui a mis à disposition ses compétences en mécanique pendant la phase de conception du prototype afin de valider mes choix.

Aurore Mathieu, merci de m'avoir aidé, avec immense disponibilité et patience, à réaliser les manip au LMCT (pour lesquelles je remercie également le stagiaire Yohann Sotton). Même si les résultats obtenus n'ont pas été reportés dans le manuscrit, cette expérience en laboratoire a été fondamentale pour les tests effectués sur le vrai prototype et surtout c'était très agréable de travailler au quotidien avec toi.

Tous les experts avec lesquels j'ai eu des échanges techniques et scientifiques sur les technologies sodium et la perméation d'hydrogène: Laurent Brissonneau, Hélène Lorcet, Marianne Girard, Kevin Paumel, Daniele Vivaldi, Jean-Baptiste Genin. Merci en particulier à Thierry Gilardi qui, malgré l'engagement parallèle dans une autre thèse, a suivi mon travail avec intérêt, étant toujours disponible à des discussions intéressantes, et a fourni une relecture attentive et critique de mon manuscrit.

Remerciements

Les experts matériaux de l'INP avec lesquels j'ai eu des échanges très intéressants et qui m'ont donné des idées fondamentales pour l'interprétation des résultats: Laurent Cassayre, Christine Blanc, Eric Andrieu.

Tous les collaborateurs externes qui ont aidé à construire le prototype expérimental: les sociétés SDMS et ServInstrumentation, pour avoir collaboré avec moi de manière professionnelle, me permettant de fabriquer avec succès un prototype dans les délais impartis, satisfaisant toutes mes demandes.

Merci à Fabrice Michel de la société Vegatec pour les compétences qu'il m'a transmises sur les technologies du vide et sur la spectrométrie de masse. Sans sa contribution, je n'aurais pas pu obtenir des mesures aussi précises.

Enfin, je voudrais remercier de manière particulière deux personnes déjà mentionnées, sans lesquelles je n'aurais jamais pu terminer ce travail.

Le premier est Gwendal Blevin: pendant quelques mois nous avons passé chaque jour côte à côte à Superfennec et je me souviendrai avec plaisir de cette période (et de la combinaison orange!). Journées très chargées, commençant souvent tôt le matin et se terminant tard le soir pour finaliser tous les tests à temps, avec les imprévus toujours dans les parages. Sans ton expérience sur le terrain et ton efficacité à résoudre les problèmes techniques, je n'aurais jamais terminé toutes mes expériences juste deux semaines avant le confinement Covid, et cette thèse serait certainement moins riche.

La deuxième personne est Christian Latgé: en 2017, lorsque j'ai choisi de commencer un doctorat au CEA, il fut essentiel de te rencontrer. J'ai été frappé par ton enthousiasme pour la recherche et tes connaissances à 360°. Merci de m'avoir accompagné au fil des années, pour ton intérêt et pour les encouragements toujours présents du début à la fin. Surtout, merci pour ton dévouement pendant le confinement et la période de rédaction, qui ont probablement été les mois les plus durs: ta positivité et ta présence m'ont toujours réconforté et m'ont donné envie de continuer, surtout dans les moments les plus difficiles.

Cette thèse n'a pas été seulement une expérience professionnelle comme une autre, mais elle a impliqué pour moi des changements radicaux dans ma vie personnelle: j'ai démissionné d'un emploi d'ingénieur pour le désir de faire de la R&D, j'ai quitté ma famille et les amis d'une vie, je suis arrivé dans un nouveau pays dont je ne connaissais pas la langue et où je me suis senti souvent étranger. Je ne cache pas que tout cela, combiné aux difficultés de la thèse, m'a mis à l'épreuve à plusieurs reprises, m'amenant à me demander s'il valait la peine d'avoir pris ce choix. Ma réponse à la fin de cette aventure est «oui», mais je suis sûr que mon sens de responsabilité ainsi que ma passion pour le travail tous seuls, n'auraient jamais été suffisants pour me permettre de continuer. Je tiens donc à remercier toutes les personnes et amis, proches et lointains, qui m'ont toujours soutenu de manière souvent imprévisible, me faisant sentir chez moi et me permettant de ne pas lâcher prise.

Merci à Pierre, Vincent, Josselin, Aurore, Stéphanie, Assia pour votre soutien au labo et pour les moments ensemble en dehors du travail; merci à qui, au sein du LCMT, a contribué à rendre ma vie quotidienne au labo agréable.

Merci au groupe italien de Cadarache: les déjeuners du mardi m'ont toujours fait sentir un peu en Italie, malgré le menu de la cantine !

Remerciements

Merci à l'équipe de football ASCEA Cadarache, avec laquelle j'ai pu disputer une finale des Atomiades au stade de Varese Calcio (un rêve devenu réalité!).

Merci aux amis d'Aix en Provence, anciens et nouveaux, qui m'ont aidé à m'intégrer dans une nouvelle réalité et avec qui une véritable amitié est née: Vincent, Guillaume, Alexis, Emmanuelle et Jean-Baptiste, Paul et Marie-Liesse, Claire, Clotilde, Père Thomas, Marie-Aimée et Nicolas, Pauline et Jean-Gael, la Chorale Laetare, les alpins et tous les amis du Saint Esprit que je ne peux pas citer un par un.

Non moins importants sont tous les amis italiens cerveaux échappés, avec lesquels je partage ma vie d'expatrié et pas que: Francesco, Marco, Virgilio et Clara, Turo et Chiara, Bore et Fede, Charlie et Ila.

Merci à Mira: la plupart de ces trois ans, nous étions les deux seuls doctorants au laboratoire, et je pense qu'il y a certaines choses que seulement toi et moi pouvons comprendre. Nous nous sommes relayés pour nous tirer le moral vers le haut (ou vers le bas !), mais à la fin nous avons tous les deux réussi. Merci pour ton soutien, ta compagnie et ton amitié. Merci à Ziad de m'avoir supporté surtout les soirs où le thème « thésards en crise » prenait le dessus, pour les dîners, les discours sur le libano-italo-français; maintenant nous t'attendons ici dans le sud « gros ».

Merci à Silvio et Alessandra, Giulia et Pietro et Mati pour votre précieuse compagnie pendant ces derniers mois. Merci de m'avoir supporté de si près.

Merci Cavallo Ziggio d'avoir passé un an de « chevallades » folles avec moi à Aix, pour ton enthousiasme contagieux, pour les conquêtes à vélo, pour les huîtres, pour l'huile de truffe sur le banon, pour la "cazz'i sauercream", pour l'appartement et d'avoir été mon premier fils putatif; maintenant nous attendons ton retour à Aix avec impatience.

Merci à tous mes amis en Italie qui ont toujours été présents et continueront de le faire (merci aussi à Zoom® qui nous a fait sentir moins distants): Giulio et Sara, Antonio et Tamara, Pippio, Omar, Villo, tous les amis de la Fraternité Sanbuca, tous les amis de Bisuschio, Varese et Milan.

Merci à la Bovisa car si je n'étais pas passé par là, je ne serais pas ici aujourd'hui.

Merci à Don Silvano de m'avoir appris à aimer la vie, d'une manière jamais vu en personne d'autre.

Merci à ma famille: merci à mes parents de m'avoir tout donné, de m'avoir appris à vivre dans le monde, à travailler dur, avec humilité, et à apprécier les choses les plus simples de la vie. Merci de m'avoir donné l'opportunité d'étudier en suivant mes aspirations et de m'avoir toujours soutenu lorsque je devais faire des choix difficiles. Merci à ma sœur et mon frère, Pucci et Matteo: même si nous n'échangeons pas souvent, nous sommes toujours unis avec le cœur et c'est ce qui compte. Merci à ma grand-mère Adriana: je pense avoir appris de toi la ténacité et l'esprit de sacrifice qui m'ont permis d'arriver jusqu'ici. Bien que je ne vous le dise jamais, je vous aime tous et je vous dois tout.

Merci aussi à ma belle-famille, Giovanni et Angela, Giulio et Marta, pour m'avoir accueilli parmi vous comme un fils et comme un frère et pour nous accueillir à chaque fois avec une immense disponibilité. Merci de nous accompagner toujours avec affection et discrétion.

Dulcis in fundo, merci à la personne sans qui je n'aurais pas résisté plus que quelques mois. Merci à ma femme Anna, qui a tout accepté, de m'épouser, de venir en France, à la suite de ma folle intuition. En revanche, tu m'as donné toute toi-même et plus encore. Merci de m'avoir supporté en cette expérience. On le sait tous les deux, tu as été souvent le rocher qui m'a permis de pas m'effondrer

Remerciements

dans les moments les plus durs. Nous avons tous les deux beaucoup appris au fil de ces trois ans et maintenant c'est à moi de te suivre: une nouvelle aventure va bientôt commencer, non sans incertitudes, mais je suis certain (et je n'ai pas de raisons de croire le contraire, vu tout le bien qu'on a déjà reçu) que le chemin sera beau et fascinant.

Ringraziamenti

Innanzitutto, vorrei ringraziare la Prof. Giulia Bozzano e il Prof. Eric Favre, che hanno accettato di essere rapporteur di questa tesi.

Un ringraziamento sentito va a Pierrette Guichardon e Remy Dupraz, che si sono resi disponibili a valutare il mio lavoro come membri esterni della giuria.

Grazie alla direttrice della tesi Xuan Meyer e al co-direttore Xavier Joulia dell'INP di Tolosa; nonostante la distanza geografica avete potuto seguirmi con regolarità e con grande dedizione. I nostri scambi sono sempre stati molto fruttuosi e mi hanno permesso di avanzare nel lavoro da un punto di vista scientifico con grande qualità. Ho apprezzato molto la vostra attenzione e il tempo dedicatomi e spero di aver svolto un lavoro all'altezza del vostro rigore scientifico.

Grazie all'equipe encadrante del CEA, che mi ha accompagnato in questi tre anni: Aurélien Chassery, Thierry Gilardi e Christian Latgé.

Grazie al laboratorio LMCT che mi ha accolto e mi ha permesso di realizzare questa tesi ; grazie all'ex responsabile del progetto TECNA Lionel Cachon che ha finanziato la mia attività sperimentale e mi ha dato fiducia. Nonostante tutto, spero che i risultati ottenuti con questo lavoro possano un giorno essere utili allo sviluppo dei reattori RNR-Na.

Questo lavoro è frutto di una collaborazione di lunga data tra CEA e Laboratoire de Génie Chimique dell'INP di Tolosa, e non avrebbe potuto realizzarsi senza il contributo fondamentale di alcune persone, appartenenti a entrambe le istituzioni, che tengo a ringraziare particolarmente qui di seguito.

Laurent Ayrault e il laboratorio LETS che mi ha ospitato sulla boucle Superfennec e mi ha permesso di realizzare tutta la campagna sperimentale. Grazie in particolare a Gwendal Blevin, Bruno Morassano, Pierre Charvet e Caroline Bomy per il supporto tecnico.

Pierre Lamagnère che ha messo a disposizione le sue competenze in meccanica in fase di design per validare le mie scelte.

Aurore Mathieu, grazie per la tua disponibilità e la tua pazienza nell'aiutarmi a realizzare gli esperimenti al LMCT (per cui ringrazio anche lo stagista Yohann Sotton). Anche se i risultati ottenuti non sono stati scritti nella tesi, questa esperienza in laboratorio è stata fondamentale per i test realizzati sul vero prototipo e soprattutto è stato molto piacevole lavorare con te.

Tutti gli esperti con cui ho avuto degli scambi a livello tecnico e scientifico riguardo alle tecnologie Sodio e alla permeazione dell'idrogeno: Laurent Brissonneau, Hélène Lorcet, Marianne Girard, Kevin Paumel, Daniele Vivaldi, Jean-Baptiste Genin. Grazie in particolare a Thierry Gilardi che, nonostante l'impegno parallelo su un'altra tesi, ha seguito sempre con interesse il mio lavoro, è sempre stato disponibile a interessanti discussioni e ha fornito una rilettura attenta e critica del mio manoscritto.

Gli esperti di materiali dell'INP con cui ho avuto scambi interessantissimi e che mi hanno dato spunti fondamentali per l'interpretazione dei risultati : Laurent Cassayre, Christine Blanc, Eric Andrieu.

I collaboratori esterni che hanno contribuito a costruire il prototipo sperimentale : le società SDMS e ServInstrumentation per aver collaborato con me in modo professionale, permettendomi di fabbricare con successo un prototipo nei tempi stabiliti, assecondando tutte le mie richieste.

Fabrice Michel della società Vegatec per le competenze che mi ha trasmesso in materia di vuoto e spettrometria. Senza il suo contributo non avrei potuto ottenere misure così accurate.

Infine, vorrei ringraziare in modo speciale due persone già citate, senza le quali mai avrei potuto portare a termine questo lavoro. La prima è Gwendal Blevin: per qualche mese abbiamo passato fianco a fianco tutti i giorni a Superfennec e mi ricorderò con piacere di questo periodo (e della tuta arancione!). Giornate molto intense, spesso cominciate al mattino presto e terminate tardi la sera per realizzare in tempo tutti i test, con gli imprevisti sempre dietro l'angolo. Senza la tua esperienza sul terreno e la tua efficacia nel risolvere i problemi tecnici non avrei mai terminato tutti i miei esperimenti giusto due settimane prima del lockdown Covid, e questa tesi sarebbe sicuramente meno ricca.

La seconda persona è Christian Latgé: nel 2017 quando scelsi di iniziare un PhD al CEA è stato fondamentale incontrarti. Restai colpito dal tuo entusiasmo per la ricerca e dalle tue conoscenze a 360°. Grazie per avermi accompagnato in questi anni, per il tuo interesse e i tuoi incoraggiamenti dall'inizio alla fine. Soprattutto grazie per la tua dedizione durante il periodo del lockdown e della redazione, che sono stati forse i mesi più duri: la tua positività e la tua presenza mi hanno sempre confortato e dato voglia di continuare, soprattutto nei momenti più difficili.

Questa tesi non è stata soltanto un'esperienza professionale qualunque, ma ha comportato per me dei cambiamenti radicali nella mia vita personale: ho dato le dimissioni da un lavoro da ignorare per il desiderio di fare della R&D, ho lasciato famiglia e amici di una vita, sono arrivato in un nuovo paese di cui non conoscevo la lingua e in cui spesso mi sono sentito straniero. Non nascondo che tutto ciò, unito alle difficoltà della tesi, mi ha messo alla prova più volte, portandomi a domandarmi se fosse valsa la pena intraprendere questa strada. La mia risposta alla fine di questa avventura è « sì », ma sono sicuro che il mio senso di responsabilità e la passione per quello che facevo, da soli non sarebbero mai stati sufficienti a farmi continuare. Perciò voglio ringraziare tutte quelle persone e amici, vicini e lontani, che in modo spesso imprevedibile mi hanno sempre sostenuto, facendomi sentire a casa anche qui e permettendomi di non mollare.

Grazie a Pierre, Vincent, Josselin, Aurore, Stéphanie, Assia per aver reso la vita di tutti i giorni al laboratorio più piacevole.

Grazie al gruppo italiano di Cadarache : i pranzi del martedì mi hanno fatto sempre sentire un po' in Italia, nonostante il menu' della cantina.

Grazie alla squadra di calcio ASCEA Cadarache, con cui ho potuto giocare una finale delle Atomiadi nello stadio del Varese Calcio (un sogno che si realizza !).

Grazie agli amici di Aix en Provence, vecchi e nuovi, che mi hanno aiutato a integrarmi in una realtà nuova e con cui è nata una vera amicizia : Vincent, Guillaume, Alexis, Emmanuelle e Jean-Baptiste, Paul e Marie-Liesse, Claire, Clotilde, Père Thomas, Marie-Aimée e Nicolas, Pauline e Jean-Gael, la Chorale Laetare, il coro alpino e tutti gli amici di Saint Esprit che non posso citare ad uno ad uno.

Non meno importanti tutti gli amici italiani cervelli in fuga con cui condivido la vita da espatriati e non solo: Francesco, Marco, Virgilio e Clara, Turo e Chiara, Bore e Fede, Charlie e Ila.

Ringraziamenti

Grazie a Mira : siamo stati per la maggior parte del tempo i due soli tesisti del laboratorio, e credo che ci sono certe cose che solo io e te possiamo capire. Abbiamo fatto a turno a tirarci su (o giù) il morale a vicenda ma alla fine ce l'abbiamo fatta tutti e due. Grazie per il sostegno, la compagnia e la tua amicizia. Grazie a Ziad per aver sopportato anche me nelle serate in cui l'argomento « tesisti in crisi » prendeva il sopravvento, per le cene, i discorsi sui libano-italo-francesi; adesso ti aspettiamo qui al sud gros.

Grazie a Silvio e Alessandra, Giulia e Pietro e Mati per la vostra preziosa compagnia degli ultimi mesi. Grazie per avermi sopportato così da vicino.

Grazie Cavallo Ziggio per aver passato insieme un anno di scavallate folli a Aix, per il tuo entusiasmo contagioso, per le imprese ciclistiche, per le ostriche, per gli oli al tartufo sui banon, per la « cazz'i sauercream », per la casa e per essere stato il mio primo figlio putativo; ora aspettiamo con ansia il tuo ritorno.

Grazie a tutti i miei amici in Italia che ci sono sempre stati e continueranno a farlo, (grazie anche a Zoom® che ci ha fatto sentire meno lontani): Giulio e Sara, Antonio e Tamara, Pippio, Omar, Villo, tutti gli amici della Fraternità Sanbuca, tutti gli amici di Bisuschio, di Varese e di Milano.

Grazie alla Bovisa perchè se non fossi passato di lì, oggi non sarei qui.

Grazie al Don Silvano, per avermi insegnato ad amare la vita in un modo che non ho ancora visto fare a nessun altro.

Grazie alla mia famiglia : grazie ai miei genitori per avermi dato tutto, per avermi insegnato a stare al mondo, a lavorare sodo, con umiltà ed ad apprezzare le cose più semplici della vita. Grazie per avermi dato la possibilità di studiare seguendo le mie aspirazioni e per avermi sempre sostenuto anche quando ho dovuto intraprendere scelte difficili. Grazie a mia sorella Pucci e mio fratello Matteo: anche se non ci sentiamo spesso, siamo sempre uniti con il cuore e questo è ciò che conta. Grazie alla mia Nonna Adriana: credo di avere imparato da te la tenacia e lo spirito di sacrificio che mi hanno portato sin qui. Anche se non ve lo dico mai, vi voglio bene e vi devo tutto.

Grazie anche alla mia famiglia acquisita, Giovanni e Angela, Giulio e Marta, per avermi accolto tra voi come un figlio e fratello e per accoglierci ogni volta con immensa disponibilità. Grazie per accompagnarci sempre con affetto e discrezione.

E *dulcis in fundo*, grazie alla persona senza la quale non avrei resistito più di qualche mese. Grazie a mia moglie Anna, per aver accettato tutto, di sposarmi, di venire in Francia, seguendo me e il mio folle intuito. In cambio mi hai dato tutta te stessa e anche di più. Grazie per avermi supportato e sopportato sempre in questa esperienza. Lo sappiamo tutti e due, spesso sei stata tu per me la roccia che mi ha permesso di non crollare nei momenti più difficili. Abbiamo entrambi imparato molto in questi anni e ora è il mio turno di seguirti: una nuova avventura inizierà presto, non senza incertezze, ma sono sicuro (e non ho ragione di credere il contrario, visto tutto il bene che abbiamo già ricevuto) che sarà un cammino bello e affascinante.

Table of contents

Remerciements	iii
Ringraziamenti	vii
Table of contents.....	x
List of figures.....	xiii
List of tables	xvii
Nomenclature	xix
General introduction	xxiii
1 Context and motivations	1
1.1 Sodium cooled Fast Reactors (SFR): impact studies, necessity to master the tritium release to environment.....	2
1.2 ASTRID project – Brayton cycle case: tritium issue.....	5
1.3 Thesis subject and motivation	7
2 State of the art	9
2.1 Hydrogen permeation through metals	10
2.2 Hydrogen-Nickel permeation	25
2.3 Hydrogen-Sodium system.....	34
2.4 Hydrogen-Nickel-Sodium permeation applications: state of art	36
3 Experimental methods	41
3.1 Motivation and goals	42
3.2 Prototype design	42
3.3 Experimental setup.....	57
3.4 Measurement techniques	62
3.5 Conclusion	68
4 Experimental results	71
4.1 Test procedure and tested conditions	72
4.2 Measurement techniques validation on the gas-vacuum system	74
4.3 Results post treatment methods	78
4.4 Permeation’s law assessment.....	81
4.5 Gas-sodium test: permeate (sodium) side measurements	85
4.6 Discussion on results	91
4.7 Conclusion	105

Table of contents

5	CFD Study.....	109
5.1	Motivation and goals.....	110
5.2	Model's equations and parameters.....	110
5.3	Geometry and mesh.....	114
5.4	Simulation cases and solver settings.....	116
5.5	Results.....	117
5.6	Comparison with 1-D model and experimental results.....	127
5.7	Conclusion.....	128
5.8	Annex: summary of model's hypotheses, equations, parameters and variables.....	130
	Conclusions and perspectives.....	141
	Bibliography.....	145
	Annexes.....	149
I.	Analytical resolution of the 1D model on the radial direction.....	150
II.	Gas supply system PID diagram.....	151
III.	Residual gas analysis (RGA) technique.....	152
IV.	Experimental uncertainties and data reconciliation.....	159
V.	Integrated permeation law demonstration.....	167
VI.	Hydrogen equilibrium at the sodium-cover gas interface.....	168

List of figures

Figure 1-1 Scheme of a SFR reactor: tritium production source and transport.....	2
Figure 1-2 Hydrogen solubility in sodium according to Wittingham [2]	5
Figure 2-1. Permeation across different domains: gas-metal-gas (a) and gas-metal-liquid (b)	12
Figure 2-2 Scheme of hydrogen permeation through metals [18]	13
Figure 2-3 Palladium-hydrogen phase diagram [20].....	15
Figure 2-4 Hydrogen permeation physics in a gas-metal-gas configuration with pure hydrogen on both membrane's sides	18
Figure 2-5 Hydrogen-metal solubilities as function of temperature at hydrogen pressure of 1 bar	22
Figure 2-6 Hydrogen-metal enthalpies of solution [20].....	22
Figure 2-7 Hydrogen-metal solubility and permeability [19].....	23
Figure 2-8 Hydrogen-metal diffusivity [20].....	23
Figure 2-9 Permeation transient in a Nickel membrane (122 micron) : comparison between theoretical 2 nd Fick's law solution and experimental results [30].....	24
Figure 2-10 Hydrogen-metal permeability dependence with temperature[37].....	25
Figure 2-11 Ni-H phase diagram at high pressures [42]	27
Figure 2-12 Ni-H phase diagram at low pressures [43].....	27
Figure 2-13 H-Ni solubility isobar lines (55 mbar-185 mbar-1 bar) between 200°C and 500°C. Comparison between Bourgeois' model [43] and solubility calculated with main literature coefficients	28
Figure 2-14 H-Ni diffusivity : calculated values for temperatures 300°C-500°C from the main literature coefficients.....	29
Figure 2-15 H-Ni permeability : calculated values for temperatures 300°C-500°C from the main literature coefficients	31
Figure 2-16 Pressure-composition phase diagram for Na-H system [62]	35
Figure 2-17 Hydrogen activity-meter by Vissers [7]	37
Figure 2-18 SPHYNX system for hydrogen detection.....	38
Figure 2-19 On-line hydrogen meter calibration system [70].....	40
Figure 3-1 Hydrogen permeation physics in a shell and tube gas-Na configuration membrane	45
Figure 3-2 Schematic diagram of mass transfer resistance with electrical analogy	47
Figure 3-3 Temperature effect on hydrogen mass transfer: mass transfer coefficients in gas, nickel, sodium (a) and global mass transfer rate per unit length (b)	50
Figure 3-4 Gas flowrate effect on hydrogen mass transfer: mass transfer coefficients in gas, nickel, sodium (a) and global mass transfer rate per unit length (b)	50
Figure 3-5 Gas pressure effect on hydrogen mass transfer: mass transfer coefficients in gas, nickel, sodium (a) and global mass transfer rate per unit length (b)	51
Figure 3-6 Influence of Na velocity on mass transfer resistances of gas, Ni and Na phase, for three membrane thickness 50 µm (c), 150 µm (b) and 300 µm(a). Influence of thickness on the global mass transfer rate per unit length (d).	52
Figure 3-7 Hydrogen bulk concentration of gas (a) and Na (b) phase influence on mass transfer rate per unit length.....	53

Figure 3-8 Discretization of the radial hydrogen mass transfer along the membrane length	55
Figure 3-9 Permeator prototype: before installation (a) and section view (b)	56
Figure 3-10 Superfennec overview	57
Figure 3-11 Superfennec sodium loop simplified diagram: circulation plan and main components. Cold trap (CT), Test Section (TS), Plugging Indicator (PI) and Heating Tank (HT)	58
Figure 3-12 Gas-sodium permeation: test section diagram	59
Figure 3-13 Test section before (a) and after (b) installation for gas-sodium test: details of sodium side (orange), gas side (blue) and UHV side (green)	59
Figure 3-14 Gas-vacuum permeation: test section diagram	60
Figure 3-15 Test section installed for gas-vacuum test: details of gas supply system (blue) and UHV (green) connections	60
Figure 3-16 RGA system diagram	62
Figure 3-17 RGA system installation on Superfennec	62
Figure 3-18 Thermocouples positions on permeator	63
Figure 3-19 Permeator simplified diagram: application of total and hydrogen molar balances	65
Figure 4-1 Typical pressure gauge signal evolution during a gas-vacuum permeation test	74
Figure 4-2 Gas-vacuum test - Hydrogen permeation vs gas pressure: μ GC (a) and pressure gauge (b) measurements	75
Figure 4-3 Hydrogen permeation vs temperature: μ GC (a) and pressure gauge (b) measurements	75
Figure 4-4 Gas-vacuum test - Comparison between μ GC and pressure gauge measurements of hydrogen permeation flowrate for T_{mean} 293°C to 434°C	76
Figure 4-5 μ GC relative standard uncertainty on hydrogen permeation flowrate measurements	77
Figure 4-6 Gas-vacuum test - Percentage deviation between reconciled data and experimental measurements with μ GC (a) and pressure gauge (b)	78
Figure 4-7 Gas-vacuum test - Hydrogen permeation flowrate vs mean partial pressure square root: RD for temperatures from T1 to T7 with regression lines	81
Figure 4-8 Gas-vacuum test - $QH_2, p/A\delta$ ratio vs mean partial pressure square root: permeability coefficient determination from T1 to T7	82
Figure 4-9 Gas-vacuum test - $\ln(p_e)$ vs $1/T$: permeability law with temperature	82
Figure 4-10 Gas-sodium test - Hydrogen permeation flowrate vs mean partial pressure square root: μ GC measurements for temperatures from 375°C to 450°C with regression lines	84
Figure 4-11 Gas-sodium test - $QH_2, p/A\delta$ ratio vs mean partial pressure square root: permeability coefficient determination from 375°C to 450°C	84
Figure 4-12 Gas-sodium test - $\ln(p_e)$ vs $1/T$: permeability law with temperature	85
Figure 4-13 Gas-sodium test: plugging indicator (PI) temperature (green) and sodium flowrate (blue) evolution during sodium purification	86
Figure 4-14 Hydrogen-meter permeability estimation : experimental measurements of SMS, H_2 at different temperatures for a given hydrogen concentration inside sodium	87
Figure 4-15 Gas-sodium test: DH-mass spectrometer signal evolution during a single permeation test (T7-P8)	88
Figure 4-16 Gas-sodium test: DH-signal evolution during sodium purification between two permeation tests (T7-P2 and T7-P3)	89

Figure 4-17 Gas-sodium test, QH_2, p measurements : comparison between μGC and QMS measurements at 375°C (a), 400°C (b), 425°C (c) and 450°C (d)	90
Figure 4-18 Hydrogen permeation flowrate vs mean partial pressure square root: comparison between gas-vacuum and gas-sodium results.....	91
Figure 4-19 $\ln(p_e)$ vs $1/T$: permeability law with temperature – comparison between gas-vacuum and gas-sodium test. Estimation of an equivalent temperature for gas-vacuum test.....	92
Figure 4-20 $\ln(p_e)$ vs $1/T$: permeability law with temperature - comparison between main literature and gas-sodium experimental results	94
Figure 4-21 Experimental hydrogen permeation rates compared with hydrogen-nickel solubility on isotherm lines (375, 400, 425 and 450°C) given by Bourgeois’ model[43]	96
Figure 4-22 Hydrogen permeation flowrate vs mean partial pressure square root: comparison between gas-sodium experimental results, 1D model and integrated permeation law. Model’s permeability coefficient is taken from Robertson “Best fit”[44]	99
Figure 4-23 Hydrogen permeation flowrate vs mean partial pressure square root: comparison between gas-sodium experimental results and integrated permeation law. The law’s permeability coefficient is taken from experimental results regression	100
Figure 4-24 Gas-sodium test - Hydrogen permeation flowrate vs mean partial pressure square root: μGC measurements for temperatures from 375°C to 450°C with regression lines in the form “ $y=ax+b$ ”	101
Figure 4-25 Gas-sodium test - Hydrogen permeation flowrate vs mean partial pressure square root: experimental measurements (Exp) with regression “ $y=ax$ ” (solid) and regression “ $y=ax+b$ ” (dashed)	102
Figure 5-1 Schematic representation of the physical domains for the CFD study	111
Figure 5-2 Geometry comparison between CFD study (a) and experimental prototype (b). Gas phase is marked in blue and sodium phase in orange.	114
Figure 5-3 CFD study mesh: coarse (a) and fine (b)	116
Figure 5-4 CFD study: radial profiles of gas (a) and sodium (b) velocity at inlet, half tube and outlet	118
Figure 5-5 CFD study: hydrogen concentration radial profiles in gas (a) and sodium (b) at inlet, half tube and outlet. Axial profiles at the membrane’s boundary in gas (c) and sodium (d).	119
Figure 5-6 CFD study: axial profile of hydrogen permeation flux at the membrane’s boundary	120
Figure 5-7 CFD study: axial profile of hydrogen partial pressure [$Pa^{0.5}$] at the membrane’s boundary in gas (blue) and sodium (green) phase. The difference is marked in red.	121
Figure 5-8 Mesh refinement study - H mass fraction radial and axial profiles in sodium for three mesh refinements: coarse (a, b), normal (c, d) and fine (e, f)	123
Figure 5-9 Sodium flowrate sensitivity study - Na velocity and mass fraction radial profiles for three Q_{Na} [m^3h^{-1}]: 0.075 (a, b), 0.125 (c, d), 0.375 (e, f).....	125
Figure 5-10 Gas flowrate sensitivity study - Na velocity and mass fraction radial profiles for three Q_{gas} [$Nml\ min^{-1}$]: 25 (a, b), 100 (c, d), 200 (e, f).....	127
Figure 5-11 CFD study: permeation flowrate (x4 tubes) against hydrogen mean partial pressure square root in gas phase. Comparison with 1D model for all simulated cases	128
Figure 0-1 QMS principle.....	153
Figure 0-2 Pressure Gauge Bayard-Alpert principle.....	154

List of figures

Figure 0-3 Hydrogen equilibrium at the Na-Ar interface, calculated at 450°C for a hydrogen injection of 200 ppb168

List of tables

Table 2-1 Sieverts constant for H-Ni system.....	28
Table 2-2 H-Ni solubility [H/Ni] at 400°C and 55 mbar-185 mbar-1 bar. Comparison between Bourgeois’ model [43] and solubility calculated with main literature coefficients	29
Table 2-3 Diffusivity coefficients for H-Ni system.....	29
Table 2-4 Permeability coefficients for H-Ni system	30
Table 2-5 H-Ni permeability : calculated values for 300°C-350°C-400°C-450°C with main literature coefficients.....	30
Table 2-6 Literature studies concerning possible permeation deviation from Richardson’s law	32
Table 3-1 Design constraints of the SFR (as established in initial Astrid design)	43
Table 3-2 Mass transfer resistance model’s parameters and variables.....	48
Table 3-3 1D model sensitivity analysis: main parameters variation range.....	49
Table 3-4 1D model sensitivity analysis: physical parameters impact on permeation	54
Table 3-5 Driving parameters for the permeator prototype design	55
Table 3-6 Ni201 tubes diameter and thickness available commercial combination (source Goodfellow)	55
Table 3-7 Temperature measurements during gas tests and sodium tests.....	63
Table 3-8 observed variables and physical parameters of the experimental study.....	68
Table 4-1 Gas-vacuum test: tested conditions temperature and gas pressure	72
Table 4-2 Gas-sodium test: tested conditions temperature and gas pressure	73
Table 4-3 Gas-vacuum temperature assessment: mean and equivalent temperature values	92
Table 4-4 Permeability pre-exponential factors, activation and calculated values between 375°C and 450°C. Comparison between main literature, gas-sodium experimental results for the permeator prototype and hydrogen-meter	94
Table 5-1 Summary of bulk and interfacial hydrogen molar concentrations [mol m ⁻³] on the gas, membrane and sodium domains.....	111
Table 5-2 Comparison between CFD study and experimental main dimensions and flow features at 450°C.....	115
A sensitivity study on the mesh refinement is presented in Section 5.5.3.1, which justify the use of the “normal” mesh four our simulations. Table 5-3 CFD study mesh: main elements of coarse, normal and fine meshes	116
Table 5-4 CFD study: simulated cases and input parameters	117
Table 5-5 CFD study - Hydrogen permeation flowrates [mol s ⁻¹] evaluated according to three different methods	122
Table 5-6 Sodium flowrate sensitivity study: simulated cases with related values of sodium flowrate, velocity, Re and hydrogen permeation flow	124
Table 5-7 Gas flowrate sensitivity study: simulated cases with related values of gas flowrate, velocity, Re; hydrogen partial pressure and permeation flow	126
Table 0-1 Hydrogen molar flowrate calculation methods in the RGA system	155
Table 0-2 Data reconciliation parameters	159
Table 0-3 List of measured and non-measured variables for gas test	166



Nomenclature

LATIN LETTERS		
	<i>Description</i>	<i>Units</i>
<i>A</i>	Membrane surface	m ²
<i>C</i>	Molar concentration	mol m ⁻³
<i>D</i>	Diffusivity	m ² s ⁻¹
<i>D₀</i>	Diffusivity : pre-exponential constant	m ² s ⁻¹
<i>d</i>	Diameter	m
<i>d_h</i>	Hydraulic diameter	m
<i>d_o</i>	External diameter	m
<i>E</i>	Turbulent dissipation	
<i>E_d</i>	Diffusion activation energy	J mol ⁻¹
<i>E_S</i>	Dissolution activation energy	J mol ⁻¹
<i>E_p</i>	Permeation activation energy	J mol ⁻¹
<i>h</i>	Mass transfer coefficient	m s ⁻¹
<i>J</i>	Molar flux per unit surface	mol m ⁻² s ⁻¹
<i>K</i>	Turbulent kinetic energy	
<i>k</i>	Equilibrium constant	
<i>K_{MS}</i>	Mass spectrometer calibration constant	(mol s ⁻¹) Torr ⁻¹
<i>K_P</i>	Pressure gauge calibration constant	(mol s ⁻¹) mbar ⁻¹
<i>K_S</i>	Sievert constant	mol m ⁻³ Pa ^{-0.5}
<i>K_{S0}</i>	Sievert constant : pre-exponential factor	mol m ⁻³ Pa ^{-0.5}
<i>L</i>	Length	m
<i>M</i>	Mass	kg
<i>MM</i>	Molar mass	g mol ⁻¹
<i>ṁ</i>	Mass flowrate	kg s ⁻¹
<i>N_{TUBES}</i>	Number of membrane tubes	
<i>P</i>	Pressure	Pa
<i>pe</i>	Permeability	mol m ⁻¹ s ⁻¹ Pa ^{-0.5}
<i>pe₀</i>	Permeability : pre-exponential constant	mol m ⁻¹ s ⁻¹ Pa ^{-0.5}
<i>Q</i>	Molar flowrate	mol s ⁻¹
<i>R</i>	Gas constant	J mol ⁻¹ K ⁻¹
<i>r</i>	Radius	m
<i>r_i</i>	Membrane internal radius	m
<i>r_o</i>	Membrane external radius	m
<i>r_m</i>	Membrane mean radius	m
<i>r_{sh}</i>	Shell radius	m
<i>Re</i>	Reynolds number	
<i>S</i>	Solubility	mol m ⁻³ or atom fraction
<i>Sc</i>	Schmidt number	

Nomenclature

S_{MS}	Mass spectrometer signal	Torr
T	Temperature	K
t	Time	s
t_{perm}	Permeation time	s
U	Equivalent mass transfer coefficient	$m^2 s^{-1}$
V	Volume	m^3
v	Gas velocity	$m s^{-1}$
\dot{V}	Volumetric flowrate	$m^3 s^{-1}$
v_{PI}	Pumping speed of ionic pump	$m^3 s^{-1}$
w	Na velocity	$m s^{-1}$
x	Spatial coordinate	m
X_i	Molar fraction of i-component in a solution or mixture	mol; mol ⁻¹ or %
y_i	Mass fraction of i-component in a solution or mixture	kg; kg ⁻¹ or wppm
GREEK LETTERS		
	<i>Description</i>	<i>Units</i>
δ	Membrane thickness	m
μ	Dynamic viscosity	Pa s
μ_T	Turbulent viscosity	
ρ	Density	kg m ⁻³

SUBSCRIPTS	
in	Permeator inlet side
r	Permeator retentate side
p	Permeator permeate side
f	Permeator feed side
DH	“Détection Hydrogène” or Hydrogen meter
QMS or MS	(Quadrupolar) Mass spectrometer
IP	Ionic Pump
TP	Turbo-molecular Pump
gas	Gas phase
Na	Sodium phase
Ni	Nickel membrane
H	Atomic hydrogen
H ₂	Molecular hydrogen
Ar	Argon
H ₂ ,gas	Molecular hydrogen inside a gas mixture
H,Ni	Atomic hydrogen inside Nickel
H,Na	Atomic hydrogen inside sodium
z	Permeator axial coordinate
r	Permeator radial coordinate
SUPERSCRIPTS	
s	At saturation point
*	At interface with the membrane

ACRONYMS	
SFR	Sodium cooled Fast Reactors
CEA	Commissariat à l'énergie atomique et aux énergies alternatives
ECS	Energy Conversion System
IHX	Intermediate Heat Exchanger
SGU	Steam Generator
ASTRID	Advanced Sodium Technological Reactor for Industrial Demonstration
T	Tritium
CT	Cold trap
ANL	Argonne National Laboratory
TS	Test Section
PI	Plugging Indicator
HT	Heating Tank
DH	Hydrogen-meter
PTC	Pressure Transmitter and Controller
FTC	Flow Transmitter and Controller
QMS	Quadrupolar Mass Spectrometer
μGC	Gas Chromatograph
UHV	Ultra-High-Vacuum
PT	Pressure Transmitter
TT	Temperature Transmitter
PSV	Pressure Security Valve
RGA	Residual Gas Analysis
BA P Gauge	Bayard-Alpert Pressure Gauge
RD	Reconciled Data
IP	Ionic Pump
TP	Turbomolecular Pump

General introduction

As author of this thesis, I would like to address some introductory remarks to the readers, in order to give them an idea of the guidelines and the interests which accompanied me, under the constant supervision of my directors, all along the development of this work. The results obtained during these years and the way to present them in this manuscript, reflect a deep commitment in trying to conciliate the scientific subjects with the specific technical application dedicated to the development of Sodium Fast Reactors, which actually is at the origin of this research work.

The main objective of the work presented here is to study and model the entire hydrogen mass transfer process from a gas mixture to liquid sodium, including the permeation through a metallic membrane, which should provide a controlled hydrogen supply to the liquid sodium phase. The final goal is to have a global understanding of the main phenomena involved (from both a theoretical and experimental point of view) and to provide a validated simulation tool to enhance the development of an associated technological option.

This subject, due to the implication of different physico-chemical phenomena, offered at the beginning several possible approaches: the micro-scale hydrogen-metal interaction analysis, the hydrogen-sodium chemistry, the mechanical behavior of the manufactured nickel membrane, the thermodynamics, the overall integrated process. Trying to take into account all the above-cited approaches, which a priori could have a fundamental impact, the attention has been mainly focused on the study of the hydrogen global mass transfer process from a macroscopic point of view. A particular emphasis has been given to the experimental part: in fact, when we look a process in its entirety, it is always difficult to integrate an in-depth numerical and theoretical analysis of all the aspects of the problem. Therefore, in order both to obtain a better understanding of the physico-chemical phenomena involved and to achieve an industrial objective, the attempt was to be very pragmatic, by developing an experimental study on a prototype at the pilot-scale. In this way, the obtained results could be integrated in an industrial scale-up process.

The theoretical approaches as well as the modeling activity, have been largely involved in our study, in order to establish a better phenomenological comprehension and to assess a simulation tool, aimed to be in the future the basis of a design support tool. The maximum effort has been done in order to include the main physical processes, having a potential impact on the global hydrogen permeation process, according to the up to date knowledge resulting from an in-depth literature state of the art review. We found that this effort has produced results comparable with the experimental activity, under certain operating conditions. This experimental-modeling comparison approach could be a first important step in supporting the development of a design tool and later engineering of an industrial application.

Nevertheless, following the scientific questioning, a strong commitment has been engaged in trying to explain some unattended behaviors, appeared during the experimental activity in a certain range of operating conditions. Different potential causes have been investigated and several questions have raised. Of course, the models here developed can not be exhaustive, because some hypothesis and simplifications are made. Since the focus at the beginning of this study was put more on a macroscopic process approach, a lack of information appears in the description of micro-scale phenomena

occurring inside the membrane and at its surface, which could be most probably the reasons of the observed deviations. Due to the complexity of this aspect, belonging more to the field of the materials expertise, we could only propose at the end of this work some interpretations and hypotheses, which could open new tracks of research, if it is necessary to extend the operational domain of the permeation device.

Finally, this investigative approach on the unattended results has stimulated insights and rich discussions, providing interesting suggestions to be proposed for further studies in perspective.

The present manuscript has been structured in different Chapters as follows:

1. Context and motivation
2. State of the art review
3. Experimental methods
4. Experimental results
5. CFD study

Chapter 1 presents the Sodium Fast Reactors (SFR) features and the associated R&D critical issues, describing the context and the technical reasons for which this study has been proposed.

The state of the art review, presented in Chapter 2, gives a global comprehension of the physical phenomena that play a role into the hydrogen mass transfer process, with a main focus on the permeation through metals. Moreover, it presents the laws and models that describe the hydrogen-sodium interaction in a SFR application's operating conditions and identifies the key parameters that drive the overall process. Comparison with existing similar applications and membrane's material choice is also a key point of this part.

The experimental activity at pilot-scale, aims to verify the validity of the models applied to describe the permeation through a permeator prototype, as well as to obtain quantitative results in terms of permeability coefficients of the chosen material. At the same time, the objective is to evaluate the overall performances of the prototype into an experimental sodium loop, working under operating conditions typical of a SFR. Hence, the prototype and the related integrated process are validated for industrial scale-up.

The experimental facilities and methods, the measurement techniques and a 1D analytical model, based on a multi-physics approach, supporting the prototype design activity, are presented in Chapter 3.

Chapter 4 reports the experimental results, their comparison with the theoretical models and the literature, together with a detailed analysis and a final critical discussion.

CFD simulations, performed in a 2D axisymmetric domain with the software COMSOL Multi-physics, allow a better understanding of the transport phenomena taking place and provide a benchmark for the validation of the more elementary analytical model. The results are presented in Chapter 5.

Finally, the main results obtained and the perspectives on the industrial scale-up of the permeator are resumed in the Conclusion chapter.

Chapter

1 Context and motivations

1.1 Sodium cooled Fast Reactors (SFR): impact studies, necessity to master the tritium release to environment

Among Fast Neutron Reactor Systems, developed within the framework of the Generation IV Nuclear Reactors, the Sodium cooled Fast Reactor (SFR) has the most comprehensive technological basis, thanks to the experience gained from worldwide operation of several experimental, prototype, and commercial size reactors since the 1940s. This experience corresponds to about 40 years of operation by end of 2017. Nevertheless, several studies are still carried out at CEA to demonstrate some innovative options and to improve its reliability, operability and safety. This reactor uses liquid sodium as a coolant to transport the energy produced by the fission reactions from the core to the Energy Conversion System (ECS). To do this, two main sodium circuits are set up (cf. Figure 1-1):

- the primary circuit, a “pool type” vessel directly in contact with the fuel assemblies to extract thermal energy from them and to control the temperature of the hot and cold plenum. It is characterized by the presence of Intermediate Heat Exchangers and Primary Pumps, immersed in the primary sodium.
- the secondary circuit, a closed loop where the liquid Na circulates and transfers thermal energy from the primary sodium to the tertiary loop, so-called Energy Conversion System (ECS), by means of two distinct heat exchangers.

In a standard configuration, the tertiary loop is basically a steam/water circuit connected to a steam turbine which converts the thermal energy received from the sodium into mechanical and electrical power. The thermal exchange between the secondary sodium and the water cycle takes place into a steam generator (SGU). This Steam Generator can be monolithic or modular. Several secondary loops are connected to the primary vessel, through the Intermediate Heat Exchanger.

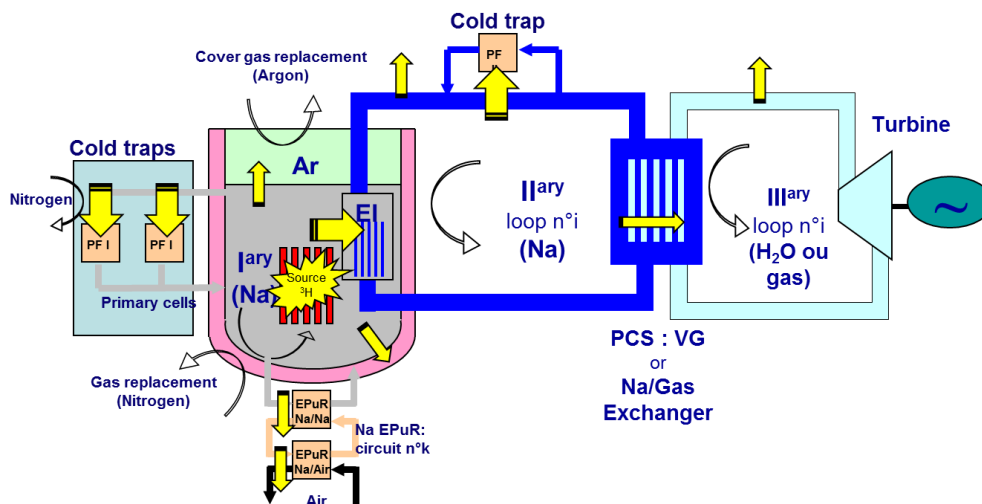


Figure 1-1 Scheme of a SFR reactor: tritium production source and transport

1.1.1 SFR's impurities

A main issue of the SFR is the control of the sodium chemistry, in particular its purification from impurities. The main sodium impurity sources are constituted by oxygen, hydrogen and Tritium, mainly coming from:

- any air and moisture ingress into the circuits, due to maintenance operations;
- fuel assemblies handling, which provides metallic oxides, less thermodynamically stable than sodium oxide, according to Ellingham diagram.

Additionally, other processes constitute a source of hydrogen isotopes, in particular

- Hydrogen (^1H or H or protium), is produced by the aqueous corrosion of the structural material of the pipes of the SGU and by the partial thermal decomposition of hydrazine (N_2H_4) used to limit the dissolved oxygen content, and consequently the aqueous corrosion. The produced hydrogen permeates through the metallic wall and diffuses into the secondary sodium in contact with the steam generator, in the ionic form H^- , thanks to a difference of H partial pressure between the secondary loop and the tertiary circuit. A part of the hydrogen produced at the interface between metal and magnetite, permeates directly through the metal towards the secondary sodium.
- Hydrogen can be also introduced in the secondary sodium after a so-called "sodium-water interaction", induced by a crack or rupture of one or several pipes, which produces with a very high kinetic sodium hydroxide (NaOH), hydrogen and heat. NaOH then reacts with sodium to produce and dissolve O^- and H^- into liquid sodium, with kinetics depending on local conditions (i.e. temperature, hydrogen partial pressure)
- Tritium (^3H or T), is mainly produced (99%) into the core by plutonium ternary fission and by irradiation of boron control rods, then it partially diffuses inside the primary sodium.

Oxygen contributes to corrosion of steel and the activated corrosion products are transported from the core towards the components and deposited mainly on the reactor structures, especially the coldest parts of the intermediate exchangers leading to their contamination. All the elements constituting steel (Fe, Cr, Ni, Mn, C) are susceptible to be dissolved in sodium. In order to limit the corrosion, it is generally considered that a SFR requires to be operated with [O] below 3 wppm, in steady state conditions.

Hydrogen, produced continuously by aqueous corrosion in its most natural form H, needs to be controlled. In fact, in order to be able to detect as soon as possible a sodium-water reaction (which produces hydrogen) and to avoid a propagation of this event to the neighboring pipes, so-called "wastage effect", the hydrogen concentration in sodium should be maintained as low as possible (< 0.1 wppm), thanks to a purification system.

It is then necessary to control as much as possible the content of these impurities, by means of purification devices [1]. In particular, this thesis focuses on the sodium purification from hydrogen isotopes protium (H) and tritium (T), in the secondary sodium loop.

1.1.2 Tritium

Tritium is the hydrogen radioactive isotope containing one proton and two neutrons inside its nucleus. Characterized by β -type emission, it has a half-life of 12.3 years. It has the same chemical properties of hydrogen from a macroscopic point of view: it is extremely mobile into the environment and in all biological systems. In particular, its capacity to diffuse through metals at high temperature (i.e. above 300°C) can be related to that of hydrogen. Often, to simulate the tritium behavior inside metals, hydrogen or deuterium are used in experimental studies.

In a SFR, H and T are strictly related one to each other: both of them, in fact, have the capability to permeate through metallic piping walls of intermediate heat exchangers (IHX) and to diffuse through the liquid sodium.

Due to its radioactivity, Tritium control is of a critical importance. As already said, it is produced inside the core and is transported by primary sodium until the walls of Na I/Na II IHX: thanks to its permeation capacity, it diffuses through the steel walls of the exchanger and it is then transported all around the secondary sodium loop, with a very limited contamination of both the water circuit and the environment. Nevertheless, it is necessary to control this contamination magnitude, in order to demonstrate that the release is in agreement with the environmental requirements.

1.1.3 Tritium release mitigation

All SFRs already built were equipped with SGU, the Energy Conversion system being based on a Rankine cycle. Thanks to aqueous corrosion developed in SGU, the hydrogen produced continuously allows to trap simultaneously H and T.

The system adopted to purify the sodium from hydrogen is the so-called “cold trap” (CT): it exploits the fact that hydrogen is more or less soluble in sodium depending on the temperature. The respective solubility of oxygen and hydrogen is very low; the solubility reaching a value around nil, near the melting temperature i.e. 97.8°C (this is a property specific to sodium, in comparison with other liquid metals, used as coolants).

For hydrogen, the solubility value is given by Wittingham law [2]:

$$\log_{10}[H(ppm)] = 6.467 - \frac{3023}{T(K)}$$

When the sodium temperature is lowered below the saturation temperature, the hydrogen in excess crystallize forming NaH. Practically the sodium is cooled down under the saturation temperature corresponding to the desired concentration (cf. Figure 1-2), and the optimal condition for the nucleation and growth of NaH crystals is created in a cold vessel, on the cold walls, or in a metallic steel knitted mesh. The cold trap is installed on an auxiliary circuit and in this way it can purify sodium from hydrogen [3]. Due to the fact that T has the same chemical properties as H and consequently the same solubility law, T is trapped in the form of NaT, thanks to a so called “co-crystallization” mechanism. Thus, the presence of H plays a fundamental role for the T trapping in cold traps. The crystallized NaT quantity in fact depends on the following relationship:

$$\frac{[T]_{Na}}{[H]_{Na}} = \frac{[NaT]}{[NaH]} \quad 1-1$$

Moreover, a secondary potential trapping mechanism is supposed to exist, based on isotopic exchange between an H atom contained in NaH crystals and a tritium atom dissolved in sodium, as follows:



Therefore, it is obvious that a good control of hydrogen content inside the sodium circuit is necessary to correctly trap the tritium [4].

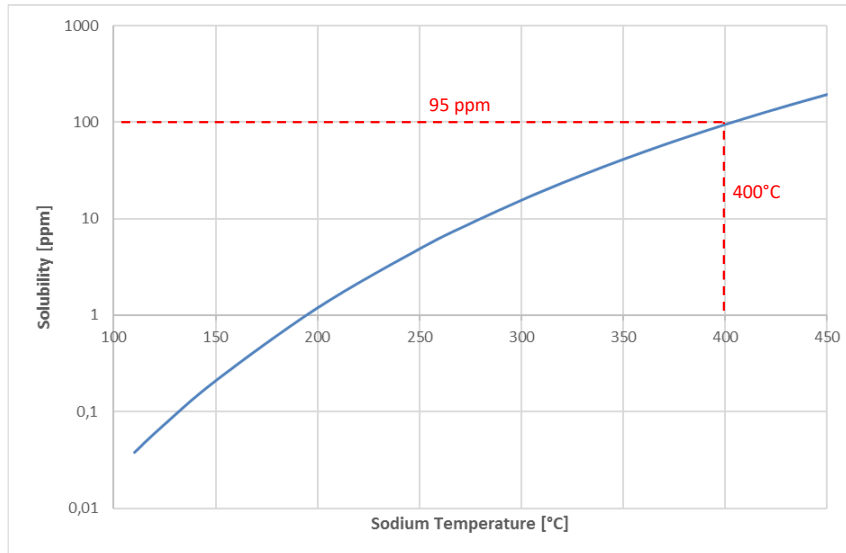


Figure 1-2 Hydrogen solubility in sodium according to Wittingham [2]

1.1.4 T and H mass transfer modeling

The distribution of these two isotopes in the different media of the reactor is governing tritium activities in liquid and gaseous releases, as well as tritium activities built-up in units such as the cold traps. A code, called KUTIM, has been developed at CEA in the 70's, in order to achieve the following objectives:

- Assess tritium releases to the environment (gaseous and aqueous) at the operating stage, in order to guarantee that they are below the authorized limits.
- Assess tritium activities in the different media, in particular tritium built-up in the CT in order to be able either to regenerate them for re-use or to reprocess them as wastes.

The methodology used to model the T and H distribution in a SFR is based on the identification of the related T and H sources and pools, as well as the transport phenomena involved. The mathematical formulation of the problem, resolved by a differential equations system, has been validated by the comparison with experimental values issued from operating reactors (PHENIX and SUPERPHENIX).

1.2 ASTRID project – Brayton cycle case: tritium issue

In the already built and operated sodium reactors, the ECS is a Rankine Cycle based on water/steam circuit. However, for ASTRID project (Advanced Sodium Technological Reactor for Industrial Demonstration), a gas ECS has been proposed, based on a Brayton Cycle: a gas (pure nitrogen) will circulate inside the tertiary loop, receiving thermal energy from the secondary sodium through a

Na/gas heat exchanger, and moving a gas turbine. Thus, several issues linked to the potential sodium-water reaction would be avoided, providing an easier and more reliable technology, even if the overall thermodynamic efficiency of a Brayton cycle is lower than the Rankine's efficiency, respectively around 0.37 and 0.42. On the other hand, due to the absence of water in the tertiary loop, corrosion of steels and its corresponding hydrogen production will not take place, thus making impossible the tritium trapping by co-crystallization in secondary loops.

As basis for this study, we considered the ASTRID-600 design case: inside the secondary sodium loop, the lack of a hydrogen flux of around 40×10^{-6} g/s has been assessed by the KUTIM code calculations [5]. More precisely, this value corresponds to the equivalent hydrogen flux that would be provided by the corrosion of a hypothetical SGU, in case of a water/steam tertiary circuit.

For these reasons, different solutions have been proposed by CEA to enable the tritium trapping in order to avoid its dispersion into the environment, like gas purification, permeation barriers or hydrogen introduction inside sodium. Among them, the voluntary introduction of hydrogen inside sodium has been identified as the most feasible solution in order to enable the tritium co-crystallization inside the cold traps.

Three main processes have been proposed to introduce a controlled hydrogen flux inside sodium [4]:

- a) Dissolution of solid NaH solid crystals
- b) Direct gaseous hydrogen injection (bubble column or gas nozzle)
- c) Gaseous hydrogen permeation through a dense metallic membrane.

The first one presents some critical issues linked to the solid state of NaH. In this case, in fact, a non-continuous introduction process would not guarantee a stable control of the injected flux, due to the fluctuation of NaH active surface, which induces variations of the dissolution rate.

Concerning the gaseous hydrogen introduction, a former study [5] has analyzed and compared gas permeation (c) and gas injection (b) technologies. The two different physical principles were briefly presented and a process pre-design has been proposed for both solutions, based on the expected operating condition of ASTRID-600. Finally, a shell and tube type permeator has been compared to an absorbing bubble column, enlightening the main advantages and disadvantages as well as the feasibility of each technology. One main disadvantage of the direct injection is the risk of plugging for the nozzle, caused by the hydrogen crystallization on the nozzle surface; to avoid this an elevate dilution with inert gas is necessary, with a consequent risk of accumulation in the sodium loop.

As a result, the permeation process through nickel membranes has been identified as the best choice, due to the following main advantages:

- A better control of the hydrogen flux introduced in sodium.
- Physical separation between gas and liquid phase, thus avoiding any risk of sodium dispersion.
- Easier integration of a more compact device into the nuclear reactor.

Furthermore, hydrogen dissolves in sodium in its ionic form H^- , thanks to sodium high reducing behavior; the introduction by permeation should provide to sodium atomic hydrogen H, thanks to the H_2 molecules dissociation that takes place inside the membrane. In this way, the direct contact between sodium and gaseous H_2 molecules is prevented, thus avoiding the risk of non-complete H_2 dissociation and gas loss in the cover gas.

1.3 Thesis subject and motivation

The previous studies carried out at CEA ([4], [5]) have proposed a preliminary design of a permeation device (permeator), which allows the introduction of hydrogen from a gaseous side to the liquid sodium. In particular, the design-concept consists of a nickel multi-tube permeator, where a gas mixture containing hydrogen (limited to a maximum concentration of 3% molar to respect ASTRID security issues) is put in contact with one side of the nickel membrane, while sodium flows on the other side. However, all the calculations made are based on several hypothesis and assumptions that need to be verified and analyzed more in detail, in order to provide a more reliable and solid technical solution.

Therefore, these studies have expressed the need of a more in-depth analysis of the mechanisms involved in the hydrogen transport through the entire physical domain (gas phase, metallic membrane and liquid sodium). In particular, some hypothesis and simplifications have been made on some fundamentals aspects, thus leaving the following open points to be investigated:

- The choice of Nickel as material for the permeator's membrane is inspired by previous applications in the context of SFR, in particular the PRIAM [6] process and hydrogen-meters [7]. A more detailed study on permeation through different metals should be carried out, in order to properly justify this choice.
- A calculation of the hydrogen permeation flux in stationary condition has been performed, depending on different operating conditions and parameters. It is based on the Richardson's law [8], which is valid only under certain physical assumptions. The validity of them in the range of operating conditions of the permeator, should be proved by means of a careful detailed study on permeation; the comparison with other laws or models is necessary in order to find the most suitable for our scope.
- The reference Nickel permeability to hydrogen is taken from a study made in 1964 by Webb [9] and confirmed by experimental measurements made at CEA in 1984 [10] on small-size membranes. A complete review of experimental measurements carried out on Nickel is advisable, as well as a new experimental campaign, if the uncertainties and their consequences on the understanding of the phenomena are significant.
- Many physical phenomena were not considered, such as the hydrogen mass transfer resistance provided by the gas and sodium phase inside the permeator. A complete multi-physics analysis should be then considered in order to individuate the phenomena that can influence the entire mass transfer process.

To approach the comprehension of the hydrogen-to-sodium permeation, we can refer to some studies carried out at CEA on hydrogen transfer from sodium to a circuit under vacuum, in the framework of the development of a process called PRIAM[6], used for the regeneration of the cold traps. In the case of PRIAM, hydrogen is present into sodium as ionic form H^- and diffuses through a Nickel membrane to a vacuum side. For this study, on the contrary, a transfer of hydrogen from a gas phase to liquid sodium is needed : gaseous hydrogen is in its diatomic state H_2 , it diffuses through Nickel in its atomic

form H and then dissolves to sodium as H^- ions; therefore, the physical process involved here is quite different.

Moreover, at LMCT laboratory the transfer of a deuterium-tritium mix from a gas phase to another gas phase, separated by a Pd-Ag membrane, has been studied so far and the permeation laws have been established [11]. However, because of the unconventional situation described in this study, mainly due to the presence of sodium on one side of the membrane, the mechanisms involved are probably different and have never been precisely studied before. In fact sodium, being a liquid metal, could provide a mass transfer resistance to hydrogen which could be potentially non-negligible if compared to that one of a gas phase. Additionally, Pd-Ag provides different permeation properties if compared to nickel.

More recently, a similar application has been developed for the hydrogen isotopes injection into the lead-lithium (PbLi) blanket of a fusion reactor [12]: it consists of a multi-tube component made of niobium membranes, able to inject hydrogen into PbLi at temperatures around 500°C. However, the hydrogen behavior inside PbLi is very different from what happens inside sodium. Therefore, even if this study can be taken as reference in terms of approach, its application cannot be proposed for a SFR.

Starting from all these considerations, the necessity to set up a R&D effort has been pointed out. In particular, the aim of this thesis is to study the above cited transfer mechanisms and to identify the important parameters that will allow a precise control of the hydrogen flux transferred from the gas to the liquid sodium.

Chapter

2 State of the art

When the thesis subject was initially approached from a theoretical point of view, it was immediately clear that its purpose involves several physical phenomena, each one studied by different scientific communities and object of more or less detailed studies, including articles or theses. It was obviously impossible to focalize on each single aspect with the same accuracy, but here is the attempt to give an overview of the general features for each of them.

From a practical point of view, this review is divided in two categories, not necessarily independent one from each other. The first includes the fundamental studies of the physical phenomena at the base of our application, such as theoretical models or experimental investigations, while the second one concerns the state of the art of the industrial applications (typically from the nuclear power industry) which involve similar processes to that one analyzed here.

The herein studied hydrogen permeation process consists in hydrogen interactions with three main systems: a gaseous medium, a metallic membrane and the liquid sodium. Among the physical phenomena appearing, two main were identified as significantly important for this study: the hydrogen permeation through the metallic membrane and the hydrogen transport inside the liquid sodium. We did not consider in detail the hydrogen transport inside a gaseous medium for one main reason: we deal with a binary gas mixture in ideal gas conditions ($P < 10$ bar, $300^{\circ}\text{C} < T < 500^{\circ}\text{C}$) with low hydrogen concentrations (around 3% molar), which allow us to consider it as a dilute solution, where the conventional mass transfer mechanism by convection and diffusion take place. In terms of complexity, the mass transfer in such a domain is much better known, if compared to the transport phenomena inside the metallic membrane or the liquid sodium, that we will not dedicate an in-depth literature review to it.

As anticipated, this state of the art review aims to:

- investigate the main features of the above mentioned physics and understand them;
- individuate the most significant issues that could impact on our specific application;
- give the criteria and some hypothesis for a general model describing the entire transfer process;
- give the basis for a correct approach for the development of an experimental investigation campaign.

In view of the above reasons, this chapter is divided into the followings subchapters:

- Hydrogen permeation through metals.
- Focus on hydrogen-Nickel permeation parameters.
- Hydrogen-Sodium system.
- Hydrogen permeation through nickel membrane in contact with liquid sodium: technological state of the art.

2.1 Hydrogen permeation through metals

Before to start with a detailed analysis of the existent literature on the gas-metal permeation, it is advisable to make a few clarifications that can help in the follow-up and remove some typical doubts about this matter.

First clarification: permeation or diffusion?

The permeation is generally defined as the penetration of a permeate (such as liquid, gas or vapor) through a solid, caused by a concentration or partial pressure gradient of the permeate across the solid barrier. Therefore we are dealing with a particular mass transfer mechanism. However, despite it is closely related to what is generally known as “diffusion”, particular attention should be paid to not confuse one phenomenon with each other. Many papers in fact talk erroneously about permeation confusing it with the simple diffusion term.

The diffusion in fact is the exchange of a quantity (energy, mass, momentum) strictly due to a related potential gradient (temperature, chemical potential and pressure respectively) within a spatial domain, described by certain fundamental laws such as: Fourier’s law (energy diffusion), Fick’s law (mass diffusion) or Newton’s law of viscous fluids (momentum diffusion), which links the diffusion flux to a spatial gradient of the same quantity through a diffusion coefficient, depending on the material’s properties and operating conditions. So the diffusion can only take place through a certain medium (solid, liquid or gaseous) and does not include other transport or exchange phenomena besides that due to the potential gradient.

For our particular case dealing with mass transfer domain, we will talk about diffusion always referring to the Fick’s laws formulation.

In particular the first Fick’s law, which expresses the diffusive flux density (per surface area unit) under steady state conditions:

$$J = -D \frac{\partial C}{\partial x} \quad [\text{mol m}^{-2} \text{s}^{-1}] \quad 2-1$$

And the second Fick’s law, which predicts how diffusion causes the concentration change with time:

$$\frac{\partial C}{\partial t} = D \frac{\partial}{\partial x} \left(\frac{\partial C}{\partial x} \right) \quad [\text{mol m}^{-3} \text{s}^{-1}] \quad 2-2$$

Where J is the diffusive flux, D [$\text{m}^2 \text{s}^{-1}$] is the diffusion coefficient, C is the molar concentration [mol m^{-3}], x is the spatial coordinate vector and t is time.

On the other hand, the permeation through a solid membrane represents more broadly the entire mass transfer process through a series of multiple media (i.e. gas-solid-gas, gas-solid-liquid, gas-solid-liquid metal, etc.) and can include different phenomena other than the Fick’s diffusion (such as surface reactions, adsorption, dissolution, desorption, lattice trapping, grain boundary and dislocations effect and so on), which can occur in some particular conditions especially for gas-metal permeation.

Second clarification: the physical domain

In the previous paragraph, we talked about different possible domains where the permeation can occur; as already said, the domain of application for this study is composed by a pure or diluted gaseous hydrogen, a solid metal (membrane) and liquid sodium, constituting a gas-metal-liquid (g-m-l) system (Figure 2-1 (b)). In particular, the hydrogen mass transfer takes place, thanks to a positive concentration gradient between the gaseous medium (pure or diluted hydrogen, high concentration side) and the liquid sodium (low concentration side).



Figure 2-1. Permeation across different domains: gas-metal-gas (a) and gas-metal-liquid (b)

However, the most important part of the existent bibliography refers to gas-metal-gas (g-m-g) systems (Figure 2-1(a)), leading to permeation from a rich gas side to a poor gas side, or more commonly to a full vacuum side. This is substantially due to the fact that the most common application of hydrogen permeation is the hydrogen separation from a gas phase, which normally involves a membrane between two gas sides. Nevertheless, it is interesting to investigate this literature, naturally assuming an analogy between gas-metal interactions both for the g-m-g and for g-m-l system. We will assume that transfer phenomena of the two first steps at gas metal interface and in metal membrane are equivalent for both cases g-m-g and g-m-l systems.

For these reasons, we now approach the gas-metal permeation as a general phenomenon, while we will investigate later in paragraphs 2.3 and 2.4 the interactions with the liquid sodium side.

Third clarification: hydrogen solubility

The solubility of a solute (in our case hydrogen) in a solvent (in our case both the metallic membrane and the liquid sodium) is generically referred as the saturation concentration, where adding more solute does not increase the concentration of the solution. In this study, the same word “solubility” is used both for hydrogen-metal interface and for hydrogen-sodium system, in accordance with the existing literature on both subjects. However, in order to avoid confusion, a distinction between these two needs to be clarified:

- For the hydrogen-metal system (ref. to paragraph 2.1.1.2), the hydrogen solubility consists in the equilibrium concentration obtained at the interface for a given temperature and pressure, according to the Sieverts’ law. It is not linked to a saturation of the metal, with the consequent formation of a precipitate (i.e. hydrides).
- For the hydrogen-sodium system (ref. to paragraph 2.3.3), the hydrogen solubility consists in the saturation concentration given at a certain temperature, where the addition of further hydrogen would not increase the concentration providing hydride precipitation. For lower hydrogen concentrations, a Sieverts’ law is effectively established, but on the contrary of hydrogen-metal system, we will not speak about solubility.

2.1.1 Physics

2.1.1.1 Permeation process

The permeation leads to a hydrogen flux across the metallic membrane due to a difference of hydrogen chemical potential between the two membrane sides. In the case of two gaseous sides (g-m-g), under the hypothesis of ideal gas, the hydrogen concentration in the gas can be related to its partial pressure.

From a global thermodynamic point of view, the hydrogen transfer from a region of partial pressure $P_{H_2,1}$ to a region of partial pressure $P_{H_2,2}$ (i.e. the two gas sides) is driven by a free molar enthalpy difference, $\Delta\mu_{H_2}$ given by:

$$\Delta\mu_{H_2} = -RT \ln \frac{P_{H_2,1}}{P_{H_2,2}} \quad 2-3$$

Where R is the gas constant and T is the absolute temperature. As long as $P_{H_2,1} > P_{H_2,2}$, ΔG is negative and the transfer process occurs spontaneously. However, in the case of permeation through a metallic dense membrane, this physical barrier (i.e. the membrane) prevents this simple process; anyway, it is possible that under certain conditions (namely high temperatures), dense metals become permeable to gas like hydrogen, whose atomic dimension is very small compared to the metal lattice, thus constituting a real transit medium for the gas.

In the case of a diatomic gas like hydrogen, going into the physics details, it is largely recognized from many authors [11], [13]–[19] that the permeation process through a metallic membrane **in a g-m-g system**, without considering the transport phenomena inside the gaseous phase, takes into account the following steps (cf. Figure 2-2):

1. *Dissociative adsorption (or chemisorption)* : the H_2 molecules on the feed side at the interface with the membrane surface undergo dissociative adsorption on surface sites forming adsorbed atoms H;
2. *Absorption or dissolution (surface to bulk)*: H atoms infiltrate bulk lattice, occupying the sub-surface interstitial sites;
3. *Bulk diffusion*: the H atoms diffuse through the membrane bulk lattice, by interstitial diffusion in between the lattice structure of the membrane's crystalline elements;
4. *De-solubilisation (bulk to surface)* : approaching the permeate side, the H atoms exit from the bulk to the surface;
5. *Associative de-sorption (recombination)*: the absorbed H atoms associatively desorb at the surface as H_2 molecules on the permeate side.

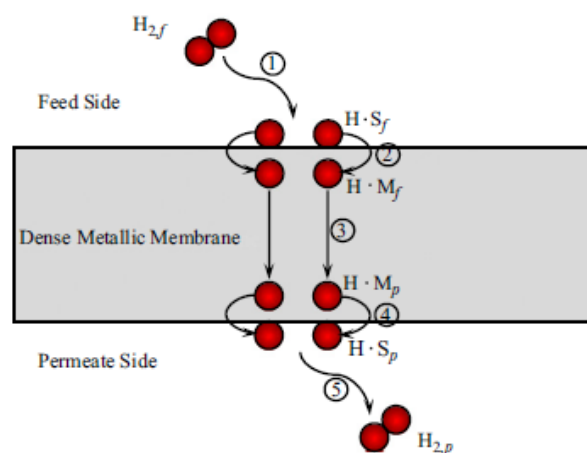


Fig. 1. A schematic of the hydrogen permeation process through dense metallic membranes involving sequential steps of surface dissociative adsorption, subsurface penetration, bulk metal diffusion, egress to surface, and reassociation of H atoms on the surface. Two each of steps 2, 3, and 4 are required for permeation of one molecule of H_2 .

Figure 2-2 Scheme of hydrogen permeation through metals [18]

Each one of the above steps takes place in a different region of the membrane: while the steps 1 and 5 occur at the metallic surface in contact with the gas phase, the steps 2 and 4 involve the internal metallic layers and the step 3 is related to the central part (bulk). It is quite evident that each of them can influence the overall permeation process and be the rate-limiting step, depending on the particular conditions of the permeation. In 2.1.2 we will analyze how different authors try to model the permeation process, giving more or less importance to these mechanisms.

IMPORTANT NOTE: It is also important to remark that the gas-metal-gas permeation normally refers to the H_2 molecules, since that is the chemical state of hydrogen in gas phase both at feed and at permeate side, leading to a molar flux defined per H_2 mole. However, as the bulk diffusion concerns H atoms, some authors report their results referring to the atomic hydrogen. That's why some variables such as solubility or permeability coefficients, which depend on the hydrogen concentration, could be expressed both in term of molecular (H_2) and atomic (H) hydrogen, depending on the authors. It's easy to understand that a coefficient expressed by mole of molecular hydrogen [mol_{H_2}] is simply the half value of the same coefficient expressed in term of atomic hydrogen [mol_H], since each mole of H_2 corresponds to two moles of H.

For simplicity, when we will define a hydrogen flux or a related coefficient, we will generally refer to moles of hydrogen [mol], by specifying if it is defined for molecules or atoms to choose the most appropriate molar unit.

2.1.1.2 Metal-hydrogen equilibrium: Sieverts' law

The steps 2 and 4 of permeation process, as described in paragraph 2.1.1.1, involve the dissolution of hydrogen atoms in the metal. When hydrogen dissolves in a metal, depending on temperature and hydrogen concentration, the metal-hydrogen system (called also M-H system) will reach different equilibrium states, corresponding to different phases. As example, below (Figure 2-3) is reported the Pd-H phase diagram [20], where the different phases are shown; at sufficiently low concentrations, the interstitial hydrogen is always found dissolved in solid lattice, usually called α -phase or solid solution. At higher hydrogen concentrations, the solid lattice becomes saturated and hydrides are

formed and co-exist with the metal in the so called β -phase. Between these two, a transition region where two phases with different hydrogen concentrations coexist.

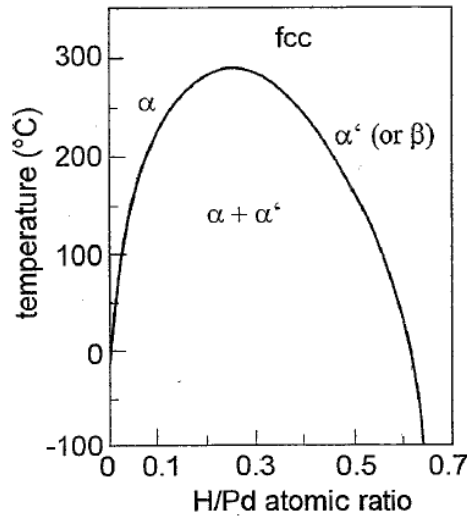


Figure 2-3 Palladium-hydrogen phase diagram [20]

When the hydrogen is dissolved in low quantities in solid solution (α -phase), its concentration can be expressed by means of the Sieverts' law [21], commonly recognized and often cited by the authors to set up their model or as a comparison for their results. This law in fact describes the concentration equilibrium at gas-metal interface:



The solubility of gas in a material is defined as the concentration of the gas dissolved at the chemical equilibrium, under a given partial pressure and temperature. In particular, the Sieverts' law establishes the relationship, at thermodynamic equilibrium, between the partial pressure P_i of the gas i and the gas atom concentration at the interface $g-m$. Practically this law describes the step 2 (dissolution) when it is at the equilibrium by means of a solubility coefficient K_s , commonly called Sieverts' constant:

$$C_{H-m} = K_S(T) \sqrt{P_{H_2}} \quad [\text{mol m}^{-3}] \quad 2-5$$

with

$$K_S(T) = K_{S0} e^{\frac{-E_S}{RT}} \quad [\text{mol m}^{-3} \text{ Pa}^{-0.5}] \quad 2-6$$

where C_{H-m} is the hydrogen atoms molar concentration inside the metal (generically called "solubility" in all the permeation literature), K_s [$\text{mol m}^{-3} \text{ Pa}^{-0.5}$] is the Sieverts' constant, function of temperature, P_{H_2} [Pa] is the molecular hydrogen partial pressure inside the gas, and E_S [J mol^{-1}] is the heat of solution, including both dissociation and solution energy. This law is valid when a local equilibrium is reached at the interface between the gas and the metal, namely when the hydrogen contained in the gaseous layer in contact with the metal is dissociated and dissolved into the metallic substrate until reaching a fixed equilibrium concentration.

This law has a theoretical explanation, argued by Ciampichetti in his review [22]: in fact, if we assume a reaction between the gaseous molecular hydrogen and the dissolved atomic hydrogen inside the metal, we obtain the following relationship:



where, at the equilibrium, the reaction equilibrium constant K can be expressed as

$$K(T) = \frac{C_H^2}{P_{H_2}} \quad 2-8$$

From this equation, we obtain easily the relationship by Sieverts' law in Equation 2-5.

The driving parameters of hydrogen dissolution into the metal are then its partial pressure and temperature; in particular, we can observe that:

- At fixed temperature, C_H increases linearly with the square root of the hydrogen partial pressure,
- At fixed pressure, C_H increases with temperature if the hydrogen dissolution is endothermic ($E_s > 0$),
- At fixed pressure, C_H decreases with temperature if the hydrogen dissolution is exothermic ($E_s < 0$).

2.1.2 Available models

2.1.2.1 Richardson's law: the diffusion-limited permeation

Permeation of gas through metals was initially treated as a metal bulk phenomenon only, modelling the permeation as a pure diffusive mechanism. In this first approach, a macroscopic point of view was applied, trying to set an expression of the whole permeation flux, without considering the micro-scale surface effects. Furthermore, this model describes only the g-m-g system and it is valid only at the local scale, since it gives expression of the molar flux per unit surface. Despite its simplifications, this approach could be valid under certain conditions and this explains why, even in more recent papers, we do not find a clear distinction between permeation and diffusion. However, it is known from the beginning that the bulk diffusion is conducted by atomic hydrogen and not by hydrogen molecules.

The earliest model was proposed by Richardson [8], considering the steady state permeation of hydrogen across a membrane with a negligible hydrogen concentration downstream, typically maintained under vacuum for experimental purposes. The permeating flux is given by:

$$J = \frac{a}{\delta} P_{H_2}^{1/2} e^{-\frac{b}{T}} \quad [\text{mol m}^{-2} \text{s}^{-1}] \quad 2-9$$

Where J is the hydrogen permeation flux for surface unit, P_{H_2} is the hydrogen partial pressure upstream, T is the temperature, δ is the thickness of the metal, a and b are constants for the gas-metal system. We find here the same proportionality to $P_{H_2}^{1/2}$ and to the exponential of temperature $e^{-\frac{b}{T}}$ as for the Sieverts' law, and this is not random: Andrew [16] and Ciampichetti [22] well explained the physical meaning of the Richardson's law, obtaining a slightly different formulation that is more commonly applied by most of the authors for generic permeation cases [23].

With reference to the scheme in Figure 2-4, if we assume the permeation as purely diffusive (no surface effects as adsorption, dissociation, etc.), in stationary conditions, we can write the permeation flux between two internal sides 1 and 2 of a flat membrane according to the 1st Fick's law in Equation 2-1:

$$J = -D \frac{\partial C_{H-m}}{\partial x} \quad [\text{mol m}^{-2} \text{ s}^{-1}] \quad 2-10$$

which, once integrated in 1D across the membrane thickness δ , gives:

$$J = \frac{D}{\delta} (C_{H-m,1} - C_{H-m,2}) \quad [\text{mol m}^{-2} \text{ s}^{-1}] \quad 2-11$$

where $D [\text{m}^2 \text{ s}^{-1}]$ is the hydrogen-metal diffusivity, $C_{H-m,1}$ and $C_{H-m,2} [\text{mol}_H \text{ m}^{-3}]$ are the atomic hydrogen molar concentrations at the two membrane internal sides 1 and 2. Similarly to the Sieverts' constant, also the diffusivity coefficient is expressed as function of temperature by means of an Arrhenius law:

$$D = D_0 e^{\frac{-E_d}{RT}} \quad [\text{m}^2 \text{ s}^{-1}] \quad 2-12$$

where $E_d [J \text{ mol}^{-1}]$ is the diffusion activation energy. Assuming that hydrogen atom concentration in the metal substrate is locally in equilibrium with the gas molecule concentration at both membrane sides, we can express $C_{H-m,1}$ and $C_{H-m,2}$ according to the Sieverts' law in Equation 2-5. So we obtain:

$$J = \frac{D}{\delta} K_S (\sqrt{P_{H_2,1}} - \sqrt{P_{H_2,2}}) \quad [\text{mol m}^{-2} \text{ s}^{-1}] \quad 2-13$$

A new coefficient is defined as the product of D and K_S , called permeability:

$$pe = DK_S \quad [\text{mol m}^{-1} \text{ s}^{-1} \text{ Pa}^{-0.5}] \quad 2-14$$

Since both D and K_S vary with temperature in an Arrhenius manner, also pe can be written as:

$$pe = pe_0 e^{\frac{-E_p}{RT}} \quad [\text{mol m}^{-1} \text{ s}^{-1} \text{ Pa}^{-0.5}] \quad 2-15$$

$$E_p = E_S + E_D \quad [J \text{ mol}^{-1}] \quad 2-16$$

where E_p is the activation energy for the permeation. The equation 2-13 can be rewritten as follows:

$$J = \frac{pe_0}{\delta} e^{\frac{-E_p}{RT}} (\sqrt{P_{H_2,1}} - \sqrt{P_{H_2,2}}) \quad [\text{mol m}^{-2} \text{ s}^{-1}] \quad 2-17$$

which in case of $P_{H_2,1} \gg P_{H_2,2}$ (negligible hydrogen concentration at the outlet side), reduces to the Richardson's original formulation in Equation 2-11. However, the equation 2-17 is the one applied by the most of the authors who commonly call it Richardson's equation, even it differs slightly from the original formulation.

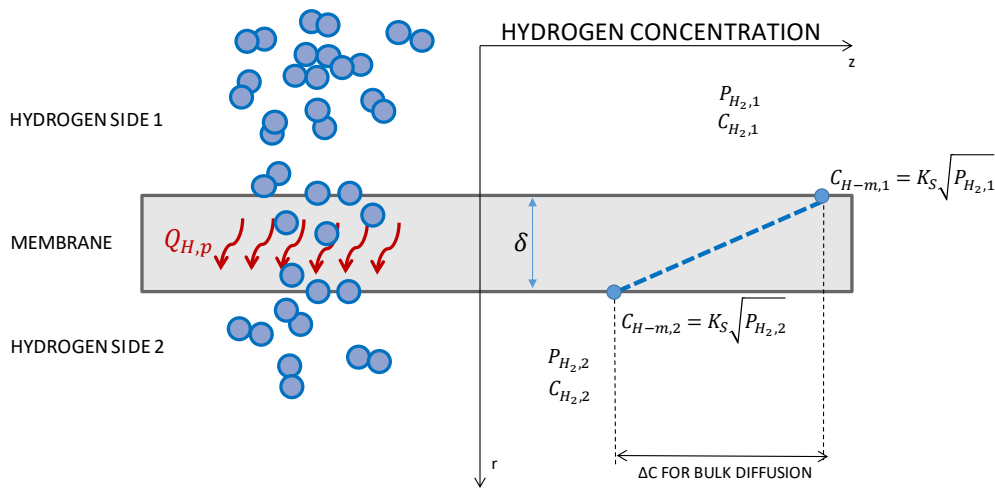


Figure 2-4 Hydrogen permeation physics in a gas-metal-gas configuration with pure hydrogen on both membrane's sides

Resuming, this formula expresses the hydrogen permeation flux per unit surface across a metallic membrane, under the following hypothesis:

- Gas-metal-gas domain.
- Steady state conditions.
- Local uniform concentration on the membrane's surface.
- The metallic membrane is isothermal.
- Gas side mass transfer resistance is negligible.
- Atomic hydrogen interstitial bulk diffusion is the limiting step determining the permeation flux; therefore any other effect (such adsorption, absorption, desorption, trapping, grain boundary and dislocations or metal's defects effects etc.) is neglected or considered much quicker than the diffusion, so that it cannot influence the overall process. Fick's 1st law of diffusion is then applicable.
- Mono-dimensional diffusion, across the membrane thickness.
- The gaseous molecular hydrogen is in equilibrium with the dissociated atomic hydrogen inside the metal, on both sides of the membrane, so that Sieverts' law is applicable.
- Diffusion, solubility and permeability coefficients are not dependent from hydrogen concentration but only on metal temperature and physical properties.

We will investigate in details in paragraph 2.1.3, in which experimental conditions these hypothesis can be considered true and which are the limits of applicability. But as a general rule this model can be applied when hydrogen concentration in metal is low, relatively high temperatures and thick membranes [18].

2.1.2.2 Complementary models: surface and trapping effects

Despite its broad employment by several authors, many experimental results showed deviation from Richardson's law, especially for very thin membranes (few microns), low temperatures and very low pressures. This explains why this law has been subject of different critics along the time, and many authors implemented more complete (and more complex) models in an attempt to obtain a model applicable on a larger range of conditions and comprehensive of all the physical phenomena involved.

However, in most of the cases, they show how their complex models can be reduced in some particular conditions to the Richardson's law, recognized by all as the "father" of the permeation models.

Smithells and Ransley [24] remarked that Richardson's equation was not good to predict experimental results at very low pressure, when the permeation flux was found to be no more proportional to the square root of pressure but become directly proportional to P . The \sqrt{P} relation indicates that gas molecules undergo dissociation when entering into the metal. If this is no more valid, it means that another mechanism dominates on the permeation. They try to explain this behavior at low pressures adding an adsorption coefficient Θ , dependent from pressure according to the Langmuir's form, so modifying the Richardson's law with success even at very low pressures.

Successively Wang [13] developed a more complete model, including adsorption/desorption, absorption/desolubilisation effects at both membrane surfaces, atom recombination, as well as the atomic diffusion inside the membrane. For each of these micro-scale mechanisms, he set up an expression of the hydrogen flow rate as function of pressure. With the hypothesis that in steady state conditions, the flow rate is equal between each elementary mechanism, he equalized all the flow rate expressions from each single contribution, obtaining a global expression of the hydrogen flux as function of pressure. This approach is very important because several authors set up their model starting from Wang's theory.

Some decades later, Pick and Sonnenberg [15] set up a kinetic model for hydrogen/metals interaction with a focus on the difference between molecular hydrogen and atomic hydrogen incident flux on metal surface. As for Wang, they gave expression of the different flux rates due to the different permeation steps: chemisorption, defining a sticking probability, desorption, adsorption, surface to bulk dissolution and vice-versa, bulk diffusion. In this case, they gave the equation of hydrogen flux as function of hydrogen concentration (and not pressure). They demonstrated analytically that the recombination of these equations under the condition of the stationary state and equilibrium at gas-metal, leads to Sieverts' law: expression of the equilibrium concentration as function of gas pressure. They stated that this concentration is a material bulk property and should only depend on the solution energy; the surface barriers can only influence the rate at which equilibrium is reached.

Andrew [16] provided a review of hydrogen permeation models, with a particular attention to the Wang's model; he analyzed it for different limiting cases, demonstrating that:

- For low fluxes, the hydrogen permeation flux is linear with pressure. Only half of the incident flux is permeating with a 50% probability for an atom to be desorbed,
- For very high pressures, permeation flux is limited by adsorption rate and desorption rate,
- For intermediate fluxes: if the membrane is thick enough, the permeation flux expression reduces to Richardson's law.

Ward and Dao [17] based their model on the Pick's [15] one, considering both the diffusion and surface effects with some adaptation; they included also the external mass transfer (i.e. hydrogen in feed gas) contribution to the global permeation. In the same way, they obtained an expression for the permeation flux as function of hydrogen concentration, which takes into account all the different rate contributions. Moreover they compared the theoretical calculations for different operating conditions with some experimental results for palladium membranes. The objective was to find the physical limits

where the model does not follow the Sieverts' law of equilibrium, while the surface effects become rate determining step. Their main conclusions are:

- In the absence of external mass transfer resistance, nearly diffusion-limited permeation (well described by Richardson's law) is expected for clean Pd for temperatures above approximately 573 K and membrane thicknesses down to 1 micron;
- Most of the existing permeation data for thick Pd membranes are consistent with the calculations for diffusion-limited permeation (discrepancies for membranes less than 10 microns);
- Low-temperature permeation is limited by desorption while adsorption is only expected to impact permeation at very low upstream H₂ partial pressures, or under conditions of substantially reduced sticking due to surface contamination;
- With thin membranes, external mass transfer can become a significant resistance under conditions where it would normally not be expected, especially on the low partial pressure side of the membrane and when porous support is present.

More recently (2013), Deveau [18] provided an interesting study: after a literature review where he identified the limits of Richardson's model in the range of low temperatures and thin membranes, he approached the model from Ward and Dao[17] as the global reference for the permeation. However, he found that even this one did not include the effect of non-ideal solution of metals, for which a peak of permeability is expected at the metal transition to β phase. Therefore he set up a model based on Ward and Dao[17] relationships, but including also a term for the phase transition, expressed in the more intuitive form of electrical analogy, where each step of permeation contributes as a "resistance" to the total hydrogen flow across the membrane. He compared as well his model with experimental results of permeation on Pd membranes; he found that for temperature above 200°C-250°C the diffusion step has the highest resistance on the permeation. This means that all the other resistances can be neglected and for this case, when the diffusion becomes the so called "rate determining step" or "RDS", his complex model equation reduces to the most common Richardson's law. His conclusion is very important because he stated that, despite diffusion of hydrogen has been investigated extensively since its discovery 150 years ago, the most common way to model permeation flux of hydrogen is the Richardson' law (called improperly Sieverts' law in his study), which is strictly applicable only at relatively high temperatures, thick membranes, and low hydrogen pressures.

In addition to the surface phenomena, Cummings and Blackburn [25] introduced into their permeation model the so called "trapping" effect: they stated in fact that the atomic hydrogen could be trapped into the metal lattice under certain conditions. Therefore, they developed a model, which includes both surface effects, globally modeled as a dissociation reaction, and the trapping effect, modeled as a reaction between moving atoms and trapped atoms. Each reaction has its own rate constant which contributes to the entire permeation rate. Furthermore, they proposed an experimental technique, the pressure modulation, which allows individuating which is the determining rate under different experimental conditions.

2.1.2.3 Conclusions

Richardson's law is the most primitive way to describe the hydrogen diffusion through metals, taking into account only the bulk diffusion phenomena as rate limiting step, hypothesis validated generally for high temperatures and thick membrane. Moreover, this model has been set up for a g-m-g system

and does not take into account the transport phenomena beyond the external sides of the membrane. With this model, one can obtain the local hydrogen flux per unit surface through a membrane under steady state conditions; if one wants to model only the diffusion under time-dependent conditions, the Fick's 2nd law is necessary.

More complex models describe the hydrogen permeation flux considering both surface and bulk phenomena. It is commonly accepted by the authors that the surface phenomena become important when the membrane temperature and thickness decrease. When the temperatures and the thicknesses are high, the bulk diffusion is the rate limiting process and many complex models reduce to the Richardson's law.

2.1.3 Experimental evidences

The previous chapters describe how different gas/metal interactions take place during the permeation process, each one characterized by laws and parameters: the gas-metal dissolution, characterized by the Sieverts' constant; the bulk lattice diffusion (diffusion coefficient) and the overall permeation (permeability coefficient). Each of these phenomena can be investigated with different techniques, which allow to obtain the coefficients for various operating conditions. For our purpose, we will try to give an overview on the main characteristics of the most common materials employed for permeation issues.

If we consider the steady state permeation, the permeability coefficient indicates the metal's capacity to be permeated by hydrogen for a given concentration (or partial pressure). At a fixed gas pressure, higher is the permeability, higher the hydrogen flux which go through the metal. As it is defined in equation 2-14, the permeability is the product between K_S (and then the solubility) and diffusivity D . It is then obvious that a material with a good permeability should also has a good solubility or diffusivity.

Historically, H₂ separations in gas phase (on both sides of the membrane) were performed with Pd based membranes, since they naturally catalyze the surface dissociation/re-association processes and are highly permeable to H₂ [19]. Among all the metals, the transition metals are generally recognized [26] to have great permeability to hydrogen. These include (but are not limited exclusively to) tantalum, niobium, and vanadium; moreover, unlike platinum and palladium, they are abundant and comparatively cheap.

According to Santucci et al. [27], body-centered cubic (bcc) refractory metals like Nb, V and Ta exhibit exceptionally high permeability to hydrogen, order of magnitude higher than for face-cubic-centered (fcc) metals like Pd or Ni. However the high hydrogen solubility in these metals is responsible for their high levels of embrittlement under hydrogenation, which could result in membrane failure. For these reason, the alloying of metals has been studied in order to reduce hydrogen solubility. Another drawback of metals proposed as alternatives to Pd is the strong surface resistance to hydrogen transport, because of their high reactivity with gases. To avoid the formation of surface compounds, such as oxides and nitrides, membrane surfaces could be coated with thin Pd-based films.

Since the membrane composition and configuration could be multiple, we decide here to concentrate our review on pure metals, trying then to individuate the most suitable for our application.

2.1.3.1 Solubility

At fixed pressure, the solubility of hydrogen in certain transition metals is reported as function of temperature in Figure 2-5 [20] together with their enthalpy of solution (Figure 2-6)[20] (here positive for exothermic solution and negative for endothermic ones, due to a reversed sign taken by the author in his solubility equation). It is evident that metals with exothermic solution processes have higher solubility with regards to hydrogen. This leads to a higher capacity to store hydrogen inside them but also to easier hydrides formation, i.e. at a fixed temperature, the hydrogen pressure required to form hydrides is lower. This is negative from an applicative point of view, due to the embrittlement that hydrides induce to the metal as well as lattice expansion. In Figure 2-7 [19] some values of solubility at ambient temperature are reported: among the fcc (face-centered cubic) metals, Pd has the highest value, three orders of magnitude higher than Nickel, that confirm its excellent hydrogen affinity. Another consequence of hydrogen solubility that should be taken into account for industrial application is the lattice expansion; in fact, when a hydrogen atom occupies an interstitial site of the metal, a certain volume expansion occurs. It has been generally quantified [20], [28] that an increase of around 2.9 \AA^3 in fcc metal lattice occurs for each hydrogen atom absorbed. Obviously, higher the hydrogen content (due to a higher solubility), higher is the volume expansion of the membrane. This critical issue should be carefully considered into the fabrication process of a membrane, in order to avoid excessive mechanical stress induced by the presence of hydrogen inside the metal lattice.

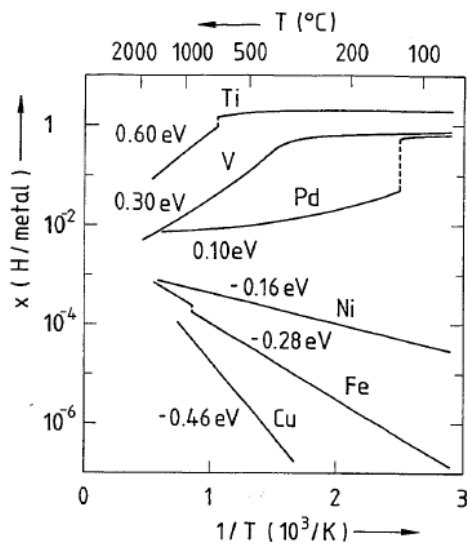


Figure 2-5 Hydrogen-metal solubilities as function of temperature at hydrogen pressure of 1 bar

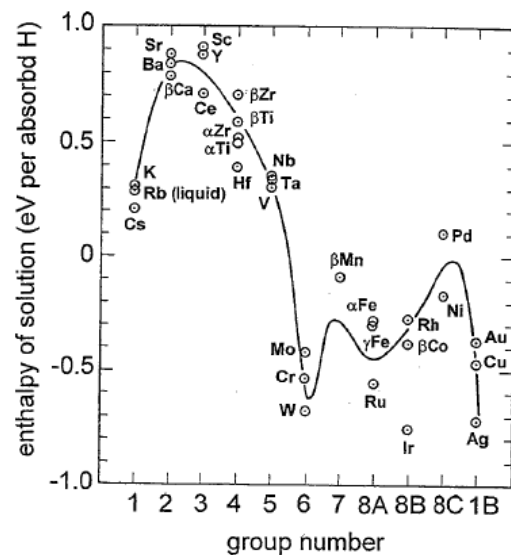


Figure 2-6 Hydrogen-metal enthalpies of solution [20]

packing	metal	hydride composition	H solubility (H/M @ 27 °C)	hydride ΔH formation (kJ/mol)	H ₂ permeability @ 500 °C (mol/ms Pa ^{1/2}) ^a
fcc	Ni	Ni ₂ H	$\sim 7.6 \times 10^{-5}$	-6	7.8×10^{-11}
	Cu		$\sim 8 \times 10^{-7}$		4.9×10^{-12}
	Pd	PdH	0.03	+20	1.9×10^{-8}
	Pt	PtH	$\sim 1 \times 10^{-5}$	+26	2.0×10^{-12}
bcc	V	VH ₂	0.05	-54	1.9×10^{-7}
	Fe	FeH	3×10^{-8}	+14	1.8×10^{-10}
	Nb	NbH ₂	0.05	-60	1.6×10^{-6}
	Ta	Ta ₂ H	0.20	-78	1.3×10^{-7}
hcp	Ti	γ -TiH ₂	$\alpha \sim 0.0014$ $\beta \sim 1.0$	-126	
	Zr	ZrH ₂	<0.01	-165	
	Hf	HfH ₂	$\alpha \sim 0.01$ $\beta \sim 1.0$	-133	

Figure 2-7 Hydrogen-metal solubility and permeability [19]

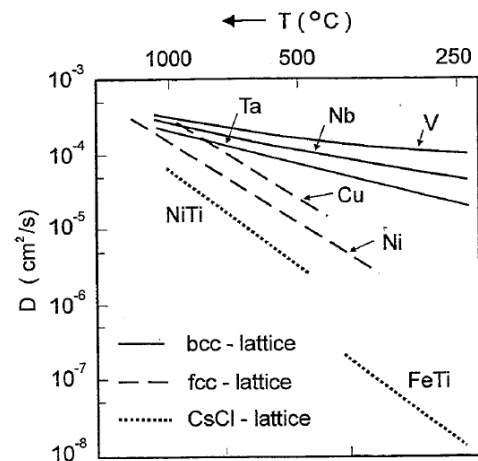


Figure 2-8 Hydrogen-metal diffusivity [20]

2.1.3.2 Diffusivity and permeability

Different techniques were adopted to study experimentally the permeation through metals: Altunoglu [29] distinguishes between microscopic and macroscopic techniques, depending on the objective of the study. Among the macroscopic techniques, the most commonly applied are the ones based on permeation flow measurements. Basically they measure the permeation through a specimen, more commonly a metallic disc of certain thickness. In the simplest form of permeation experiment, two chambers of known volume are separated by the specimen: the hydrogen enters one side of the specimen from a stable supply and is detected on the other side. In some cases, the pressure of the diffusing gas on the outlet side (under vacuum) is detected by a pressure gauge or by a mass spectrometer and converted to a flow measurement, by knowing the volume of the system. Alternatively, a Residual Gas Analysis can be applied: the permeate side is continuously evacuated by a pumping system, maintaining it under a proper vacuum level, and a mass spectrometer detects the permeating hydrogen flowrate. In both cases, a proper calibration of the mass spectrometer is necessary, in order to convert its signal into a hydrogen pressure or flowrate.

As the gas is put in contact with the membrane, the measured permeation flux grows with an initial transitory starting from zero to an equilibrium value, which then characterizes the steady state permeation. The typical permeation flow evolution along the time is reported below [30].

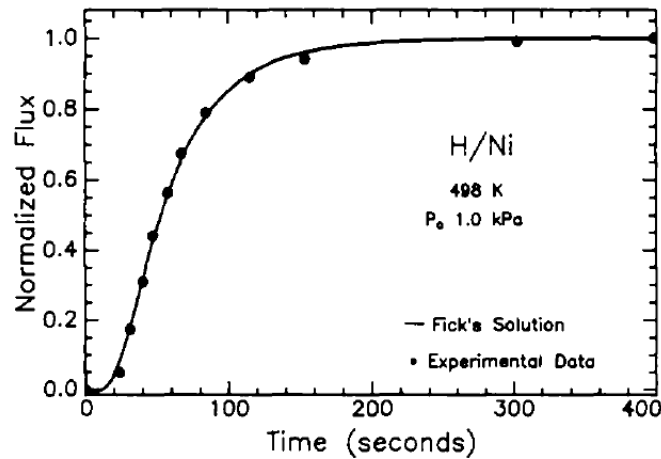


Figure 2-9 Permeation transient in a Nickel membrane (122 micron) : comparison between theoretical 2nd fick's law solution and experimental results [30]

From the comparison of the flow measurements with their theoretical values, it is then possible to obtain the permeability characteristics of the material. If the permeation is limited by diffusion, the hydrogen concentration evolution follows the Fick's laws, the 1st law in stationary conditions and the 2nd law for transient conditions. From these laws, for a mono-dimensional case with a fixed hydrogen concentration at the high pressure side (C_0) and negligible pressure on the other (vacuum side), one can express the permeation flux for:

1. Steady state conditions, constant flux expressed by Richardson law

$$J = \frac{pe_0}{\delta} e^{\frac{-E_p}{RT}} \sqrt{P_{H2,1}} \quad [\text{mol m}^{-2} \text{s}^{-1}] \quad 2-18$$

2. Transient conditions, analytical solution of the 2nd Fick's law with a Fourier transform [31]–[34]

$$J(t) = \frac{DC_0}{\delta} \left[1 + 2 \sum_{n=1}^{\infty} (-1)^n e^{\left(-\frac{Dn^2\pi^2t}{\delta^2}\right)} \right] \quad [\text{mol m}^{-2} \text{s}^{-1}] \quad 2-19$$

Therefore, having steady state measurements of the flux J at known gas pressures and temperatures, from the first relationship we can obtain the permeability coefficient at different temperatures. Knowing its Arrhenius dependence it is then possible to extrapolate a general expression of pe as function of temperature. Permeability is then obtained from steady state experiments.

To have a value of the diffusivity coefficient D , the “time lag” technique is used: a “time lag” coefficient is extrapolated from the flux-time curve (Figure 2-9), and from this coefficient the diffusivity is calculated. As for permeability, experiments at different temperatures can give an Arrhenius law of D versus temperature.

Furthermore, by performing these experiments, it is possible to verify if the permeation effectively follows or not the Fick's laws, so, if the hypothesis of bulk diffusion as rate limiting step in the overall process is true or not. For example, for steady state isothermal permeation, if the measured flows at different conditions do not follow the \sqrt{P} dependence, it could mean that the Sieverts equilibrium in Richardson's law is not respected: practically some surface effect may be rate controlling causing a non-equilibrium at the metal surface, so losing the Sieverts dependence from \sqrt{P} . Authors agree on the fact that if the hydrogen dissociation is the rate limiting step, then the flux dependence from gas

pressure becomes linear; for other intermediate cases a pressure exponent between 0.5 and 1 should be expected [29], [35], [36].

Figure 2-8 [20] reports diffusivity measurements for some metals, showing that a good diffusivity is also generally linked to a good solubility; in fact metals like Vanadium and Niobium have higher diffusivity than Nickel.

Several authors report result of permeability measurements [9], [14], [19], [37], [38] showing a good agreement between them. Looking at the Figure 2-10 and at the table reporting values at 500°C in Figure 2-7, in general we can say that Niobium, Vanadium and Tantalum are the most permeable metals respectively, followed by Palladium, one order of magnitude lower. Iron and Nickel are not so far from each other but they are 2 or 3 order of magnitude lower than Palladium. In the high temperature range, normally over 300 °C, authors generally found a good agreement with the Richardson's law, so verifying the validity of Sieverts law and diffusion limited regime hypothesis. A detailed analysis on the investigated experimental conditions for Nickel is provided in paragraph 2.2.3.

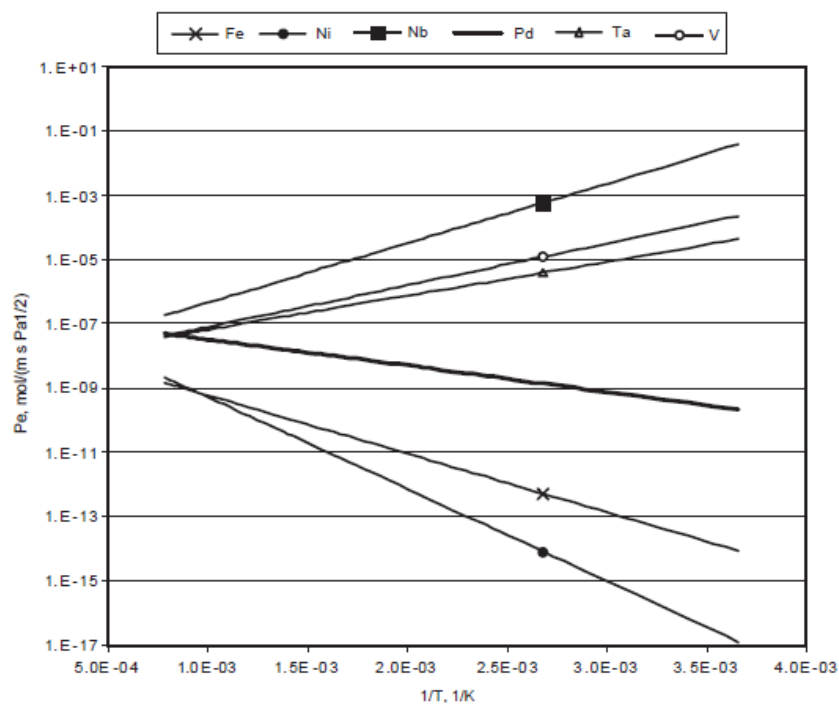


Figure 2-10 Hydrogen-metal permeability dependence with temperature[37]

2.2 Hydrogen-Nickel permeation

2.2.1 Why Nickel?

From the result shown in 2.1.3 it is evident that nickel has not the best characteristics in term of permeation. Despite this, it is often employed in membranes application for hydrogen. Moreover, for this study, we have to consider that the permeate side of the membrane will be constantly in contact with sodium at high temperatures: this particular condition could create some problems on the membrane due to material chemical compatibility with liquid sodium. Palladium, for example, dissolves into liquid sodium (6% of Pd mass weight percent at 400 °C [39]). Moreover, little quantities

of oxygen are dissolved into the sodium circuit, representing a corrosion risk for the metals which are in contact with it. This explains why in the past nickel was chosen for similar applications [6]: nickel in fact shows a very high corrosion resistance, contrarily to niobium, iron and palladium. Furthermore, if compared to materials with a higher permeability like palladium, nickel presents a lower solubility, characterized by an endothermic behavior: this means that during a permeation process, even when the membrane is cooled down at lower temperatures, a lower quantity of hydrogen is “trapped” into the metal. This means that lower lattice expansion takes place, thus reducing the risk of a mechanical failure. Another negative effect on the mechanical resistance of the membrane is represented by the hydride formation: Nickel can form hydrides only at very high pressures, far from the normal operating conditions of the membranes; hydride formation pressure in the range of 600 MPa is reported by the main reviews on Ni-H system [40], [41]. This fact allows its employment without a considerable risk of embrittlement due to hydrides.

According to Santucci et al. [27], non-noble metals like Ni are easily oxidized, and the formation of an oxide layer disturbs the hydrogen dissociation on the metal surface, thus reducing the permeability. As a solution, they proposed a Ni dense membrane covered with Pd-Ag by diffusion welding. Others proposed a porous Ni membrane covered by a Pd film. However, no experimental demonstration of oxide formation and negative impact is provided by these authors.

In the next paragraph, we focus on pure Ni, trying to find if experimental evidences show effectively results for Ni oxidation negative impact on permeation.

2.2.2 Ni-H phase diagram

According to Wayman and Weatherly [40], in equilibrium with H₂ pressures on the order of 1 atm or less, Ni exhibits the features of a classical "endothermic occluder" of H; the result is a very low solubility (interstitial) of H in Ni (order of H/Ni=10⁻⁵ at room temperature) and a positive temperature dependence of solubility.

Fukai [42] shows in his Ni-H phase diagram (Figure 2-11) that hydrides formation (phase β, on the right side of the curve) is possible for P>1GPa. If one operates at lower hydrogen pressure, the H atoms will be dissolved in Nickel as solid solution (phase α), increasingly with the temperature, without hydrides formation. This is confirmed also by a more recent theoretical study by Bourgeois [43], who provides a Ni-H phase diagram (Figure 2-12) focused on moderate hydrogen pressures (10⁵ and 10⁷ Pa), which is validated by comparison with several experimental measurements. We can observe that the two lines stay into the low values side of x (hydrogen concentration expressed as atomic ratio H/Ni) and, due to the Sieverts dependence with \sqrt{P} , at lower pressure corresponds a lower H/Ni ratio (lower solubility). Moreover we can remark that at low concentrations, in the order of 10⁻³-10⁻⁴ molar fractions, the hydrogen dissolution is an endothermic process, i.e. at fixed pressure the solubility is increased by increasing temperature, confirming what reported by Wipf [20] in Figure 2-6 for Nickel.

Furthermore, the (α) solid solution has the FCC crystal structure of Ni, with H dissolved interstitially. Because at 25 °C ~ (298 K), the maximum H content of the solid solution α-phase is low, lattice parameter changes are not expected to be large.

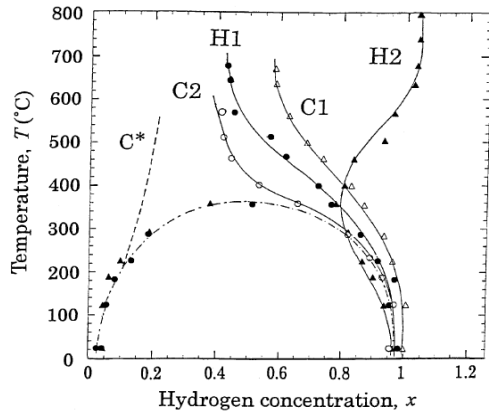


Fig. 1. Pressure-composition-temperature phase diagram of the Ni-H system. Results of heating runs H1 and H2, and cooling runs C1 and C2. Actual pressures in each run measured at room temperature, ~400 °C and the highest temperatures are H2 (4.3–4.6–5.4 GPa), C1 (1.5–2.1–2.4 GPa), H1 (1.9–2.1–2.2 GPa), and C2 (1.1–1.4–2.1 GPa), respectively. An isobar labelled C* illustrates (schematically) the expected temperature dependence at a lower pressure (≤ 1 GPa).

Figure 2-11 Ni-H phase diagram at high pressures [42]

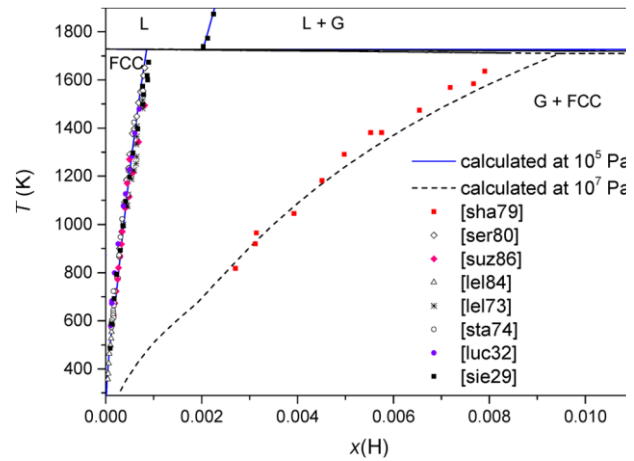


Figure 2-12 Ni-H phase diagram at low pressures [43]

2.2.3 Experimental coefficients

Hydrogen-Nickel permeation has been widely investigated, over different ranges of conditions and parameters: temperature, pressure, nickel purity, membrane thickness, surface conditions, geometries and measurements methods. All the studies presented here refer to an “ideal” single-crystal or polycrystalline nickel; in the second case specifics preliminary annealing and a polishing processes, giving a desired grain sizes and surface finishing. Structural defects like dislocations or vacancies, typically produced by cold working, are not considered hereby. Moreover, we limit our analysis to high purity nickel, with a degree varying from 99.4% to 99.999%. Finally, all the experiments were conducted on a g-Ni-g system, where pure hydrogen is on the feed side and vacuum is provided on the permeate side. Unfortunately, quite different results for solubility, diffusivity and permeability can be found depending on the study. Robertson (1973) [44] provided probably the most cited review of coefficients, giving a literature “best fit” value for each one, obtained with a statistical analysis on around 20 previous result, covering a wide range of temperatures. For this reason, his work is often considered as a reference. Most recently (2000), Sakamoto [41] proposed a very detailed review of Ni-H system, providing an updated list of coefficients, including Robertson’s ones, but without giving a detailed analysis or comparison.

In this study we compare Robertson “best fit” with more recent coefficients (we considered only authors who measured in operating conditions close to our domain of interest, i.e. 300-500 °C). It is important to remark that all these authors have found that steady state permeation under the analyzed conditions follow the Richardson’s law stated in equation 2-17:

$$J = \frac{pe_0}{\delta} e^{\frac{-E_p}{RT}} (\sqrt{P_{H_2,1}} - \sqrt{P_{H_2,2}}) \quad [\text{mol m}^{-2} \text{s}^{-1}] \quad 2-17$$

thus confirming that diffusion through Nickel bulk is the rate limiting step and hydrogen dissolution at interface follows Sieverts equilibrium.

2.2.3.1 Sieverts' constant - Solubility

We express the Sieverts' constant pre-exponential factor in the molar volumetric concentration [$\text{mol}_{\text{H}_2} \text{m}^{-3} \text{Pa}^{-0.5}$], to be coherent with the permeability expressed as [$\text{mol}_{\text{H}_2} \text{m}^{-1} \text{s}^{-1} \text{Pa}^{-0.5}$]. All the experiments were conducted on high purity Nickel, annealed, except for Ebisuzaki who analyzed a single-crystal nickel. Table 2-1 reports the main details of each study and the Sieverts constant pre-exponential factor and activation energy. It is worth noting that the activation energies are globally in accordance around 15 KJ/mol, except for Robertson "best fit" which includes

Table 2-1 Sieverts constant for H-Ni system

AUTHOR	YEAR	MATERIAL	PROCESS	TYPE	DIAMETER	THICKNESS	RANGE T	RANGE P	K_{S0}	E_s
					mm	μm	$^{\circ}\text{C}$	bar	$\frac{\text{mol}_{\text{H}_2} \text{m}^{-3}}{\text{Pa}^{0.5}}$	J mol^{-1}
Ebisuzaki[45]	1966	Ni 99.999%	single-crystal	disc		250-710	200-420	0.1-0.6	7.77×10^{-1}	15100
Robertson[44]	1973	Ni 270 >99.98%	annealed	disc	50	150-250	25-500	1-3	8.02×10^{-1}	15492
Louthan[46]	1975	Ni 99.995%	annealed	foils.rods			25-277	0.4-4	5.50×10^{-1}	15800
Robertson "best fit"[44]	1973						85-1453		4.16×10^{-1}	12477

In order to have a more precise view of the difference between each coefficient, we compare the hydrogen solubility, calculated by means of the Sieverts law in equation 2-5 taking the Sieverts constants from Table 2-1, in a given pressure and temperature range. The solubility obtained in $\text{mol}_{\text{H}_2} \text{m}^{-3}$ is then converted in the more conventional ratio H/Ni, by considering a nickel density of 8.908g/cm^3 and molar mass of 58.693g/mol . Figure 2-13 provides the solubility at three pressures (55 mbar, 185 mbar and 1 bar) in the temperature range 200°C - 500°C ; the values obtained with the above literature coefficients are compared with the Bourgeois' model [43], applied to these specific conditions. For the sake of clarity, the values at 400°C are reported in Table 2-2.

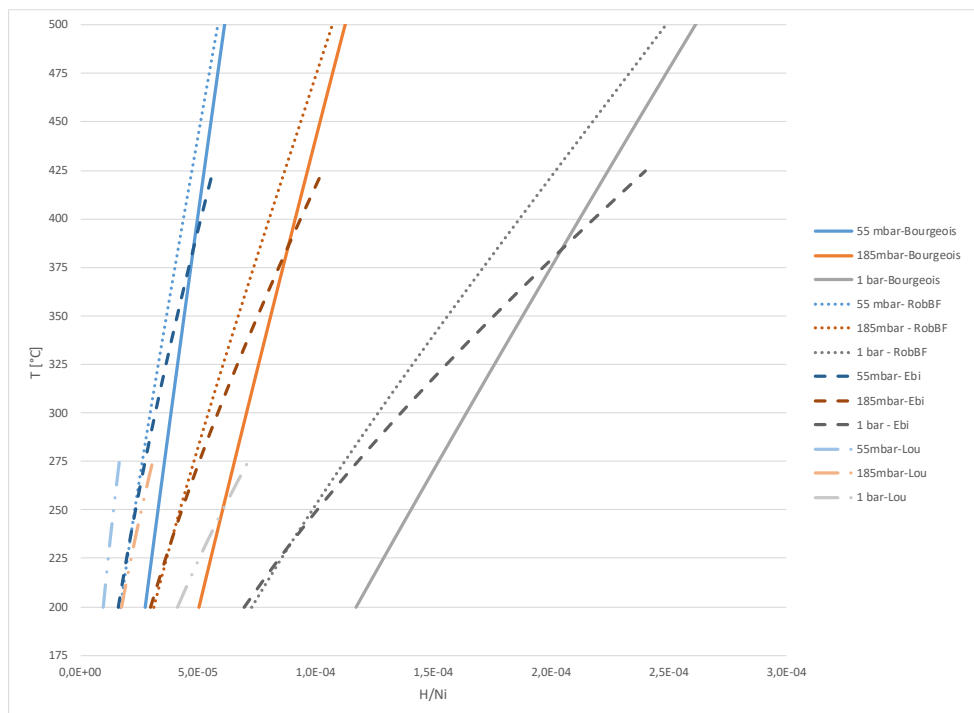


Figure 2-13 H-Ni solubility isobar lines (55 mbar-185 mbar-1 bar) between 200°C and 500°C . Comparison between Bourgeois' model [43] and solubility calculated with main literature coefficients

Table 2-2 H-Ni solubility [H/Ni] at 400°C and 55 mbar-185 mbar-1 bar. Comparison between Bourgeois' model [43] and solubility calculated with main literature coefficients

P	Bourgeois [43]	Ebisuzaki [45]	Robertson [44]	Robertson Best fit [44]
55 mbar	4.9788×10^{-5}	5.11×10^{-5}	4.92×10^{-5}	4.38×10^{-5}
185 mbar	9.1324×10^{-5}	9.38×10^{-5}	9.02×10^{-5}	8.03×10^{-5}
1 bar	2.12×10^{-4}	2.18×10^{-4}	2.10×10^{-4}	1.87×10^{-4}

2.2.3.2 Diffusivity

All the below coefficients were found in similar conditions; the only outlier is the analysis by Kuhn and Johnson [30], carried out on 99.5% purity Nickel, slightly lower than high purity Nickel (>99.9%). Figure 2-14 shows the calculated diffusivity for each author in the temperature range 300°C-500°C. The relative standard deviation, related to a mean value, is of about 25%. This means that between the lower and the higher value there is a percentage deviation of 50%. Actually, we can assess that the difference is mainly due to the pre-exponential factor, since the deviation on the diffusion activation energy is minimum.

Table 2-3 Diffusivity coefficients for H-Ni system

AUTHOR	YEAR	MATERIAL	PROCESS	TYPE	DIAMETER	THICKNESS	RANGE T	RANGE P	D ₀	E _D
					mm	μm	°C	bar	m ² s ⁻¹	J mol ⁻¹
Ebisuzaki[45]	1966	Ni 99.999%	single-crystal	disc		250-710	200-420	0.1-0.6	5.22×10^{-7}	40028
Robertson[44]	1973	Ni 270 >99.98%	annealed	disc	50	150-250	25-500	1-3	4.02×10^{-7}	39316
Louthan[46]	1975	Ni 99.995%	annealed	Foils-rods			25-277	0.4-4	7.00×10^{-7}	39500
Kuhn and Johnson[30]	1991	Ni 99.5%	ann at 900°C	disc		250-711	100-327	0.01-1	3.57×10^{-7}	37800
Lee and Lee[47]	1986	Ni 99.97%	annealed	Plate-cylind		200-5000	100-400	1	7.50×10^{-7}	39100
Altunoglu[48]	1991	Ni 99.98%	ann at 427°C	foil		300	100-400	0.07 max	7.12×10^{-7}	40640
Lee[34]	2013	Ni 99.999%	na	na	15	1000	450-580		6.41×10^{-7}	40400
Robertson "best fit"[44]	1973						0-1396		6.44×10^{-7}	40237

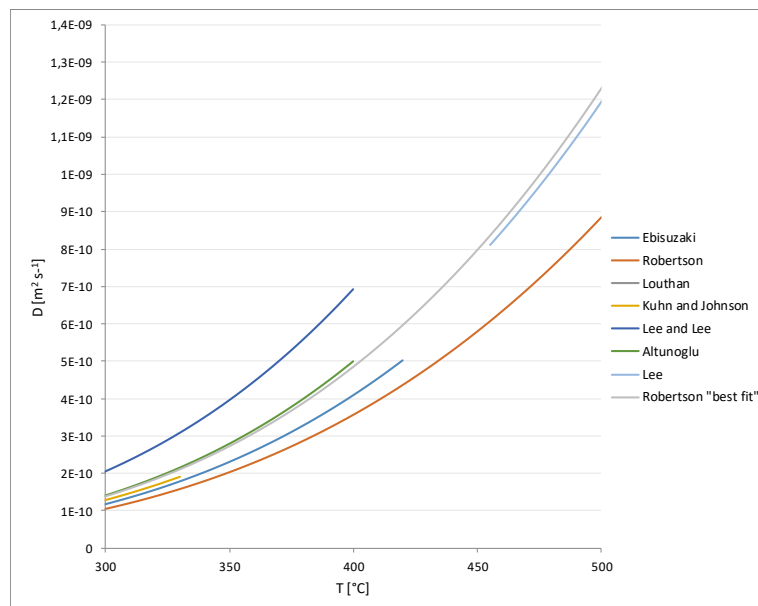


Figure 2-14 H-Ni diffusivity : calculated values for temperatures 300°C-500°C from the main literature coefficients

2.2.3.3 Permeability

As for the diffusivity, all the authors found similar values for the activation energy, in this case around 55 KJ/mol, as reported in Table 2-4. Nevertheless, a non negligible deviation is found in the pre-exponential factor: as a result, in the range of temperature 300-500 °C, we found a standard deviation varying from 5% to 28%, depending on the temperature. Some permeability values are reported as example in Table 2-5 and the entire dataset is represented in Figure 2-15.

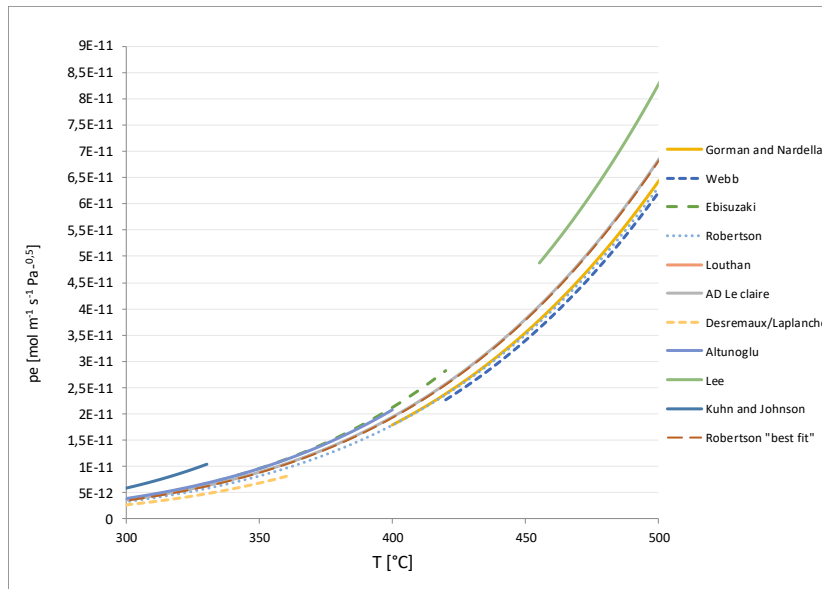
Finally, even if the several studies were carried out on different Ni purities, annealing conditions, thicknesses, we can conclude that a quite good agreement between authors is found. No correlation can be found between Nickel purity and permeability results, since both Gorman and Nardella [14] with Ni 99.4% and Kuhn and Johnson [30] with Ni 99.5%, found results in accordance with the others based on high purity Nickel.

Table 2-4 Permeability coefficients for H-Ni system

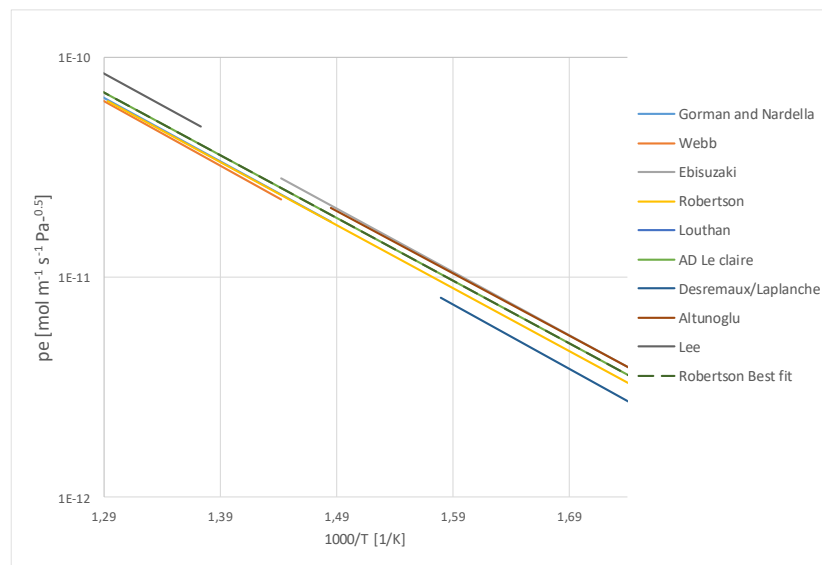
AUTHOR	YEAR	MATERIAL	PROCESS	TYPE	DIAMETER	THICKNESS	RANGE T	RANGE P	p_{e0}	E_p
					mm	μm	°C	bar	$\frac{mol_{H_2} m^{-1}}{s^{-1} Pa^{0.5}}$	J mol ⁻¹
Gorman and Nardella[14]	1962	Ni 99.4%	ann at 1000°C	cylinder	12.7	1570	400-850	0.1-1	3.49×10^{-7}	55268
Webb[9]	1964	Ni	annealed	tube	15.7	1000	420-850	1	3.84×10^{-7}	56106
Ebisuzaki[45]	1966	Ni 99.999%	single-crystal	disc		250-710	200-420	0.1-0.6	4.02×10^{-7}	55101
Robertson[44]	1973	Ni 270 >99.98%	annealed	disc	50	150-250	25-500	1-3	3.18×10^{-7}	54808
Louthan[46]	1975	Ni 99.995%	annealed	foils,rods			25-277	0.4-4	3.95×10^{-7}	55300
AD Le claire[49]	1983	Ni	na				20-1060		3.33×10^{-7}	54598
Desremaux/Laplanche[10]	1984	Ni222 99.8%	ann at 800°C	tube	7	300	200-362	1	3.46×10^{-7}	56106
Altunoglu[48]	1991	Ni 99.98%	ann at 427°C	foil		300	100-400	0.07 max	3.35×10^{-7}	54240
Kuhn and Johnson[30]	1991	Ni 99.5%	ann at 900°C	disc		15-122	0-327°C	0.01-1	5.92×10^{-7}	54900
Lee[34]	2013	Ni 99.999%	na	?	15		450-580	1	4.52×10^{-7}	55300
Robertson "best fit"[44]	1973						24-1060		3.33×10^{-7}	54598

Table 2-5 H-Ni permeability : calculated values for 300°C-350°C-400°C-450°C with main literature coefficients

T [°C]	300	350	400	450	500
Gorman and Nardella			1.79×10^{-11}	3.55×10^{-11}	6.43×10^{-11}
Webb				3.40×10^{-11}	6.22×10^{-11}
Ebisuzaki	3.82×10^{-12}	9.67×10^{-12}	2.13×10^{-11}		
Robertson	3.22×10^{-12}	8.10×10^{-12}	1.78×10^{-11}	3.50×10^{-11}	6.30×10^{-11}
Louthan					
AD Le claire	3.52×10^{-12}	8.83×10^{-12}	1.93×10^{-11}	3.79×10^{-11}	6.82×10^{-11}
Desremaux/Laplanche	2.66×10^{-12}	6.85×10^{-12}			
Altunoglu	3.82×10^{-12}	9.51×10^{-12}	2.07×10^{-11}		
Kuhn and Johnson	5.87×10^{-12}				
Lee					8.30×10^{-11}
Robertson "best fit"	3.52×10^{-12}	8.83×10^{-12}	1.93×10^{-11}	3.79×10^{-11}	6.82×10^{-11}
Standard deviation %	28.68%	13.45%	8.22%	4.68%	12.61%



(a)



(b)

Figure 2-15 H-Ni permeability : calculated values for temperatures 300°C-500°C from the main literature coefficients

2.2.4 Deviations from Richardson’s law for the H-Ni system: further studies

As showed in paragraph 2.1.2.2, many authors found that Richardson’s law is not valid in some particular conditions. Concerning the H-Ni system, both the reviews of Wayman [40] and Sakamoto [41] report that a certain number of experimental studies found deviations from the ideal case, represented by the Richardson’s law, due to two main reasons:

- Surface effects, which becomes important typically at low temperature, low hydrogen pressure and thin membranes. In particular, they affect the permeation dependence from the hydrogen partial pressure, modifying its exponent, which can vary from 0.5 (case of diffusion-limited permeation, considered in the Richardson’s law) to 1 (case of surface-limited permeation).

- **Trapping effects**, which appear when hydrogen is put in contact with a non-ideal nickel crystal. This condition is typically reached when the membrane is cold-worked or deformed. In fact, the cold-working induces inside the crystal lattice different types of defects: grain sizes non-uniformity, dislocations, vacancies. When such defects are present, the hydrogen, which in an ideal case would dissolve and diffuse only in the interstitial sites of the crystal structure, here find additional sites and ways to diffuse/dissolve. However, it is difficult to quantify the real impact on the permeation: normally, it is considered that the ideal solution/diffusion mechanism change (trapping, short-circuit diffusion, grain boundaries diffusion, etc), thus having an influence on the solubility and diffusivity coefficients.

Several authors studied permeation in some specific conditions where these effects are supposed to appear. In this paragraph, we provide a brief review of the main studies, trying to identify if some limits can be identified for the Richardson's law validity. Table 2-6 resumes the experimental conditions studied by the below-cited authors, together with their conclusion about the validity of Richardson's law.

Table 2-6 Literature studies concerning possible permeation deviation from Richardson's law

Author	Measure technique	Ni pre treatment	Ni purity	Thickness	Range T	Range P	Effects studied	Richardson validity
			%	μm	°C	bar		
Louthan (1975) [46]		Cold worked / annealed	99.98	na	300-550	0.4-4	trapping	Yes
Kiyoshi (1986) [50]	pressure	annealed	99.45	50	400	$3 \cdot 10^{-4}$ e $2 \cdot 10^{-1}$ Pa	surface	Yes
Lee and Lee (1986) [47]		Annealed 1150°C	99.97	200-5000	400	1	trapping	Yes
Cummings and Blackburn (1987) [51]	Mass spectrometer	Outgassed at 850°C	Low	500	350-480	na	Surface/trapping	Yes
Altunoglu, (1991) [48]	Mass spectrometer	Annealed at 427°C	99.98	125	100-350	0.053-0.073	surface	No
Altunoglu, (1996) [52]	Mass spectrometer	Cold worked / annealed	99.98	75	200-650	0.065-2	Trapping	Yes
Kizu and Tanabe (1999) [36]	Mass spectrometer	annealed	99.95	10-100	527-677	10^{-3} - 10^3 Pa	surface	Yes for $P > 10$ Pa
Yamakawa (2001) [53]	Mass spectrometer	Annealed at 850°C	99.99	125	125-440	0.004-0.064	surface	Yes

2.2.4.1 Surface effects

Kiyoshi[50] studied the effects of surface impurities on deuterium permeation through nickel at very low pressures at 400°C. He found that the permeation rate of nickel obeyed Richardson's equation,

meaning that the rate-limiting step is bulk diffusion. Neither carbon nor sulfur on the surface significantly affected the steady state permeation rate.

Cummings and Blackburn [51] proposed a “pressure modulated” method which is able to distinguish the surface effects from the bulk diffusion and from the trapping as well. The experimental conditions were chosen so that the data for nickel demonstrate diffusion limited flow. The experimental results were effectively best fitted by the model of diffusion limited flow. Measures of diffusivity and solubility are in accordance with Robertson.

Altunoglu [48] validated the Cummings and Blackburn models with experiments made on thinner membranes and lower temperatures and pressures. Firstly studying the influence of surface effects, at hydrogen pressures around 60 mbar, he found that for temperatures up to 623 K, the assumption that the permeation is proportional to $P^{1/2}$ (Richardson’s law) is not valid and would give imprecise estimates of permeation parameters. However, he gave measures of pe and D that are in accordance with Robertson.

Kizu and Tanabe [36] studied the surface effects on deuterium permeation through nickel at relatively high temperatures and extremely low pressures. They concluded that at above 10 Pa, the permeation flux shows the $P^{1/2}$ dependence, indicating the diffusion limited process, whereas below 10 Pa the permeation flux deviates downwards and shows the relation of $P^{0.7-0.9}$, suggesting the transition from the diffusion limited to the surface limited condition.

Yamakawa [53] compared surface effects on Pd and Ni membranes. Whilst he found that for Pd the surface contamination has an effect on permeability coefficient, for Ni he reports that the Sieverts’ law is valid and that the results are in good agreement with Robertson.

2.2.4.2 Trapping effects

According to Wayman [40] and Sakamoto [41], despite the number of experimental studies, the effects of grain boundaries and dislocations inside nickel remain uncertain.

Robertson [44] assessed, with his permeation experiments on different type of poly-crystalline nickel, that the grain size (30 to 120 micron) has no effect on the results. On the other hand, Stafford and McLellan [54] found an higher solubility in poly-crystalline nickel compared to a nickel single-crystal: in particular, they link this to the hydrogen trapping at grain boundaries. However, they not found any effect on the diffusivity. Lee and Lee [47] concluded that dislocations in nickel act as trapping sites of hydrogen. Both trapping and short-circuit diffusion at grain boundaries is found. Nevertheless, the trap activation energy appears to be lower than the activation energy for bulk diffusion, so it means that the diffusion is the rate limiting step.

Louthan [46] reported an increased permeability on cold-worked nickel and he interpreted the results as indicative of short-circuit diffusion through dislocation network. However, diffusion controlled permeation is measured in the steady state conditions. Similarly, Tseng [55] has observed higher permeation fluxes along dislocations and certain types of grain boundaries, concluding that it can be due either to higher diffusivity or higher solubility or to both. In a later study, Altunoglu [52] focused on trapping effects by cold-working, always with the modulated permeation technique: he found bulk diffusion limited flow for both nickel and nickel-thoria specimens. However, the diffusivity for cold

worked nickel is found to be lower than for annealed Ni, although the permeability is not affected by cold work.

Only to give an idea of the complexity of this subject, a PhD thesis has been recently conducted by Oudriss [56], aiming to describe the effects of nickel defects on the hydrogen diffusion and trapping. In two articles [57], [58], he stated that grain boundaries act as preferential sites for diffusion and trapping, and both strongly depends on the nature of the grain boundaries. In some cases (high-angle boundaries), an enhanced diffusion is found, due to a large excess of free volume; on other cases (low-angle boundaries), the high density of dislocations and vacancies represent potential traps for hydrogen.

Finally, although our study does not aim to in-depth investigate the metallurgic aspects of the nickel-hydrogen system, the above elements should be carefully considered in order to properly analyze and interpret our experimental results.

2.2.5 Conclusion

In the past many authors have studied experimentally the hydrogen permeation through Nickel, over high temperature range ($>300\text{ }^{\circ}\text{C}$), with the hypothesis that the diffusion is the rate limiting step. The Richardson's law was always followed by the experimental data, obtained for different conditions, thicknesses, pressures and measurements techniques.

More recently several authors have tried to identify the influence of surface and trapping effects with sophisticated measurements techniques and models. Surface effects are more focused on lower temperatures ($T < 300\text{ }^{\circ}\text{C}$), very low pressures (few pascals) and thin membranes ($<125\text{ }\mu\text{m}$).

Trapping effects, especially on cold-worked nickel, could have an influence on both hydrogen solubility and diffusivity and, as a consequence, on permeability. However, the diffusion-limited regime seems not affected and the Richardson's law is always followed.

Only two authors found a deviation from Richardson's law, because of surface effects becoming more important than bulk diffusion: this behavior was identified at very low thicknesses ($<125\text{ }\mu\text{m}$) and at combination of relatively low hydrogen pressures and temperatures (60 mbar at $350\text{ }^{\circ}\text{C}$ Altunoglu, 0.1 mbar at $527\text{ }^{\circ}\text{C}$ Kizu and Tanabe). Nevertheless, at least six authors studying similar pressure/temperature/thickness ranges did not find this deviation: looking at Table 2-6, we can conclude that Richardson's law validity is observed up to temperature of $650\text{ }^{\circ}\text{C}$ and hydrogen partial pressure of 4 bar, for thickness down to $50\text{ }\mu\text{m}$. It is worth noting that this range covers the entire application domain of this study ($300\text{ }^{\circ}\text{C} < T < 450\text{ }^{\circ}\text{C}$; $0.05 < P_{\text{H}_2} < 0.3\text{ bar}$; $300\text{ }\mu\text{m}$ thickness), which is detailed in Chapter 3.

2.3 Hydrogen-Sodium system

2.3.1 Pressure-composition equilibrium

When gaseous hydrogen is put in contact with liquid sodium below the monotectic temperature (911 K [22]), it dissolves in sodium up to a concentration beyond which solid sodium hydride (NaH), saturated with sodium metal, precipitates [59]. It is recognized that, below the saturation

concentration $C_{H,Na}^S$ (also referred as the hydrogen-sodium solubility), hydrogen is dissolved in the ionic form H^- [59], [60], as supposed by the solvation model of Thompson [61]; this is substantially due to the high reductive potential of sodium.

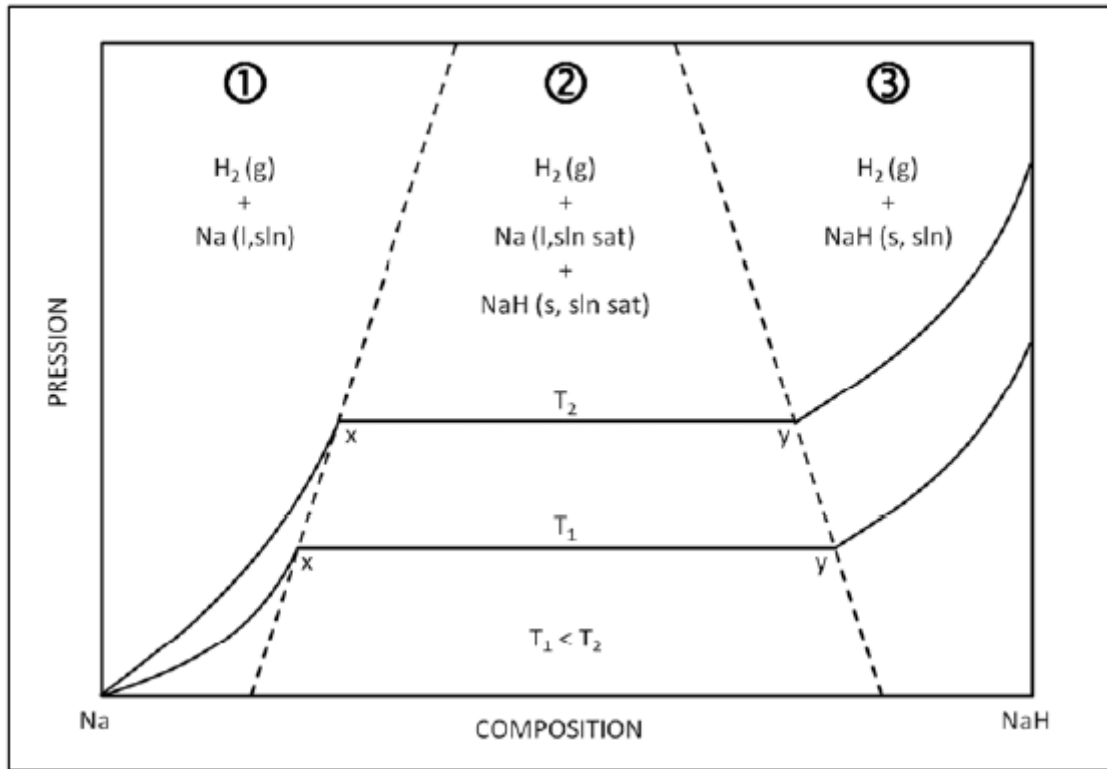


Figure 2-16 Pressure-composition phase diagram for Na-H system [62]

2.3.2 Sieverts' constant

In the single phase (zone (1) in the Figure 2-16, where liquid sodium at temperature T coexists with dissolved hydrogen at $C_{H,Na} < C_{H,Na}^S(T)$, the following equilibrium with gaseous hydrogen exists:



from where we can obtain a Sieverts equilibrium constant [59], similarly to hydrogen-solid metal equilibrium :

$$K_{S,Na}(T) = \frac{C_{H,Na}}{\sqrt{P_{H_2}}} \quad [wppm \text{ Torr}^{-0.5}] \quad 2-21$$

where $K_{S,Na}$ is the Sieverts' constant, depending from temperature, $C_{H,Na}$ is the hydrogen concentration in sodium and P_{H_2} is the equilibrium hydrogen partial pressure in the gas phase. When $C_{H,Na}$, increasing with the square root of hydrogen partial pressure, reaches the saturation value at a certain temperature (i.e. solubility), it precipitates as solid hydride NaH.

Measurements of Sieverts' constant by several authors revealed a negligible temperature dependence in the range of 603-843 K [22]. The following two expressions will be considered in this study:

- Whittingham [2] gives a constant value for the range 610-677 K :

$$K_{S,Na} = 4.6 [wppm \text{ Torr}^{-0.5}]$$

- Visser [7], reports an expression valid for T=644 K to 773 K :

$$\log_{10}[K_{S,Na}] = 0.860 - \frac{122.0}{T[K]} \quad (K_{S,Na} \text{ in } wppm \text{ Torr}^{-0.5}) \quad 2-22$$

This formula gives calculated values varying from 4.58 to 4.79 in the temperature range 610-677 K, not so far from Whittingham result, effectively confirming a negligible temperature dependence.

2.3.3 Solubility

Several authors measured hydrogen solubility as function of temperature [52]. The most recognized expression is given by Whittingham [2], by combining its own results with those by other authors :

$$\log_{10}[C_{H,Na}^S(wppm)] = 6.467 - \frac{3023}{T(K)} \quad 2-23$$

where $C_{H,Na}^S$ is the hydrogen concentration in sodium (expressed by weight part per million) at the saturation point, indicated by the "S" apex. This law is obtained from a least squares analysis in a range of T=423-673 K.

2.3.4 Transport properties: diffusivity

Trouvé and Laplanche [63] performed diffusion test through a sodium limited volume enclosed between two Nickel membranes, by measuring the time evolution of hydrogen permeating flow with a mass spectrometer. By the time lag technique, they found the following expression for hydrogen-sodium diffusivity, valid in the temperature range 469-580 °C:

$$D_{H,Na} = 2 \cdot 10^{-5} e^{\frac{-49053}{RT}} \quad [wppm \text{ Torr}^{-0.5}] \quad 2-24$$

Presently, these data are the only availables in the whole literature.

2.4 Hydrogen-Nickel-Sodium permeation applications: state of art

In the nuclear research, in particular regarding the SFRs, different technologies were developed involving hydrogen permeation through a Nickel membrane in contact with liquid Sodium at high temperature. Here we resume the most studied and more coherent with our application.

2.4.1 Membranes used for the « Hydrogen detection system »

Following a sodium-water interaction event in a Steam-Generator Unit, one way to detect hydrogen produced by the interaction and dissolved in small quantities (<1 ppm) inside sodium, is to circulate the sodium in contact with one side of a Nickel membrane, while maintaining the other side under vacuum; the difference of partial pressure, i.e. of concentration, on the two sides lets hydrogen permeates across the metallic membrane. The hydrogen permeation flux or partial pressure is detected by an ionic pump and/or a mass spectrometer, both parts of the detection system, and can be related to hydrogen concentration in sodium by means of a permeation law. This kind of technology is generally called "hydrogen-meter" or often "hydrogen-detection system, because their main goal is to measure accurately and quickly a change in the hydrogen concentration.

Roy and Rodgers [64] performed hydrogen measurement in a sodium loop between 425 °C and 700 °C by means of a 304 stainless steel tube (dimensions: 10 mm OD x 0.5 mm thickness x 500 mm length):

the sodium circulated around the tube while the inner side was maintained under vacuum by an ionic pump, whose current is proportional to permeating hydrogen pressure. The hydrogen concentration range is not specified, but the authors generically refer to values around 2 ppm. They verified that permeation from sodium to vacuum effectively follows Richardson's law, demonstrating that permeation of hydrogen dissolved in sodium was a diffusion controlled process, in their range of operating conditions.

Vissers [7], [65] performed similar measurements with a Nickel tubular membrane (6.8 mm OD x 0.25 mm thickness x 228 mm length) installed in a sodium loop. A vacuum is drawn on the membrane by an ionic pump. From the partial pressure of hydrogen on the vacuum side, a measure of hydrogen flux and the hydrogen activity in the sodium are determined by the measurement of the current to the ionic pump.

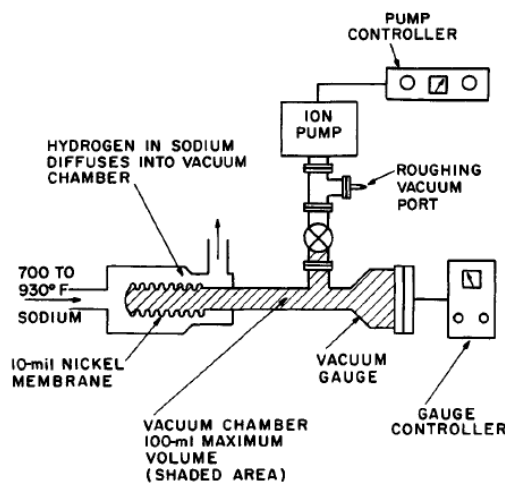


Figure 2-17 Hydrogen activity-meter by Vissers [7]

In his first study [65], the hydrogen transfer from the sodium bulk to the membrane and from the membrane to the gas phase is considered negligible; the main rate-limiting step is the hydrogen diffusion through the membrane. Thus, the stationary hydrogen permeation flux is expressed by the 1st Fick's law; Vissers then expressed hydrogen concentrations at the membrane interface (both sodium and vacuum side) by means of the Sieverts' law, accepting its validity both for sodium and gas phase. He calculates that the theoretical response time, i.e. the time to reach stationary flow, should be in the order of 10 seconds at 500 °C. Experimental measurements were made on sodium at 350 - 470 °C containing hydrogen between 0.1 ppm and 1 ppm. A good agreement was found between the hydrogen flux measurement, proportional to the ion pump current by mean of a calibration with standard leaks, and the Fick's law, thus confirming his hypothesis that the flux through the membrane should be controlled by the rate of diffusion.

In a later work [7], Vissers employed the same technology for the measurement of Sieverts constant in sodium-hydrogen system. Practically, he measured the hydrogen equilibrium pressure through the above-described activity-meter, relating this pressure to the a-priori known hydrogen concentration in sodium; the proportionality constant between them was the Sievert constant.

Hydrogen-meters constituted by Nickel membranes were developed by CEA for research studies, as well as for measurements on SFR reactors such as Phenix and Superphenix [66], to monitor the Steam

Generators Units tightness. These membranes are based on the same principle, except the fact that sodium flows continuously inside the nickel tubes, which are fixed to an external shell maintained under vacuum. The measurement of the hydrogen permeation flowrate is performed by a mass spectrometer, previously calibrated with a so-called “calibrated hydrogen leak” providing a known and well mastered hydrogen flowrate. Even in this case, the hydrogen concentration in sodium is related to hydrogen permeation flowrate respecting the Fick’s diffusion equation and the Sieverts’ law of hydrogen pressure-concentration equilibrium. By combining these two, we obtain the permeation Richardson’s law in Equation 2-17, where the side 1 (feed) is constituted by liquid sodium and the side 2 (permeate) by vacuum; if the hydrogen partial pressure in sodium is expressed as function of hydrogen concentration, by means of Sieverts law in equation 2-21, the Richardson’s law becomes:

$$J = \frac{pe_0}{\delta} e^{\frac{-E_p}{RT}} \left(\frac{C_{H,Na}}{K_{S,Na}} - \sqrt{P_{H_2,gas}} \right) \quad [\text{mol m}^{-2} \text{s}^{-1}] \quad 2-25$$

More recently, studies conducted at CEA [66], [67] compared the hydrogen detection by permeation through a membrane composed by four nickel tubes (SPHYNX) and an electrochemical detector developed by IGCAR [68]. The good agreement between the two methods suggests that the permeation equation used to convert mass spectrometer measurements into hydrogen concentrations is valid, thus confirming the validity of Fick’s diffusion law and Sieverts equilibrium hypothesis.

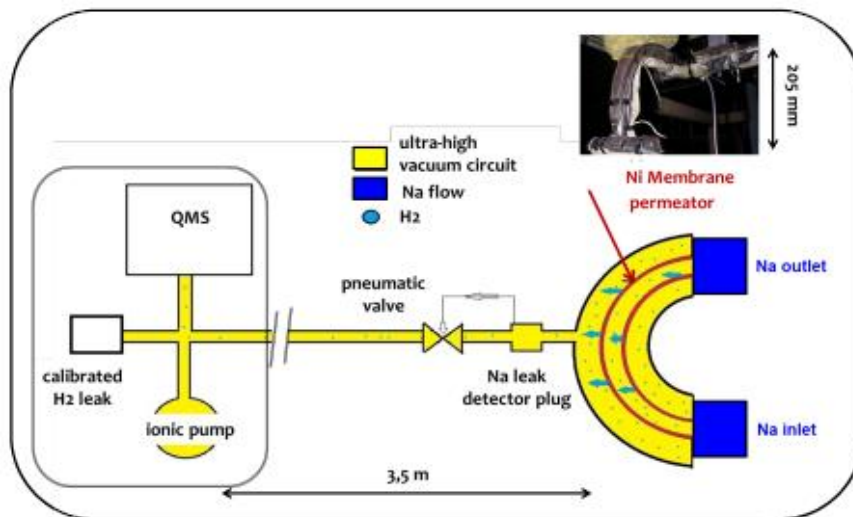


Figure 2-18 SPHYNX system for hydrogen detection

2.4.2 Cold trap purification: the PRIAM process

A regeneration process for the removal of impurities (i.e. hydrogen) from the cold traps of SFRs, loaded with sodium hydride, was developed by Latgé [6]: it consists of a bundle of Nickel thimbles (closed end tubes; diameter: 1.5mm), where sodium polluted by dissolved hydrogen, within a cold trap, flows outside the thimbles. The internal side of thimbles is maintained under vacuum, in order to produce hydrogen permeation from sodium side to vacuum side, thus allowing the sodium purification. Hydrogen permeated is then recuperated and stored. Practically, a process similar to that one of hydrogen detection membranes occurs, but with a quite different goal. If for hydrogen-meter even small quantities of hydrogen are sufficient to have a very efficient concentration measurement, here

getting a very high hydrogen flux is necessary to promote a short duration for the whole removal process in order to purify the contaminated sodium and to get an un-loaded reusable cold trap. Here, this very high hydrogen flux is obtained, thanks to a large number of so-called “permeators”, developing a large permeation surface and a very high hydrogen concentration (up-to 10 to 50 ppm), compared to the previously described hydrogen-meter, aimed to measure a steady state hydrogen content (from about 0.040 to 0.200 ppm).

Despite this difference, as for hydrogen meters, the permeation law expressed by equation 2-25 was employed for the design of the PRIAM permeators. This law, in fact, allows calculating the expected permeation flow as function of membrane surface, thickness, temperature and permeability coefficient; by these calculations, the correct membrane size was chosen in order to fulfill the desired PRIAM process performances.

First tests were conducted on membranes of 100 μm of thickness, at different membrane temperatures (450-550 $^{\circ}\text{C}$) and hydrogen concentrations in sodium (10 ppm-50 ppm), revealing that the membrane behavior is coherent with the theoretical results [69]. Later on, some other tests have shown some limited performances comparatively with the predicted ones: the difference was attributed to gaseous pressure drops inside the thimbles. Nevertheless, there was no additional tests to investigate the effect of the inner diameter of the thimbles, and to conclude that this limitation was only due to the pressure drop effect.

2.4.3 Hydrogen injection with Ni membrane for calibration of hydrogen-meters

Hydrogen-meters and PRIAM process both involved a hydrogen permeation flux moving from liquid sodium towards a gaseous side under vacuum. However, our study concerns the introduction of hydrogen in sodium, which involves a hydrogen flux moving in the opposite direction, i.e. from gaseous side towards liquid sodium.

In this regards, an interesting application was developed at Argonne National Laboratory by McKee [70]; in order to calibrate the hydrogen-meters [71], known quantities of hydrogen need to be injected in sodium. A nickel membrane was then developed to inject hydrogen by permeation in atomic form, by permeation, thus avoiding plugging issues. This membrane is a coil of Ni201 (99.5% of purity) tubing (3.175 mm OD x 0.380 mm thickness x 3960 mm length) inserted into a pipe where sodium flows through, as shown in Figure 2-19. Pure hydrogen is supplied from a feed bottle inside the nickel tube, maintained at pressure <100 kPa (it is not specified if the pressure varies or not), thus producing steady hydrogen injection rate. Hydrogen permeation flow could be measured by a mass flowmeter placed on the gas supply line. The author generically reported that test were conducted at temperatures from 430 $^{\circ}\text{C}$ to 530 $^{\circ}\text{C}$, producing steady hydrogen injection rate of 3 to 5 std cm^3/min (2.2×10^{-6} to 3.7×10^{-6} mol/s). However, from this few data, it is not possible to verify if the permeation Richardson’s law is respected (thus confirming or not the hypothesis of a diffusion-limited regime), since precise information are not given neither on the hydrogen pressure (precise values, maintained constant or pressure drop during permeation) nor on the temperature-injection rate correspondence. Moreover, in his later paper [71] McKee talks about a calibration procedure performed with this device, where the hydrogen pressure inside the feed bottle drops from 103 to 17 kPa in 9 minutes, thus revealing that an unsteady state permeation was certainly provided.

Finally, this system was successfully tested by ANL (two years of operation with no pressure-related failure) and installed by General Electric in research prototypes, since it allows the injection a known amount of hydrogen inside sodium, exploiting the permeation advantages. Nevertheless, for the interest of our study, several unknowns remain: in particular, not enough elements are provided to prove if the permeation follows a certain law, if the injection rate can be precisely controlled and provided under continuous steady conditions, and which is the actual operational range flexibility in terms of pressure and temperature. In this sense, the provided information on the injection rate variation (2.2×10^{-6} to 3.7×10^{-6} mol/s) seems to be insufficient for an industrial application, where a much wider operational range should be necessary, in order to guarantee a successful operational control.

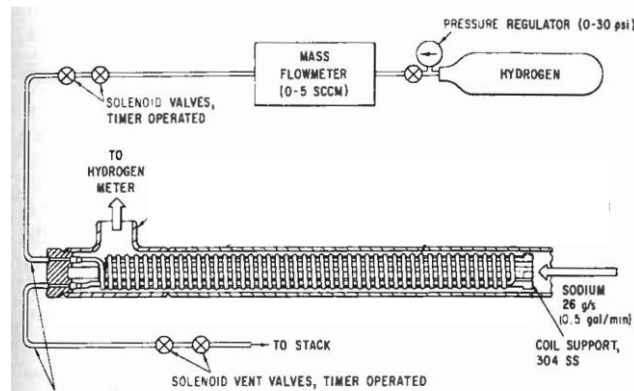


Figure 2-19 On-line hydrogen meter calibration system [70]

2.4.4 Conclusions

Various applications involving hydrogen permeation between a gaseous medium and liquid sodium were developed in the past. The most developed and consolidated one is the hydrogen-meter technology; several studies confirmed that the hydrogen permeation flux coming from sodium towards a gaseous side follows the Richardson's law, within the nominal conditions of use of this device, thus confirming that diffusion across the Nickel membrane is the rate limiting step and that Sieverts' law for Sodium-Nickel interface equilibrium is valid.

Some tests on PRIAM permeator confirmed as well the theoretical hydrogen flux established by Richardson's law, even if some additional tests highlighted some limited hydrogen flux, phenomena attributed most probably to high pressure drop within the Ni thimble.

Not only hydrogen detection systems or permeators dedicated to in-situ cold trap regeneration (PRIAM), involving a permeation flux originated from sodium side, but also a hydrogen introduction method through a nickel membrane has been already applied and its feasibility has been demonstrated by ANL. However, the operating conditions seems to be very limited and no elements about modelling or theoretical calculation have been provided, in order to verify if the Richardson's law is the most suitable way to calculate hydrogen permeation fluxes. Therefore, it is our interest to verify its validity for this particular configuration and range of operating conditions.

Chapter

3 Experimental methods

3.1 Motivation and goals

As pointed out by the state of art analysis (cf. Section 2.4.4), several applications involving hydrogen permeation between a gas mixture and liquid sodium were developed in the past, in particular hydrogen-meters, where hydrogen dissolved inside sodium permeates across a membrane towards a vacuum side, thanks to the partial pressure difference between the two sides. Nevertheless, the opposite case where hydrogen (pure or diluted in a gas mixture) is transferred to sodium by permeation has never been experimentally studied in detail: a very simple application to introduce hydrogen in sodium developed by ANL (Argonne National Laboratory), was limited to a single tube of nickel containing pure hydrogen in static condition; any detailed comparison with theory was provided by the authors. In this case, not enough details were provided in order to get an experimental validation of this application in a wide range of operating conditions.

A new experimental facility has been set up in CEA Cadarache laboratories to determine, under different operating conditions, the permeation performance of a multi-tubular nickel membrane, which transfers in a controlled way an accurate hydrogen flowrate from a gaseous mixture to liquid sodium. This experimental part aims to validate whether a global permeation law as the “Richardson’s law” is suitable to represent the permeation at the pilot scale.

The experimental study is divided into two steps:

- Step 1 – gas-vacuum test: the case of a gas-vacuum permeation is performed, in order to compare the permeation performance to available literature results.
- Step 2 – gas-sodium test: tests of permeation with sodium in the permeate side are carried out, to determine performances in operating conditions similar to a SFR and to evaluate the possible impact of sodium phase on the process.

This chapter describes successively the design of the permeator prototype, respecting all the constraints required by an application to SFR reactors as well as its integration within an existing experimental sodium loop; the development of a 1D-model aiming to support the prototype sizing; the process definition and the measurement techniques employed to quantify the prototype performances; the methods to post-treat the results and to compare them to the theoretical laws.

3.2 Prototype design

3.2.1 Main features

The permeator is a stainless steel shell and a nickel tubular bundle, which constitutes the so-called membrane. The gas mixture containing hydrogen is located within the tubes internal side, also called feed side, while the sodium is outside the tubes, confined by the external shell, in the so called permeate side. Since a continuous and stable hydrogen intake to sodium is needed, the use of static gas in the feed side is not possible, because the hydrogen consumption by permeation would reduce progressively its feed concentration and consequently the permeation rate, thus providing a non-stationary condition. Therefore, a continuous gas flow is needed inside the tubular bundle, in order to maintain controlled conditions and a stable permeation rate through the membrane in steady-state

regime. To perform this, a gas supply system is connected to the permeator feed side, thanks to one gas inlet and one gas outlet.

On the permeate side, inside the shell, one inlet and one outlet are provided as well, where the sodium circulating inside the experimental loop can get in and out the permeator respectively. When the gas-vacuum test is performed, the shell inlet is closed and the outlet is connected to a vacuum system, so that the entire shell is maintained under vacuum.

3.2.2 Design constraints

The final scope of the study is to demonstrate the possibility to apply a permeation process to introduce hydrogen into a sodium circuit of a SFR in a controlled way; in particular, the cold trap outlet, placed in the auxiliary section of the secondary sodium circuit, has been identified as the most suitable location to install the permeator. Therefore, it is necessary to take into account the related constraints and parameters, in order to design a prototype which could be easily scaled-up for the final application. In Table 3-1 the main figures are resumed.

Table 3-1 Design constraints of the SFR (as established in initial Astrid design)

Parameter	Range value	Description
T	320°C-450°C	Sodium temperature in auxiliary cold section of SFR secondary circuit
\dot{m}_{Na}	4.8 kg/s	Maximum sodium mass flowrate in the auxiliary section
$y_{H,Na}$	46 ppb	Hydrogen molar concentration at secondary cold trap outlet
$\dot{m}_{H,p}$	40 μ g/s	Target hydrogen mass flowrate introduced by permeation
$X_{H_2,gas}$	3% molar	Maximum hydrogen molar content into gas mixture to avoid explosion hazard with margin (4%)

A second constraint is given by the actual operating conditions of the experimental sodium loop, where the prototype is effectively tested. In particular, the Superfennec facility which has been chosen for tests, is limited by the following elements:

- Maximum sodium temperature in the test section of 450°C
- Maximum sodium flowrate in the test section of 1 m³/h (about 0.25 kg/s)
- Maximum free length of the test section of 800 mm

If compared to the Astrid design reported in Table 3-1, the sodium flowrate available on the Superfennec facility is around 20 times lower; this has an obvious impact on the size of the prototype, which has to respect the standard criteria on the allowable sodium velocity. Moreover, the limited free length on the Superfennec test section constitutes a limit on the maximum length of the prototype.

Finally, the prototype must respect the mechanical resistance criteria, in term of maximum pressure and temperature which will be applied, combined to the membrane geometry and dimension (diameter and thickness). As a simplified criteria for the design validation, we have considered the following formula, according to ASME B31.1:

$$\text{Minimum thickness} = \frac{P2r_o}{2SE + 2YP} + C \quad [\text{inch}] \quad 3-1$$

Where r_o [inch] is the membrane external radius, P [psig] is the design pressure, S is the material allowable stress (psi), E is the joint factor, Y is the wall thickness coefficient and C [inch] is the corrosion allowance [inch]. For practical reasons, it is worth noting that not all the possible membrane thickness and diameter combinations are available from commercial suppliers; therefore, in view of an industrial application, the choice of the dimensions should be limited to the available commercial dimension. As reference for this study, we considered the Goodfellow catalogue for Nickel tubes, already used previously by CEA.

3.2.3 Local modeling of the radial concentration profile

3.2.3.1 Model's equations and parameters

As support to the design activity, in order to quantify the whole hydrogen mass transfer rate, it is necessary to set up a model which includes all the resistances affecting the mass transfer (see Figure 3-1) occurring during the hydrogen permeation in a gas-metal-sodium configuration. In particular, the model here developed (called for simplicity "1D-model") takes into account the resistances coming from:

- the hydrogen mass transfer from the gas bulk to the gas-membrane interface;
- the hydrogen permeation through the membrane, considering it as a diffusion-limited process (cf. section 2.1.1.1);
- the hydrogen mass transfer from the membrane-sodium interface to the sodium bulk.

The considered geometry is a tubular configuration, represented by a 2D axial symmetrical domain on the radial (r) and axial (z) coordinates, constituted by the following components (cf. Figure 3-1):

- $r < r_i$: a gas mixture containing molecular hydrogen (H_2) as diluted species, flowing inside the tubular nickel membrane, with a given mass flowrate along the axial direction (z) at a given pressure;
- $r_i < r < r_o$: a nickel tubular membrane, of a known thickness, separating the gas phase from the sodium phase. Atomic hydrogen (H) permeates through the membrane from the most to the less concentrated side;
- $r > r_o$: a liquid sodium phase, flowing with a given mass flowrate along the axial direction on the external side of the Ni membrane. Atomic hydrogen (H) is dissolved in Na phase in the ionic form H^- .

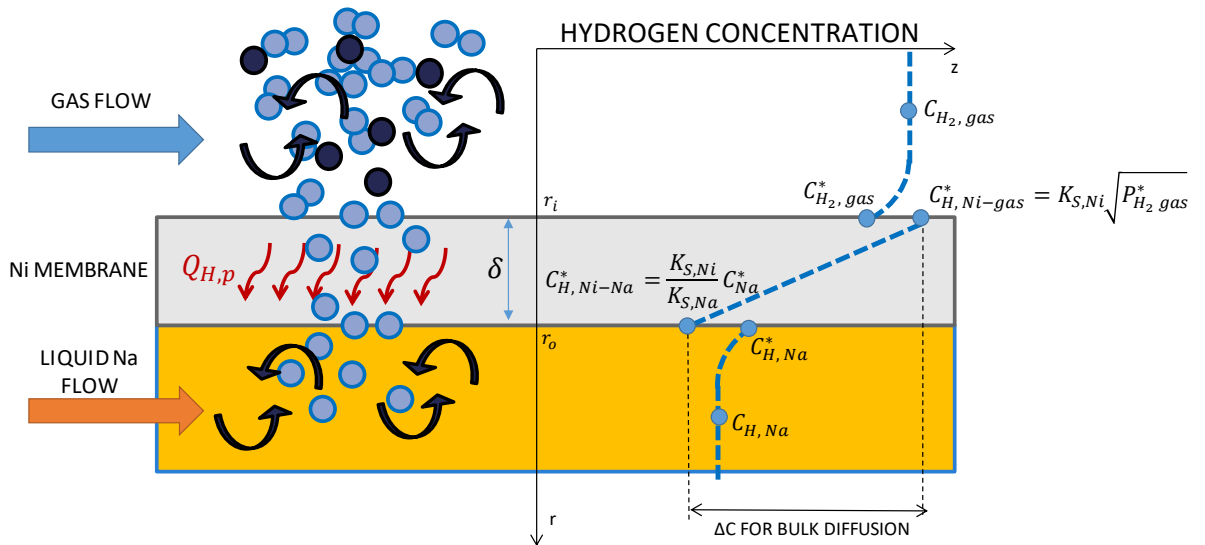


Figure 3-1 Hydrogen permeation physics in a shell and tube gas-Na configuration membrane

The following hypotheses are considered:

- the whole system is isothermal and adiabatic;
- steady state conditions are established;
- the membrane length is much greater than its thickness, thus the hydrogen diffusion through the membrane is only in the radial direction r ;
- gas mixture and liquid sodium density is constant over the domain;
- ideal gas law is assumed to be valid over the whole experimental conditions field;
- metal bulk diffusion is the rate limiting step of the permeation process through the membrane (diffusion-limited permeation) and no trapping or surface effect are considered, i.e. the permeation can be described by the Richardson's law;
- chemical-physical equilibria at interfaces follow the Sieverts law;
- the competitive adsorption of Argon at the gas-membrane interface is neglected;
- pressure drop on gas phase is neglected.

Hence, we develop the so-called "1D-model", considering the above hypothesis and an infinitesimal portion of tube length dz , where the hydrogen mass transfer rate in the radial direction can be defined as follows:

Gas phase: diffusive/convective transport of diatomic hydrogen molecules (H_2) from the gas phase bulk to the gas-membrane interface. The transfer flowrate is expressed in terms of hydrogen moles (H) in order to be compared with the others; this is why a factor 2 appears in the equation.

$$dQ_{H,gas} = 2 h_{gas} (C_{H_2,gas} - C_{H_2,gas}^*) * 2\pi r_i dz \quad [\text{mol s}^{-1}] \quad 3-2$$

Where h_{gas} [m s^{-1}] is the hydrogen mass transfer coefficient of the gas mixture, obtained from a recommended mass transfer correlation for fluid-solid interfaces, for a laminar flow through circular tube [72]. It depends on the gas velocity, the hydrogen diffusivity in the gas mixture and the membrane diameter and length.

$$\frac{h_{gas}(2r_i)}{D_{H_2,gas}} = 1.62 \left(\frac{(2r_i)^2 v}{L D_{H_2,gas}} \right)^{\frac{1}{3}} \quad 3-3$$

Ni membrane: atomic hydrogen (H) bulk diffusion through the nickel membrane is defined by the following infinitesimal correlation for cylindrical geometry

$$dQ_{H,Ni} = D_{H,Ni} (C_{H,Ni-gas}^* - C_{H,Ni-Na}^*) * \frac{2\pi}{\ln(r_o/r_i)} dz \quad [\text{mol s}^{-1}] \quad 3-4$$

Where $D_{H,Ni}$ is the hydrogen diffusivity in nickel, estimated with the Robertson 'best fit' relationship [44].

$$D_{H,Ni} = 6.44 \times 10^{-7} e^{-\frac{40237}{RT}} \quad [\text{m}^2 \text{s}^{-1}] \quad 3-5$$

Na phase: diffusive/convective transport of atomic hydrogen (H) from the Na-membrane interface to the Na bulk. It depends on the Na physical parameters (density, viscosity, velocity), the hydrogen diffusivity in Na and the hydraulic diameter.

$$dQ_{H,Na} = h_{Na} (C_{H,Na}^* - C_{H,Na}) * 2\pi r_o dz \quad [\text{mol s}^{-1}] \quad 3-6$$

Where h_{Na} [m s^{-1}] is the hydrogen mass transfer coefficient in liquid sodium, obtained from a recommended mass transfer correlation for fluid-solid interfaces, for a turbulent flow through circular pipe, given by Cussler [72].

$$\frac{h_{Na} d_h}{D_{H,Na}} = 0.026 Re^{0.8} Sc^{\frac{1}{3}} \quad 3-7$$

Where d_h is the hydraulic diameter, which, in case of a multi-tubes membrane geometry, is calculated as the ratio between four times the wetted perimeter and the sodium flow cross section.

In order to standardize the three above equations, an equivalent mass transfer coefficient U [$\text{m}^2 \text{s}^{-1}$] is defined for the three domains as follows:

$$U_{gas} = h_{gas} * 2\pi r_i \quad [\text{m}^2 \text{s}^{-1}] \quad 3-8$$

$$U_{Ni} = D_{H,Ni} * \frac{2\pi}{\ln(r_o/r_i)} \quad [\text{m}^2 \text{s}^{-1}] \quad 3-9$$

$$U_{Na} = h_{Na} * 2\pi r_o \quad [\text{m}^2 \text{s}^{-1}] \quad 3-10$$

Additionally, the following correlations for phase equilibrium defining hydrogen concentrations at the two membrane interfaces are considered:

Ni-gas interface: Sieverts law equilibrium is respected between molecular H_2 in gas phase and atomic H adsorbed in the membrane substrate, so that:

$$C_{H,Ni-gas}^* = K_{S,Ni} \sqrt{p_{H_2,gas}^*} = K_{S,Ni} \sqrt{RT C_{H_2,gas}^*} \quad [\text{mol m}^{-3}] \quad 3-11$$

Where $K_{S,Ni}(T)$ [$\text{mol m}^{-3} \text{Pa}^{-0.5}$] is the Sieverts constant (or solubility) of atomic hydrogen in nickel. Its temperature dependency is obtained by the Robertson 'best fit' relationship [44]:

$$K_{S,Ni} = 0.832 e^{-\frac{12477}{RT}} \quad [\text{mol}_H \text{m}^{-3} \text{Pa}^{-0.5}] \quad 3-12$$

Ni-Na interface: the concentrations of atomic hydrogen dissolved in nickel ($C_{H,Ni-Na}^*$) and in sodium ($C_{H,Na}^*$) both follow the Sieverts law, so that they can be expressed as function of an "equivalent" partial pressure, which corresponds to a common equilibrium pressure that gaseous hydrogen molecules H_2 would have if put in a gas phase in contact with both metals (either Ni or Na). Thus, if an equilibrium between Ni and Na hydrogen molecules exist, they should have the same equivalent partial pressure, corresponding to the following relationship:

$$\frac{C_{H,Ni-Na}^*}{K_{S,Ni}} = \frac{C_{H,Na}^*}{K_{S,Na}} \quad 3-13$$

Where $K_{S,Na}(T)$ [$\text{mol m}^{-3} \text{Pa}^{-0.5}$] is the Sieverts constant (or solubility) of atomic hydrogen in sodium, depending on temperature.

If one eliminates in equation 3-4 the terms $C_{H,Ni-gas}^*$ and $C_{H,Ni-Na}^*$ by introducing the relationships 3-11 and 3-13, and by considering the coefficients defined by 3-8, 3-9, 3-10, the three hydrogen flowrates become:

$$dQ_{H, gas} = 2 U_{gas} (C_{H_2,gas} - C_{H_2,gas}^*) dz \quad [\text{mol s}^{-1}] \quad 3-14$$

$$dQ_{H,Ni} = U_{Ni} \left(K_{S,Ni} \sqrt{RT} C_{H_2,gas}^* - \frac{K_{S,Ni}}{K_{S,Na}} C_{H,Na}^* \right) dz \quad [\text{mol s}^{-1}] \quad 3-15$$

$$dQ_{H, Na} = U_{Na} (C_{H,Na}^* - C_{H,Na}) dz \quad [\text{mol s}^{-1}] \quad 3-16$$

In order to respect the global hydrogen mass balance at steady state, the three hydrogen flowrates should be equal:

$$dQ_{H, gas} = dQ_{H, Ni} = dQ_{H, Na} = dQ_H \quad [\text{mol s}^{-1}] \quad 3-17$$

It is worth noting that, for a given hydrogen transfer rate, the higher is the mass transfer coefficient U, the lower is the difference in concentrations across the physical domain, according to the electrical resistances analogy (cf. Figure 3-2). Therefore, by comparing the values of the three mass transfer coefficients, the impact of each physics on the global hydrogen transfer rate can be assessed and compared.

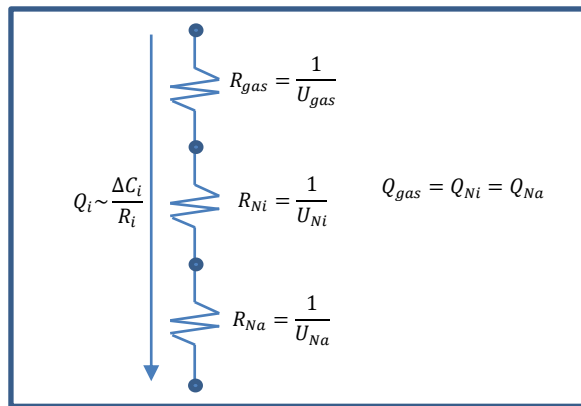


Figure 3-2 Schematic diagram of mass transfer resistance with electrical analogy

3.2.3.2 Analytical resolution on the radial direction

Let's consider the system composed by equations 3-14 to 3-17. U coefficients depend on the physical and geometrical parameters of the system: gas and Na flowrates, temperature, pressure, tube diameter and thickness. If the values of these parameters are fixed, the values of U can be calculated and remain constant; moreover, by imposing the gas and Na bulk concentrations $C_{H_2,gas}$ and $C_{H,Na}$ as input, the 5 remaining unknowns of the system reduce to $C_{H_2,gas}^*$, $C_{H,Na}^*$ and the 3 fluxes. The 5-equations system can be solved analytically (Annexe I)

The results obtained for a bundle constituted of 4 Ni tubes of diameter 7.2mm and 300 μm thickness, which are usual dimensions for existing hydrogen-meters, are reported in Table 3-2. The physical input parameters are taken from common operation of the available experimental facilities, as well as from typical operation of a SFR (cf. Table 3-1): sodium bulk concentration (typically expressed in wppm for practical reasons) is very low, normally below 0.1 wppm depending on the sodium purification degree;

here we considered a $y_{H,Na}$ value of 0.05 wppm, then converted in the input molar concentration $C_{H,Na}$. Sodium flowrate is coherent with the normal operation of the secondary loop of a SFR; the related sodium velocity is directly proportional to it and is obtained by knowing the above cited geometry. The same is done for the gas flowrate, typically expressed in $Nml\ min^{-1}$, then converted in gas velocity by knowing the membranes number and diameter. The gas molar concentration $C_{H_2,gas}$ is obtained from the more practical molar percentage $X_{H_2,gas}$, the gas pressure and the temperature by means of the ideal gas law.

Table 3-2 Mass transfer resistance model's parameters and variables

Geometrical parameters input		
r_i	mm	3.3
r_o	mm	3.6
r_{SHELL}	mm	21.2
N_{TUBES}	-	4
d_H	mm	17.5
Physical parameters input		
T	°C	450
Q_{gas}	$mol\ s^{-1}$	1.487×10^{-4}
	$Nml\ min^{-1}$	200
v_{gas}	$m\ s^{-1}$	0.013
P_{gas}	Pa	5×10^5
$X_{H_2,gas}$	% mol	3
$C_{H_2,gas}$	$mol_{H_2}\ m^{-3}$	2.495
\dot{V}_{Na}	$m^3\ h^{-1}$	1
v_{Na}	$m\ s^{-1}$	0.3
$y_{H,Na}$	wppm	0.05
$C_{H,Na}$	$mol_H\ m^{-3}$	0.042
Physical parameters		
$K_{S,Ni}$	$mol\ m^{-3}\ Pa^{-0.5}$	0.094
$K_{S,Na}$	$mol\ m^{-3}\ Pa^{-0.5}$	0.357
U_{gas}	$m^2\ s^{-1}$	$9.01 \cdot 10^{-5}$
U_{Ni}	$m^2\ s^{-1}$	$5.77 \cdot 10^{-8}$
U_{Na}	$m^2\ s^{-1}$	$2.23 \cdot 10^{-6}$
Outputs		
$C_{H_2,gas}^*$	$mol_{H_2}\ m^{-3}$	2.491
$C_{H,Ni-gas}^*$	$mol_H\ m^{-3}$	11.626
$C_{H,Ni-Na}^*$	$mol_H\ m^{-3}$	0.090
$C_{H,Na}^*$	$mol_H\ m^{-3}$	0.340
dQ_H/dz	$mol_H\ m^{-1}\ s^{-1}$	$6.65 \cdot 10^{-7}$

A first remark is that, for these fixed physical conditions, there is a great difference between the three mass transfer coefficients; in particular, gas phase has the highest value, 3 orders of magnitude bigger than the nickel, which is by far the lowest. Sodium mass transfer coefficient is between them, one order of magnitude bigger than mass transfer through nickel membrane. This means that the highest resistance to the hydrogen mass transfer is given by the nickel membrane. The second remark concerns the impact of gas and sodium phase on the hydrogen transfer rate: by considering equation 3-15, the terms in brackets corresponds to the difference ($C_{H,Ni-gas}^* - C_{H,Ni-Na}^*$); the ratio $C_{H,Ni-gas}^*/C_{H,Ni-Na}^*$ is around 130 and their difference is nearly equivalent to $C_{H,Ni-gas}^*$, since then the second term can be neglected. This is the physical result given by the so high mass transfer resistance of the membrane; moreover, the difference in concentrations across the membrane is so high that variations on the Na side seems to have no effect on the hydrogen transfer rate, while it is strongly dependent from the gas side concentration variations.

3.2.3.3 Sensitivity analysis

A sensitivity analysis is performed in order to evaluate the influence of each physical parameter variation on the calculated hydrogen mass transfer, by maintaining the other ones fixed at the values exposed in Table 3-2. The range of variation of each parameter is chosen in order to be coherent with the real operating conditions and with the membrane's resistance criteria. For the flowrates, the corresponding velocities are reported, and for the concentrations, both the practical units (wppm and %mol respectively) and the SI units are reported. The effect of each parameter's variation on the three mass transfer coefficients (U_{gas} , U_{Ni} and U_{Na}) and on the mass transfer rate per unit length (dQ_H/dz) is studied.

Table 3-3 1D model sensitivity analysis: main parameters variation range

Parameter	Units	Minimum	Maximum
T	°C	300	500
Q_{gas}	Nml min ⁻¹	100	800
v_{gas}	m s ⁻¹	8x10 ⁻³	7x10 ⁻²
P_{gas}	Pa	2x10 ⁵	10x10 ⁵
\dot{V}_{Na}	m ³ h ⁻¹	0.1	1
v_{Na}	m s ⁻¹	0.03	0.3
Membrane thickness	m	50x10 ⁻⁶	300x10 ⁻⁶
$y_{H,Na}$	wppm	0.05	10
$C_{H,Na}$	mol _H m ⁻³	0.042	4.25
$X_{H_2,gas}$	% mol	0.1	10
$C_{H_2,gas}$	mol _{H2} m ⁻³	8.31	0.08

Temperature

Temperature effect is analyzed in the range of 300°C-500°C. With the increasing temperature, all the mass transfer coefficients increase (Figure 3-3-a), as well as the hydrogen transfer rate (Figure 3-3-b); the last one follows an exponential law with temperature. In fact, U_{Ni} is directly proportional to the Nickel diffusivity, which vary with temperature according to an Arrhenius law. The fact that the

membrane transfer is by far the dominant effect is confirmed also by the value of U_{Ni} , which is always order of magnitudes lower than the others.

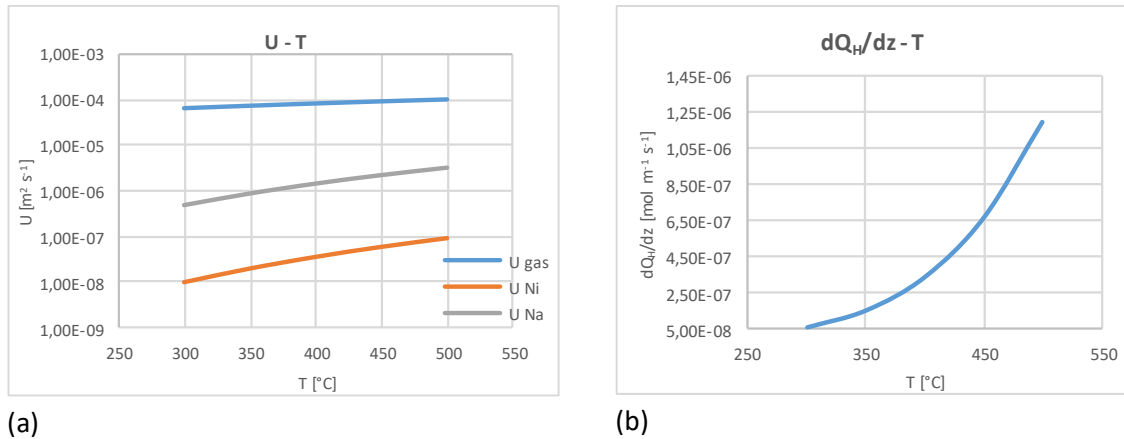


Figure 3-3 Temperature effect on hydrogen mass transfer: mass transfer coefficients in gas, nickel, sodium (a) and global mass transfer rate per unit length (b)

Q_{gas}

The gas phase is characterized by a laminar flow, due to the very low gas velocities; variations of gas flowrate are considered in the range 100 to 800 Nml/min, corresponding to gas velocities of 8×10^{-3} m/s and 7×10^{-2} m/s respectively. A velocity variation in this range can slightly affect the gas phase mass transfer coefficient, which is always orders of magnitudes higher than the others (Figure 3-4-a); as consequence, this does not have any influence on the calculated mass transfer rate per unit length, which does not vary at all (Figure 3-4-b). Physically it means that, whatever the gas velocity is, hydrogen is transferred in the radial direction much faster in gas phase than in sodium and in Nickel.

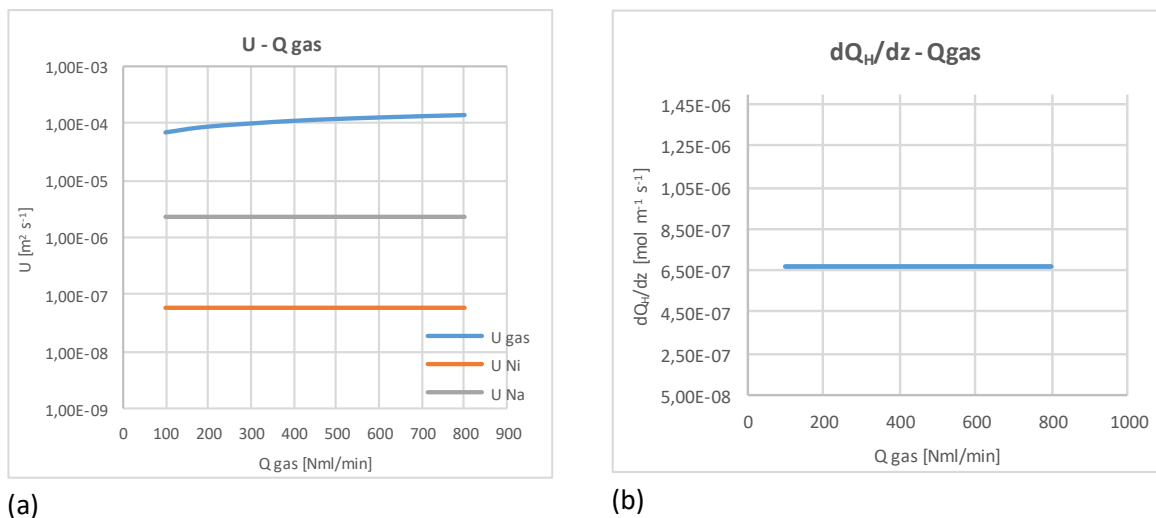


Figure 3-4 Gas flowrate effect on hydrogen mass transfer: mass transfer coefficients in gas, nickel, sodium (a) and global mass transfer rate per unit length (b)

P_{gas}

The gas pressure can also affect the mass transfer resistance of the gas phase: in fact, for the same gas flowrate and geometry, if the gas pressure increases, the gas velocity lowers, thus producing a lower mass transfer coefficient U . Pressure variations between 2 and 10 bar are considered here. In terms of mass transfer coefficient, a pressure growth up to 10 bar is not able to substantially have an effect, since the gas coefficient is always much higher than Ni and Na ones (Figure 3-5-a). On the other hand, a gas pressure increase has a direct effect on the hydrogen transfer rate (Figure 3-5-b); in fact hydrogen

concentration in gas bulk $C_{H_2, gas}$, which acts as a driving force of the mass transfer, is directly proportional to gas pressure. Therefore, if other parameters are fixed, at a higher gas pressure corresponds a higher hydrogen transfer rate.

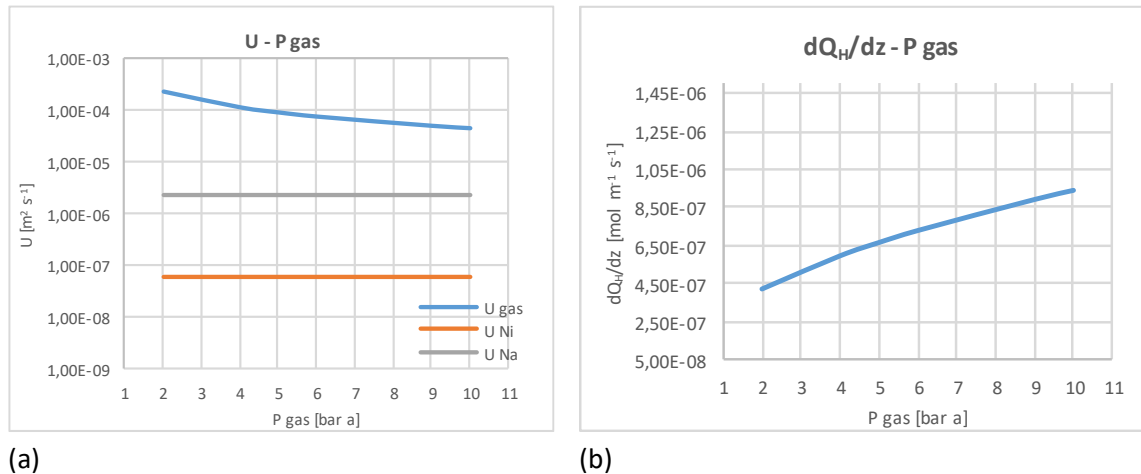


Figure 3-5 Gas pressure effect on hydrogen mass transfer: mass transfer coefficients in gas, nickel, sodium (a) and global mass transfer rate per unit length (b)

v_{Na} and membrane thickness

As for the gas phase, the Na velocity is directly proportional to the Na flowrate, and so the calculated Na mass transfer coefficient consequently; therefore, the lower is the Na flowrate, the lower is U . Na phase is characterized by a turbulent flow in SFR applications: here we analyze Na flowrates from 0.1 m³/h to 1 m³/h, corresponding to Na velocities of 0.03 m/s and 0.3 m/s and Reynolds numbers of 2×10^3 and 2×10^4 respectively, thus approaching the lower limit of a turbulent flow.

Considering a membrane thickness of 300 μ m, for the lower velocities we remark that the sodium coefficient approaches to the Nickel one, meaning that the two resistances could be comparable (Figure 3-6-a). This effect is imputable to the fact that sodium approaches the laminar regime. However, looking at hydrogen mass transfer rate variations (Figure 3-6-d, 300 μ m line), even if it is slightly reduced at lower Na flowrates, its variation (around -3%) is not comparable to the effect of the temperature and of the gas pressure.

The same analysis was repeated for lower membrane thicknesses (Figure 3-6-b,c and d): for a value of 50 μ m, which gets close to the minimum thickness for mechanical resistance, the Nickel mass transfer resistance is diminished by a factor 6; on the other hand, the sodium phase resistance can have a sensible effect only if the Na velocity approaches the laminar regime ($Re \sim 2000$). In this particular condition ($\dot{V}_{Na} = 0.1 \text{ m}^3/\text{h}$, $v_{Na} = 0.03 \text{ m/s}$), the hydrogen mass transfer rate can be significantly reduced of 25% compared to the nominal case at $\dot{V}_{Na} = 1 \text{ m}^3/\text{h}$ ($v_{Na} = 0.03 \text{ m/s}$). For an intermediate thickness of 150 μ m, the same Na flowrate decrease reduces the hydrogen transfer rate nominal value of about 10%.

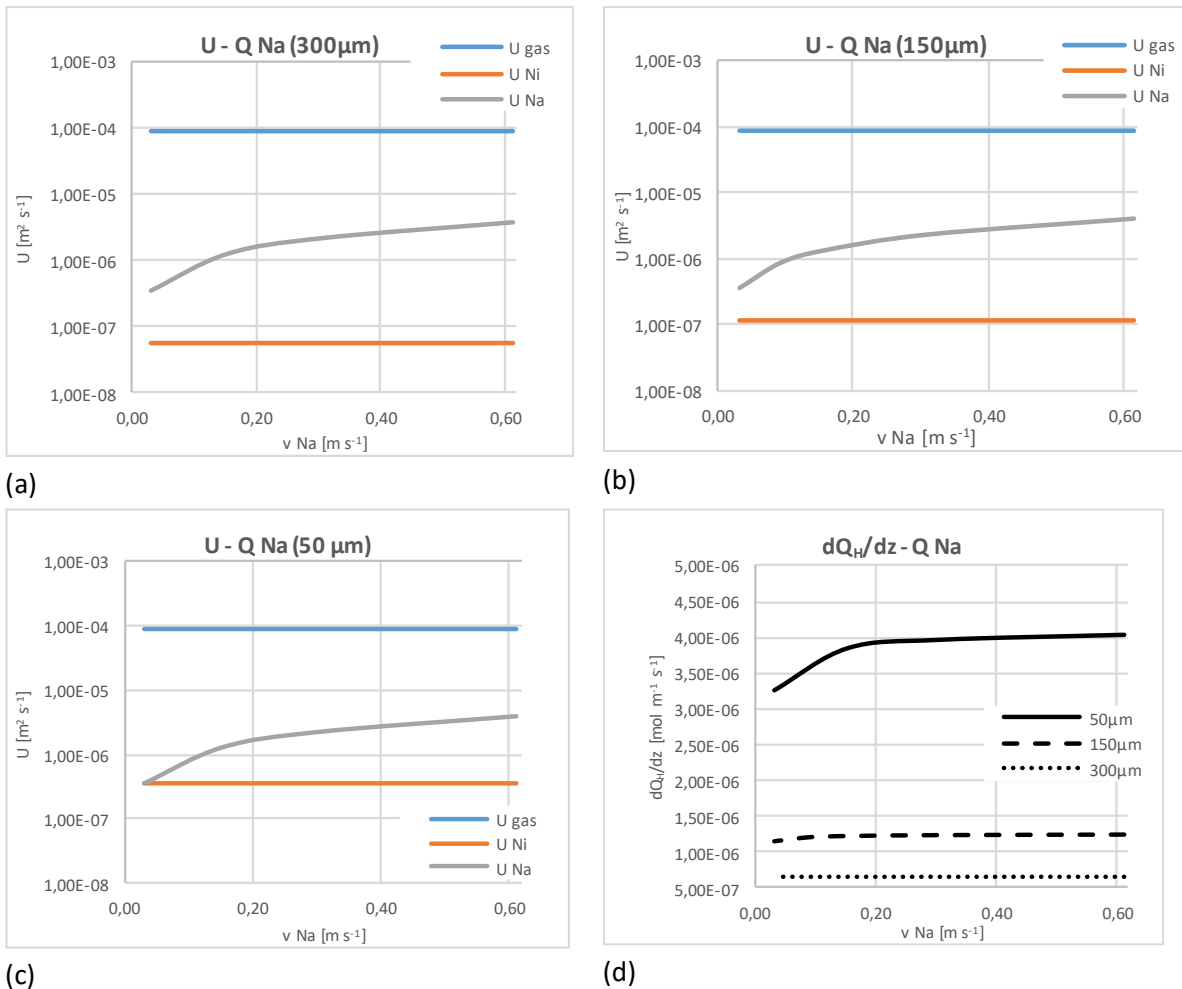


Figure 3-6 Influence of Na velocity on mass transfer resistances of gas, Ni and Na phase, for three membrane thickness 50 μm (c), 150 μm (b) and 300 μm (a). Influence of thickness on the global mass transfer rate per unit length (d).

Bulk concentrations $y_{H,Na}$ and $X_{H_2,gas}$

From a practical point of view, it will be never possible to operate with hydrogen concentrations up to 10% molar inside gas or 10 wppm inside sodium. Nevertheless, it is interesting to study the variation of these two parameters outside the limits fixed by the design constraints (cf. Table 3-3), for a scientific curiosity and to have a more complete analysis. First of all, bulk concentrations has no effect on the value of the three mass transfer resistances, since they does not affect substantially the bulk properties like density, velocity, viscosity. On the other hand, they both directly influences the absolute value of hydrogen transfer rate per unit length. As shown in the graph below, dQ_H/dz strongly depends on $X_{H_2,gas}$ while it is influenced by $y_{H,Na}$ variations only at very high values (>5 ppm); actually this range of concentration is not common at all for cooling sodium in a nuclear reactor.

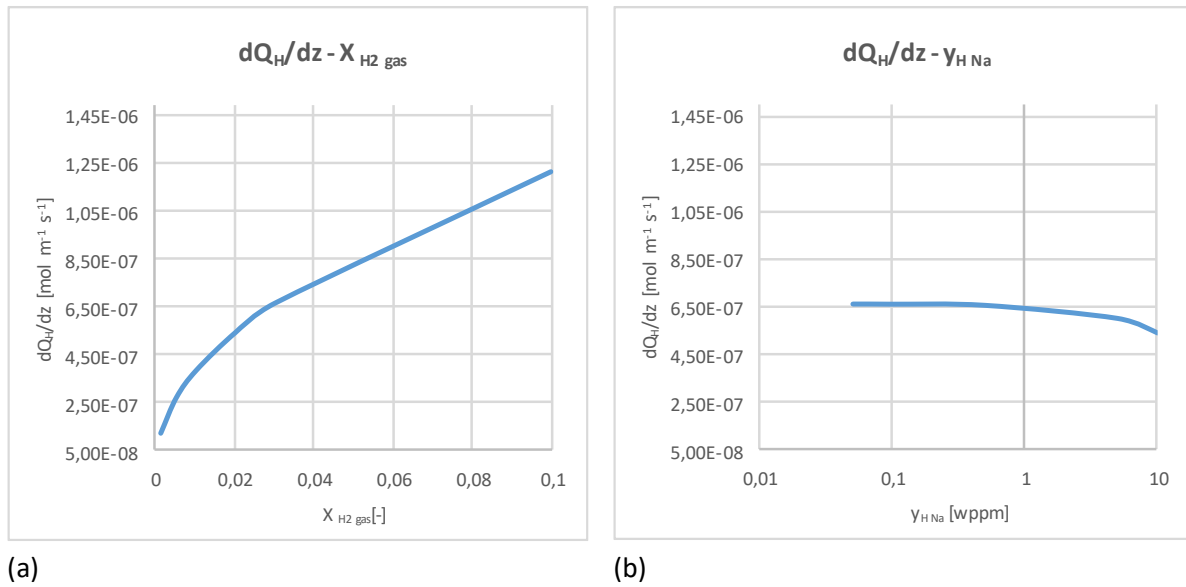


Figure 3-7 Hydrogen bulk concentration of gas (a) and Na (b) phase influence on mass transfer rate per unit length

3.2.3.4 Conclusion

The hydrogen mass transfer along the radial direction from the bulk of a gas mixture to the bulk of a liquid sodium phase, separated by a Nickel membrane, has been analyzed through modeling of the various steps of mass transfer. The mass transfer resistance of each physical domain is evaluated depending on the physical and geometrical parameters of the system. An expression of the hydrogen mass transfer rate across the three domains is given with an analytical formulation. By fixing a geometry, for a membrane thickness of 300 μ m, if the gas phase is characterized by a laminar flow and the Na phase by a turbulent flow, the most important resistance to hydrogen transfer is found to be in the nickel membrane; it overcomes by far the resistances given by the gas and Na phase. A sensitivity analysis is performed by varying the main physical parameters of the system: no changes are found on the three mass transfer coefficients ratio, confirming that Ni membrane resistance has the most important effect. On the other side, the absolute value of the hydrogen mass transfer rate per unit length dQ_H/dz is mainly determined by the temperature and by the two gas phase parameters: gas pressure and hydrogen molar concentration; no significant influence can be provided by Na phase in the standard operation range. Only for a very low thickness, of the order of 50 μ m, the Na phase resistance could have a significant influence on the mass transfer; however, the minimum membrane thickness should be imposed by mechanical constraints.

We can evaluate in quantitative terms the influence of each physical parameter on the permeation rate, by defining the following “impact” ratio:

$$I = \frac{\Delta\%(dQ_H/dz)}{\Delta\%(parameter)} \quad 3-18$$

Where the $\Delta\%(parameter)$ is the percentage variation of the physical parameter from a reference status and $\Delta\%(dQ_H/dz)$ is the corresponding percentage variation of the permeation rate. If $I < 1$, it means that the permeation percentage variation is lower than the corresponding parameter variation. For example, if a temperature variation of 30% produces a permeation variation of 60%, $I = 2$. The higher is the value of I , the higher is the impact of a parameter on the permeation, independently from their absolute values. In a practical regulation logic, parameters with a higher I will easier produce

changes on the permeation. Table 3-4 reports, for each parameter, the maximum value of I , obtained by varying the parameter from its minimum (taken as reference status) to its maximum value (cf. Table 3-3) and maintaining all the other parameters unchanged.

Table 3-4 1D model sensitivity analysis: physical parameters impact on permeation

Parameter	I_{MAX}	Impact on permeation
T	27.3	+++
Q_{gas}	0.0002	---
P_{gas}	0.41	+
\dot{V}_{Na}	0.04	-
Membrane thickness	1.7	++
$y_{H,Na}$	0.001	--
$X_{H_2,gas}$	0.9	++

Moreover, this analysis demonstrates that, for enough thick membranes ($>50 \mu\text{m}$), the hydrogen mass transfer from the gas phase to liquid sodium is limited by the permeation through the Nickel membrane; its mass transfer resistance is so high and the concentration difference between gas and Na phase so important, that the single permeation equation (i.e. Richardson's law) could estimate accurately the radial hydrogen transfer rate at a local axial coordinate z . The concentration difference between fluid bulk and membrane interface, both in gas and in sodium phase, could be neglected without any significant effect on the global hydrogen mass transfer, so that equation 3-15 becomes:

$$dQ_{H,Ni} = pe_{Ni}(T) * \frac{2\pi}{\ln(r_o/r_i)} \left(\sqrt{RT C_{H_2,gas}} - \frac{C_{H,Na}}{K_{S,Na}(T)} \right) dz \quad [\text{mol s}^{-1}] \quad 3-19$$

Where $C_{H_2,gas}^*$, $C_{H,Na}^*$ (interface concentrations) are replaced by $C_{H_2,gas}$, $C_{H,Na}$ (bulk concentrations) and the product $K_{S,Ni}D_{S,Ni}$ gives the permeability coefficient pe_{Ni} .

3.2.4 Driving parameters

In order to finalize the prototype design, all the physical and geometrical parameters which can drive the total hydrogen permeation flow through the membranes have to be identified. As a first approximation, it is reasonable to consider that for our experimental conditions the simple Richardson's law is able to provide an expression of the permeation flowrate across the membrane locally at a given axial position of the membrane, as demonstrated by the 1-D model analysis (see 3.2.3.4). In this regard, Equation 3-20 gives the hydrogen permeation flow in the radial direction $dQ_{H_2,p}(i)$, corresponding to an infinitesimal tube length dz (at a particular position z) of a single tube. Furthermore, since the hydrogen concentration in gas phase decreases along the tube length, as an effect of the permeation flux at the membrane, its axial evolution along the z -coordinate has to be considered; to do this, a discretized total and hydrogen mass balance is applied to the gas phase, according to Equation 3-21. This gas phase mass balance underlies the hypothesis that the hydrogen axial diffusive transport is negligible. In fact, it is possible to verify by means of the diffusion coefficient of the Ar-H₂ binary mixture (see table in section 5.8.3) for the conditions reported in Table 3-5, that the hydrogen diffusive flux in the axial direction is three orders of magnitude lower than the convective flux provided by the gas flow.

Finally, if the total tube length L is discretized in n elements dz (i.e. $dz = L/n$), the total hydrogen permeation flowrate from gas phase to sodium for N tubes can be obtained adding the i -contributions, according to 3-22.

$$dQ_{H_2,p}(i) = pe_0 e^{-\frac{E_{pe}}{RT}} \frac{2\pi}{\ln(r_o/r_i)} \left(\sqrt{P X_{H_2}(i)} - \frac{C_{H,Na}}{K_{S,Na}(T)} \right) dz \quad [\text{mol s}^{-1}] \quad 3-20$$

$$\left(\frac{Q_{gas\ in}}{N_{TUBES}} \right) \frac{[X_{H_2}(i-1) - X_{H_2}(i)]}{[1 - X_{H_2}(i)]} = dQ_{H_2,p}(i) \quad [\text{mol s}^{-1}] \quad 3-21$$

$$Q_{H_2,p}(L, N_{TUBES}) = N_{TUBES} \sum_{i=1}^n dQ_{H_2,p}(i) \quad [\text{mol s}^{-1}] \quad 3-22$$

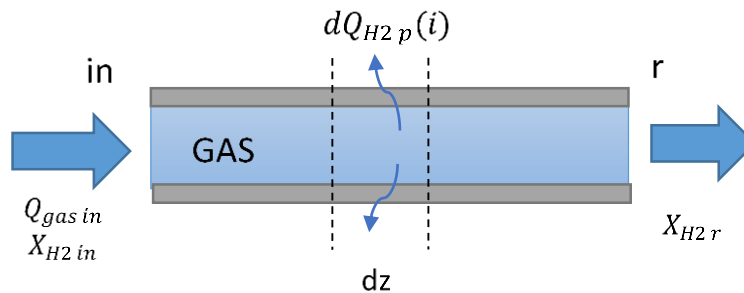


Figure 3-8 Discretization of the radial hydrogen mass transfer along the membrane length

All the driving parameters appearing in equations 3-20 to 3-22 are listed below: for each one a variability range is identified, between a minimum and a maximum value, in order to respect the constraints listed in 3.2.2.

Table 3-5 Driving parameters for the permeator prototype design

Variable parameters	Range of values	Fixed parameters	Value
T	300°C-450°C	$X_{H_2\ in}$	2.926% mol
P	1-10 bar	pe_0	Robertson "best fit"
$Q_{gas\ in}$	100-1000 Nml/min	E_{pe}	Robertson "best fit"
L	500-1000 mm	$C_{H,Na}$	50 ppb
N_{TUBES}	1-4	$K_{S,Na}$	Vissers
$(r_o; r_i)$	Obtained from Table 3-6		

For the membrane dimension (tube diameter and thickness), we considered the diameters above 5 mm taken from Goodfellow, reported in Table 3-6:

Table 3-6 Ni201 tubes diameter and thickness available commercial combination (source Goodfellow)

d_o	δ	Purity
mm	μm	%
9,5	1500	99,5
8,4	125	99,5
7,2	300	99,5
6,5	500	99,5
5,5	250	99,5

3.2.5 Sizing

The final sizing of the permeator is obtained by an iterative procedure, which takes into account the following steps:

- Choose membrane diameter and thickness.
- Verify the respect of the mechanical resistance criteria (3-1).
- Fix a membrane length and a number of tubes.
- Calculate the total hydrogen permeation flux at different T, P and $Q_{gas\ in}$ in their variability range (3-20 and 3-22).
- Verify if there is a sensible variation of the hydrogen concentration along the membrane ($X_{H_2\ out} \ll X_{H_2\ in}$).
- Fix a permeation test duration time.
- Verify if there is a sensible variation of hydrogen concentration inside the sodium volume along the permeation test.

In particular, the selected geometry is sized in order to transfer a minimum hydrogen flux, producing a significant variation of X_{H_2} and $C_{H,Na}$ during the permeation tests, both in gas and sodium phase respectively. This is necessary, because by measuring this variation we will be able to quantify the permeation rate. If a too small variation is provided, the measurements should be not enough accurate to give a reliable mass balance.

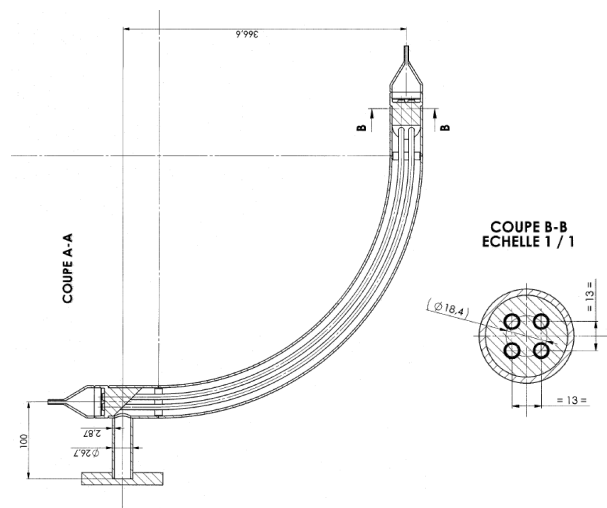
The finalized geometry consists of:

- $L=500\text{ mm}$; $N_{TUBES}=4$; $d_o=7.2\text{ mm}$; $\delta=300\ \mu\text{m}$

Since the membranes are fixed to tubesheets at the two opposite side of the permeator, a 90° bend shape is chosen for the entire prototype length (shell and membranes), in order to better support the mechanical stress coming from temperature deformations (Figure 3-9).



(a)



(b)

Figure 3-9 Permeator prototype: before installation (a) and section view (b)

3.3 Experimental setup

3.3.1 Superfennec sodium loop

The Superfennec loop in CEA Cadarache has been selected for the experimental campaign, thanks to its capacity to work under conditions close to those usually used in the secondary circuit of a SFR ($T \leq 450^\circ\text{C}$). It can work with high temperature sodium, maintained in circulation by an electromagnetic pump, and with a purification system equipped with a “cold trap”, which can provide a very pure sodium (essential for our purpose). Moreover it is endowed with a demountable test section, where the prototype can be easily installed or removed. It is also possible to install in the test section a hydrogen-meter (also called “DH” meaning “Détection d’Hydrogène”, in French language), to measure the amount of hydrogen dissolved in sodium during permeation test.



Figure 3-10 Superfennec overview

Superfennec consists of a main loop where liquid sodium circulates and three auxiliary sections, disposed in parallel, which can be isolated or connected to the main circuit by opening or closing respectively some manual valves. As reported in Figure 3-11, the main components are:

- The Test section (TS), where the permeator prototype and the hydrogen-meter (DH) are installed
- The Plugging indicator (PI) section, where a rough measurement of sodium purity is provided (also called “Plugging-meter”)
- The Cold trap (CT) section, where sodium is purified, by flowing through the cold trap

The main loop is equipped with a magnetic pump, which provides a maximum volumetric flowrate of about $2.5\text{ m}^3/\text{h}$; it can be modified by regulating the pump intensity. A heating tank (HT) is installed on the main circuit, where sodium is heated up to the desired temperature by means of electrical resistances. The maximum temperature which can be reached inside the test section is limited by the heating capacity of the tank. The maximum temperature of 450°C can be maintained stable inside the test section for a maximum flowrate of about $1\text{ m}^3/\text{h}$. The distribution of the total flowrate into the auxiliary sections can be regulated manually by modifying the valves opening.

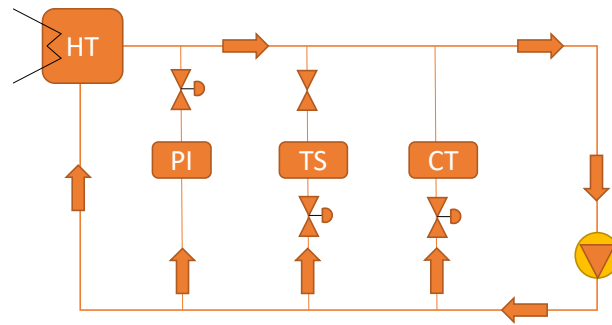


Figure 3-11 Superfennec sodium loop simplified diagram: circulation plan and main components. Cold trap (CT), Test Section (TS), Plugging Indicator (PI) and Heating Tank (HT)

3.3.2 Gas-sodium test configuration

The Test section, represented on Figure 3-12, is composed by the permeator prototype, which allows hydrogen introduction into sodium, and the hydrogen-meter (DH), which provides a measurement of the hydrogen concentration in sodium; both devices are based on hydrogen permeation property through nickel membranes. In the first one, a H_2/Ar gas mixture circulates inside tubular membranes and a part of hydrogen is transferred by permeation, diffusing through nickel's walls, to liquid sodium, which continuously flows outside the membranes. This happens thanks to the difference of hydrogen partial pressure (i.e. concentration) between gas and sodium phase, which is obtained for atmospheric or higher gas pressures and for relatively pure sodium ($y_{H,Na} < 1$ ppm); moreover, the membranes are maintained at a stable temperature, thanks to the hot sodium circulating outside them. In hydrogen-meter, the reverse process takes place: liquid sodium containing hydrogen flows inside nickel membranes, while the outer shell is maintained under Ultra High Vacuum (UHV) conditions, in order to reach a very low pressure. Thanks to the partial pressure difference, hydrogen diffuses from sodium to vacuum side and, measuring its equilibrium pressure by mass spectrometry, hydrogen concentration in sodium can be measured, if the whole system has been properly calibrated. As showed by Figure 3-12 and Figure 3-13, permeator and DH are installed in series, so that sodium flows before through the permeator, then through Hydrogen-meter; moreover, permeator's connections to the gas supply system (blue) and DH's connection to the UHV system (green) are highlighted.

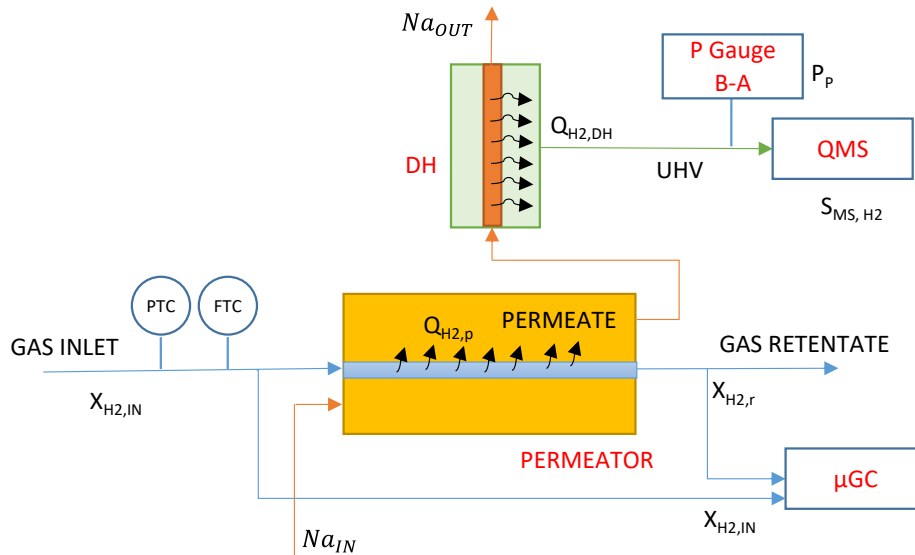


Figure 3-12 Gas-sodium permeation: test section diagram

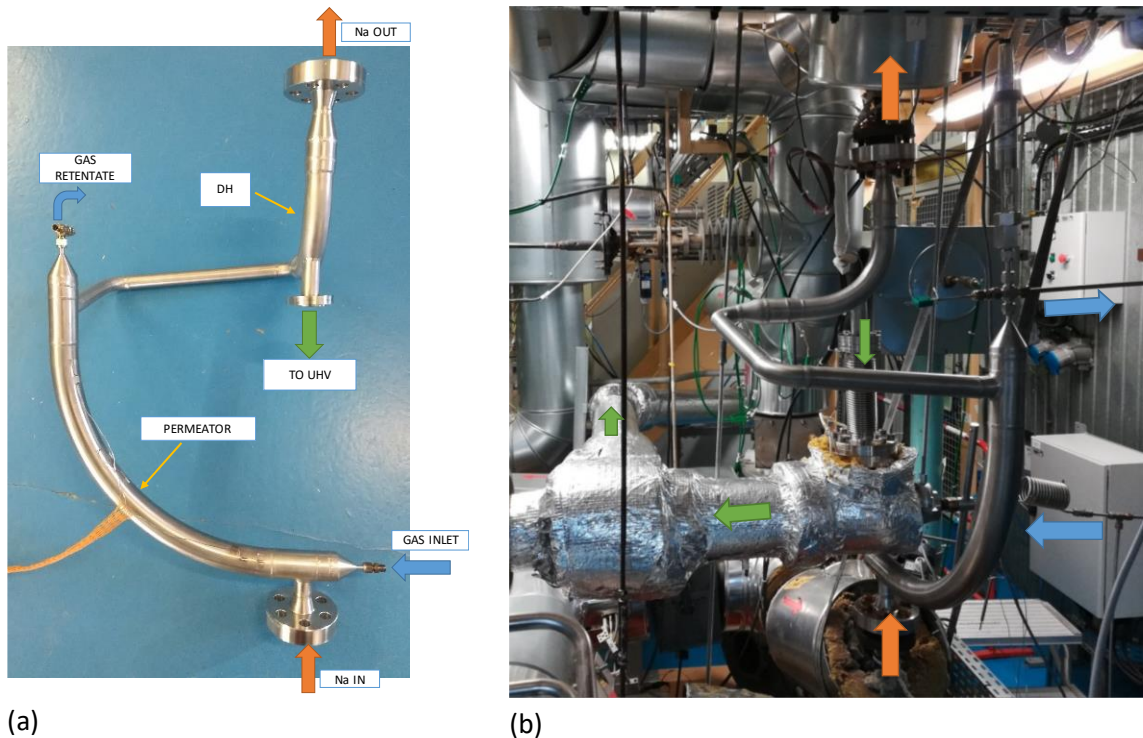


Figure 3-13 Test section before (a) and after (b) installation for gas-sodium test: details of sodium side (orange), gas side (blue) and UHV side (green)

3.3.3 Gas-vacuum test configuration

For the gas-vacuum permeation test, the permeator prototype is not connected to the sodium loop and no sodium circulates inside the shell. The high temperatures needed for the permeation to take place, without sodium, are provided by an electrical heating resistance placed on the permeator shell. As for gas-sodium test, the gas supply system feeds the permeator with a H_2/Ar gas mixture flowing inside the nickel membranes, while the shell is isolated and maintained under vacuum by the UHV system. Due to the hydrogen partial pressure difference between the feed and the permeate side, a hydrogen flow is transferred by permeation through the membranes. As a result, the molar fraction at

the permeator outlet (gas retentate) will be lower than at the inlet. Figure 3-14 and Figure 3-15 shows the test section details as well as the connections to gas supply system (blue) and UHV system (green).

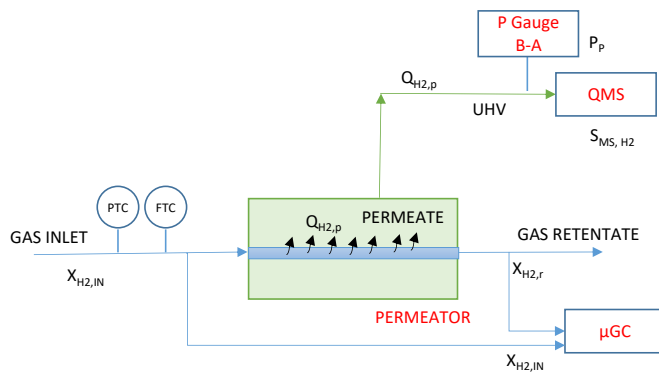


Figure 3-14 Gas-vacuum permeation: test section diagram



Figure 3-15 Test section installed for gas-vacuum test: details of gas supply system (blue) and UHV (green) connections

3.3.4 Gas supply system

The gas supply system is connected to the permeator inlet and retentate gas sides; it must guarantee a continuous gas supply to the permeator, at controlled and adjustable pressure and flowrate. A detailed PID diagram is provided in Annex II. It consists of stainless steel piping with a diameter of 4-6 mm; all fittings are Swagelock brand. It is equipped with a thermal-mass flow meter (FTC) and a pressure sensor (PT01) that controls a control valve (PCV04). A pressure relief valve (PSV01) is also provided for safety reasons, as well as a non-return valve (CV01) at the outlet to prevent the circuit from being contaminated by ambient air. A gas preheating system is provided and the gas temperature is measured at the inlet and outlet of the permeator by thermocouples (TT01, TT03). Two bottles (Crystal mixture by Air Liquide) can feed the circuit: one containing a mixture Ar (97% mol) - H₂ (3% mol) for permeation tests, the other containing an inert gas (Ar) to purge the entire circuit before and after each test. In the "gas-sodium" configuration, two spark plugs for the detection of potential sodium leaks are installed on two "tees" just at the Permeator inlet and outlet, followed by coils to cool and freeze the possible leak.

Gas pressure can be adjusted in the range of 1 to 10 bar by the pressure controller (PTC), while gas flowrate can vary from 100 to 1000 Nml/min by regulating the FTC.

Two sampling lines are installed at permeator inlet and outlet respectively, connected to a gas chromatograph (μGC), which provides a measurement of the hydrogen molar concentration into the gas sample. Pneumatic automated valves and a control system allow remote operations during tests.

3.3.5 Residual Gas Analysis (RGA) system

The RGA system installed at Superfennec allows to analyze hydrogen permeation coming from a membrane: in particular, it is applied both to the hydrogen-meter during gas-sodium test (Figure 3-12)

and to the permeator prototype during gas-vacuum test (Figure 3-14). In both case, in fact, the shell is connected to the RGA system and maintained under vacuum by its pumps; the hydrogen flowing inside the membranes (dissolved in liquid sodium for the first or contained in a gas mixture for the second), permeates through them to the shell side, thanks to the hydrogen partial pressure difference maintained by the pumping system. The goal of RGA system is to provide a measurement of the hydrogen permeation flowrate which take place across the membranes, whatever its origin.

As showed by Figure 3-16 and Figure 3-17 RGA system consist of:

- An *UltraHighVacuum (UHV) piping*: length 3,5 m approximately, diameter CF63 (63 mm), connecting the shell containing permeation membranes to the pumping/analyse skid;
- a *turbo molecular pump* (AGILENT/VARIAN – V81-M): it is connected to the UHV piping after the Pressure Gauge; a manual ON/OFF valve allows to isolate it from the vacuum system;
- a *ionic pump* (AGILENT VACION PLUS150): connected to the end of UHV piping and isolated by an automatic valve with three possible position (OPEN/INTERMEDIATE/CLOSED). This pump is isolated during gas-vacuum test, since the pressure inside the system is too high;
- A *membrane pump*: connected in series to the Turbopump, to provide the primary vacuum for start-up operations;
- A *Quadrupole Mass Spectrometer - QMS* (HIDDEN – HAL201-RC): it is connected coaxially to the UHV piping coming from the membranes. The Ion Source is immersed into the molecular flux coming from the permeator. The maximum operating pressure is 1×10^{-4} mbar;
- A *Bayard-Alpert+ Pirani Pressure gauge* (INFICON – BPG400): for low pressures, the BA gauge is used; the Pirani system allows pressure measurement up to the atmospheric pressures. The gauge switch automatically between the two measurement systems. It is connected perpendicularly to the UHV piping, after the QMS;
- A hydrogen *calibrated leak*: connected to the UHV piping next to the QMS and isolated by means of a manual valve.

The entire UHV piping is thermally insulated and electrically traced to be warmed up by the electrical resistance to a maximum temperature of 200°C; in this way, by adjusting the system at a stable temperature, the influence on pressure and QMS measurement is minimized. As well as, the humidity and other gases trapped in the metal during stand-by periods, can be easily degassed before to start permeation test.

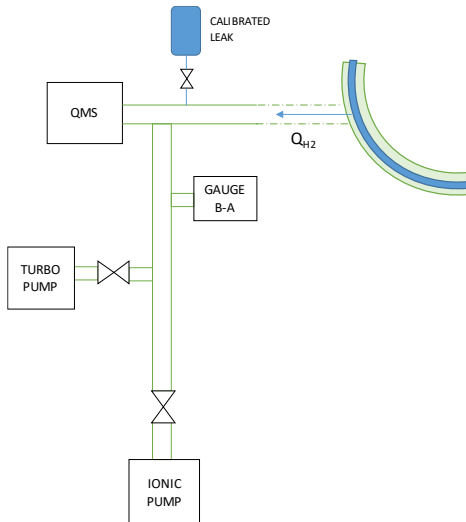


Figure 3-16 RGA system diagram

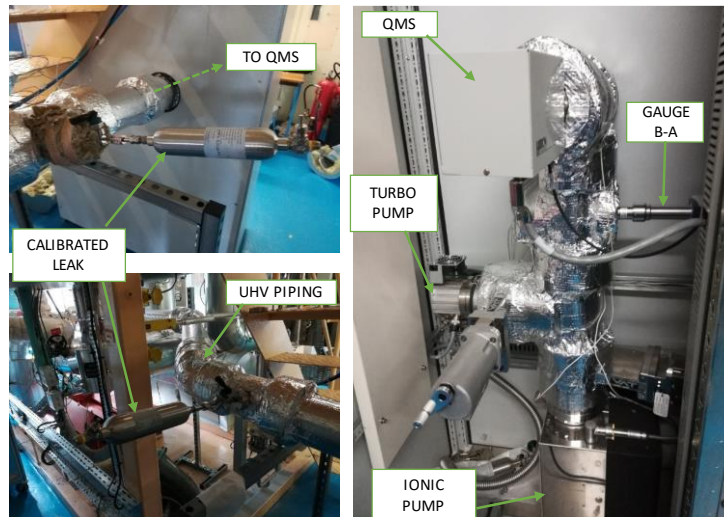


Figure 3-17 RGA system installation on Superfennec

3.4 Measurement techniques

A dedicated metrological system has been set up in order to provide an evaluation of the permeator performance for all the tested operating conditions. Some variables are measured directly, while others are obtained by an indirect measurement. All these variables are so-called observed variables. Some variables are measured only during gas-vacuum test, while others are provided only for gas-sodium test. The gas chromatography (μ GC) on the gas retentate side is provided for both test types.

3.4.1 Direct measurements

3.4.1.1 Temperature

In order to analyze the experimental results, it is fundamental to estimate with a good accuracy the temperature of the nickel membranes placed inside the permeator shell. To do this, temperature measurement on 4 locations is provided, as shown in Figure 3-18:

- 3 type K thermocouples are placed on the external side of the stainless steel shell, containing the 4 nickel membranes; the shell is then thermally insulated.
- 1 type K thermocouple is placed in the gas stream at the membrane outlet (gas retentate).

A mean shell temperature is estimated as the arithmetic mean between TT1, TT2 and TT3 (T_{mean}).

For gas-sodium test, since the shell is insulated and continuously fed with a hot sodium flow, which provides an excellent heat transfer, we can assume that the temperature is uniform elsewhere: this is confirmed by the fact that TT1, TT2 and TT3 have practically the same value, as showed in

Table 3-7. Moreover, we can consider that nickel membranes and the external shell are at the same temperature, since both are in contact with the same sodium flow; therefore, T_{mean} is considered as a very good estimation of the membranes uniform temperature.

Nevertheless, during gas-vacuum test, a non-uniform temperature distribution was measured on the shell: TT1 and TT2 were in agreement, while TT3 always reported a lower temperature. This is probably due to a non-perfect heat insulation provided in the lower part of the permeator.

Moreover, since the shell is maintained under vacuum in quasi-static conditions, it cannot be assumed that nickel membranes and the shell are at the same temperature, like for gas-sodium test. Additionally, the gas outlet temperature gives us a useful comparison between gas and sodium tests: since it flows directly in contact with nickel membranes, its temperature gives a quantitative estimation of the heat provided to the membranes. As reported in

Table 3-7, for the same shell mean temperature, the gas outlet temperature is lower during gas tests than sodium tests; this could mean that, for a given shell temperature, the internal membranes are actually colder during gas tests, due to the heat loss to the vacuum side, which is not present during sodium tests.

Nevertheless, even the comparison of $T_{gas,out}$ between gas-vacuum and gas-sodium test is not enough accurate; in fact, between the two test the heat tracing and the thermal insulation has been removed and re-installed, thus giving a possible bias on the outlet gas measurement. In conclusion, we have not enough elements to estimate more precisely the temperature of the membranes for gas-vacuum tests.

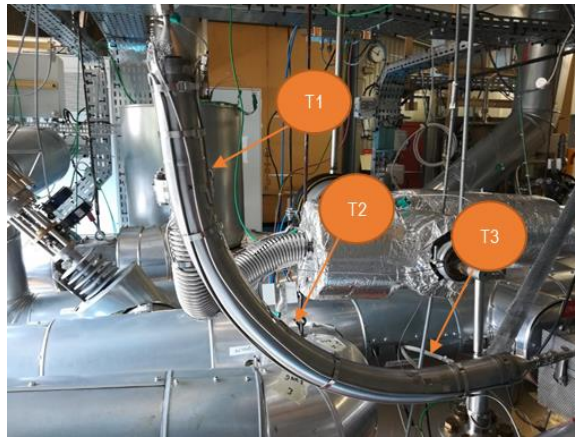


Figure 3-18 Thermocouples positions on permeator

Table 3-7 Temperature measurements during gas tests and sodium tests

	Test ID	T imposed (°C)	TT1 (°C)	TT2 (°C)	TT3 (°C)	T gas out (°C)	T mean (°C)
GAS-VACUUM TESTS	T1	300	291.2	300	285	189.8	292.1
	T2	325	324.3	325	302.7	213.4	317.3
	T3	350	348.0	350	324.4	225.1	340.8
	T4	375	376.5	375	343.3	245	365.0
	T5	400	399.9	400.1	361.1	258.5	387.0
	T6	425	424.2	425	380.5	272.3	409.9
	T7	450	450.8	450	401.8	291.1	434.2
GAS-SODIUM TESTS	T4	375	377.4	375.8	375.3	257.1	376.1
	T5	400	401.8	400.3	400.1	289.0	400.7
	T6	425	426.9	425.1	424.9	308.0	425.6
	T7	450	451.2	449.5	449.2	325.0	449.9

3.4.1.2 Pressure and gas flowrate

The feed gas total pressure (P_{gas}) is measured by a Pressure Transmitter placed at the permeator inlet (see PT01). The pressure inside the permeator is considered to be the same as indicated by the PT, meaning that the pressure drop along the permeator is neglected. This hypothesis is confirmed by pressure measurements done on the permeator outlet as well.

The inlet gas flowrate ($Q_{gas\ in}$) is controlled and measured by a mass flow controller (Brooks): since it has been calibrated for pure Argon, we will apply a correction factor of 0.9886 (given by constructor) for measurements made on the gas mixture Ar/H₂. For example, when the measured flowrate is 200 Nml/min, the actual Ar/H₂ flowrate is 198 Nml/min.

Details on the uncertainty estimation are provided in Annex IV.

3.4.1.3 Gas retentate hydrogen concentration

Hydrogen retentate concentration ($X_{H_2\ r}$) is measured during permeation test by a gas chromatograph (μ GC), by sampling the gas at the permeator outlet. This measurement is performed both for gas-sodium and for gas-vacuum test, as showed in Figure 3-12 and Figure 3-14. Measurements are repeated all along the permeation duration, in order to have enough measurements for a robust statistical post treatment.

The μ GC is calibrated with a single point measurements, made on the feed bottle, which contains a 2.926% H₂/Ar mixture (Air Liquide Crystal). Details on the uncertainty estimation are provided in Annex IV.

3.4.1.4 Gas-vacuum test: permeate pressure

During gas-vacuum tests, the permeator shell, i.e. the permeate side, is maintained under vacuum by the turbomolecular pump and the Bayard-Alpert pressure gauge measures the permeate total pressure (P_p), as showed in Figure 3-14. Under the condition that only the hydrogen permeating through the membranes goes into the vacuum system, the pressure gauge signal reaches an equilibrium value which is directly proportional to the permeate hydrogen flowrate (see details on RGA system in Annex III). A calibration procedure is performed with the hydrogen calibrated leak, in order to convert P_p in a hydrogen molar flow.

For gas-vacuum test this is the only way to have a measurement on the permeate side: in fact, the mass spectrometer signal is not available, since the vacuum pressure exceeds its maximum operating pressure of 1×10^{-4} mbar.

3.4.1.5 Gas-sodium test: QMS signal

During gas-sodium test, the hydrogen-meter shell is connected to the RGA system, where the Quadrupolar Mass Spectrometer measures the abundancy of each molecular mass from 1 to 40. For the interest of this study, the molecular mass 2, corresponding to H₂, is given by the QMS signal S_{MS,H_2} . Similarly to the permeate pressure for the gas-vacuum test, since hydrogen is the only element permeating through the hydrogen-meter, the QMS signal S_{MS,H_2} reaches an equilibrium value directly proportional to the permeate hydrogen flowrate coming from the DH. As for the B-A pressure gauge,

a calibration procedure is performed with the hydrogen calibrated leak, in order to convert S_{MS,H_2} in a hydrogen molar flow.

3.4.2 Hydrogen permeation flowrate indirect measurements

3.4.2.1 Mass balance on gas retentate side

An indirect measurement of the hydrogen permeation flowrate through the permeator membranes is obtained by applying a mass balance on the feed/retentate side. This technique is applicable both in gas-vacuum and gas-sodium test.

Hydrogen inlet concentration is equal to the feed bottle concentration: its value is of 2,926% molar. Hydrogen retentate concentration is given by the μ GC measurement.

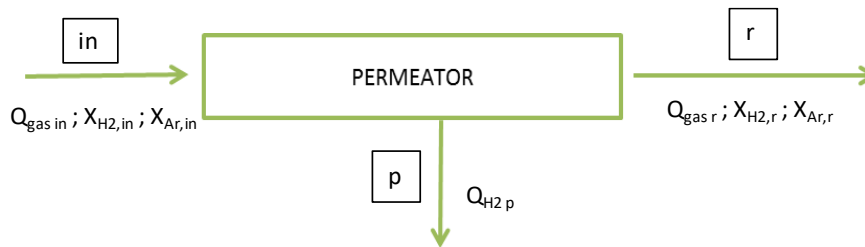


Figure 3-19 Permeator simplified diagram: application of total and hydrogen molar balances

The inside of nickel membranes is considered as a fixed volume, with one inlet (in), one retentate (r) and one permeate side (p), constituted by liquid sodium or vacuum depending on the test type; additionally, the following hypotheses are considered:

- Stationary conditions: i.e. experimental conditions are stable (constant gas flowrate, gas pressure and membrane temperature), so that hydrogen permeation rate is constant as well during the test duration
- $X_{Ar,p} = 0$: only hydrogen can permeate through nickel walls, due to the non permeability of argon through metals

Therefore, with reference to Figure 3-19, we can write the total and hydrogen molar balances equations as follows:

$$Q_{gas\ in} = Q_{gas\ r} + Q_{H_2\ p} \quad [\text{mol s}^{-1}] \quad 3-23$$

$$Q_{gas\ in} X_{H_2\ in} = Q_{gas\ r} X_{H_2\ r} + Q_{H_2\ p} \quad [\text{mol s}^{-1}] \quad 3-24$$

and by combining 3-23 and 3-24 we obtain:

$$Q_{H_2\ p} = Q_{gas\ in} \frac{X_{H_2\ in} - X_{H_2\ r}}{1 - X_{H_2\ r}} \quad [\text{mol s}^{-1}] \quad 3-25$$

Finally, 3-25 gives an indirect measurement of $Q_{H_2\ p}$, starting from the direct measurements of $Q_{gas\ in}$, provided by the FTC, and of $X_{H_2\ r}$, provided by the μ GC.

3.4.2.2 Gas-vacuum tests: RGA on vacuum permeate side

Only for gas-vacuum test, we can obtain a measurement of hydrogen permeation flowrate, starting from the pressure gauge signal, as follows:

$$Q_{H_2 p} = K_p P_p \quad [\text{mol s}^{-1}] \quad 3-26$$

Where P_p is the permeate pressure given by the Bayard-Alpert gauge and K_p is the calibration constant of the gauge, taken from a hydrogen calibrated leak measurement as follows:

$$K_p = \frac{Q_{leak}}{P_{leak}} \quad [\text{mol s}^{-1} \text{ mbar}^{-1}] \quad 3-27$$

3.4.2.3 Gas-vacuum tests: data reconciliation

During gas-vacuum tests, two different techniques can be used to obtain an indirect measurement of $Q_{H_2 p}$, by means of equations 3-25 and 3-26. The two techniques do not necessarily give the same result, for given experimental conditions, due to the different uncertainties which affect the measurements, depending on their range of operation: therefore, in order to obtain a “best estimated” measurement for each tested condition, a data reconciliation (RD) method is implemented. Details are provided in Annex IV.

3.4.2.4 $Q_{H_2 p}$ measurements summary

Finally, we distinguish three distinct measurements of the hydrogen permeation flowrate, according to the technique employed:

- $Q_{H_2 p}(\mu GC)$: both for gas-sodium and gas-vacuum tests, obtained by Equation 3-25 (see 3.4.2.1).
- $Q_{H_2 p}(P \text{ Gauge})$: only for gas-vacuum tests, obtained by Equation 3-26 (see 3.4.2.2).
- $Q_{H_2 p}(RD)$: only for gas-vacuum tests, obtained by data reconciliation (see Annex IV).

3.4.3 Hydrogen concentration in sodium estimation

During gas-sodium tests, a measurement of hydrogen concentration in the sodium (i.e. the permeate side of the permeator prototype) is given by a hydrogen-meter (DH), as shown in 3.3.2. Hydrogen-meters based on nickel permeation membranes have been widely used for hydrogen detection in sodium reactors, as presented in paragraph 2.4.1. The DH used for our tests is made from the same design as the one used for a recent test on the Phenix reactor [66]: it is composed by four nickel membranes of 320 mm x 7.2 mm x 0.3 mm (length, outside diameter and thickness respectively). The hydrogen molar rate per unit surface permeating from liquid sodium, which circulates inside the DH membranes, to vacuum, outside the membrane, can be expressed by equation 2.25 (cf. Section 2.4.1) which combines the Richardson’s law and the Sieverts law for a hydrogen-sodium system. By assuming that the tubular geometry can be well approximated by a plane geometry (hypothesis valid when the tube thickness is much lower, at least 10 times, than the tube radius) and that the hydrogen concentration inside sodium $y_{H,Na}$ is homogeneous along the DH membranes, the total permeation flowrate becomes:

$$Q_{H_2, DH} = \left(\frac{A}{\delta}\right)_{DH} p e_{0, DH} \exp \frac{-E_{p, DH}}{RT} \left(\frac{y_{H, Na}}{K_{S, Na}} - \sqrt{P_{H_2, vacuum}}\right) \quad [\text{mol s}^{-1}] \quad 3-28$$

Where A is the membrane’s surface at the mean diameter and $P_{H_2, vacuum}$ is the hydrogen partial pressure on vacuum side. The permeability coefficient $p e_{0, DH}$ and the activation energy $E_{p, DH}$, specific of the DH membrane, are obtained with a procedure described in 4.5.2. For our application, $y_{H, Na}$

varies in the range 50 ppb to 500 ppb, while $K_{S,Na}$ depends on the temperature and its expression is given by Vissers [7]:

$$\log(K_{S,Na}) = 0.86 - \frac{122}{T[K]} \quad [\text{ppm Torr}^{-0.5}] \quad 3-29$$

To have coherent units in equation 3-28, $K_{S,Na}$ is converted to $[\text{ppb Pa}^{-0.5}]$. It is worth noting that the ratio $\frac{y_{H,Na}}{K_{S,Na}}$ is orders of magnitude higher than the vacuum pressure, so that the term in brackets $\sqrt{P_{H2,vacuum}}$ can be neglected, and equation 3-28 can be rewritten, making $y_{H,Na}$ explicit, as follows:

$$y_{H,Na} = \frac{Q_{H2,DH} K_{S,Na}(T)}{\left(\frac{A}{\delta}\right)_{DH} p e_{0,DH} \exp \frac{-E_{p,DH}}{RT}} \quad [\text{ppb}] \quad 3-30$$

By considering that the hydrogen flux $Q_{H2,DH}$ is proportional to the QMS signal corresponding to the molecular hydrogen (see details in Annex III), the expression of $y_{H,Na}$ becomes:

$$y_{H,Na} = \frac{K_{MS} S_{MS,H2} K_{S,Na}(T)}{\left(\frac{A}{\delta}\right)_{DH} p e_{0,DH} \exp \frac{-E_{p,DH}}{RT}} \quad [\text{ppb}] \quad 3-31$$

Where $S_{MS,H2}$ [Torr] is the mass spectrometer signal corresponding to mass 2 and K_{MS} [$\text{mol s}^{-1} \text{Torr}^{-1}$] is the calibration constant obtained by calibrated leak measurement, as follows:

$$K_{MS} = \frac{Q_{leak}}{S_{MS H2 leak}} \quad [\text{mol s}^{-1} \text{Torr}^{-1}] \quad 3-32$$

Therefore, by means of equation 3-31, it is possible to obtain an estimation of hydrogen molar concentration in liquid sodium; it is worth noting that, for a given temperature, all parameters except for $S_{MS,H2}$ are constants: this means that $y_{H,Na}$ and any possible variation of it will be directly proportional to the QMS signal.

3.4.4 Summary of measured variables and physical parameters

Table 3-8 resumes all observed variables, together with the physical and geometrical parameters used in the formulas presented above.

Table 3-8 observed variables and physical parameters of the experimental study

Directly measured variables		
Variable	Units	Instrument
P_{gas}	bar a	PT01
$Q_{gas\ in}$	Nml min ⁻¹	FTC
$T_{1,2,3}$	°C	Thermocouple
$X_{H_2\ r}$	% mol	μGC
$S_{MS\ H_2}$	Torr	QMS
$S_{MS\ H_2\ leak}$	Torr	QMS
P_p	mbar	BA Pressure Gauge
P_{leak}	mbar	BA Pressure Gauge
Indirectly measured variables		
Variable	Units	Formula
$Q_{H_2\ p}(\mu GC)$	mol s ⁻¹	Equation 3-25
$Q_{H_2\ p}(GP\ auge)$	mol s ⁻¹	Equation 3-26
$Q_{H_2\ p}(RD)$	mol s ⁻¹	Data reconciliation
$y_{H,Na}$	ppb	Equation 3-31
Constants		
	Units	Value
$X_{H_2\ in}$	% mol	2.926
Q_{leak}	mol s ⁻¹	$2.19 \times 10^{-7} / 1.56 \times 10^{-9}$
Physical and geometrical parameters		
Parameter	Units	Value/Expression
$K_{S,Na}(T)$	ppm Torr ^{-0.5}	Equation 3-29
$\left(\frac{A}{\delta}\right)_{DH}$	m	72.2
$\left(\frac{A}{\delta}\right)_p$	m	144.5
R	J mol ⁻¹ K ⁻¹	8.314
$pe_{0,DH}$	mol m ⁻¹ s ⁻¹ Pa ^{-0.5}	7.84×10^{-8}
$E_{p,DH}$	J mol ⁻¹	47782,7

3.5 Conclusion

The full design procedure of a permeator prototype has been presented, starting from scratch to the final sizing, with respect of the constraints coming from the final application (SFRs) and from the available experimental facility.

An analytical model (called for simplicity 1D model) aiming to represent locally the permeation process in the radial direction through gas phase, nickel membrane and sodium phase has been developed as support for the prototype sizing. The hydrogen permeation through the nickel membrane is considered a diffusion-limited process and others mechanisms such as dislocation transport or surface effects are

not included in the model. As main result, we found that the gas and sodium phase resistances to hydrogen mass transfer can be neglected, when a turbulent sodium flowrate is provided and if the membrane thickness is $>50 \mu\text{m}$. Therefore, according to this model, the hydrogen diffusion across the nickel membrane could be considered as the mass transfer driving step. The main driving parameters have been identified and their impact on permeation has been quantified: temperature, membrane thickness, hydrogen concentration in gas and sodium phase, gas pressure, from the more to the less effective. A simplified theoretical law (Equation 3-19) has been assessed to describe the local hydrogen permeation through an infinitesimal membrane length.

By integrating the Equation 3-19 over the prototype geometry, assuming a plug-flow in gas phase, the final sizing of the prototype has been assessed, with respect of all the technical and practical constraints, in order that the hydrogen permeation flowrate could be accurately measured during the experiments.

The facility setup, the measurement techniques based on gas chromatography, RGA analysis and mass spectrometry have been set up, in order to quantify the hydrogen permeation flowrate through the prototype in two different configurations: gas-vacuum and gas-sodium.

Chapter

4 Experimental results

The permeator prototype has been fabricated according to the features presented in Chapter 3. Once the experimental setup has been installed and all the preliminary activities realized (instrumentation calibrations, mechanical resistance and leakage tests, preliminary tests), the experimental campaign has been performed before in gas-vacuum and successively in gas-sodium configuration.

In this chapter results for both gas-vacuum and gas-sodium are presented; a post treatment method is developed, in order to be able to assess the correspondence of the experimental results with the theoretical models; finally, an in-depth discussion is provided, consolidating the main results and proposing hypothesis of interpretation for some open points.

4.1 Test procedure and tested conditions

4.1.1 Gas-vacuum test

Permeator is maintained at a stable temperature thanks to the electrical tracing system, placed on the shell; as for gas-sodium, the permeation test starts when the permeator is fed with Ar- H₂ and it lasts 1 hours. During this time, gas side and vacuum side measurement are performed. When a test ends, after purging with pure Argon, the next operating conditions are performed.

Gas-vacuum permeation is experimentally investigated over seven temperatures (from 300°C to 450°C); for each temperature different gas pressures are tested, ranging from 2 bar to 10 bar. The entire list of tested condition is provided in Table 4-1.

The other main operating parameters are maintained constant for all the tested conditions. They are reported here below:

- $X_{H_2, gas, IN} = 2.926\%$ molar ;
- $Q_{gas} = 200 \text{ Nml min}^{-1}$.

Table 4-1 Gas-vacuum test: tested conditions temperature and gas pressure

Test ID		T7- P2	T7-P3	T7-P4	T7	T7-P5	T7-P6	T7-P7	T7-P8	T6 - P2	T6	T6 - P6	T6-P7	T6-P8
T	°C	450	450	450	450	450	450	450	450	425	425	425	425	425
P_{gas}	bar a	2	3	4	5	6	7	9	10	2	5	7	9	10
n° of repeats		3	2	3	2	3	3	3	3	1	2	1	1	1

T5 - P2	T5 - P4	T5	T5-P6	T5-P7	T5-P8	T4 - P2	T4	T4-P6	T4-P7	T4-P8
400	400	400	400	400	400	375	375	375	375	375
2	4	5	7	9	10	2	5	7	9	10
2	2	3	2	2	1	1	2	1	1	1

T3 - P2	T3	T3-P6	T3-P7	T3 - P8		T2 - P2	T2	T2-P6	T2-P7	T2 - P8		T1 - P2	T1	T1-P6	T1-P7	T1 - P8
350	350	350	350	350		325	325	325	325	325		325	300	325	325	325
2	5	7	9	10		2	5	7	9	10		2	5	7	9	10
2	2	2	2	2		1	2	1	1	2		1	3	1	1	2

4.1.2 Gas-sodium test

When sodium is at stable temperature and at low hydrogen content (typically $y_{H,Na} < 100$ ppb), the CT section is isolated, so that purification stops and a stable hydrogen concentration is set up; with reference to Figure 3-11, only TS and PI are open during a permeation test. Sodium circulates into the main circuit with a total flowrate of 2.5 m³/h, composed of 1 m³/h through TS and the remaining 1.5 m³/h through the HT; a negligible flowrate of around 0,07 m³/h circulates through the PI.

Permeation test starts when Ar-H₂ gas mixture starts to feed the permeator at given pressure and flowrate, so that hydrogen permeation takes place and measurements both in gas and sodium side are performed; these conditions are maintained stable for the entire test duration of 1 hour. Then, H₂ permeation is stopped by sending pure argon into the permeator, thus purging the membrane feed side from the residual hydrogen. As a new equilibrated hydrogen concentration is obtained inside sodium, the following test can be launched with the same procedure. When the maximum allowed hydrogen concentration inside sodium of 500 ppb is approached, a purification session is performed by connecting the CT section to the main circuit.

Gas-sodium permeation is experimentally investigated over four temperatures (from 375°C to 450°C); for each temperature six gas pressures are tested, ranging from 2 bar to 10 bar. The entire list of tested condition is provided in Table 4-2.

The other main operating parameters are maintained constant for all the tested conditions. They are reported here below:

- $X_{H_2,gas,IN} = 2.926\%$ molar ;
- $\dot{V}_{Na} = 1 \text{ m}^3 \text{ h}^{-1}$, through the permeator test section ;
- $Q_{gas} = 200 \text{ Nml min}^{-1}$.

Additionally, the condition T7 is tested at two lower sodium flowrates: 0.5 m³ h⁻¹ and 0.2 m³ h⁻¹ respectively.

Table 4-2 Gas-sodium test: tested conditions temperature and gas pressure

Test ID		T4-P2	T4-P3	T4	T4-P6	T4-P7	T4-P8	T5-P2	T5-P3	T5	T5-P6	T5-P7	T5-P8
T	°C	375	375	375	375	375	375	400	400	400	400	400	400
P _{gas}	bar	2	3,5	5	7	9	10	2	3,5	5	7	9	10
Test ID		T6-P2	T6-P3	T6	T6-P6	T6-P7	T6-P8	T7-P2	T7-P3	T7	T7-P6	T7-P7	T7-P8
T	°C	425	425	425	425	425	425	450	450	450	450	450	450
P _{gas}	bar	2	3,5	5	7	9	10	2	3,5	5	7	9	10

4.2 Measurement techniques validation on the gas-vacuum system

4.2.1 Permeation transient

When permeation test starts by feeding hydrogen into the permeator, both pressure gauge and μGC signals are recorded. In Figure 4-1, the typical signal evolution of pressure gauge is presented, revealing the hydrogen pressure evolution on permeate side during a test.

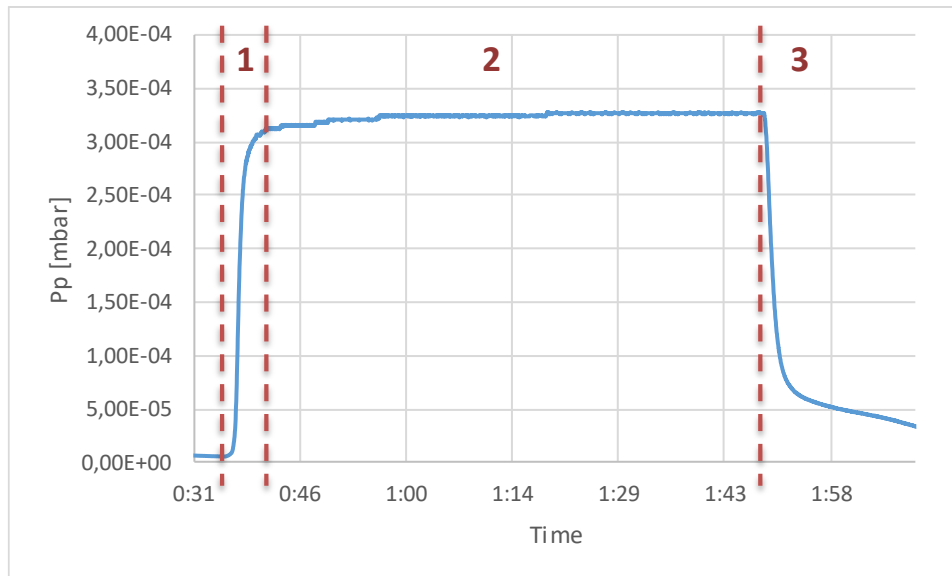


Figure 4-1 Typical pressure gauge signal evolution during a gas-vacuum permeation test

From this graph, we can identify three phases:

1. **Initial permeation transitory:** as Ar/H₂ mixture flows inside the permeator, hydrogen molecules begin to diffuse through Nickel membranes to the permeate side; therefore the pressure gauge, which is placed on permeate side, records an increment of hydrogen pressure, until the diffusion reaches its equilibrium
2. **Steady state permeation:** when hydrogen diffusion is at its equilibrium, steady state permeation through Nickel membranes continues until the upstream conditions are modified
3. **Purge – permeation turn off transitory:** pure Ar flows inside the permeator, in order to purge it from residual hydrogen and to stop the permeation test. The permeate pressure suddenly decreases since no more hydrogen is permeating through the membranes.

The initial transitory (1) is of the order of a minute, while we take measurements of steady state permeation along one hour approximatively. The reason of a so long test comes from the slower measurement time required by μGC . In particular, it produces concentration measurement each two minutes, due to its intrinsically long period of analysis. This means that the initial transitory cannot be recorded with the μGC , but it can give several measurements of steady state permeation, if the test duration is long enough.

4.2.2 Measurement repeatability

Repeatability of experiments is demonstrated by taking measurements of the same experimental conditions at different times and with different experimental procedures. For example, for a fixed temperature, we measure permeation at different gas pressures both by increasing the pressure from

P1 to P8 and by decreasing it from P8 to P1. Three measurement series are performed for the highest temperature T7 (here is reported its mean value of 434°C, see

Table 3-7). In Figure 4-2 are reported the results of both $Q_{H_2,p}(\mu GC)$ and $Q_{H_2,p}(Gauge P)$ measurements, obtained according to Table 3-8. The hydrogen permeation flowrate $Q_{H_2,p}$ is plotted on y axis versus the gas pressure on x axis. The uncertainty of each measured value is reported as well. We can remark that for both μGC and pressure gauge we have a very good repeatability among the three different series (1,2 and 3), since the variation between the points is much lower than the measurement uncertainty.

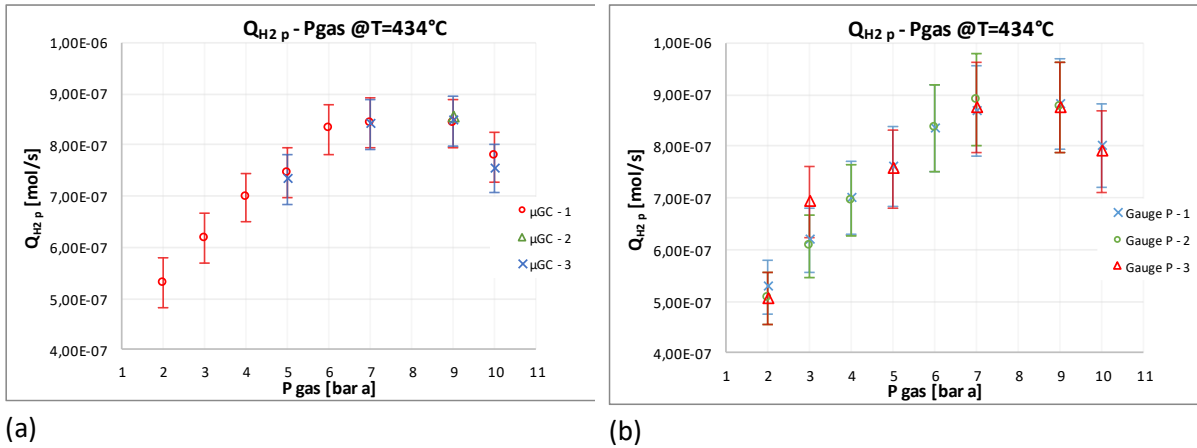


Figure 4-2 Gas-vacuum test - Hydrogen permeation vs gas pressure: μGC (a) and pressure gauge (b) measurements

The same is done for temperature variations. Two distinct series of measurements are performed for a fixed gas pressure (5 bar a) and temperatures varying from T1 to T7. Also in this case we notice a good repeatability of measurement (Figure 4-3).

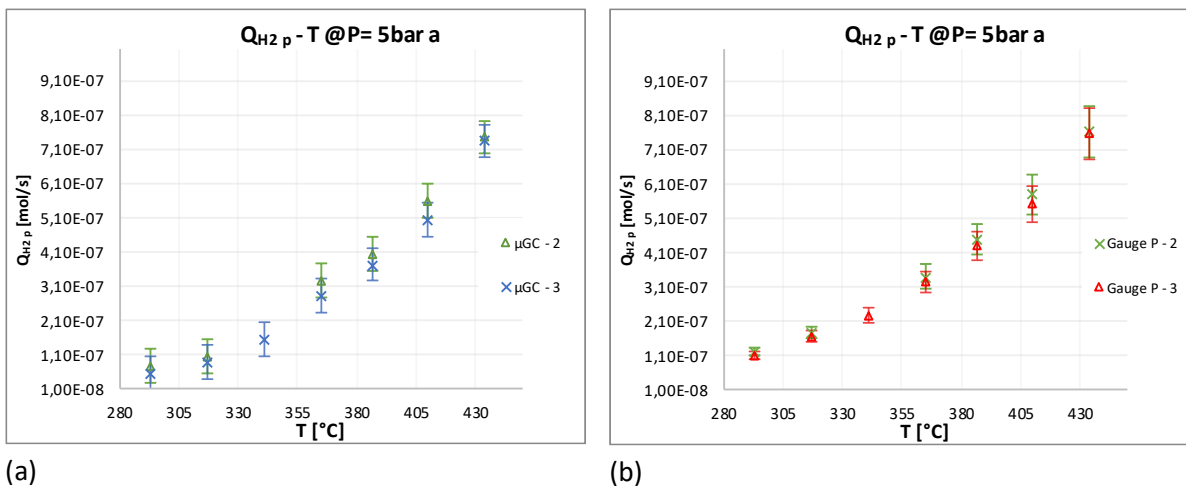


Figure 4-3 Hydrogen permeation vs temperature: μGC (a) and pressure gauge (b) measurements

4.2.3 Retentate-permeate side comparison: validation of μGC measurements

During gas-vacuum test, data of hydrogen permeation flowrate ($Q_{H_2,p}$) are obtained from measurements both by Pressure gauge on permeate side and by μGC on retentate side. It is important to compare the two techniques in order to validate them and to comprehend the data reconciliation (RD) results.

In Figure 4-4, we compare for each tested condition the permeation flowrate obtained with the two techniques (a) and we plot their percentage deviation (b), calculated as:

$$\Delta Q_{H_2 p} \% = \frac{Q_{\mu GC} - Q_{GAUGE}}{Q_{GAUGE}} * 100$$

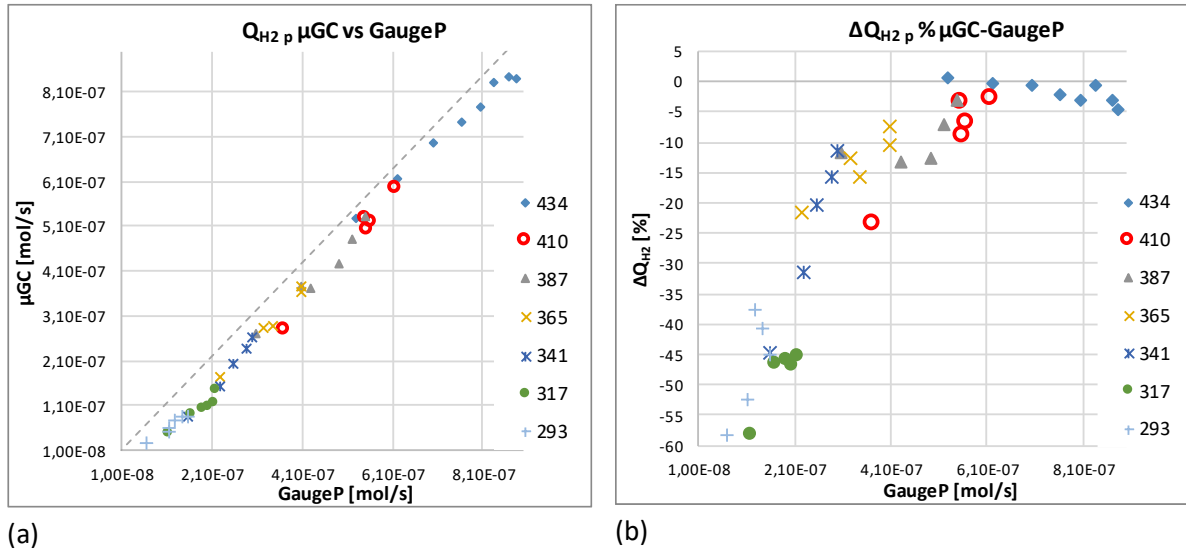


Figure 4-4 Gas-vacuum test - Comparison between μGC and pressure gauge measurements of hydrogen permeation flowrate for T_{mean} 293°C to 434°C

It can be noticed that for higher permeation rates, the two techniques are quite well in accordance; then, the lower is the measured flowrate, the higher is the percentage deviation between μGC and pressure gauge; in particular μGC gives much lower estimations of $Q_{H_2 p}$. The percentage deviation is below 10% for $Q_{H_2 p} > 4 \times 10^{-7}$ mol/s, while it reaches values of around 55% for the lowest permeation rates.

This increasing deviation at lower flowrates can find a possible explanation in the measurements uncertainties (see Annex IV): on one side, pressure gauge has the same precision on the whole measurement range, since the calibration constant relative uncertainty (10%) does not change. On the other hand, $Q_{H_2 p}$ measured from μGC is less precise at lower rates. Thus, we have to identify over which range of measurements μGC can be sufficiently reliable and if it has a correspondence with the pressure gauge measurements.

From this perspective, it is interesting to see that μGC uncertainty seems to follow the deviation from pressure gauge measurements, as showed in Figure 4-5; typically, for $Q_{H_2 p} > 4 \times 10^{-7}$ mol/s the uncertainty is below 10%, while it grows at lower flowrates. Finally it seems that more precise μGC measurements are better in accordance with gauge pressure measurements. This would confirm the coherence of both measurements techniques by considering their range of uncertainties.

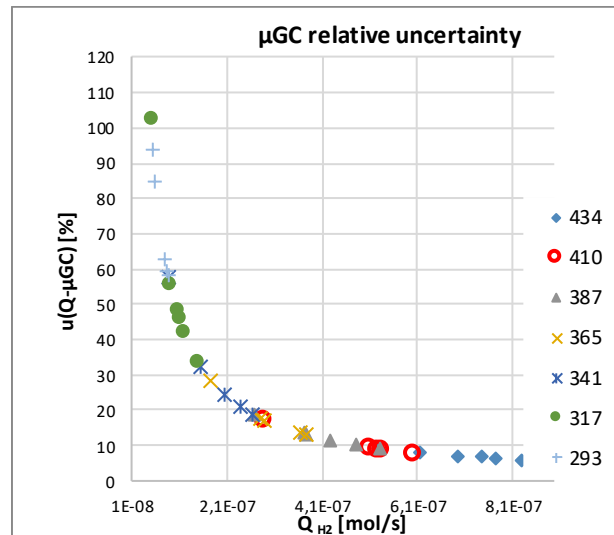


Figure 4-5 μ GC relative standard uncertainty on hydrogen permeation flowrate measurements

This analysis is useful to validate the μ GC technique: we can conclude that it is possible to obtain a coherent estimation of the hydrogen permeation flowrate with both techniques, if we stay in the range of $Q_{H_2 p} > 4 \times 10^{-7}$ mol/s. This result comes not simply from an uncertainty analysis of μ GC measurements, but it is confirmed also by the comparison with the pressure gauge results. This conclusion is very important to qualify the μ GC measurement which is employed during gas-sodium test as well.

4.2.4 Reconciled data

Since we have a measurement redundancy, we search by data reconciliation the best estimation of $Q_{H_2 p}$, which is the most respectful of the hydrogen mass balances of the system, weighting each experimental measurement by its uncertainty. It is evident that reconciled data (RD) will be closer to measurements affected by the smaller uncertainty. In this case, we calculate RD for each experimental condition tested and we compare their percentage deviation from μ GC and pressure gauge measurements. RD slightly differ (deviation of $\pm 5\%$) from Gauge P for all measurements and from μ GC for measurements higher than 4×10^{-7} mol/s (Figure 4-6). Instead, they deviate more and more from μ GC measurements decreasing under this value. This behavior correspond perfectly to the fact that pressure gauge data have a fixed uncertainty, while μ GC is less accurate in estimating lower hydrogen permeation fluxes, so that data reconciliation gives values much closer to pressure gauge in this range. According to the data reconciliation theory, the reconciled data uncertainty is always lower than the experimental measurement ones. Therefore, since the experimental relative uncertainty is of $\pm 10\%$ for pressure gauge and varies up to highest values for the μ GC (see Figure 4-5), we can expect a relative uncertainty for reconciled data lower than $\pm 10\%$.

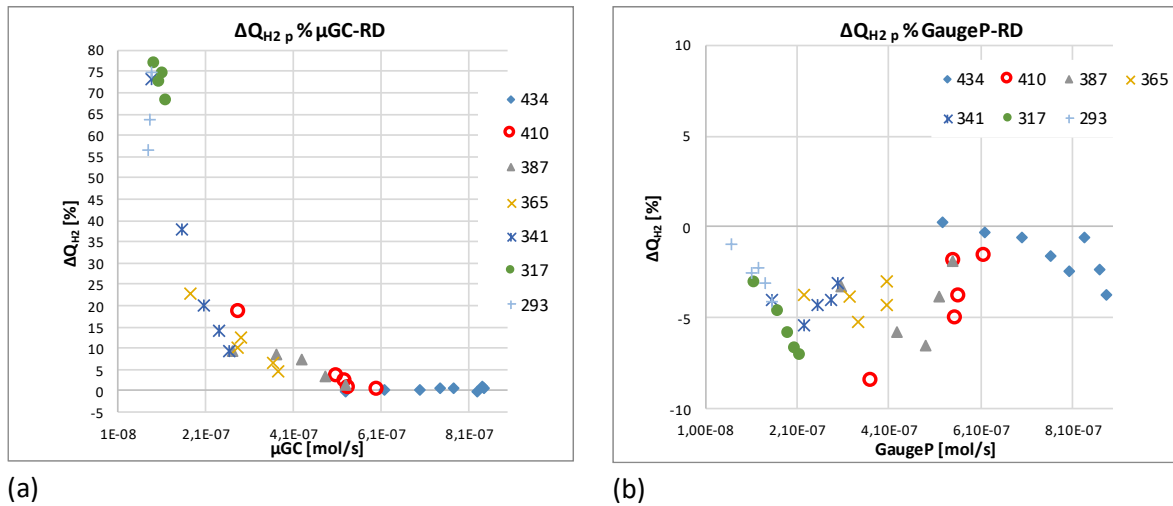


Figure 4-6 Gas-vacuum test - Percentage deviation between reconciled data and experimental measurements with μ GC (a) and pressure gauge (b)

4.3 Results post treatment methods

The goal of the results post treatment is to compare the experimental measurements, including their uncertainty, with a theoretical law, which is supposed to drive the permeation across the prototype over the tested conditions variability range. As highlighted by the state of the art study and following the 1-D model analysis (paragraph 3.2.3.4), the Richardson's law is the most suitable reference to describe the local permeation under the experimental conditions tested here. This law, applied locally to an infinitesimal membrane length, has been integrated on a tubular geometry for the permeator design (paragraph 3.2.4); in fact, once the prototype geometry is fixed, by taking a theoretical permeability coefficient as input, it is possible to estimate the expected permeation flowrate for a given experimental condition.

For the result post treatment, the reverse process is implemented: the local Richardson's law is integrated on the prototype geometry and rewritten in a single-equation form (i.e. representing the whole prototype geometry and the physics with a single equation), valid under certain hypothesis (listed in Section 4.3.1); then, the experimental results are compared with it. As a result, if this law represents well the experiments, we can extrapolate from the experimental data the actual permeability coefficient of the prototype. In order to have a coherent comparison, the hypothesis made to set the theoretical law must be experimentally verified as well.

4.3.1 An integrated law to represent experimental results

The hydrogen permeation flowrate over an infinitesimal surface dA , crossing the membrane from the Ar/H₂ gas mixture to liquid sodium, is given by equation 4-1 under the following hypothesis:

- i. Steady state conditions
- ii. Bulk diffusion is the rate limiting step of permeation
- iii. H₂ dissociation/recombination at membrane surfaces are at equilibrium (Sieverts law validity) and Argon competitive adsorption is neglected.
- iv. Gas and sodium phase mass transfer resistance is negligible
- v. Plane geometry approximation (see 3.4.3)

- vi. Ar/H₂ mixture is considered as an ideal gas

$$dQ_{H_2,p} = \left(\frac{dA}{\delta}\right)_p p e_0 \exp\left(\frac{-E_p}{RT}\right) \left(\sqrt{P_{H_2,gas}} - \frac{y_{H,Na}}{K_{S,Na}}\right) \quad [\text{mol s}^{-1}] \quad 4-1$$

Where the local hydrogen partial pressure in gas phase $P_{H_2,gas}$ can be expressed as follows:

$$P_{H_2,gas} = P_{gas} X_{H_2,gas} \quad [\text{Pa}] \quad 4-2$$

With reference to Figure 3-19, in our experimental conditions we have a constant gas flowrate with constant hydrogen concentration at the permeator inlet. Permeation is carried out through 4 Ni tubes: these 4 tubes constitute the so-called “membrane”. We consider the following additional hypothesis:

- vii. Temperature is uniform over the membrane (both in radial and axial direction)
 viii. Gas inlet flowrate is uniformly distributed over the 4 nickel tubes (membrane)
 ix. $\sqrt{P_{H_2,gas}} \gg \frac{y_{H,Na}}{K_{S,Na}}$
 x. $Q_{H_2,p} \ll Q_{gas\ in}$
 xi. The hydrogen axial diffusive transport in the gas phase is negligible (if compared to the axial convective transport).

If we integrate the law reported in 4-1 along the membrane, coupled with the hydrogen convective mass transfer in gas phase in the axial direction only (gas assumed as plug flow), we can obtain an analytical solution, giving the global hydrogen permeation flowrate as a function of a mean hydrogen partial pressure:

$$Q_{H_2,p} = \left(\frac{A}{\delta}\right)_p p e_0 e^{\frac{E_{pe}}{RT}} \sqrt{\overline{P_{H_2}}} \quad [\text{mol s}^{-1}] \quad 4-3$$

where $A = 2\pi \left(\frac{r_o+r_i}{2}\right) LN_{tubes}$ is the total membrane exchange surface calculated at the mean thickness diameter and the mean partial pressure square root is:

$$\sqrt{\overline{P_{H_2}}} = \sqrt{P_{gas} \overline{X_{H_2}}} = \sqrt{P_{gas} \frac{X_{H_2\ r} + X_{H_2\ in}}{2}} \quad [\text{Pa}^{0.5}] \quad 4-4$$

where the mean hydrogen concentration $\overline{X_{H_2}}$ is calculated as the arithmetic mean between inlet and retentate side. This expression is valid if the hydrogen concentration varies linearly along the permeator. A mathematical demonstration of equation 4-3 is provided in Annexe V.

4.3.2 $\sqrt{\overline{P_{H_2}}}$ dependence

According to equation 4-3, at a fixed temperature, the hydrogen permeation flowrate should increase linearly with the hydrogen mean partial pressure square root, since all the other parameters are constant. For each tested condition, we obtain experimental measurements of $Q_{H_2,p}$ as explained in 3.4.2.4, and the mean hydrogen partial pressure square root $\sqrt{\overline{P_{H_2}}}$ according to Equation 4-4. P_{gas} is the measured gas pressure at permeator inlet, $X_{H_2\ in}$ is equal to 2.926% and $X_{H_2\ r}$ is the retentate hydrogen molar fraction measured by μGC . For each temperature distinctly, we plot on a x-y graph the $Q_{H_2,p}$ measurements as a function of $\sqrt{\overline{P_{H_2}}}$, in order to verify the mathematical relationship between the two variables. If the dependence is linear, it means that the theoretical law in equation 4-3 is respected by the experimental results, over the pressure range of interest. In particular, it means that the Sieverts law is valid, since the hydrogen permeation flowrate increases linearly with the square

root of the hydrogen partial pressure, thus demonstrating that the hydrogen molecules dissociation at the membrane surface is at equilibrium (equilibrium between dissociation and recombination).

To check the linearity between $Q_{H_2,p}$ and $\sqrt{P_{H_2}}$, a linear regression (Excel tool) is applied to the experimental data, for each temperature dataset separately; in particular a zero intercept is imposed (i.e. regression line of the type $y = ax$), in order to be coherent with the law in 4-3. However, the aim is to compare the linear regression with the law in 4-3 over the pressure range experimentally investigated only. We are not allowed to extrapolate data up to very low (approaching the zero) or very high pressures, where some hypotheses made to establish the permeation law (i.e. ii, iii, ix, x in paragraph 4.3.1) may not be valid any-more. Once the regression line is established, the linearity goodness is evaluated by means of the R^2 coefficient; if clear deviation from linearity are found for some data, they should not be considered for the following analysis.

4.3.3 Temperature dependence: permeability coefficient's law

For a fixed hydrogen partial pressure, the permeation should follow exponentially the temperature, due to the permeability coefficient Arrhenius law type. However, to verify this dependence we proceed by two steps: at first, we obtain the permeability coefficient at each temperature; then, we verify the temperature dependence of the set of coefficients. In fact, if we consider a single temperature, the permeability coefficient links linearly the permeation flowrate to the partial pressure square root; therefore, we can easily obtain its value from equation 4-3 as explained below.

By considering the data which well respect the $Q_{H_2,p} - \sqrt{P_{H_2}}$ linearity, the expression in 4-3 can be rewritten as follows:

$$\frac{Q_{H_2,p}}{\left(\frac{A}{\delta}\right)_p} = pe(T) \sqrt{P_{H_2}} \quad [\text{mol s}^{-1} \text{m}^{-1}] \quad 4-5$$

where the permeability coefficient at the temperature T is $pe(T) = pe_0 e^{-\frac{E_{pe}}{RT}}$. Therefore, from the experimental data, we can obtain the values of $pe(T)$ for each tested temperature: if we plot on y-x the ratio $Q_{H_2,p}/\frac{A}{\delta}$ (y) versus $\sqrt{P_{H_2}}$ (x), the angular coefficient a of the regression line $y = ax$, corresponds precisely to $pe(T)$.

Then, the dependence from temperature can be checked by rewriting the permeability exponential law as follows:

$$\ln[pe(T)] = -\frac{E_{pe}}{R} \frac{1}{T} + \ln(pe_0) \quad 4-6$$

where the logarithm has been applied to both side of the equation. By plotting on a y-x chart $\ln[pe(T)]$ (y) versus $\frac{1}{T}$ (x), we can verify by a linear regression of the type $y = a_1x + b_1$ if the law in 4-6 is respected. If so, it means that the permeability coefficient follows well the temperature exponential behavior as predicted from the theoretical permeation law. Moreover, by comparing the regression line with equation 4-6, we obtain the permeation activation energy and the pre-exponential factor, respectively, as follows:

$$E_{pe} = -a_1R \quad [\text{J mol}^{-1}] \quad 4-7$$

$$pe_0 = e^{b_1}$$

$$[\text{mol s}^{-1} \text{m}^{-1} \text{Pa}^{-0.5}] \quad 4-8$$

4.4 Permeation's law assessment

4.4.1 Gas-vacuum test

Following the method presented in paragraph 4.3.2, by plotting the $Q_{H_2,p}(RD)$ measurements as function of $\sqrt{\overline{P}_{H_2}}$, for each tested temperature, we can verify if the experimental results follow the integrated permeation law form of equation 4-3. Figure 4-7 reports $Q_{H_2,p}(RD)$ for temperatures from T1 ($T_{\text{mean}}=293^\circ\text{C}$) to T7 ($T_{\text{mean}}=434^\circ\text{C}$) and at least five gas pressure (2, 5, 7, 9 and 10 bar a); the corresponding values of $\sqrt{\overline{P}_{H_2}}$ are between $70 \text{ Pa}^{0.5}$ and $170 \text{ Pa}^{0.5}$. The relative uncertainty of the $Q_{H_2,p}(RD)$ measurements is expected to be lower than $\pm 10\%$, as explained in section 4.2.4.

The following comments can be done:

- at higher temperatures correspond higher permeation rates, as expected from theory;
- from T1 to T5, $Q_{H_2,p}$ increases linearly with $\sqrt{\overline{P}_{H_2}}$ for all the gas pressures;
- for T6 and T7, $Q_{H_2,p}$ increases linearly up to $\sqrt{\overline{P}_{H_2}}=140 \text{ Pa}^{0.5}$;
- for T6 and T7, at $\sqrt{\overline{P}_{H_2}} > 140 \text{ Pa}^{0.5}$ $Q_{H_2,p}$ does not linearly increase, actually it is stable or it decreases (T7). Possible explanations of this behavior are provided in paragraph 4.6.5.

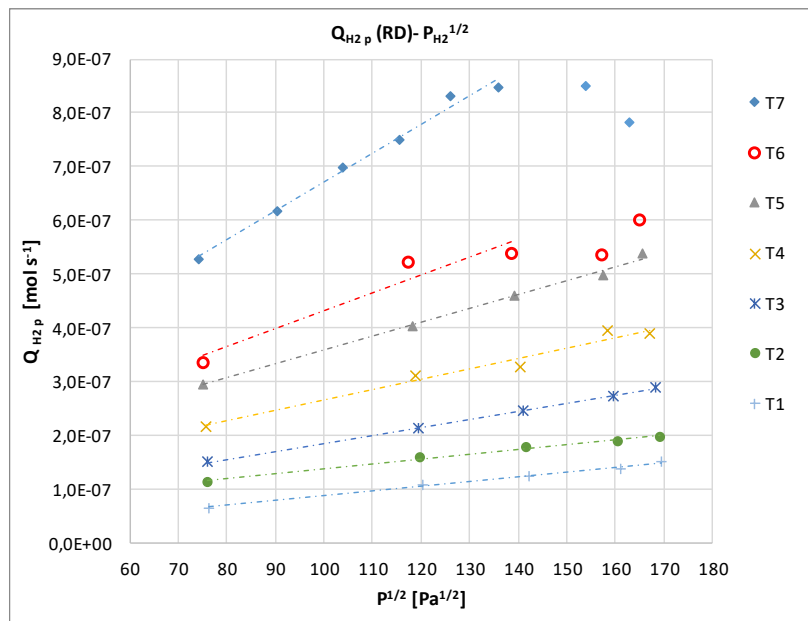


Figure 4-7 Gas-vacuum test - Hydrogen permeation flowrate vs mean partial pressure square root: RD for temperatures from T1 to T7 with regression lines

As explained in 4.3.3, by excluding the points which do not respect the linearity, we obtain the permeability coefficients for all temperatures from T1 to T7. Figure 4-8 reports the ratio $Q_{H_2,p}/\frac{A}{\delta}$ versus the partial pressure: for each temperature the corresponding regression line equation is reported, whose angular coefficient corresponds to the permeability coefficient expressed in $[\text{mol s}^{-1} \text{m}^{-1} \text{Pa}^{-0.5}]$.

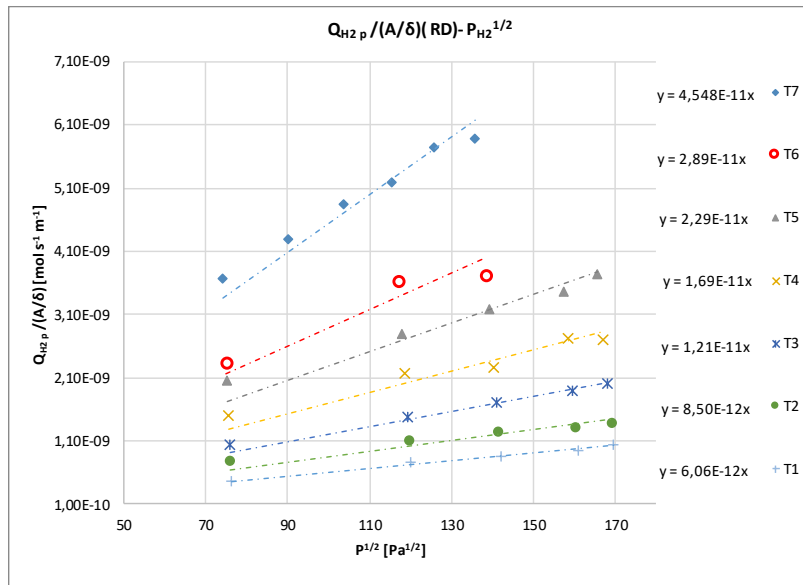


Figure 4-8 Gas-vacuum test - $Q_{H_2,p}/\frac{A}{\delta}$ ratio vs mean partial pressure square root: permeability coefficient determination from T1 to T7

If we consider T_{mean} as the average temperature of the membrane during tests, we can trace the permeability law coefficients from the linear regression showed in Figure 4-9 as function of $1/T$, confirming the Arrhenius law of permeability. In particular, we obtain $E_p = 46309 \text{ [J mol}^{-1}\text{]}$ and $p_{e_0} = 1.08 \cdot 10^{-7} \text{ [mol m}^{-1} \text{ s}^{-1} \text{ Pa}^{-0,5}\text{]}$.

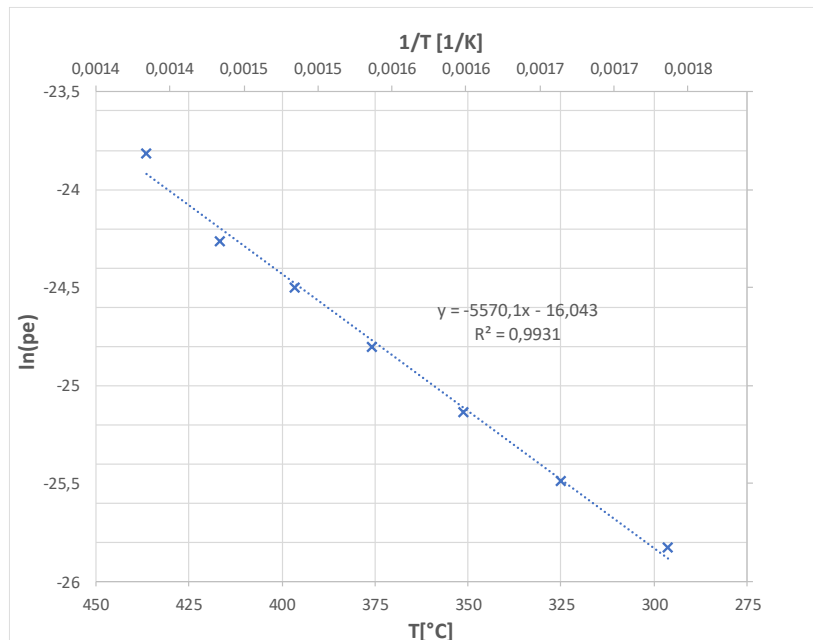


Figure 4-9 Gas-vacuum test - $\ln(pe)$ vs $1/T$: permeability law with temperature

As explained in paragraph 3.4.1.1 during gas-vacuum test, temperature is not uniform over the permeator shell length, presenting deviations of the order of 20°C to 50°C according to the test (see Table 3-7); moreover, there is no evidence that the membrane is at the same temperature of the shell, since radiative heat loss can occur in the vacuum, in absence of sodium, thus creating a temperature delta in the radial direction. Therefore, the mean temperature used to estimate the permeation coefficients is certainly not the “real” temperature of the membrane. Nevertheless, it is worth noting

that a good linear dependence between $\ln(pe)$ and $1/T$ is found, confirming the Arrhenius law of permeability. If we look at Figure 4-9, deviations seem to appear for the two highest temperatures (T_{mean} of 410°C and 434°C respectively). This means that, globally, the mean temperature estimations are coherent with each other. However, we may consider that the entire line could be shifted up or down, according to the possible mean temperature under or overestimation respectively. Of course, this will produce an estimation of the permeability coefficients different from that one proposed here. A comparison with gas-sodium result is provided in 4.6.1 in order to give more explanations.

4.4.2 Gas-sodium test

During gas-sodium test, the estimation of the hydrogen permeation rate is given exclusively by the retentate concentration measurement by gas chromatography, since there is no possibility to have a direct measurement on permeate side, as for gas-vacuum test. Moreover, the tested conditions provide a permeation rate high enough in order to have a low uncertainty and consequently a high confidence on μGC measurements (see paragraph 4.2.3). In particular, the relative standard uncertainty of $Q_{H_2,p}(\mu\text{GC})$ varies from a maximum of 15% to a minimum of 3%, for the lowest and the highest measured flowrate respectively.

Measurements of $Q_{H_2,p}(\mu\text{GC})$ are plotted versus $\sqrt{\overline{P_{H_2}}}$. As shown in Figure 4-10, we can highlight the following points:

- For $\sqrt{\overline{P_{H_2}}} < 140 \text{ Pa}^{0.5}$, $Q_{H_2,p}$ increases linearly with $\sqrt{\overline{P_{H_2}}}$ for all the temperatures;
- For $\sqrt{\overline{P_{H_2}}} > 140 \text{ Pa}^{0.5}$ $Q_{H_2,p}$ does not linearly increase, in fact it is stable or it decreases

In particular, a clear discontinuity appears between the points corresponding to gas pressures of 7 bar and 9 bar, where the linear increment of permeation flux is no more respected and a pseudo-saturation condition seems to be achieved. Moreover, the permeation decrease at 375 °C - 10 bar deviates from the theoretical fundamentals of permeation; this incoherence cannot be explained by the measurement incertitude and let us suppose that permeation could be limited at higher pressures by another resistance mechanism not considered by the integrated permeation law. Moreover, this behavior reflects the same results found for the higher flowrates and pressures measured during gas test.

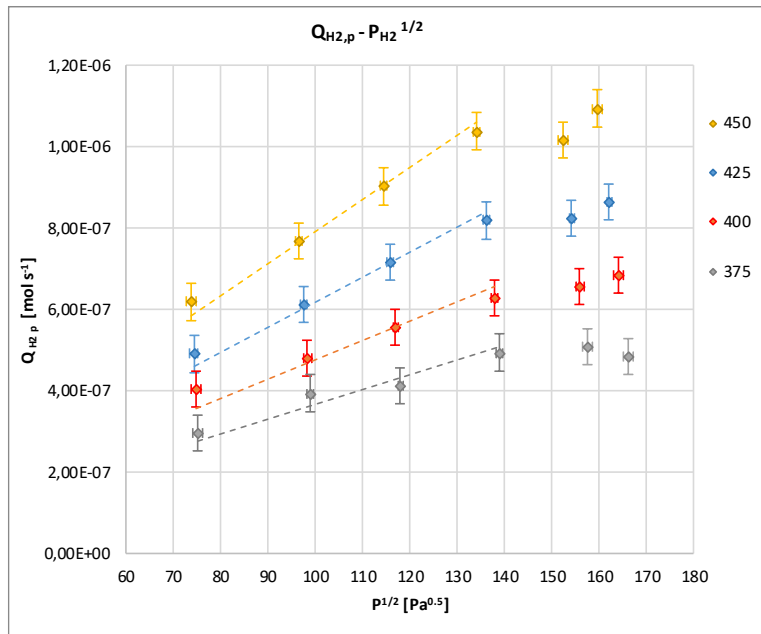


Figure 4-10 Gas-sodium test - Hydrogen permeation flowrate vs mean partial pressure square root: μGC measurements for temperatures from 375°C to 450°C with regression lines

We focus our analysis on the linear “region” (i.e. $\sqrt{P_{\text{H}_2}} < 140 \text{ Pa}^{0.5}$) and we obtain, according to 4.3.3, the permeability coefficients and their relationship with the temperature. In particular, with reference to Figure 4-11 and Figure 4-12, we obtain $E_p = 40757 \text{ J mol}^{-1}$ and $p_{e_0} = 4.80 \cdot 10^{-8} \text{ [mol m}^{-1} \text{ s}^{-1} \text{ Pa}^{-0.5}]$. It is worth noting, as for the gas test, the good linearity between the permeability and the temperature, confirmed by the very high R^2 value.

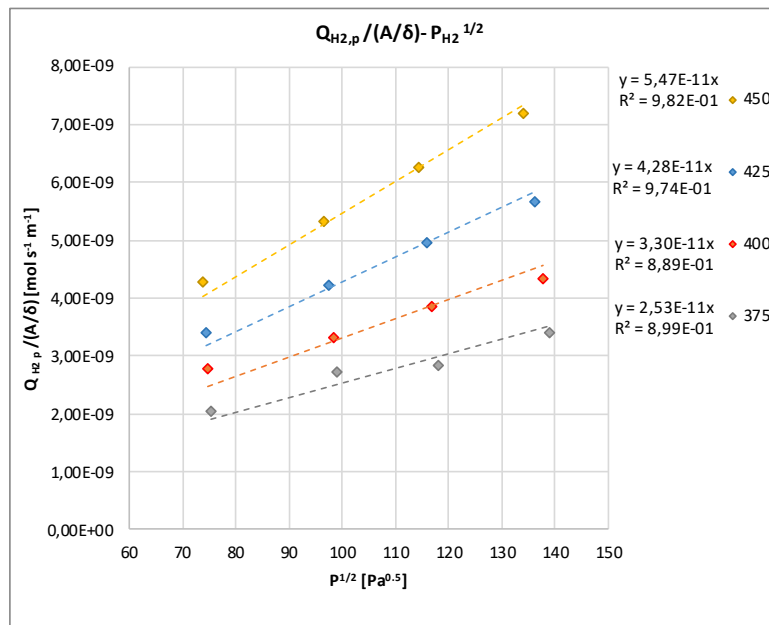


Figure 4-11 Gas-sodium test - $Q_{\text{H}_2,p}/\frac{A}{\delta}$ ratio vs mean partial pressure square root: permeability coefficient determination from 375°C to 450°C

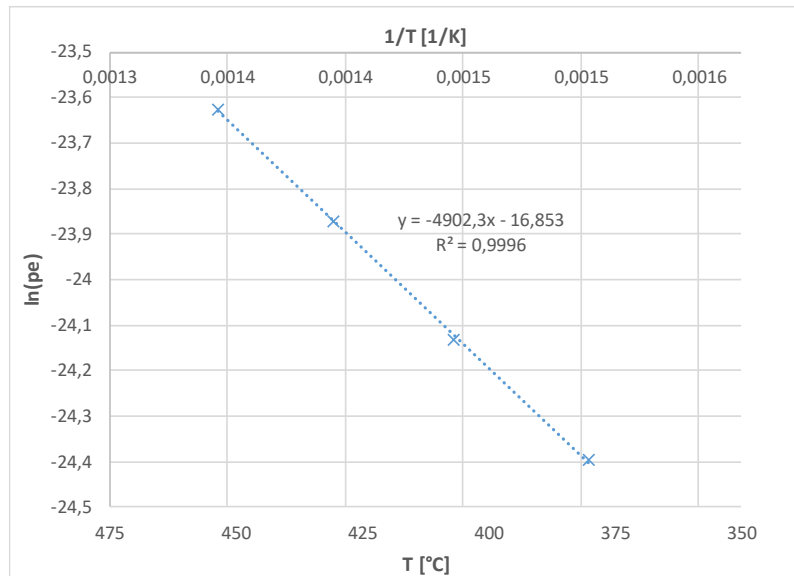


Figure 4-12 Gas-sodium test - $\ln(pe)$ vs $1/T$: permeability law with temperature

4.5 Gas-sodium test: permeate (sodium) side measurements

4.5.1 Plugging indicator and sodium purification

Before to start a permeation test, sodium is purified in order to reach a very low hydrogen concentration (typically below 100ppb), which depends from the coldest point inside the cold trap, its efficiency and the circuit global pollution content. During the purification phase, with reference to Figure 3-11, both plugging indicator (PI), cold trap (CT) and test section (TS) are open. The PI gives a qualitative estimation of the hydrogen content inside the circuit: during a measurement cycle, sodium which circulates inside PI is cooled down and, as the hydrogen contained in sodium crystallizes in the PI pellet's grooves, the sodium flowrate decreases, as consequence of the PI pellet cross section reduction. The temperature corresponding to the first reduction of the flowrate is called Plugging temperature. Then the cooling is stopped, Na temperature increases and the impurities dissolve when the Na temperature is higher than the respective impurity's saturation temperature. The highest the hydrogen content is, the fastest the sodium flowrate decreases inside PI grooves. As reported in Figure 4-13, six PI cooling cycles are performed over about 36 hours (look at the green line, corresponding to sodium temperature at the coldest point of the PI: it can be seen that at the beginning of the purification campaign, the hydrogen content is high and the slope of the curve $Q_{Na} = f(\text{time})$, is also high; as the hydrogen content decreases, the slope is reduced and consequently the period of the cyclic measurement elongates. At the end, a stationary condition is reached, when the PI sodium flowrate does not decrease more, meaning that the sodium purification has allowed to trap all the impurities dissolved (Hydrogen saturation temperature in the sodium is equal to the cold point temperature in the cold trap, at equilibrium).

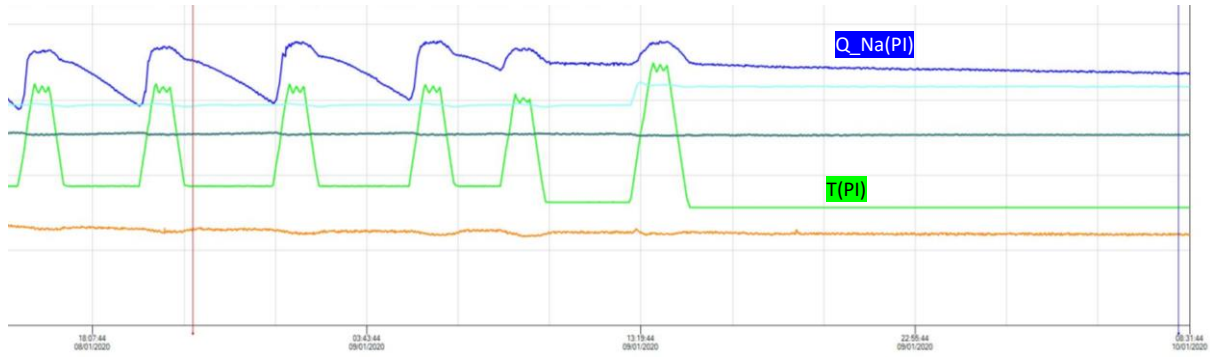


Figure 4-13 Gas-sodium test: plugging indicator (PI) temperature (green) and sodium flowrate (blue) evolution during sodium purification

When the stationary condition, with regards hydrogen content is reached and a stable temperature is maintained inside the test section, the measurement with hydrogen-meter and permeation test can start. The PI is isolated in order to avoid any perturbation of the hydrogen content in the main loop due to partial retention induced by the hydrogen trapping in the PI during the measurement of the so-called plugging temperature.

4.5.2 Hydrogen meter permeability estimation

For our experimental purpose, there are two ways to apply Equation 3-31, which links the hydrogen concentration inside sodium ($y_{H,Na}$) to the mass spectrometer signal ($S_{MS,H2}$):

1. we know “a priori” the value of the hydrogen-meter permeability coefficients, i.e. $pe_{0,DH}$ and $E_{p,DH}$, and we obtain $y_{H,Na}$ values corresponding to different $S_{MS,H2}$ measurements
2. we know “a priori” the value of $y_{H,Na}$ and we obtain $pe_{0,DH}$ and $E_{p,DH}$ values corresponding to different $S_{MS,H2}$ measurements

In our case, we do not know a priori the DH permeability. Some literature references are available, with a certain dispersion between each other, but the “real” DH permeability could currently be different from the chosen literature reference, then the calculated $y_{H,Na}$ could be consequently affected by an error. Therefore we try, by means of a dedicated procedure, to estimate more precisely the “real” permeability coefficient of the hydrogen-meter. In practical terms, we perform hydrogen-meter measurements of the same known hydrogen concentration at different temperatures, without any hydrogen injection or sodium purification, so that we can consider the $y_{H,Na}$ value as constant during the test. Therefore, we obtain the permeability law with temperature; in fact, we can rewrite equation 3-31 as follows:

$$pe_{0,DH} \exp \frac{-E_{p,DH}}{RT} = \left[\frac{K_{MS} K_{S,Na}(T)}{\left(\frac{A}{\delta}\right)_{DH} y_{H,Na}} \right] S_{MS,H2} \quad [\text{mol m}^{-1} \text{s}^{-1} \text{Pa}^{-0.5}] \quad 4-9$$

Let us call the term in the brackets C . By dividing by C and applying a logarithm on both side we obtain

$$\ln(S_{MS,H2}) = -\frac{E_{p,DH}}{R} \frac{1}{T} + \ln\left(\frac{pe_{0,DH}}{C}\right) \quad 4-10$$

The term C is calculated considering a mean $K_{S,Na}$ value (412 ppb $\text{Pa}^{-0.5}$, calculated according to Equation 3-29) between the highest and the lowest temperature, 450°C and 375°C respectively; in particular, there is a relative deviation of $\pm 2\%$ between the mean and the minimum/maximum value.

The value of $y_{H,Na}$ is estimated at 450°C, after the injection T7-P8 (cf. Table 4-2), by means of Equation 3-31, using a “first attempt” permeability value, taken from literature (Robertson “best fit” [44], i.e. $E_p = 54560$ [J mol⁻¹] and $pe_0 = 3.33 \times 10^{-7}$ [mol m⁻¹ s⁻¹ Pa^{-0.5}]). In particular, we obtain $y_{H,Na}$ equal to 335 ppb, with a relative uncertainty of around 10% (cf. Annex IV-B). Therefore, since the term C is constant and having measurements of S_{MS,H_2} at different temperatures, we can obtain the value of $E_{p,DH}$ and $pe_{0,DH}$ by linear regression of experimental data compared to Equation 4-10. In Figure 4-14 the experimental measurements of S_{MS,H_2} are reported as function of temperature: the perfect linearity between $\ln(S_{MS,H_2})$ and $\frac{1}{T}$ demonstrates the validity of the Arrhenius law of the permeability. By comparing the regression line equation on the graph with Equation 4-10, we obtain the following permeability values: $E_{p,DH} = 45782,7$ [J mol⁻¹] and $pe_{0,DH} = 7.84 \times 10^{-8}$ [mol m⁻¹ s⁻¹ Pa^{-0.5}]. It is worth noting that $E_{p,DH}$ depends only on the constant parameter R , while $pe_{0,DH}$ depends on the value of C . In particular, the sensitivity of $pe_{0,DH}$ correspondent to the above reported variability of $K_{S,Na}$ and $y_{H,Na}$, is of $\pm 1\%$ and $\pm 8\%$ respectively. A comparison of $E_{p,DH}$ and $pe_{0,DH}$ with some literature values and with the experimental results obtained for the permeator prototype in gas-sodium configuration is reported in Table 4-4.

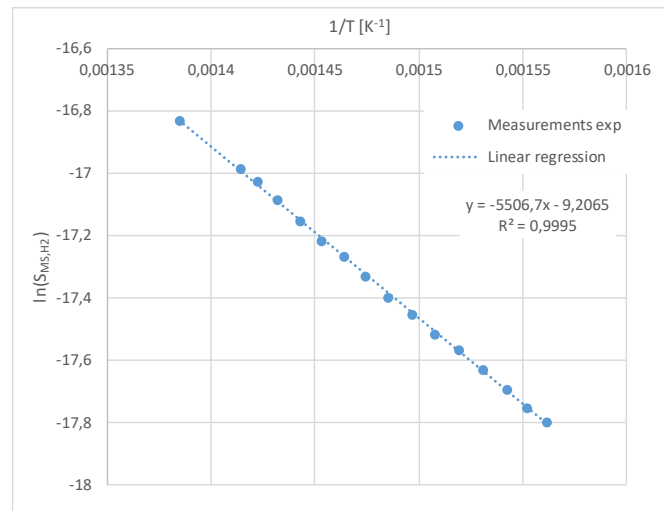


Figure 4-14 Hydrogen-meter permeability estimation : experimental measurements of S_{MS,H_2} at different temperatures for a given hydrogen concentration inside sodium

4.5.3 Hydrogen concentration transient in sodium

Figure 4-15 shows the mass spectrometer signal associated to the hydrogen-meter during a permeation test; we will call it DH-signal or QMS-signal indistinctly. In particular, time is reported on the x-axis, while a double y-axis is provided by the QMS analysis software: the total pressure given by the Bayard-Alpert gauge in mbar on the left and the QMS-signal in Torr on the right, with different colors according to the molecular mass detected. The red line corresponds to mass 2, i.e. molecular hydrogen; it is worth noting that the total pressure and the mass 2 signal are perfectly in accordance, thus confirming that hydrogen is the only element present in the system; this is confirmed also by the almost nil signals of mass 18 (water vapor) and mass 28 (air). Nevertheless, for our analysis we will refer only to the hydrogen signal (red line), called elsewhere S_{MS,H_2} .

We can clearly identify three phases: at the beginning, when sodium purification has ended, the signal is stable meaning that the hydrogen concentration is not changing. The second phase, as the permeation test start hydrogen circulates inside the permeator membranes and diffuses to sodium, is characterized by the hydrogen-meter signal linear increase until the permeation test end; this behavior corresponds to a hydrogen concentration constant increase inside sodium, caused by a constant intake provided by the permeation. In the third phase, once the test ends, the signal becomes stable again, since no more hydrogen is introduced inside sodium. This analysis constitutes a very important result in qualitative terms, because it shows a coherent and nearly instantaneous response of the DH to the test which indicates a potentially good flexibility of this permeation system for a quick adjustment of hydrogen concentration in sodium.

Moreover, by means of equation 3-31 the value of S_{MS,H_2} is converted into ppb concentration, therefore a quantitative analysis is possible; in particular, since the temperature is constant all along a permeation test, the $y_{H,Na}$ increase is directly proportional to the DH-signal one.

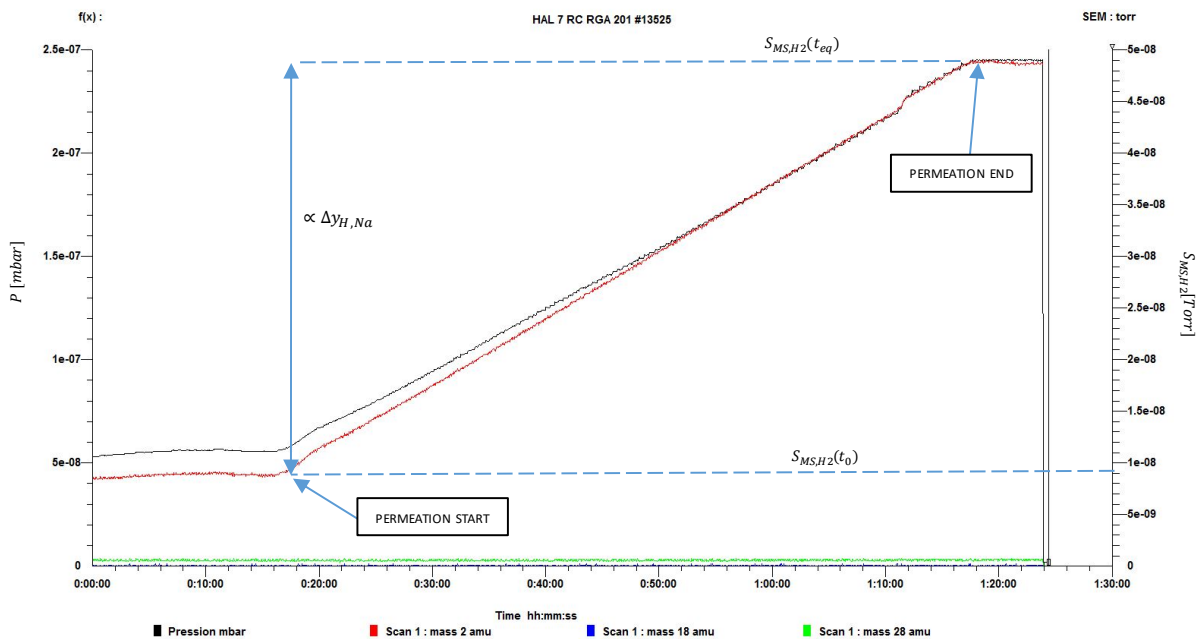


Figure 4-15 Gas-sodium test: DH-mass spectrometer signal evolution during a single permeation test (T7-P8)

When a permeation test is over, the next one can be started unless the hydrogen concentration inside sodium is too high; when this happens, a purification is performed before to launch permeation tests again. The corresponding signal evolution during a purification is reported in Figure 4-16; this measurement is useful to validate the purification process and to demonstrate its effectiveness in reducing the hydrogen content inside sodium.

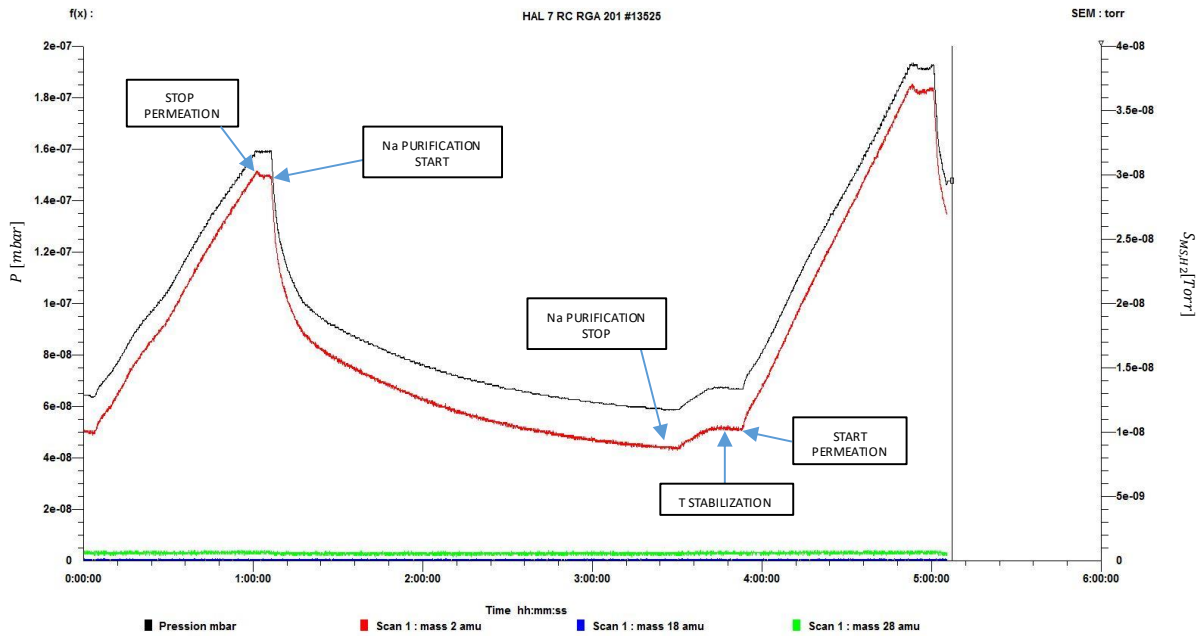


Figure 4-16 Gas-sodium test: DH-signal evolution during sodium purification between two permeation tests (T7-P2 and T7-P3)

4.5.4 Permeation flux estimation

With reference to $y_{H,Na}$ measurements at the beginning and at the end of a permeation test, the hydrogen concentration variation over a test is defined as follows:

$$\Delta y_{H,Na} = y_{H,Na}(t_{eq}) - y_{H,Na}(t_0) \quad [\text{ppb}] \quad 4-11$$

The measured hydrogen increase is entirely imputed to the permeation flux intake coming from the permeator. From a theoretical point of view, since the sodium contained inside the circuit is in contact with a cover gas (Argon) for security reasons, a small part of the hydrogen dissolved inside sodium would then dissolve into the cover gas, thus causing a hydrogen loss. Nevertheless, a theoretical calculation based on the Sieverts equilibrium (see Annex VI) between sodium and the cover gas, demonstrates that this loss is negligible.

Assuming that permeation is constant along the test (i.e. steady state), an estimation of the hydrogen permeation flowrate is given by:

$$Q_{H_2 p} = \rho_{Na} V_{Na} \frac{\Delta y_{H,Na} [\text{ppb}]}{2 t_{perm} M_{H} * 10^6} \quad [\text{mol s}^{-1}] \quad 4-12$$

Where t_{perm} [s] is the duration of the permeation test, ρ_{Na} [kg m³] is the sodium density considered homogeneous, V_{Na} [m³] is the sodium volume circulating during the permeation test (calculated as internal piping volume of test section, Plugging Indicator section, main circuit and heating tank), M_H [g mol⁻¹] is the hydrogen molar mass, the factor 2 is applied to convert H to H₂ moles and the factor 10⁶ is to convert ppb to g/kg. However, data referring to sodium are affected by high uncertainty: in fact sodium temperature, and hence density, is not homogeneous over the different circuit parts; moreover the sodium volume is calculated making some approximations on the internal volumes. Details on volume calculation and the related uncertainty estimation is provided in Annex IV. Nevertheless, it is interesting to obtain this data in order to have a comparison with the retentate side measurements.

4.5.5 Retentate-permeate sides comparison

A comparison between gas side measurements, by gas chromatography, and sodium side measurements, by mass spectrometer, is provided in Figure 4-17; it reports $Q_{H_2,p}$ measured with both techniques (μ GC and QMS) for all the tested conditions. A good agreement is found at the two highest temperatures, with a relative percentage difference between the two measurement techniques below 10% (d) and 20% (c) respectively. At lower temperatures the deviation is of around 30% (b) and 40% (a), which is pretty high and denotes a worst agreement.

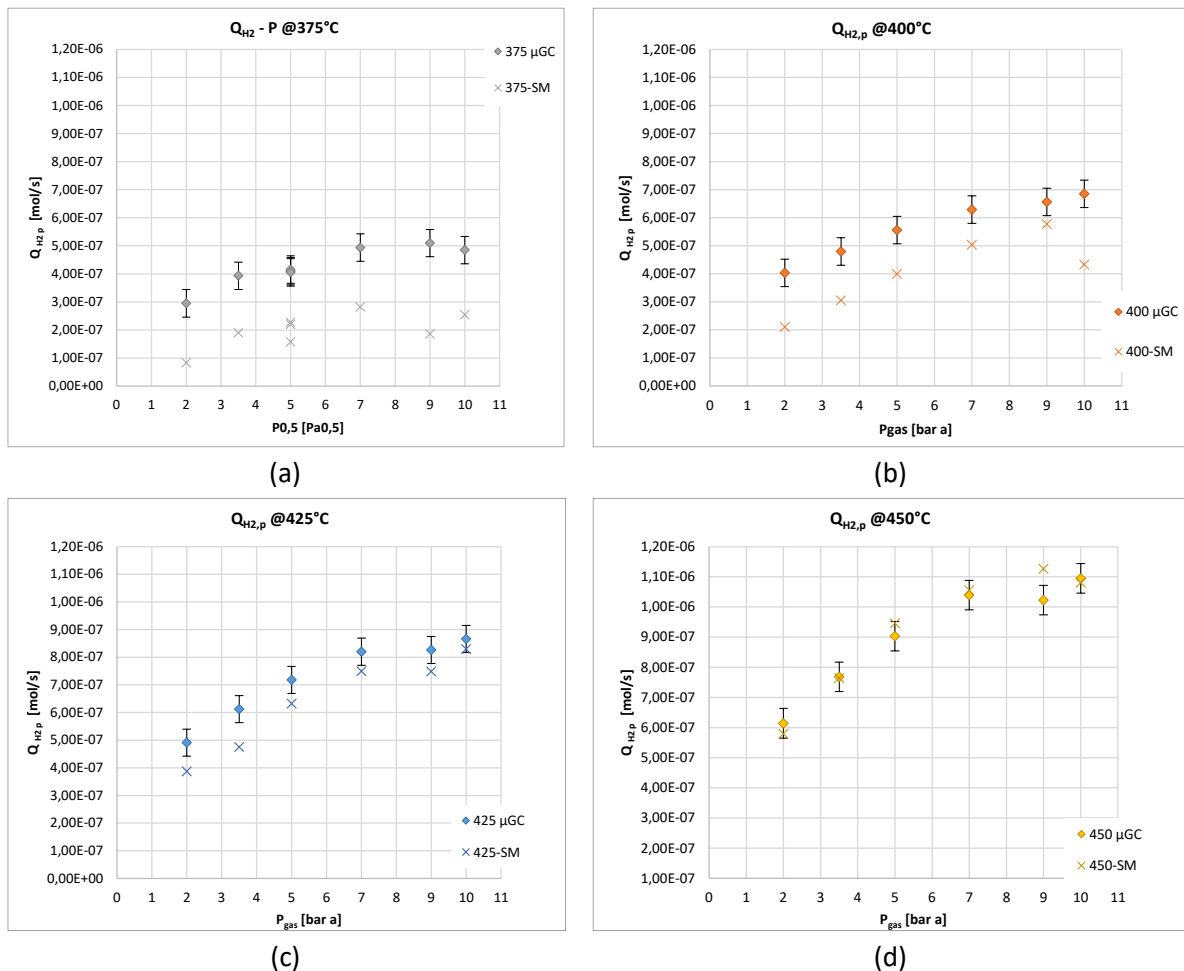


Figure 4-17 Gas-sodium test, $Q_{H_2,p}$ measurements : comparison between μ GC and QMS measurements at 375°C (a), 400°C (b), 425°C (c) and 450°C (d)

However, QMS measurements should be considered by far less reliable, since they are affected by a quite high uncertainty, coming from the spectrometer calibration procedure, combined with uncertainty of sodium parameters composing equation 4-12, as reported in Annex IV. Ultimately, sodium side measurements can be useful to validate approximately the hydrogen mass balance through the permeator, but can not be used to obtain a precise estimation of the hydrogen permeation rate. Nevertheless, the role of the results showed in Figure 4-17, is then to confirm that hydrogen content variation of sodium corresponds to the hydrogen source coming from the permeator, at least as order of magnitude. This result could be trivial, but it demonstrates a reliable validation of the entire process application and measurement techniques and very promising perspectives for a precise control of dissolved hydrogen concentration in sodium circuits.

4.6 Discussion on results

4.6.1 Gas-vacuum and gas-sodium comparison

The comparison between gas-vacuum and gas-sodium results is useful especially if we want to have information on potential experimental deviation of membrane temperature during gas test. In fact, if we assume that the permeation integral law is valid, we should have the same results at the same temperature both for gas-vacuum and gas-sodium test. This is motivated by the following reasons:

1. The membrane is the same and the permeability coefficient is assumed to be equal for both tests.
2. The permeate partial pressure (i.e. vacuum side and sodium side respectively) is negligible in both cases if compared to the feed/retentate side partial pressure, so the integral law is reduced to the same form, giving the same permeation flowrate.
3. No additional resistance in the sodium phase is theoretically predicted.

If we look at Figure 4-18, in both cases the permeation looks to be driven linearly by the partial pressure square root only up to a certain partial pressure and temperature, where we can assume the permeation law validity. If we assume for the gas-vacuum test the mean temperatures from Table 3-7 (i.e. T4=365°C, T5=387°C, T6=410°C, T7=434°C), the permeation flowrates seems to be incoherent if compared to the gas-sodium results. In particular, T7-gas results are between 425-Na and 450-Na, quite in agreement with the T_{mean} value of 434°C; T6-gas points are all below the 400-Na points, while T_{mean} is 410°C; T5-gas seems to coincide with the 375-Na points, while T_{mean} is 387°C. It seems that the T_{mean} is not a good estimation of the real equivalent membrane's temperature during gas-test, since we cannot find a coherence in the results distribution compared to the gas-sodium results.

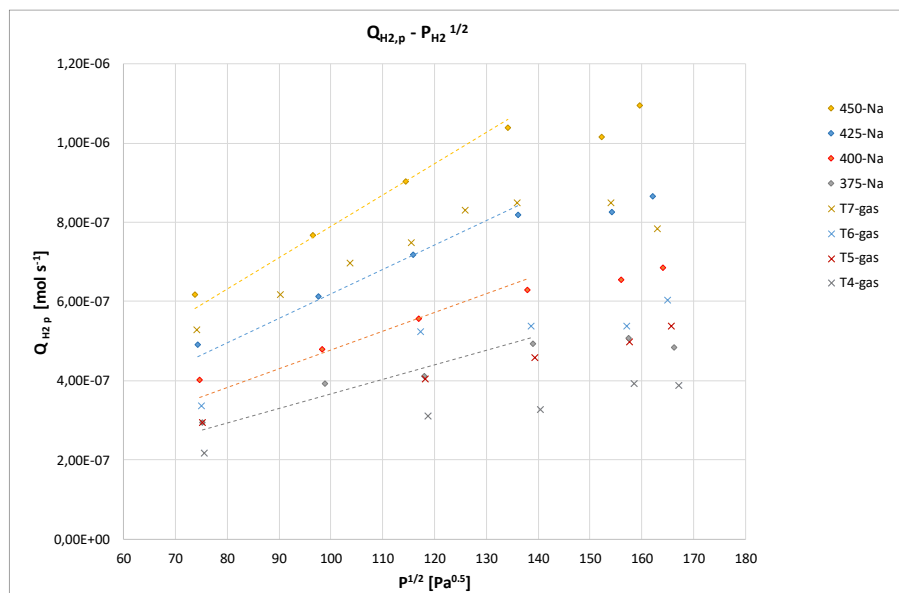


Figure 4-18 Hydrogen permeation flowrate vs mean partial pressure square root: comparison between gas-vacuum and gas-sodium results

If we compare on the same graph the permeability coefficients at different temperatures, the above consideration are clarified: when T_{mean} is used to estimate the gas-vacuum test membrane temperature (gray points "Gas- T_{mean} "), a lower permeability coefficient is found. This is not coherent with the hypotheses above listed: it would imply that the high-vacuum permeate side adds a higher

resistance to the permeation than the one provided by sodium, while the hydrogen partial pressure inside vacuum is much lower than that one inside sodium. On the other hand, it seems much more reasonable to think that the real membrane temperature is simply over-estimated by T_{mean} .

As an example, we have plotted in Figure 4-19 the same permeability values as a function of an “equivalent” temperature (yellow line “Gas-T eq”), in such a way that the permeability regression line coincide with the gas-sodium results. Table 4-3 reports the equivalent temperature values and their deviations from T_{mean} . Except for T7, it seems reasonable to think that a constant bias of around 20°C separates the T_{mean} estimation from the membrane real temperature during gas-vacuum test, because of the temperature non-uniformity along the permeator and the probable heat losses.

Table 4-3 Gas-vacuum temperature assessment: mean and equivalent temperature values

		T4	T5	T6	T7
T_{mean}	[°C]	365	387	410	434
T_{eq}	[°C]	344	366	390	430
$T_{eq}-T_{mean}$	[°C]	-21	-21	-20	-4

Nevertheless, a much lower deviation is found for T7, meaning that or the temperature is less underestimated or a real change in permeation takes place. In particular, it is worth noting that gas-vacuum tests were performed before gas-sodium tests, starting from the lower temperature (T1) to the highest (T7). The above results could be explained by the hypothesis that a “aging” process of the membrane occurs, for sufficiently high temperature and high pressure, producing microstructural changes inside the membrane affecting the hydrogen permeation. In our case, this could happen during gas tests at T6 for the two highest pressures, where the linearity is not respected, then providing a modified permeation behavior for the following tests performed at T7. A more in-depth analysis on this point is provided in section 4.6.5.

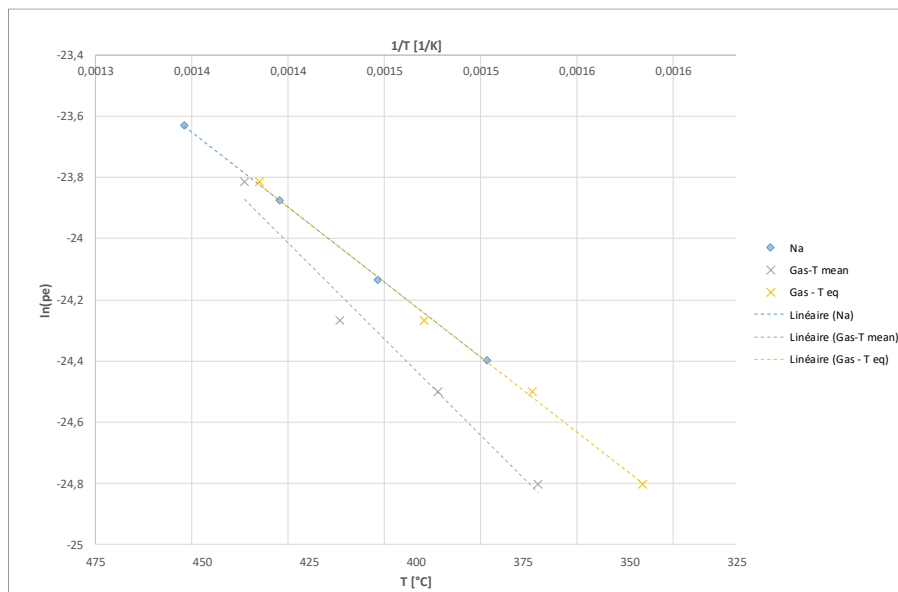


Figure 4-19 $\ln(pe)$ vs $1/T$: permeability law with temperature – comparison between gas-vacuum and gas-sodium test. Estimation of an equivalent temperature for gas-vacuum test

4.6.2 Comparison with the literature

The objective of this experimental study is not to give a precise estimation of the nickel coefficients concerning hydrogen permeation, diffusion and solution properties. The aim is rather to evaluate the global performance of the prototype, in comparison with a theoretical law. Nevertheless, it is interesting to compare the permeability coefficients obtained for the permeator prototype during gas-sodium experiments (par 4.4.2) with previous literature results, in order to understand if our results are coherent with them, at least qualitatively. Moreover, the permeability coefficient obtained for the hydrogen-meter membrane (par. 4.5.2) is reported for comparison. We will not consider gas-vacuum results for this analysis, which request a precise knowledge of the membrane temperature, since they are affected by a considerable uncertainty on the temperature measurements, as explained in paragraph 4.4.1 .

Permeability-temperature dependence, already presented in Figure 4-12, is here compared in Figure 4-20 with main literature correlations, reported both in paragraph 2.2.3 and in Sakamoto's review [41], concerning nickel permeation properties. The corresponding pre-exponential factors and activation energies, together with calculated permeability between 375°C and 450°C are reported in Table 4-4. It is worth noting that our experimental results for the prototype and the hydrogen-meter are globally in accordance with the dispersion of previous results. In particular, the literature dispersion is due to differences both on the pre-exponential factor (oscillating between 1×10^{-7} and 8×10^{-7} mol m⁻¹ s⁻¹ Pa^{-0.5}) and on the activation energy (50000-60000 J mol⁻¹). It is worth noting that the hydrogen-meter and the prototype activation energies are both lower than all the literature values. In particular, focusing on the permeator prototype, two main evidences can be highlighted:

1. Our permeability coefficients are higher than the majority of the literature analyzed. Only Belyakov and Ionov, Gel'd and Smithells and Ransley report higher values.
2. Both our permeation pre-exponential factor and activation energy are considerably lower than all previous results and out of the observed variability range. Even if this double deviation leads to a permeability coefficient in accordance with or slightly higher than previous results, we cannot ignore this discrepancy.

Chapter 4 - Experimental results

Table 4-4 Permeability pre-exponential factors, activation and calculated values between 375°C and 450°C. Comparison between main literature, gas-sodium experimental results for the permeator prototype and hydrogen-meter

Author	Range T		p_{e0}	E_p	$p_{e0} e^{-\frac{E_p}{RT[K]}}$			
	°C	°C			$mol_{H_2} m^{-1} s^{-1} Pa^{-0.5} \times 10^{11}$			
	T_{min}	T_{max}			375°C	400°C	425°C	450°C
Lombard	370	693	4.48	59410	0.73	1.10	1.61	2.29
Deming and Handricks	403	745	3.94	62130		0.59	0.88	1.28
Borelius and Lindblom	180	550	7.26	57740	1.61	2.40	3.4	4.90
Ham	376	600	4.65	55310	1.62	2.37	3.38	4.70
Smithells and Ransley	248	750	3.42	50380	2.97	4.21	5.81	7.84
Shcherbakova	350	600	3.18	53350	1.60	2.31	3.24	4.46
Gorman and Nardella	400	850	3.60	55230		1.86	2.65	3.68
Belyakov and Ionov	350	600	5.42	53140	2.83	4.08	5.73	7.86
Gel'd	360	850	7.55	50210	6.78	9.59	13.2	17.8
Fischer	150	723	1.99	52430	1.19	1.70	2.38	3.25
Robertson "best fit"	24	1060	3.33	54560	1.34	1.95	2.76	3.82
AD Le claire	20	1060	3.33	54598	1.33	1.93	2.74	3.79
Desremaux/Laplanche	200	362	3.46	56106				
Altunoglu	100	400	3.35	54240	1.42			
Kuhn and Johnson	0	327	5.92	54900				
This study								
Prototype (exp gas-Na)	375	450	0.48	40757	2.49	3.30	4.28	5.46
Hydrogen-meter	375	450	0.78	45783	0.98	1.34	1.80	2.36

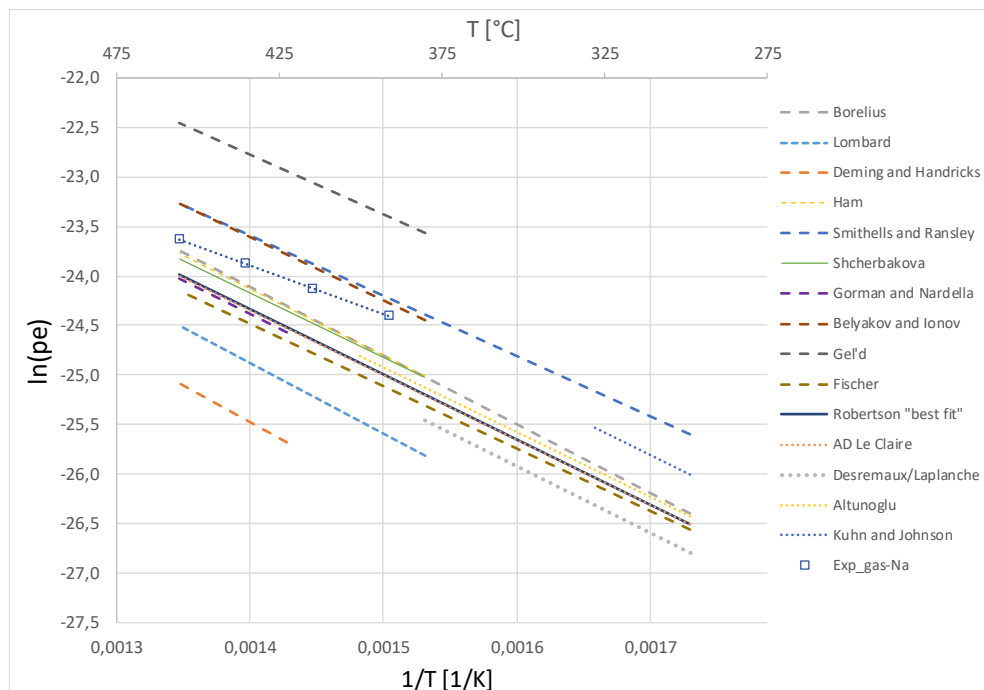


Figure 4-20 $\ln(pe)$ vs $1/T$: permeability law with temperature - comparison between main literature and gas-sodium experimental results

Trying to give an explanation to the difference between our experimental permeability coefficients and the literature, we should remember that the permeability is a conventional parameter, originally defined as the product of the diffusion coefficient and the Sieverts constant. Therefore, a deviation on the permeability coefficient underlies a deviation on diffusivity or on Sieverts constant (and consequently on the hydrogen solubility in nickel) or on both. In this study we do not have the possibility to measure nor the diffusivity nor the solubility of hydrogen inside nickel, since it needs a time-dependent analysis of the permeation in the initial transitory and more complex measurement techniques; therefore, we can only try to give qualitative explanations in this sense. For example, it is interesting to compare our permeability with the diffusivity and solubility coefficients presented in chapter 2 (ref to paragraph 2.2.3). In fact, we can rewrite the permeation flow as follows:

$$Q_{H_2,p} = \left(\frac{A}{\delta}\right)_p \left(D_0 e^{-\frac{E_D}{RT}}\right) \left(K_{S_0} e^{-\frac{E_S}{RT}}\right) \sqrt{P_{H_2}} \quad [\text{mol s}^{-1}] \quad 4-13$$

Where the product $\left(K_{S_0} e^{-\frac{E_S}{RT}}\right) \sqrt{P_{H_2}}$ gives the hydrogen solubility in nickel. At a fixed temperature, since the diffusivity is constant, the permeation increases linearly with the partial pressure square root; in particular the increase should be directly proportional to the solubility increase. Practically, when we increase the hydrogen partial pressure, while the diffusivity is maintained constant, we increase its solubility inside the membrane, thus increasing the permeation: we could say that, when working on an isotherm, we ideally should have a “solubility” driven permeation. Therefore, it is interesting to compare on an isotherm the rates of increase of the measured hydrogen permeation flows with the hydrogen-nickel solubility provided by the literature. Figure 4-21 reports on the same graph the experimental hydrogen permeation flowrates (expressed in term of H moles), compared with the H-Ni solubility given by Bourgeois [43], expressed as atomic ratio H/Ni. Both values are plotted on the x-axis (upper and lower respectively), against the hydrogen partial pressure square root on the y-axis. Although it is not possible to do a comparison in absolute terms, it can be clearly noticed that, for each temperature, the rate of increase with the partial pressure is different for the two datasets: in particular, the experimental flowrates reach a maximum percentage increase (at a partial pressure between 140 Pa^{0.5} and 150 Pa^{0.5}) of about 70% of its minimum value at 75 Pa^{0.5}. Instead, the Bourgeois theoretical solubility increases linearly all over the pressure range, with a percentage increase of 120% between 75 Pa^{0.5} and 160 Pa^{0.5}. This result clearly denotes that, even if a good linearity with the partial pressure square root is maintained up to 140 Pa^{0.5}, the solution mechanism found in our experiments is different from what is provided by the literature.

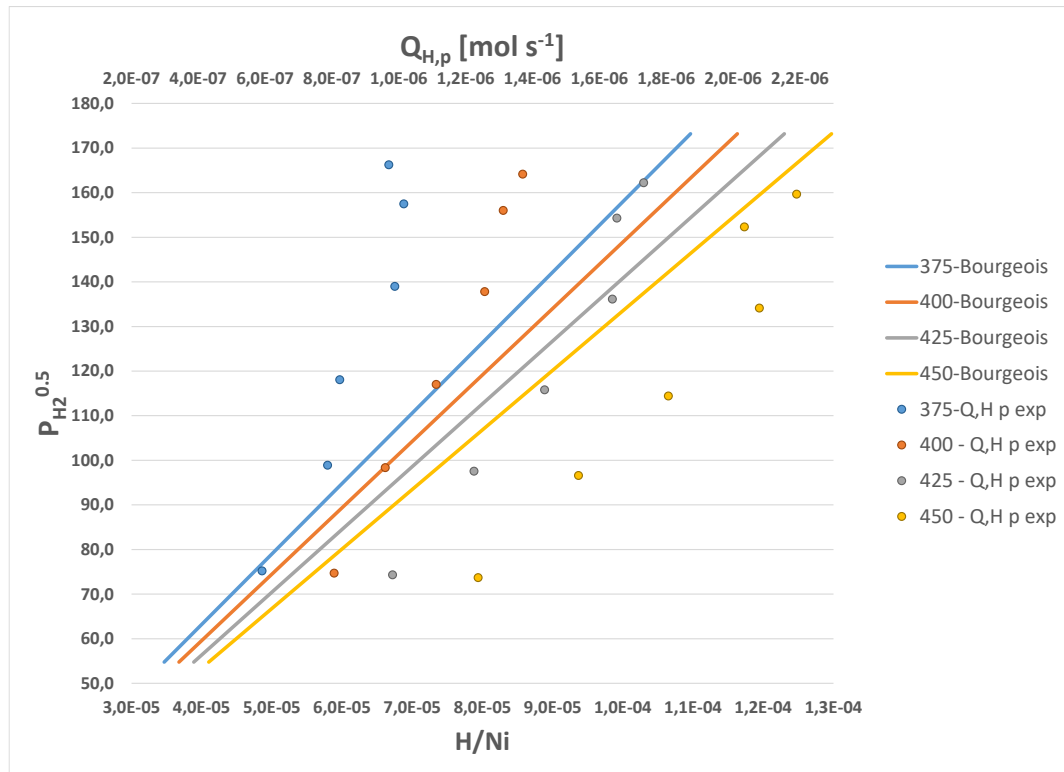


Figure 4-21 Experimental hydrogen permeation rates compared with hydrogen-nickel solubility on isotherm lines (375, 400, 425 and 450°C) given by Bourgeois' model[43]

However, once noticed that the observed solution behavior is not in line with previous results, we have not explained yet why we found a relatively higher permeability coefficient, with a lower activation energy. In fact, without having information on the solubility absolute values or on the diffusivity value, we can not state if it is a product of a higher solubility, or a higher diffusivity or both.

Nevertheless, a reflection about the nature of the literature studies is necessary at this stage. It is worth noting that Bourgeois work [43] refers to an ideal single crystal system, where the hydrogen is dissolved only in the interstitial sites. Moreover, main literature experiments, which are globally in accord with Bourgeois model, are mainly conducted by measurements on small-size nickel samples of plane geometry, with a static pure hydrogen in contact with the membrane, in well controlled and homogeneous conditions (i.e. the sample is placed in a closed hot cell with stable temperature, hydrogen partial pressure is uniform on the membrane). Both single crystal and polycrystalline nickel were analyzed: in the second case, the grain sizes is well known and normally is obtained by means of a dedicated annealing process. On the influence of the grain size on the permeation properties, no clear interpretation is available. On one side Robertson[44] stated that there is no influence of the grain size on the permeation in a polycrystalline nickel; however, in his very detailed review, Sakamoto[41] reports that some authors found that hydrogen solubility can be affected by the presence of grain boundaries and dislocations inside nickel; as a result, the permeability also is affected. In particular Louthan [46] found a higher permeability for a cold worked membrane, due to the higher presence of dislocations if compared to an annealed membrane. He interpreted the results as indicative of short-circuit diffusion through dislocation network. Other authors also have observed higher fluxes along dislocations and have concluded that the higher hydrogen permeability can be due either to larger diffusivity or to a higher solubility or both.

These considerations give as a possible explanation of our data. In fact, the tubular membrane of the permeator prototype is obtained by rolling nickel sheets. Moreover, in order to obtain the specific prototype 90° bended geometry, a cold-working is provided during the commercial fabrication process, being certainly source of dislocations inside the nickel lattice and non-uniformity in terms of grain boundary. Since annealing was not provided after the cold-working, due to technological reasons, it is reasonable to think that, due to the strong deformation, a high degree of dislocation was still present during our test. If a higher content of hydrogen can be dissolved when dislocations are present, this could approximately explain the fact that we obtain a permeability higher than the main literature results. In particular, this could be linked to a higher solubility inside the nickel imperfections such as grain boundaries and dislocations. If this hypothesis is true, we could also explain the fact that the relative solubility increase during the experiments is lower than what is found in the literature: it is possible that, since the solution mechanism includes the dislocations in addition to the interstitial sites, a different solubility law takes place.

Finally, when doing a comparison with literature results, particular regard should be paid to the fact that our experiments were conducted on a multiple tubular membranes prototype at the pilot-scale, taking into account hydrogen partial pressure variation along the membrane due to the gas circulation, an extended 3D geometry and possible non uniformities in terms of temperature and hydrogen concentration. Moreover, our coefficients are obtained by comparison with an integrated law (Equation 4-3) which is based on theoretical hypothesis and assumptions, potentially not fully respected during experiments. For example, we have no demonstration that the gas flowrate is perfectly equally distributed over the four nickel tubes. These elements are simple example of parameters that are not under our control and which were not deeply investigated in this study, which is more focused on process issues. Therefore, without any other clear explanation, they could be proposed for further investigations.

Actually, the most likely conclusion is that our results do not correspond to the “ideal” local permeability coefficient that can be measured on a nickel sample without defects with a dedicated study, but they rather include some “pilot-scale” and non-ideality effects which slightly deviates from the main literature measurement. Nevertheless, the permeability coefficient obtained in this study should be considered as an empirical parameter, which allows us to accurately represent the prototype performances by means of the theoretical law proposed in Equation 4-3.

4.6.3 Comparison with theoretical models

In this chapter we have used two approaches to describe the permeation from a theoretical point of view:

- The first is the 1D model, which takes into account the gas and Na phase convective/diffusive resistances as well as the membrane diffusion resistance. It needs as input the hydrogen diffusion coefficients into the three domains, the fluid dynamic characteristics and the geometry of the system, which directly determines the mass transfer coefficients, by means of literature relationships between the main dimensionless numbers. Moreover, it has to be integrated along the permeator, in order to provide the expected permeation over the entire geometry. This implies a certain numerical complexity and effort.

- The second is the integrated permeation law, a single equation relationship which links the permeation flow to the temperature and the hydrogen mean partial pressure inside the permeator. It needs as input the membrane's geometrical factor and it directly depends from the permeability coefficient. It is a simplification of the more complex 1D model, which reduces to this law when some specific conditions are verified (see paragraph 4.3.1). In particular, the gas and Na phase mass transfer resistances are not considered by this law. From a numerical point of view, its application is immediate, since a single equation explicitly connects all the parameters. However, if one wants to obtain the permeation flow at certain conditions (T and gas pressure), the hydrogen mean partial pressure has to be given as an a-priori input, since this simpler approach is not able to calculate it, as the 1D model does.

When we compare the experimental results to these two theoretical models, it is also necessary to assess if the two models are coherent with each other, i.e. if the simplifications made to obtain the integrated law from the 1D model are valid.

At this purpose, Figure 4-22 reports the comparison between gas-sodium experimental results and the two above models, assessed considering the Robertson "best fit" permeation coefficients (permeability for the integrated law, diffusivity and Sieverts constant for the 1D model). The following evidences can be pointed out:

- The 1D model and the integrated law are well in accordance over the entire pressure and temperature domain; a very slight deviation is present mainly at higher temperatures, where the 1D model provides a smaller permeation flux (2% to 5% lower than integrated law). This is due to the impact of the higher hydrogen partial pressure in Na phase, which occurs when higher permeation fluxes are provided, producing a higher hydrogen content inside sodium during the test. Nevertheless, despite of this slight deviation which is even lower than the measurement uncertainty, it can be assessed that the two models provides globally the same result.
- Experimental results are not in accordance with the models based on Robertson best fit coefficients, in particular they shows higher permeation fluxes for every temperature/pressure combination. This reflects the facts that the actual experimental permeability is higher than the Robertson best fit one.

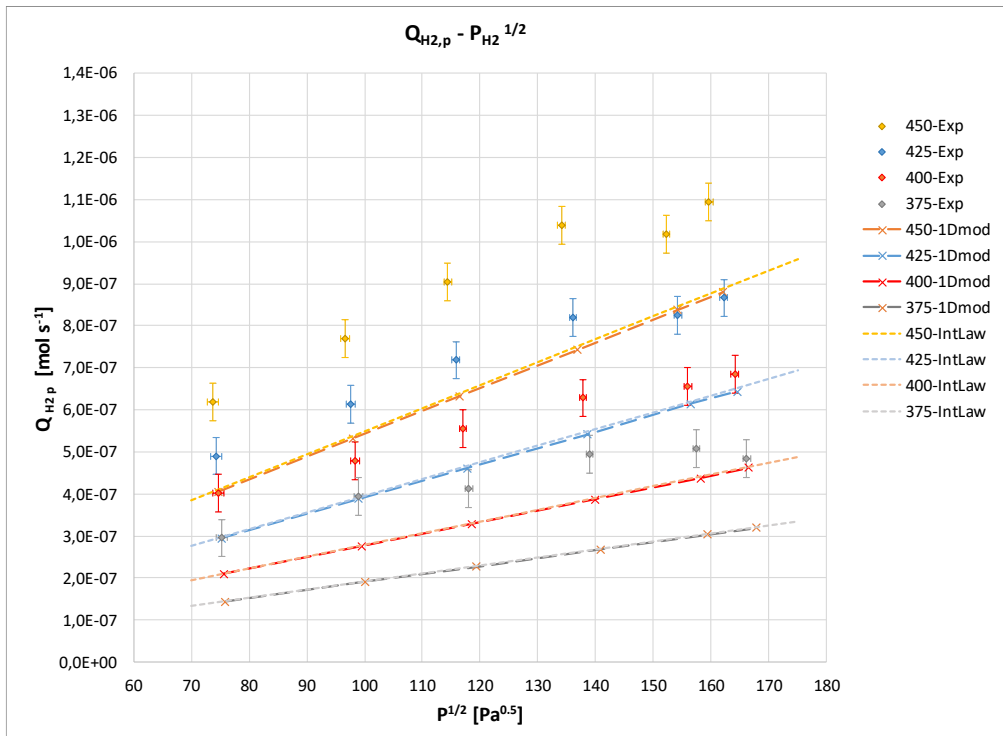


Figure 4-22 Hydrogen permeation flowrate vs mean partial pressure square root: comparison between gas-sodium experimental results, 1D model and integrated permeation law. Model's permeability coefficient is taken from Robertson "Best fit"[44]

Since an experimental permeability coefficient has been obtained in this study (reported in Table 4-4), it is interesting to provide model predictions taking as input the experimental permeability coefficient, instead of a literature one. Figure 4-23 reports the comparison between the same experimental results and the integrated law model, calculated with the experimental permeability coefficient. It is not possible here to compute the 1D model, since it is based on the diffusivity coefficient and Sieverts constant, which are not available from our experimental results. However, as showed in Figure 4-22, we can assume that the 1D model is in accordance with the integrated law results. Two main points can be highlighted:

- In this case, the integrated law predict very well the experimental results at every temperature up to a partial pressure square root of around 140 Pa^{0.5}. This is a trivial result, since the experimental permeation coefficient has been obtained by comparing experimental results with the integrated law; nevertheless, this analysis confirm the fact that, using the appropriate permeability coefficient, we are able to correctly predict a-priori the permeation performances of the system in a certain interval range.
- At pressures higher than 140 Pa^{0.5} the model is not able to correctly predict the experimental performance of the permeator. A detailed discussion on this point is provided in paragraph 4.6.5.

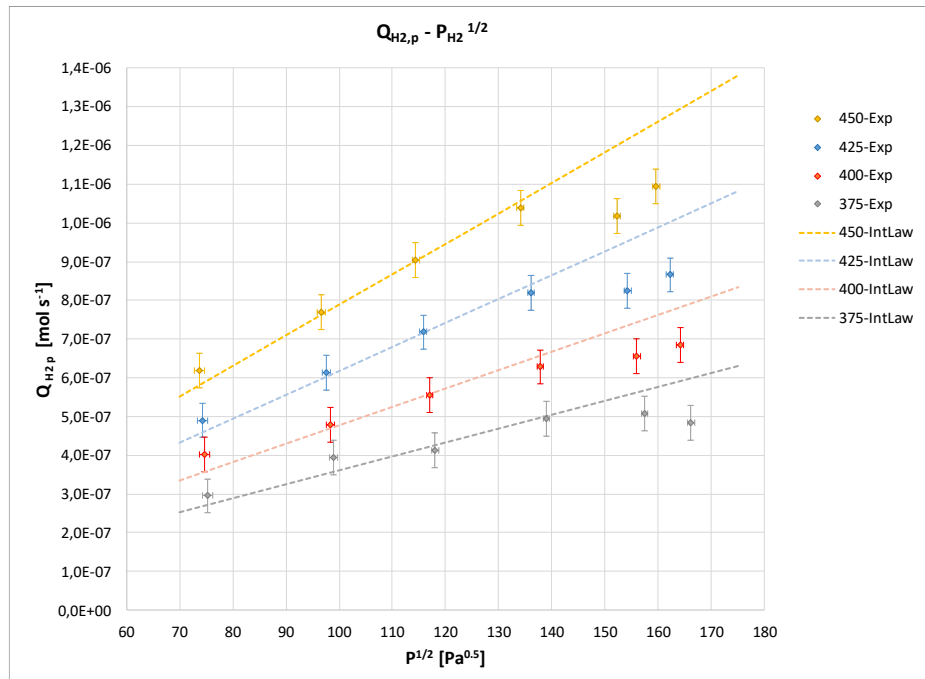


Figure 4-23 Hydrogen permeation flowrate vs mean partial pressure square root: comparison between gas-sodium experimental results and integrated permeation law. The law's permeability coefficient is taken from experimental results regression

4.6.4 A surrogate model: effect of non-ideality on the integrated permeation law

All along this analysis, the experimental results are represented in comparison with the integrated permeation law of Equation 4-3, which is basically a linear relationship in the form “ $y=ax$ ”, where “ y ” is the permeation flux, “ x ” is the hydrogen partial pressure square root. Therefore, by imposing a linear regression of the results in the form “ $y=ax$ ”, we obtain a permeability coefficient and we find that the experimental results are pretty well in accordance with the theoretical law, up to $\sqrt{P_{H_2}} \sim 140 \text{ Pa}^{0.5}$.

However, by looking more in-depth the linear regression “ $y=ax$ ” (see Figure 4-10 and Figure 4-11), it can be noticed that the lines do not perfectly fit the experimental points. In particular, the regression lines are lower than the experimental data at low pressures and higher at high pressures, as a result of the fact to force the regression to the form “ $y=ax$ ”, passing from the axis origin.

Actually, a better fitting (i.e. a higher regression coefficient R^2) would be found if a linear regression in the form “ $y=ax+b$ ” is applied to data at $\sqrt{P_{H_2}} < 140 \text{ Pa}^{0.5}$, as showed by Figure 4-24. It is worth noting that the lines fit better the experimental points all over the linear pressure range. However, the existence of a non-zero “ b ” coefficient in the regression, does not match with Equation 4-3. Therefore, in order to keep a link between the experimental data and the theory, it can be rewritten in the form:

$$Q_{H_2,p} = \left(\frac{A}{\delta}\right)_p p e_0 e^{-\frac{E_{pe}}{RT}} \sqrt{P_{H_2}} + b \quad [\text{mol s}^{-1}] \quad 4-14$$

Where the coefficient b , written in this form, would correspond to a non-zero permeation flowrate for a zero $\sqrt{P_{H_2}}$.

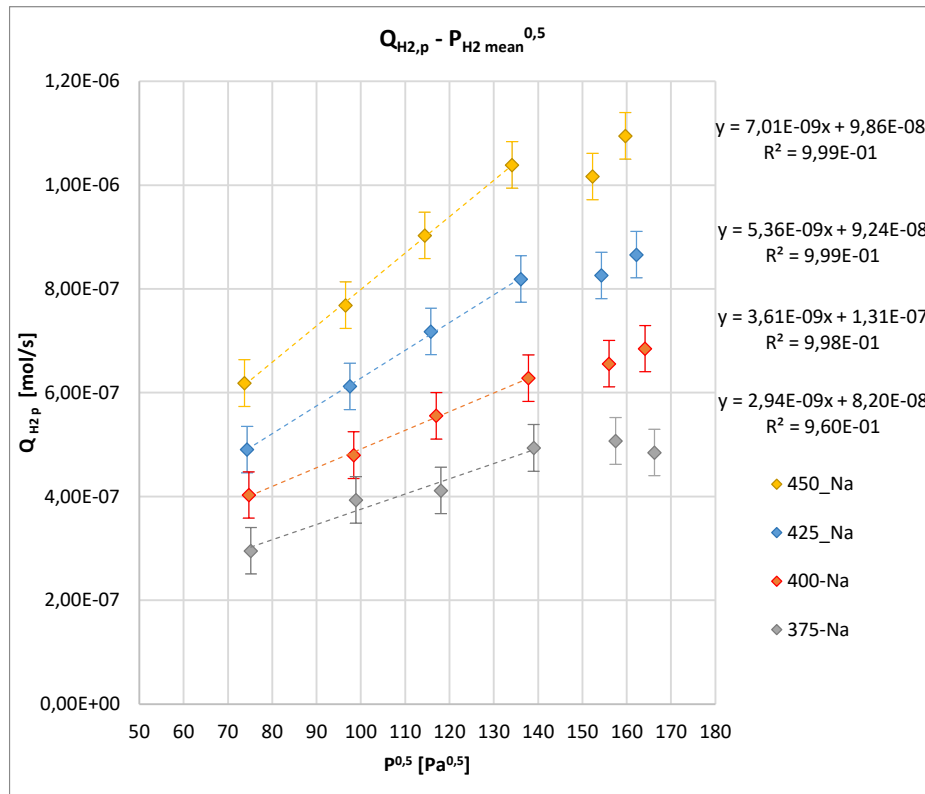


Figure 4-24 Gas-sodium test - Hydrogen permeation flowrate vs mean partial pressure square root: μGC measurements for temperatures from 375°C to 450°C with regression lines in the form “ $y=ax+b$ ”

Actually, this interpretation has not a physical meaning, for the following reasons:

- When the hydrogen partial pressure in the feed side is zero, the permeation is nihil by definition.
- The integrated permeation law can not be extrapolated at very low pressures, approaching zero, where some of the hypothesis done to set it up are no more valid (cf. paragraph 4.3.1, hypothesis ii, iv and ix).

However, the fact that the experimental measurement does not reflects perfectly the Equation 4-3 form, could be explained by the hydrogen transport mechanism along the dislocations induced in the nickel membrane by the cold-working, as reported in paragraph 4.6.2. In particular, the hydrogen which eventually is trapped by the membrane dislocations and defects, could produce an hysteresis effect in the permeation- $\sqrt{\overline{P}_{H_2}}$ dependence, which results in a deviation from the “ $y=ax$ ” ideal form.

In order to have a quantitative evaluation of this deviation, we compare the surrogate model (regression “ $y=ax+b$ ”) with the regression based on the theoretical law (regression “ $y=ax$ ”). Figure 4-25 reports the experimental data with their uncertainty bars and both the regression methods, for the temperatures 375°C to 450°C, at $\sqrt{\overline{P}_{H_2}}$ ranging from 75 Pa^{0.5} to 140 Pa^{0.5}. Although the surrogate model lines are better in accordance with the experiments, the difference between the two methods is always smaller than the measurement uncertainty. In particular, the percentage deviation varies from a maximum of 12% to a minimum of 1%.

Therefore, we can conclude that the low difference between the surrogate model and the ideal law in the regression of the experimental results, being below the measurement uncertainty, together with the fact that the surrogate model has not a strong theoretical basis (but is only based on hypothesis)

and can not be implemented in physical models, bring us to consider the theoretical law (regression “ $y=ax$ ”) as the reference for our analysis.

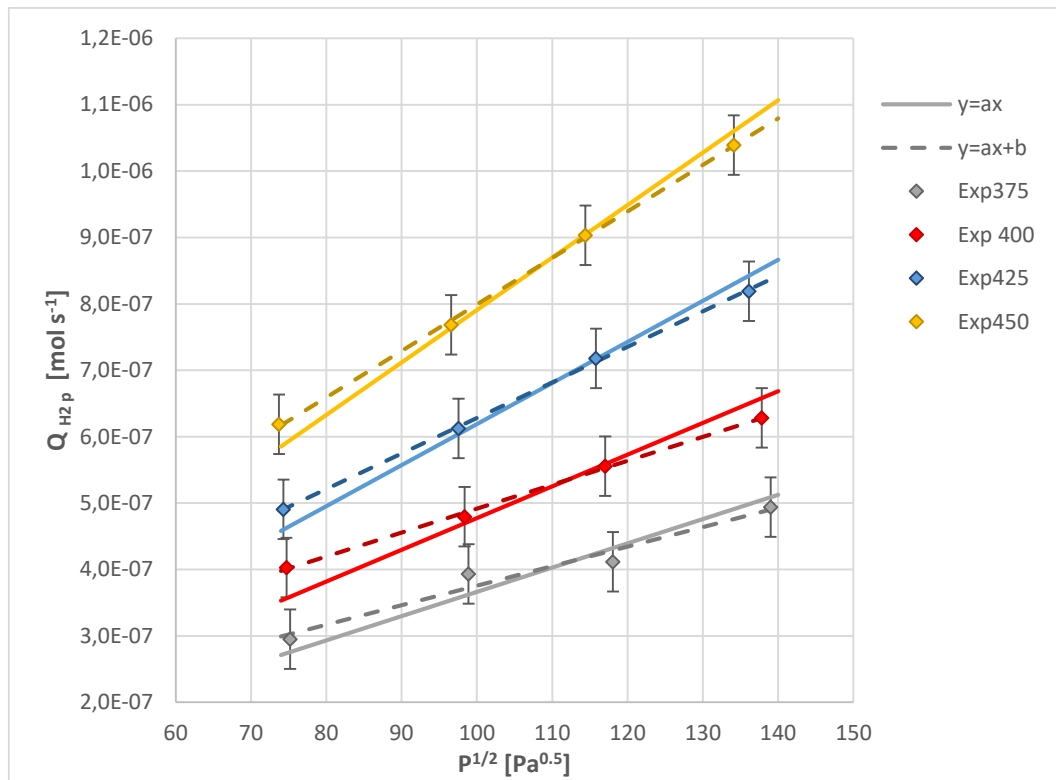


Figure 4-25 Gas-sodium test - Hydrogen permeation flowrate vs mean partial pressure square root: experimental measurements (Exp) with regression “ $y=ax$ ” (solid) and regression “ $y=ax+b$ ” (dashed)

4.6.5 Deviations from the linearity at high pressure

As pointed out by paragraphs 4.4.1 and 4.4.2 and resumed in Figure 4-18, the hydrogen permeation flowrate does not increase linearly with $\sqrt{P_{H_2}}$ over the entire measurement range, as it is predicted from the integrated permeation law (equation 4-3), both in gas-vacuum and gas-sodium tests. In particular, the linear increase is constant up to $\sqrt{P_{H_2}} \sim 140 \text{ Pa}^{0.5}$, corresponding to a hydrogen partial pressure of around $2 \times 10^4 \text{ Pa}$ (equivalent to 200 mbar and to a gas pressure of 7 bar), then the permeation flowrate deviates below the linear trend at the two highest pressure tested. This behavior appears for all the temperatures tested in gas-sodium configuration ($375^\circ\text{C} < T < 450^\circ\text{C}$), while it concerns only the two highest temperatures (T6 and T7) in gas-vacuum test, corresponding to a T_{mean} of 410°C and 434°C respectively (ref. to Table 4-3). Therefore, it can be established that deviation from the integrated permeation law occurs at hydrogen partial pressures over 200 mbar (i.e. gas pressures over 7 bar) and temperatures over 375°C . Additionally, this phenomenon has been clearly measured by two distinct and independent measurement techniques and instruments: in fact for gas-vacuum test, both μGC on retentate side and pressure gauge on permeate side revealed the same result, a repeated number of times (ref to Figure 4-2). We cannot explain this behavior as a simple measurement error or an instrument detection limit. Therefore, it can be assessed that a physical reason of this behavior, independent from the permeate side (it appears both with vacuum and sodium), should reside in some phenomenon affecting the nickel membrane or the gaseous feed/retentate side.

Even if we are interested in validating the permeator prototype operation in the “linear region”, it is of scientific interest to search an explanation to this deviation from theory. Moreover, a more in-depth analysis will consolidate the results which are coherent with the theoretical law. The above considerations bring us to propose and discuss the following possible reasons, which could lead to a deviation from theory as observed experimentally:

1. The **saturation of the membrane’s surface** active sites, which could appear at high pressures.

Waelbroek [73] proposes a theoretical model which takes into account this effect, finding that the permeation flux does not depend more from the hydrogen partial pressure over a certain saturation level. It reports that for nickel membranes, the hydrogen partial pressure leading to saturation should be around 10^{-4} mbar. Nevertheless, several experimental results showed that the hydrogen permeation flowrate grows linearly up to partial pressures of the order of the bar (see paragraphs 2.2.3 and 2.2.4). These values cannot explain our experimental results, since we find a possible saturation over a hydrogen partial pressure of around 200 mbar, for temperatures ranging from 375°C up to 450°C. Without more precise elements we are not able to establish if this could be the real cause of the deviation from the theoretical law; nevertheless, we propose it as possible explanation which has to be investigated more in detail in further studies.

2. The **polarization effect**, which could affect the permeation when hydrogen is diluted in a gas mixture flowing in the feed/retentate side.

Practically it consists into the limitation of the permeation due to the gas phase resistance becoming important inside the boundary layer, when the permeating hydrogen flow is comparable to the inlet hydrogen flow. In principle, this could be coherent with our results at high pressures, when the gas velocity is lower and the permeation rate higher. According to some literature studies [74], [75], this effect is observed when very thin membranes (thickness of the order of few microns) with a high permeability coefficient, typically Pd/Ag membranes, which have a permeability coefficient 2 or 3 orders of magnitude higher than nickel. This effect makes the hydrogen permeation to not linearly follow the partial pressure square root and limits the permeation to an asymptotic value with the growing pressure. In particular, Catalano[74] found both theoretically and experimentally, for different hydrogen concentrations in the feed gas mixture, this non-linear behaviour with the hydrogen partial pressure, driving to an upper asymptotic limit. His study concerns a Pd/Ag membrane of 2.5 μm thickness, tested between 400°C and 500°C and at hydrogen partial pressures between 100 and 600 mbar. Despite his experimental results could qualitatively be similar to our results (i.e. permeation saturation to an asymptotic value at high pressures), it is worth noting that the very low thickness (2 orders of magnitude lower than our prototype) and the Pd/Ag higher permeability than Ni, provide a permeation flux around 10^3 to 10^4 times higher than our study, for the same temperature and pressure. Consequently, the gas polarization effect is much more fostered in his conditions. Moreover, his model, which shows predictions in agreement with his experimental results, is qualitatively similar to our 1D mass transfer model, but includes into the gas phase mass transfer equation an extra convective term in the radial direction, linked to the permeation stream flow. This is typical when one refers to a concentrated solution (i.e. he models the gas phase boundary layer as a hydrogen concentrated solution) and when the permeation convective contribution is comparable to the gas convection.

Despite this fundamental difference, we have applied Catalano's model to our experimental conditions, considering the same mass transfer parameters of our 1D model; nevertheless, we did not find evidence of a possible polarization effect in our experimental conditions. Actually, we obtain the same results given by our 1D model, reported in part 3.2.3.3, which does not show any influence of the gas phase resistance on the permeation.

3. The **competitive adsorption of Argon** at the gas-membrane interface

In order to set up our models (cf. sections 3.2.3.1 and 4.3.1), we made the hypothesis that the hydrogen contained in the Ar-H₂ mixture is adsorbed at the nickel surface according to the Sieverts law, without taking into account an interaction of argon molecules at the surface, which potentially could affect the H-Ni equilibrium (i.e. competitive adsorption effect). This choice was justified by some literature studies reported in section 2.2.4.1. Nevertheless, some literature studies [76], [77] on palladium-based membranes reported that the hydrogen permeation could be reduced by the competitive adsorption of other gases present in the gas mixture (e.g. CO and CO₂). Even though our study concerns nickel instead of palladium, we cannot exclude the hypothesis that the competitive adsorption of Argon could take place, producing a non-negligible impact on the hydrogen permeation, above a certain critical pressure.

4. The **non-ideal membrane's dislocations effect induced by high mechanical constraints**

In paragraph 4.6.2, we present the hypothesis that an additional hydrogen transport mechanism through nickel defects, such as dislocations, could take place depending on the experimental condition tested. We call it a non-ideal transport mechanism, to distinguish it from the diffusion-limited permeation (i.e. Richardson's law) considered as basis for our theoretical analysis. Firstly, it seems likely that dislocations and defects (e.g. vacancies) are introduced inside nickel lattice by the strong deformation provided by the cold working of the membrane before the tests. Clearly, such defects could modify the hydrogen permeation process, i.e. diffusion process, at all experimental conditions tested, by comparison to a non-deformed membrane. However, the deviations from the "ideal" permeation rate observed at high pressures, from temperatures higher than T6 (T_{mean}=410°C) in gas-vacuum and 375 °C in gas-sodium tests, could be explained by hydrogen transport mechanism along the mobile dislocations introduced in the nickel membrane due to the high pressures. This has to be related to Ashby maps showing the evolution of the mechanical properties of pure nickel as a function of temperature and stress. For an adequate temperature range, taking into account the thickness of the membrane, plastic deformation of the nickel membrane probably occurs for high pressures leading to the production of mobile dislocations. This would suggest that hydrogen permeation would be associated with both diffusion and transport processes in this pressure range and for this temperature range. However, recovery process should modify the density of mobile dislocations during the experiments so that a decrease in the permeation rate at high pressures would be observed. Furthermore, hydrogen trapping by dislocations and defects (e.g. vacancies) could not be neglected. This suggested that , for sufficiently high temperatures, two different pressure regions have to be defined, where two different mechanisms drive the permeation: the first, up to a gas pressure of 7 bar, limited by the

classical interstitial sites diffusion, the second, at gas pressures higher than 7 bar, affected by the dislocations transport mechanism. However, with the data available, it is not possible to evaluate the contribution of each process, i.e. diffusion from one side and transport on the other side. Moreover, it is of high importance to consider that the deformation processes affecting the membrane at high pressures and high temperatures correspond to aging processes. Considering that the experiments are all conducted with the same membrane, the experiments being performed from low to high temperatures, and low to high pressures, this means that, when the aging process occurs, for sufficiently high temperature and high pressure, the membrane remains then affected by the microstructural changes. This could explain that the deviation from the ideal law is observed for temperatures higher than 410 °C in gas-vacuum, whereas it is observed even at low temperature, i.e. 375 °C in gas-sodium configuration, considering that gas-vacuum experiments had been performed before those in sodium. For more clarity, for a same set of experiments, e.g gas-vacuum or gas-sodium, during an experiment conducted at a given but sufficiently high temperature, the density of mobile dislocations increases from a sufficiently high pressure, then it decreases due to recovery process as explained before. Therefore, when another experiment is conducted at a higher temperature, the permeation is controlled by diffusion process only for low pressures, but with a deformation-affected membrane. When a critical pressure is reached, additional plasticity is introduced and the deviation from the linear law is observed. For an aged membrane, i.e. after a large number of experiments, the critical temperature required to observe such a deviation is decreased due to microstructural changes, explaining why the deviation from the linear law is observed even at 375 °C for experiments conducted in sodium.

Finally, a combination of hypotheses presented at points 3 and 4 seems to be the most reasonable and coherent with our experimental results, but further experimental studies, more focused on these particular behavior at high pressures should be provided, in order to give more data and eventually a clearer interpretation. In particular, some tests where the gas pressure is fixed at a low value (for example at 2 bar) and different hydrogen concentrations inside the gas mixture are used (up to 15%), could be performed. In this way, the same hydrogen partial pressure range could be investigated without applying an increasing mechanical constraint on the membrane. Moreover, by increasing the hydrogen concentration in the gas mixture, the potential competitive adsorption of Argon would be reduced. By means of these tests, it could be verified if the deviation from linearity is effectively linked to the increasing gas pressure effect or not.

4.7 Conclusion

The main results of this chapter can be resumed by the following highlights:

- Permeation through a multi-tube nickel membrane prototype has been observed at pilot-scale and the measurement techniques have been validated with an experimental campaign in a gas-vacuum configuration, by measuring the permeation of hydrogen both on retentate (μGC) and permeate (Pressure Gauge) side. In particular, a good agreement is found between measurements on retentate and permeate side, validated by means of data reconciliation. An uncertainty analysis establish that the μGC measurements on retentate side are enough

accurate alone (uncertainty <10%), for $Q_{H_2 p} > 4 \times 10^{-7}$ mol/s. This result validate the use of μ GC by itself for the gas-sodium campaign.

- A results post-treatment method have been proposed, which allows to compare the experimental results with a single-equation law, obtained by the integration of the theoretical diffusion-limited permeation law over the prototype geometry. This so-called “integrated permeation law”, reported by Equation 4-3, links the hydrogen permeation flowrate to the temperature and to the hydrogen mean partial pressure.
- The prototype performances in gas-vacuum configuration have been established: a good agreement with the integrated permeation law has been found for hydrogen partial pressures up to 2×10^4 Pa ($\sqrt{P_{H_2}} = 140$ Pa^{0.5}, $P_{gas} = 7$ bar). A non-uniform temperature is measured along the membrane length, thus not allowing to establish accurately a permeability coefficient value (mean temperatures between 293°C and 434°C). Nevertheless, if we consider the average temperature of the membrane during tests, the permeability law coefficients are a linear function of $1/T$, confirming the Arrhenius law of permeability. In particular, we obtain $E_p = 46309$ [J mol⁻¹] and $p_{e_0} = 1.08 \cdot 10^{-7}$ [mol m⁻¹ s⁻¹ Pa^{-0.5}].
- The prototype performances in gas-sodium configuration have been established: a good agreement with the integrated permeation law has been found for hydrogen partial pressures up to 2×10^4 Pa ($\sqrt{P_{H_2}} = 140$ Pa^{0.5}, $P_{gas} = 7$ bar) and for temperatures from 375°C to 450°C. By a linear regression on the experimental data coherent with the theoretical law, an experimental permeability coefficient has been obtained: $E_p = 40757$ [J mol⁻¹] and $p_{e_0} = 4.80 \cdot 10^{-8}$ [mol m⁻¹ s⁻¹ Pa^{-0.5}].
- Measurements of hydrogen concentration inside sodium have been provided during gas-sodium test, based on the well-known hydrogen-meter technology. Despite the high uncertainty on several parameters, thanks to a dedicated estimation of the hydrogen-meter permeability ($E_{p,DH} = 45782,7$ [J mol⁻¹] and $p_{e_0,DH} = 7.84 \times 10^{-8}$ [mol m⁻¹ s⁻¹ Pa^{-0.5}]), together with a transient analysis during the permeation tests, coherent results have been found. In particular, the global hydrogen mass balance between gas and sodium phases is respected (in particular better agreement is obtained for 450°C and 425°C, than for 400°C and 375°C), thus confirming that the entire hydrogen transferred by permeation is dissolved inside sodium.
- Finally, an in-depth discussion on the mains results has been provided, in order to given insights and perspectives for further studies:
 - The comparison between gas-vacuum and gas-sodium provides globally the same permeation features: this demonstrates the theoretical prediction that the sodium phase does not add a significant mass transfer resistance. Moreover, it allows to identify an overestimation of the temperature during the gas-vacuum test of around 20°C, except for T7.

- A comparison of the gas-sodium permeability coefficient, related to the full prototype, with previous literature results for small-size nickel samples, showed that some non-ideal hydrogen transport mechanism, probably linked to the membrane deformation by cold-working, could affect the hydrogen permeation in this study. In fact, quite higher permeation with a lower activation energy is found here if compared to the literature.
- The gas-sodium experimental results are well predicted both by the integrated permeation law and by the 1D-model presented in Chapter 3, when the experimental permeability coefficient is used as input for the models. This is valid up to hydrogen partial pressures of around 2×10^4 Pa.
- A surrogate model is proposed to represent the experimental results without taking into account a theoretical law. Although it fits better with the experimental data, its precision is weakly higher than the integrated permeation law, therefore is not considered for further developments.
- Experimental results deviate from the linear dependence of $Q_{H_2 p}$ from $\sqrt{\overline{P_{H_2}}}$, when $\sqrt{\overline{P_{H_2}}} > 140 \text{ Pa}^{0.5}$ and $P_{\text{gas}} > 7$ bar, for all the temperature tested in gas-sodium ($T > 375^\circ\text{C}$) and for the two highest temperatures in gas-vacuum ($T_{\text{mean}} 410^\circ\text{C}$ and 434°C). Some hypotheses are provided for further investigations, but one reasonable explanation of this deviation could be the modification of the membrane crystalline structure (caused by the presence of dislocations), induced by the higher mechanical constraint, obtained at the higher pressures and temperatures. In addition, the competitive adsorption of Argon at the membrane surface at high pressure could also be considered. Further studies at a fixed gas pressure and variable hydrogen concentration should be carried out to confirm the validity of these hypotheses.

Chapter

5 CFD Study

5.1 Motivation and goals

An analytical model aiming to evaluate the hydrogen mass transfer resistance in three adjacent domains (gas, nickel and liquid sodium) was presented in Chapter 3. It was based on mass transfer correlations taken from literature and it provided an estimation of the hydrogen mass transfer in the radial direction on an infinitesimal membrane length (1D). To support the design of the permeator prototype, this model was integrated axially along a tubular geometry, coupled to the axial gas phase flow (assumed to be a plug-flow), while sodium flowrate was found to not provide a significant mass transfer resistance.

Although the 1D analysis provided results in agreement with the experimental tests under certain conditions, some aspects remains neglected. In particular, the gas and sodium mass transfer resistances should be analyzed in more detail, paying a particular attention to the boundary layer's effect to the radial hydrogen mass transfer. The 1D model is based on literature correlations specific to one particular geometry (flow through pipes), which is not necessarily perfectly representative of the whole prototype shell and tube configuration. Hence, the coupling of gas and sodium axial flows with the radial hydrogen permeation through the nickel membrane, should be taken into account over the entire domain, including the radial dimension. In both phases, a distinction between bulk and boundary layer should be taken into account.

Therefore, a CFD model is set up: the aim is to have a more complete comprehension of the hydrogen mass transfer in both radial and axial directions, without using pre-established correlations, but implementing the fundamental transport equations over a discretized domain.

COMSOL Multiphysics has been chosen as modeling tool, due to the strong multi-physical structure of the problem.

The simulations are performed for the conditions selected for the experimental tests in gas-sodium configuration (cf. Section 3.7.1). A comparison with 1D-model results is presented, in order to assess if the assumptions and simplifications which were drawn are acceptable or not.

5.2 Model's equations and parameters

5.2.1 Hypothesis and features

The following hypotheses are considered:

- i. steady state conditions are established;
- ii. the whole system is isothermal and adiabatic;
- iii. the ideal gas law is valid;
- iv. liquid sodium density is constant over the domain;
- v. gas mixture and liquid sodium properties (viscosity, hydrogen diffusivity) are constant over the domain;
- vi. metal bulk diffusion is the rate limiting step of the permeation process through the membrane (diffusion-limited permeation) and no trapping or surface effects are considered;
- vii. chemical-physical equilibria at interfaces follow the Sieverts law;
- viii. the membrane length is much greater than its thickness, thus the hydrogen diffusion through the membrane is mainly in the radial direction r ;

- ix. the competitive adsorption of Argon at the gas-membrane interface is neglected.

Under steady state condition and (vi) assumption, the permeation process through the metallic membrane follows the Richardson’s law. This leads to the well-known stationary linear concentration’s profile along the membrane thickness, between the two hydrogen concentrations at the two membrane’s interfaces. Due to this trivial result, there is no benefit in modelling the membrane thickness as a geometrical and physical domain, but it can be simply reduced to a domain boundary separating gas and Na phases, where the permeation law equation is applied. In fact, we have no interest in visualizing the linear profile concentration within the metal membrane, but rather we want to study the boundary layer distribution in the gas and sodium phases. Moreover, by considering a diffusion-limited permeation, the model does not take into account any additional hydrogen transport effect inside the membrane, such as the dislocations transport or the trapping inside vacancies, which could affects the membrane at the highest pressures and temperatures (cf. Section 4.6.5).

Finally, three domains are considered in the model as showed in Figure 5-1; for the sake of clarity, the corresponding physical meaning of each variable in the three domains is reported in Table 5-1.

Table 5-1 Summary of bulk and interfacial hydrogen molar concentrations [mol m⁻³] on the gas, membrane and sodium domains

Variable name	Physical meaning	Physical domain
$C_{H_2, gas}$	Molecular hydrogen (H ₂) concentration in gas phase bulk	Gas phase
$C_{H_2, gas}^*$	Molecular hydrogen (H ₂) concentration in gas phase at membrane interface	Gas phase
$C_{H, Ni-gas}^*$	Atomic hydrogen (H) concentration in Nickel at Ni-gas interface	Membrane boundary
$C_{H, Ni-Na}^*$	Atomic hydrogen (H) concentration in Nickel at Ni-Na interface	Membrane boundary
$C_{H, Na}^*$	Atomic hydrogen (H) concentration in Na phase at Ni-Na interface	Liquid Na phase
$C_{H, Na}$	Atomic hydrogen (H) concentration in Na phase bulk	Liquid Na phase

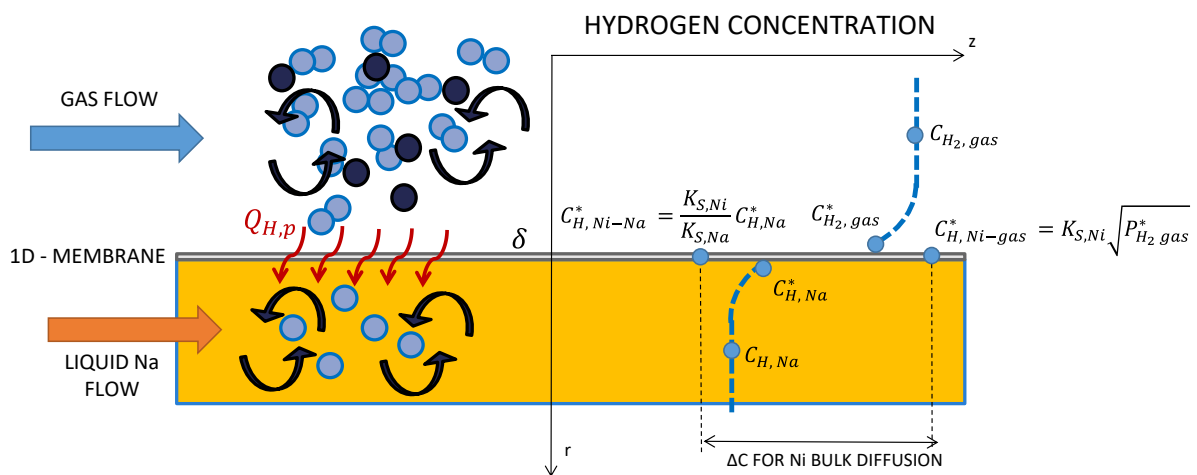


Figure 5-1 Schematic representation of the physical domains for the CFD study

5.2.2 Gas phase

The inlet gas phase is a Ar-H₂ mixture with 2.926% of hydrogen molar content. The gas density is calculated by means of the ideal gas law (valid in this operational range). Gas viscosity and hydrogen

diffusivity in argon are provided by the Chapman-Enskog relationships [78]. Since the system is isothermal and the pressure drop across the permeator is negligible (cf. Sections 3.4.1.1 and 3.4.1.2), we can assume constant temperature and pressure in the gas phase: consequently, gas viscosity and hydrogen diffusivity are constant. Nevertheless, even though the density can be considered a constant, the compressible gas model is used in Comsol, thus producing negligible density variations in the gas phase. Moreover, as already reported for the 1D-model analysis (cf. Section 3.2.3.1), the operational gas flowrates lead to a Reynolds number range of 5 to 20, thus providing a laminar flow.

Due to its low concentration (<3% molar), the hydrogen mass transport, referring to the molecular hydrogen H_2 , is taken into account in the Comsol “*transport of diluted species*” model. Practically, it consists of a mass transport equation for the chemical species H_2 , which includes the diffusive and convective term; since no chemical reactions occurs, a zero rate of production is imposed.

Finally, we apply the following transport equations to the gas phase domain:

- Gas mass transport – continuity.
- Momentum transport: compressible gas and laminar flow.
- Hydrogen mass transport: molecular H_2 transport as diluted species.

The following boundary conditions are imposed:

- Inlet:
 - gas mass flow normal to the gas inlet;
 - H_2 uniform concentration.
- Outlet:
 - the gas pressure at the gas outlet: since a negligible pressure drop is produced between inlet and outlet (see Section 3.4.1.2), the imposed outlet pressure corresponds to the experimentally measured inlet pressure.
- Membrane boundary:
 - wall no-slip condition;
 - outward H_2 flux by permeation.

5.2.3 Sodium phase

Sodium phase is considered as an incompressible liquid, according to hypothesis (iv). Its density and viscosity are calculated by mean of recommended relationships given by the IAEA NAPRO [79]. The operational sodium flowrates lead to a Reynolds number range of 3500 to 18000, thus providing a turbulent flow. The $k - \varepsilon$ turbulence model is employed for this study; the sodium boundary layer in contact with the membrane surface is modeled by means of wall functions, reported in section 5.8.1.

Hydrogen is dissolved inside liquid sodium under its atomic form (H^\cdot) at very low concentrations (between 50 and 500 wppb). Therefore, as for the gas phase, the “*transport of diluted species*” model is used to describe the H transport inside sodium.

Here below, the transport equations applied to the sodium phase domain are summarized:

- Sodium mass transport – continuity.
- Momentum transport: incompressible liquid and turbulent flow.

- $k - \varepsilon$ turbulence model.
- Hydrogen mass transport: atomic H transport as diluted species.

The following boundary conditions are imposed:

- Inlet:
 - Na mass flow normal to the sodium inlet;
 - H uniform concentration.
- Outlet:
 - the sodium pressure at the sodium outlet.
- Membrane boundary:
 - wall no-slip condition;
 - inward H flux by permeation.

5.2.4 Membrane boundary

The nickel membrane thickness is condensed in the mono dimensional boundary (no geometrical thickness) which separates the gas phase from the sodium phase. Therefore, since it does not represent a physical domain, no transport equations are applied to it. Nevertheless, some hypothesis allows writing on this boundary the expression of the hydrogen permeation flux, which goes through the membrane. In particular, by considering the hypothesis (vi), (vii), (viii) and, since the membrane thickness (0.3 mm) is 24 times lower than the membrane external diameter (7.2 mm), the tubular geometry is well approximated by a plane geometry (see Section 3.4.3). Therefore, the hydrogen permeation flux can be written as follows:

$$J_{H,p} = \frac{1}{\delta} 2pe_{H_2,Ni} \left(\sqrt{C_{H_2,gas}^* RT} - \frac{C_{H,Na}^*}{K_{s,Na}} \right) \quad [\text{mol}_H \text{ s}^{-1} \text{ m}^{-2}] \quad 5-1$$

Where the molar flux $J_{H,p}$ is referred to atomic H moles; δ is the thickness of the membrane (assumed to be plane); $pe_{H_2,Ni}$ is the hydrogen permeability through nickel given for H_2 moles and the factor 2 is to be coherent with $J_{H,p}$; $C_{H_2,gas}^*$ is the variable solved at the membrane's boundary by the hydrogen mass transport equation in the gas phase; R is the universal gas constant and T is the temperature; $C_{H,Na}^*$ is the variable solved at the membrane's boundary by the hydrogen mass transport equation in the sodium phase; $K_{s,Na}$ is the Sieverts constant of H-sodium system converted in $[\text{mol}_H \text{ m}^{-3} \text{ Pa}^{-0.5}]$.

The expression in 3-28 defines the output and input hydrogen fluxes, which respectively leave the gas phase and penetrates into the sodium phase.

5.2.5 Model synthesis

For readability reasons, the synthesis of the model (model's equations, parameters and variables) is given in Section 5.8.

5.3 Geometry and mesh

5.3.1 Geometry

The experimental prototype geometry (cf. Section 3.2.5) consists of a four-nickel tubes membrane, disposed axially in a tube shell; gas and sodium phases flow co-currently from the permeator inlet to the outlet. Nevertheless, the entire system is 90° bended between inlet and outlet. The only way to represent the whole system is to set-up a 3D geometry. Nevertheless, the purpose of this study is to analyze the influence of the gas and sodium phases on the hydrogen mass transfer; in particular, the focus is on the effects of boundary layers, which need a very fine mesh to be correctly represented. Moreover, the most critical point is the turbulence solving in the Na phase, which demands the higher computational effort. In this sense, a 3D geometry represent a critical issue: for our purpose, the effort to set up and solve a very detailed 3D model could not be compensated by the benefits that we should have. To have an in-depth comprehension of the hydrogen mass transfer at the membrane' interfaces, a 2D model seems to be sufficient, in the first instance. Therefore, we set-up, with some simplifications, a 2D axial-symmetric model. In particular, we make the following assumptions:

- The prototype 90° bended geometry can be represented by a linear geometry with the same tubes length;
- The permeation is distributed equally among the four nickel tubes and they are independent from each other; therefore, for simplification, the study can be reduced to a single nickel membrane only.

The CFD studied system is then constituted by a single nickel tube, included coaxially in a tube shell. Since the geometry is straight, we can represent it with a 2D axial-symmetric geometry, as showed in Figure 5-2-a. In order to respect the similitude criteria between the experimental prototype (Figure 5-2-b) and the CFD study, an appropriate geometry must be chosen.

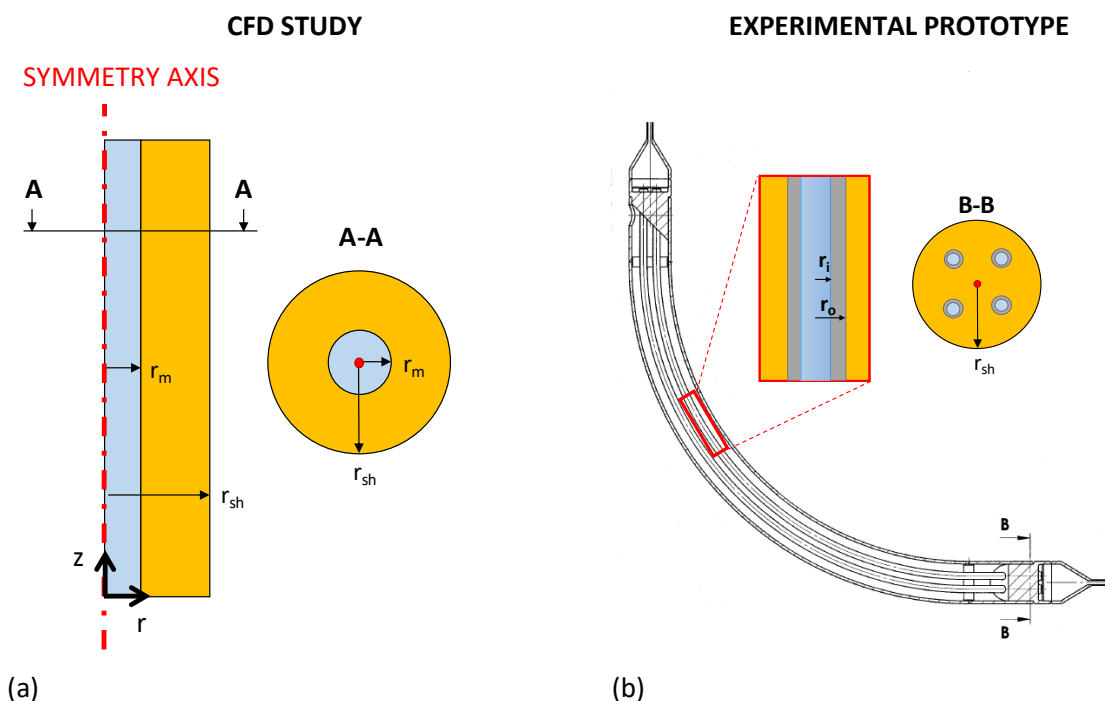


Figure 5-2 Geometry comparison between CFD study (a) and experimental prototype (b). Gas phase is marked in blue and sodium phase in orange.

For the gas phase, we change from four tubes to one single tube: if we maintain the same tube radius, the cross sectional area is reduced by four. To maintain the similitude (same Reynolds number), the inlet gas flowrate has to be divided by four as well. Actually, since the membrane is modeled in COMSOL as a 1D boundary (no geometrical thickness), the mean radius ($r_m=3.45$ mm) between the internal (r_i) and the external (r_o) is chosen, in order to be coherent with the simplification of the tubular geometry using a plane geometry.

Regarding the sodium phase, since the permeation coming from gas phase is reduced by a factor four, the sodium flowrate should be consequently reduced, to have the same mass-flow ratio between hydrogen and sodium. Nevertheless, if we want to maintain the same sodium Reynolds number, the shell radius (r_{sh}) should be reduced to 4.6 mm. In this case, there would be a free space of only 1.15 mm between the nickel membrane and the shell; this condition is not representative at all of the reality. Therefore, we chose to keep the sodium velocity constant (and not the Reynolds number): in this case, we have a r_{sh} of 9.2 mm, which is much more coherent with the real geometry. The correspondent Reynolds number is of the same order than the experimental one. A dedicated study will demonstrate the impact of the sodium Reynolds number on the permeation.

The final geometry dimensions and flow features at a given operating condition at 450°C, compared with the experimental prototype, are resumed in Table 5-2:

Table 5-2 Comparison between CFD study and experimental main dimensions and flow features at 450°C

Parameter	Units	CFD Study	Experimental prototype
Length	mm	500	500
N° of nickel membranes	-	1	4
Membrane radius	mm	3.45 (r_m)	3.3/3.6 (r_i / r_o)
Membrane's thickness	mm	0.3	0.3
r_{sh}	mm	9.2	18.4
Gas cross-sectional area	m ²	3.74×10^{-5}	1.37×10^{-4}
Na cross-sectional area	m ²	2.29×10^{-4}	9.04×10^{-4}
\dot{V}_{Na}	m ³ h ⁻¹	0.25	1
v_{Na}	m s ⁻¹	0.3	0.3
Re _{Na}	-	≈12000	≈18000
Q _{gas}	Nml min ⁻¹	50	200
Re _{gas}	-	≈4	≈4

5.3.2 Mesh

Three meshes have been set-up with a different refinement degree: here, they will be called “coarse”, “normal” and “fine”. The elements are both quadrilateral and triangular type: the first ones are employed at the wall boundaries (i.e. membrane boundary and shell wall), in order to describe with a higher resolution in the radial direction the boundary layers; the second ones cover the rest of the domains (i.e. the gas bulk and sodium bulk). The main elements of each mesh are reported in Table 5-3 and a visual comparison of the mesh refinement is provided in Figure 5-3.

A sensitivity study on the mesh refinement is presented in Section 5.5.3.1, which justify the use of the “normal” mesh for our simulations. Table 5-3 CFD study mesh: main elements of coarse, normal and fine meshes

	Coarse	Normal	Fine
N° of elements	27795	71574	111946
N° of triangles	16800	50499	85621
N° of quads	10995	21075	26325
Edge elements	1881	3498	4380
1 st BL element thickness [mm]	0.07	0.035	0.02

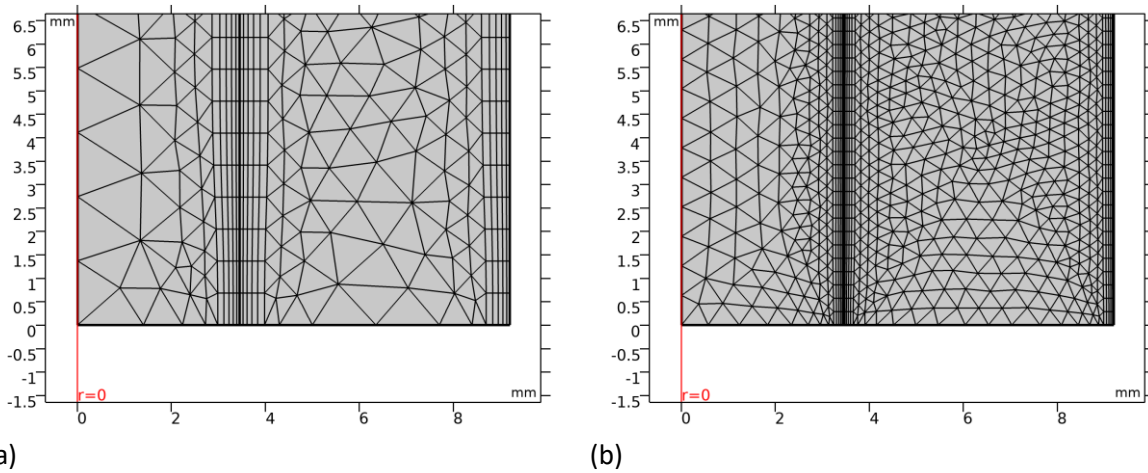


Figure 5-3 CFD study mesh: coarse (a) and fine (b)

5.4 Simulation cases and solver settings

Simulations are performed for the same experimental conditions tested in gas-sodium configuration (cf. Section 4.1.1). The inlet H₂ molar fraction in the gas phase is always set at 2.926%. The inlet H fraction in sodium is taken as the mean value between the initial and the final value measured during the experiments; this value depends on the experimental test. The gas and sodium inlet flowrates are set to 50 Nml/min and 0.25 m³ h⁻¹ respectively, i.e. one fourth of the corresponding experimental ones. Nevertheless, a sensitivity study on the flowrates variation is provided in paragraph 5.5.3, where higher and lower flowrates are considered for simulations. The mesh “fine” is used to compute all the conditions; additionally, a dedicated sensitivity study is provided to validate the use of this mesh.

The permeability coefficient is taken from the Robertson “best fit” [44].

The simulated cases are resumed in Table 5-4.

Table 5-4 CFD study: simulated cases and input parameters

Sim ID		T4-P2	T4-P3	T4	T4-P6	T4-P7	T4-P8	T5-P2	T5-P3	T5	T5-P6	T5-P7	T5-P8
T	°C	375	375	375	375	375	375	400	400	400	400	400	400
P gas	bar	2	3.5	5	7	9	10	2	3.5	5	7	9	10
$y_{H,Na}$	ppb	137	76	173	243	140	191	98	83	171	279	418	124
Sim ID		T6-P2	T6-P3	T6	T6-P6	T6-P7	T6-P8	T7-P2	T7-P3	T7	T7-P6	T7-P7	T7-P8
T	°C	425	425	425	425	425	425	450	450	450	450	450	450
P gas	bar	2	3.5	5	7	9	10	2	3.5	5	7	9	10
$y_{H,Na}$	ppb	137	114	264	435	267	463	139	163	192	224	232	201

Simulations are performed with the COMSOL Multiphysics® solver: it solves simultaneously the gas laminar flow and sodium turbulent flow, coupled to the diluted species mass transport in both domains. The relative tolerance for the convergence criteria is set at 5×10^{-5} .

5.5 Results

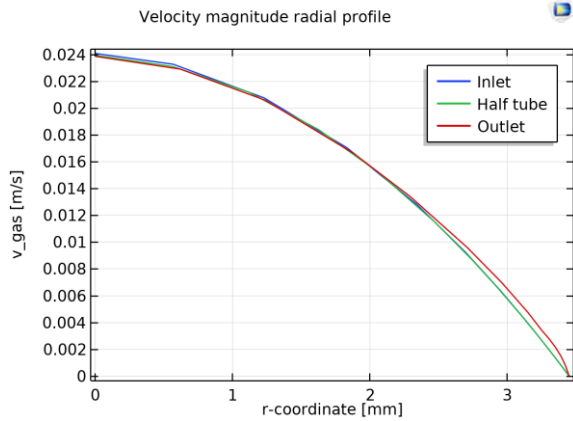
Results are analyzed and compared in qualitative terms, by plotting on different section lines the values of the more relevant variables: hydrogen concentration, velocity, partial pressure and permeation flux. Both radial and axial profiles are provided. This analysis is provided in Section 5.5.1 for the case T7 as an example, but it is representative, qualitatively, of all the other simulated cases reported in Table 5-4.

Additionally, since we are mainly interested in the hydrogen permeation, a quantitative evaluation of the global and hydrogen mass balances is provided by computing the mass flux surface integrals at the inlet, outlet and at the membrane's interface.

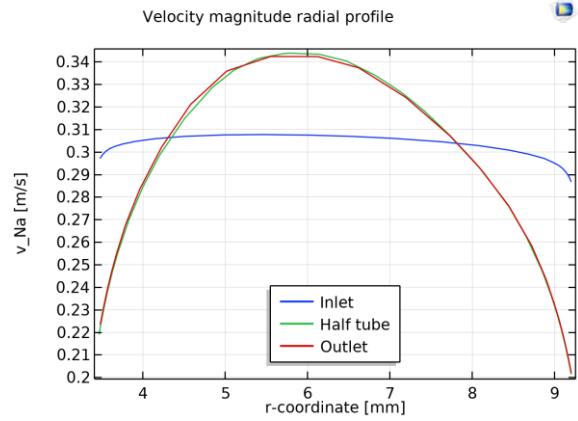
5.5.1 1D plot profiles

5.5.1.1 Gas and sodium velocity

The radial profiles of gas and sodium velocity magnitude are reported at three axial coordinates: $z=0$ mm (inlet), $z=250$ mm (half-tube) and $z=500$ mm (outlet). For each condition, the same behavior is found: the typical laminar parabolic profile of the gas phase does not evolve axially, meaning that the flow fluid dynamics is suddenly established. Instead, the sodium profile at the inlet (where an almost flat profile is found) is quite different from the profiles at half-tube and outlet; this means that the sodium flow takes the first 100-200 mm to reach a stable condition. Moreover, it is worth noting that COMSOL does not plot the sodium velocity at the walls (where the velocity is zero by the imposition of the no-slip condition), but it arrives up to the first boundary layer cell. Since we have used a turbulent model including the wall functions, the velocity profile inside the boundary layer is mathematically computed by the wall functions, but Comsol cannot give it graphically as output plot. The plot of the condition T7 is given as example in Figure 5-4.



(a)



(b)

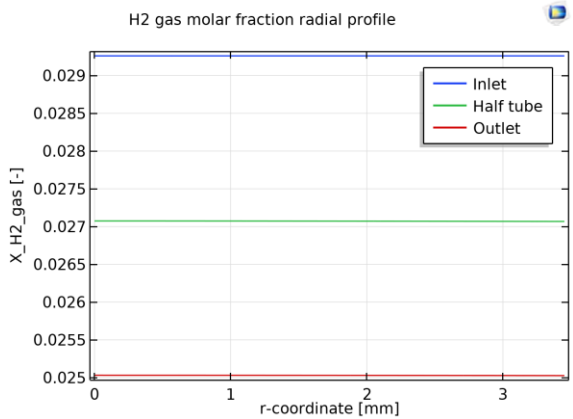
Figure 5-4 CFD study: radial profiles of gas (a) and sodium (b) velocity at inlet, half tube and outlet

5.5.1.2 H₂ and H molar concentration

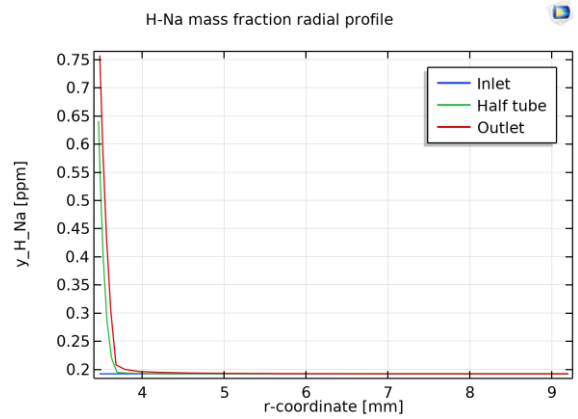
Similarly to the velocity, the H₂ and H concentration, in gas and sodium phase respectively, are reported on the three axial coordinates inlet, half-tube and outlet. For practical reasons, the molar concentrations are converted to molar fractions, for the gas phase, and mass fractions (expressed in wppm), for the sodium phase.

Concerning the gas phase H₂ concentration, two main evidences are found:

- the radial profile, at each axial coordinate, is constant (Figure 5-5-a). This means that the gas phase, for every simulated case, does not provide a mass transfer resistance in the radial direction sufficient to produce a concentration gradient between the bulk and the membrane's boundary.
- The axial evolution is coherent with the permeation physics, i.e. the hydrogen concentration progressively reduces from the permeator inlet to the outlet, since a part of hydrogen moves by permeation from the gas to the sodium phase. This is confirmed both by Figure 5-5-a and by Figure 5-5-c, which shows the axial profile at the membrane's boundary. In particular, the profile is linear along the entire axial coordinate.



(a)



(b)

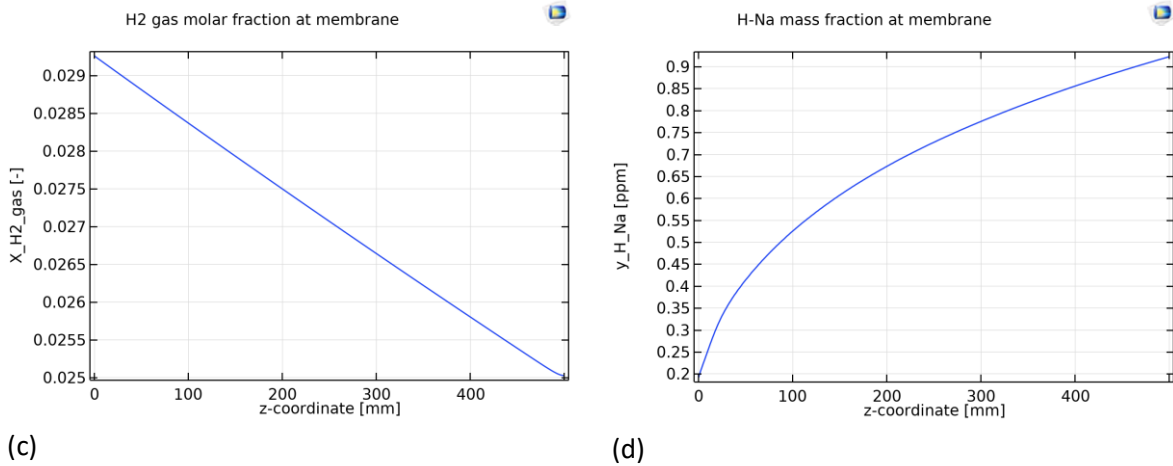


Figure 5-5 CFD study: hydrogen concentration radial profiles in gas (a) and sodium (b) at inlet, half tube and outlet. Axial profiles at the membrane's boundary in gas (c) and sodium (d).

For the H concentration in sodium phase, similar considerations can be done:

- the radial profile (Figure 5-5-b) at the inlet is constant at the given inlet H concentration, since the permeation does not take place yet. Then, at half tube and at the outlet a strong concentration gradient is concentrated in the first 2-3 mm adjacent to the membrane's boundary, in correspondence of the boundary layer. In particular, the concentration at the membrane's boundary is 3 to 5 times (depending on the axial coordinates) higher than the bulk concentration. This denotes that the sodium mass transfer resistance is mainly due to the presence of the laminar boundary layer. Outside the boundary layer, the H concentration is practically constant all over the sodium bulk up to the shell wall, at the same value of the inlet concentration;
- in the axial direction the concentration increases, since the hydrogen permeation flux coming from the membrane provides an increase of the global hydrogen content inside sodium. However, this increase is obtained only in the nearest of the membrane's wall. Figure 5-5-d represents the axial profile at the membrane's boundary: after the first 100-200 mm, where the sodium flow is not established yet, the H concentration increase is quite linear. It is worth noting that the values here reported are slightly higher than the corresponding values in Figure 5-5-b. This is because COMSOL, as for the sodium velocity, plots the H concentration in sodium only up to first boundary layer cell.

As general comment, these results are well in accordance with the 1D-model presented in Chapter 3; in fact, similar results are found for the gas and sodium phase radial concentration profiles (see Table 3-2).

5.5.1.3 Permeation flux

The hydrogen permeation flux per unit surface ($J_{H_2,p}$) is evaluated at the membrane's boundary. Figure 5-6 shows its axial profile: it decreases linearly along the axial coordinate, in accordance with the H_2 concentration in the gas phase. This indicates, qualitatively, that the main driving force of the permeation is given by the hydrogen concentration, and consequently its partial pressure, in the gas phase. A rough numerical evaluation between $z=0$ and $z=500$, shows that the same percentage

variation (around -15%) is found for the hydrogen concentration in gas phase (Figure 5-5-c) and for the permeation flux (Figure 5-6).

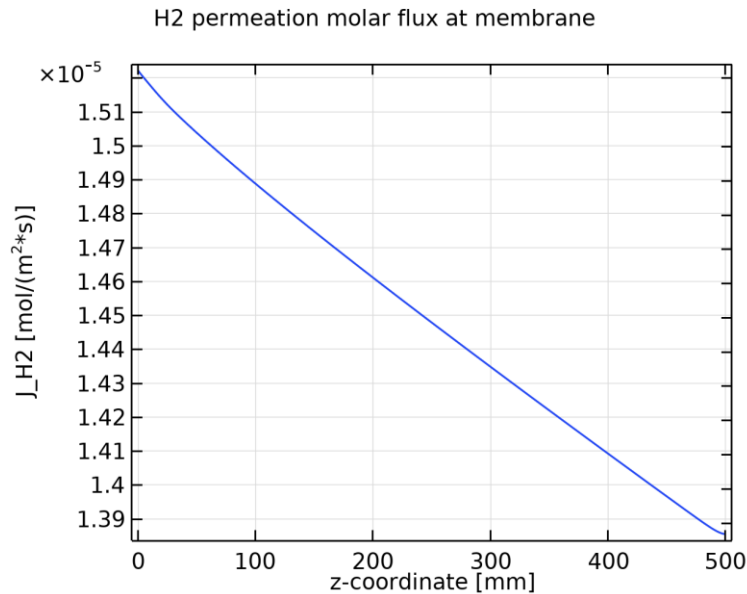


Figure 5-6 CFD study: axial profile of hydrogen permeation flux at the membrane's boundary

5.5.1.4 Hydrogen partial pressure

In order to have a clearer view on the impact of gas and sodium phases on the permeation, it is interesting to compare on the same graph the hydrogen partial pressure at the membrane's boundary, both in gas and sodium phase (equivalent partial pressure in equilibrium with hydrogen concentration in sodium). With reference to equation 3-28, the square root of these two partial pressures are given

by the term $\sqrt{C_{H2,gas}^* RT}$, for gas phase, and $\frac{C_{H,Na}^*}{k_{s,Na}}$ for sodium phase.

Figure 5-7 shows their axial profile at the membrane's boundary, as well as their difference, i.e. the term in brackets in equation 3-28, which actually drives the permeation. It can be underlined that from the permeator inlet to outlet, the hydrogen partial pressure in the gas phase is around two orders of magnitude higher than the sodium phase one. In particular, for the lower gas pressure tested (2 bar)

$\sqrt{C_{H2,gas}^* RT}$ is around $75 \text{ Pa}^{0.5}$, while $\frac{C_{H,Na}^*}{k_{s,Na}}$ is at around $2 \text{ Pa}^{0.5}$, when the $C_{H,Na}^*$ concentration is at 1 ppm. As a result, the difference (red line) between them is practically equal to the gas phase partial pressure. Even if the sodium phase provides a certain resistance in the boundary layer, which leads $C_{H,Na}^*$ at values around 1 ppm (see Figure 5-5-d), this is not sufficient to provide a enough high partial pressure, so that it could have a significant impact on the permeation.

Finally, the permeation is essentially driven by the hydrogen partial pressure in the gas phase.

It is worth noting that this result confirms the conclusion obtained from the 1D-model analysis (Section 3.2.3.4).

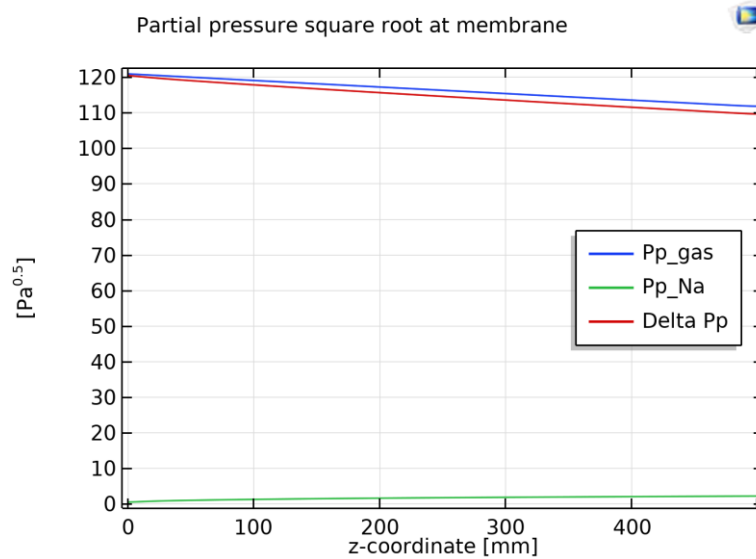


Figure 5-7 CFD study: axial profile of hydrogen partial pressure [$\text{Pa}^{0.5}$] at the membrane's boundary in gas (blue) and sodium (green) phase. The difference is marked in red.

5.5.2 Permeation flowrate and mass balances

A quantitative evaluation of the total hydrogen permeation flowrate $Q_{H_2,p}$ [mol s^{-1}], can be performed in COMSOL by means of the following methods:

1. Surface Integral (SI) of the hydrogen permeation flux ($J_{H,p}$) on the membrane's boundary.
2. Balance of the molar flow on the H_2 species in the gas phase; SI on gas inlet – SI on gas outlet.
3. Balance of the molar flow on the H species in the sodium phase; SI on Na outlet – SI on Na inlet.

where the surface integral of the molar flow, in gas and sodium phase respectively, is defined by the following relationships:

$$\int_{\partial\Omega} C_{H_2,gas}(v \cdot n) dS \quad [\text{mol s}^{-1}] \quad 5-2$$

$$\int_{\partial\Omega} C_{H,Na}(w \cdot n) dS \quad [\text{mol s}^{-1}] \quad 5-3$$

The permeation flowrates obtained with methods 1 to 3 are all converted into H_2 moles and compared with each other. To illustrate, Table 5-5 summarizes the permeation flowrates obtained for the simulations cases at 450°C . Despite the negligible differences due to the numerical resolution and the finite discretization of the system, we can conclude that the three methods are in good agreement. This result validates the convergence of the mass and momentum transport equations solving.

We will consider the method 1 to evaluate the permeation flowrate for the rest of the analysis.

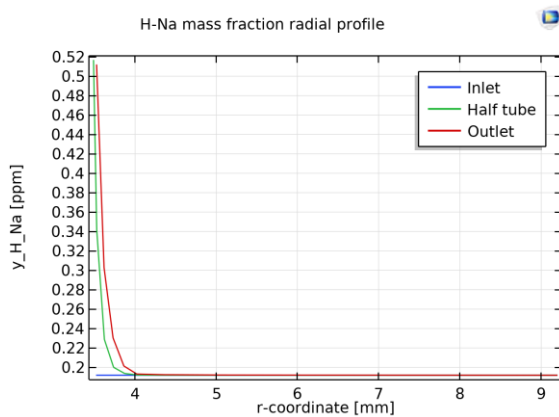
Table 5-5 CFD study - Hydrogen permeation flowrates [mol s^{-1}] evaluated according to three different methods

Test	METHOD 1 $J_{H,p}$ Surface Integral	METHOD 2 H_2 gas Mass Balance	METHOD 3 H Na Mass Balance
	$\times 10^{-7}$ mol/s	$\times 10^{-7}$ mol/s	$\times 10^{-7}$ mol/s
T7-P2	1.01	1.00	1.00
T7-P3	1.32	1.31	1.32
T7	1.57	1.56	1.57
T7-P6	1.84	1.83	1.84
T7-P7	2.08	2.06	2.08
T7-P8	2.19	2.17	2.18

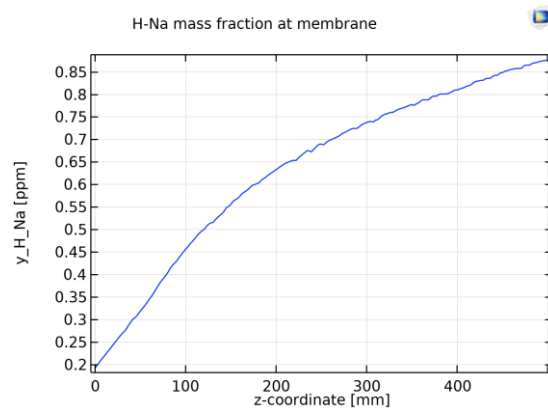
5.5.3 Sensitivity study

5.5.3.1 Mesh refinement

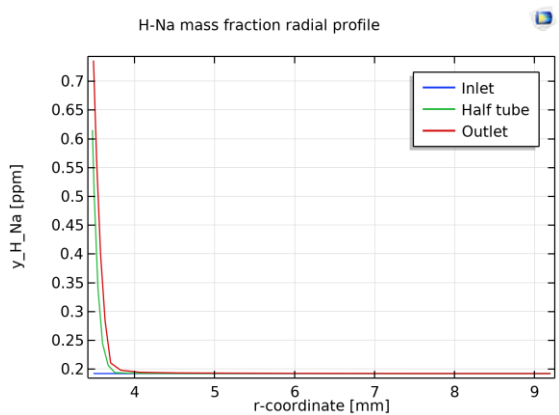
The three meshes presented in paragraph 5.3.2 are tested on the same simulation case (T7), in order to provide a mesh refinement convergence study. Figure 5-8 provides a comparison of the H-Na mass fraction profiles for the three meshes. It is worth noting that, the more the mesh is refined, the better the profiles resolution; moreover, the coarse mesh provides lower values in general, while the normal and the fine mesh have nearly the same profiles. This means that the convergence is reached for the fine mesh, i.e. a finer mesh would not provide a more accurate solution. For this reason, all the simulation presented in this chapter are performed with the fine mesh.



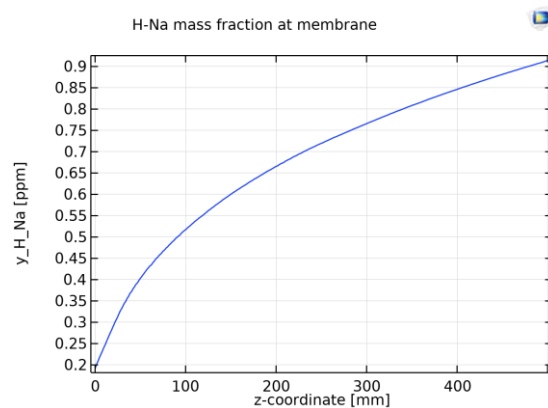
(a)



(b)



(c)



(d)

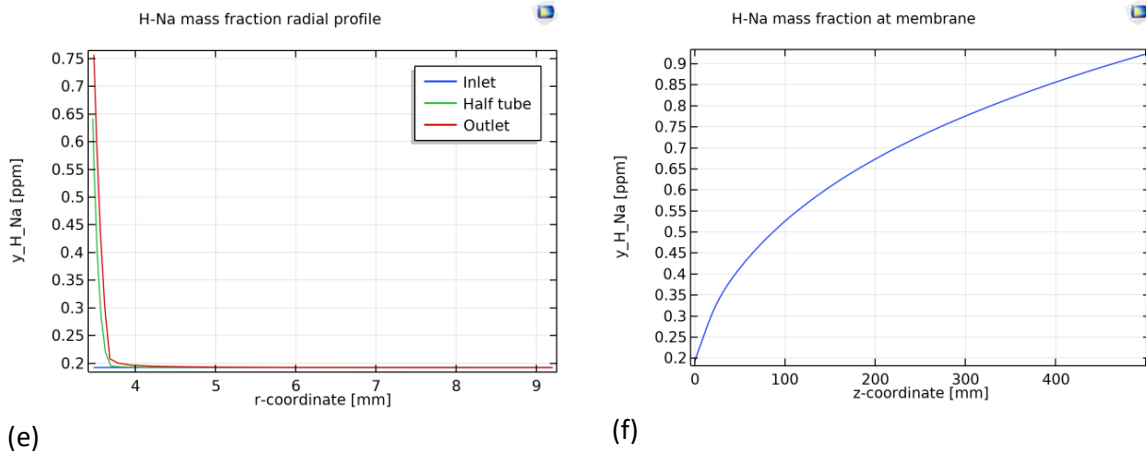


Figure 5-8 Mesh refinement study - H mass fraction radial and axial profiles in sodium for three mesh refinements: coarse (a, b), normal (c, d) and fine (e, f)

5.5.3.2 Sodium flowrate and Reynolds number

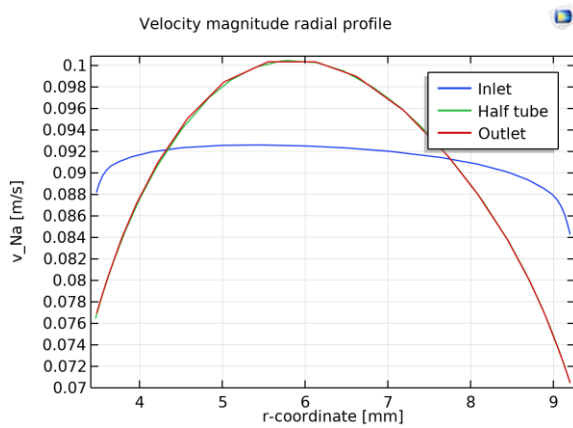
The geometry and Na flowrate taken as input data for the present CFD study (cf. paragraph 5.3.1), give the same average velocity but a slight different Reynolds number of the sodium phase, if compared to the experimental study. This is due to the geometry simplification from 4 to 1 membrane with axial-symmetry. Therefore, it is important to evaluate the effect of a sodium Reynolds number variation on the permeation. To do this, a sensitivity study on the input sodium flowrate is performed with reference to the case T7: the main data are reported in Table 5-6. Sodium flowrates varies in order to obtain Reynolds numbers up to the experimental value (T7-0.375), and down to the minimum value approaching the laminar regime (T7-0.075).

It can be noticed that the Reynolds variation has a small impact (<1% of percentage variation) on the hydrogen permeation flow: in particular, the lower the Re number, the lower the permeation flow. As represented on Figure 5-9 (Na velocity and hydrogen mass fraction radial profiles), when the Na flowrate is higher (e), the hydrogen concentration at the membrane is around 0.6 ppm (f). When the Na flowrate is lowered (a), the lower Reynolds number induces an increase of the sodium mass transfer resistance; therefore, the hydrogen concentration gradient in the Na boundary layer increases, thus giving higher H concentrations at the membrane, about 1.2 ppm (b). As a result, the higher hydrogen partial pressure (see column $\frac{C_{H,Na}^*}{k_{s,Na}}$ in Table 5-6) in sodium adds resistance to the permeation, resulting in a lower permeation flowrate. However, as showed by Figure 5-7, the partial pressure difference with the gas phase is high enough not produce significant permeation variations, even if the sodium partial pressure doubles (as it is the case hereby).

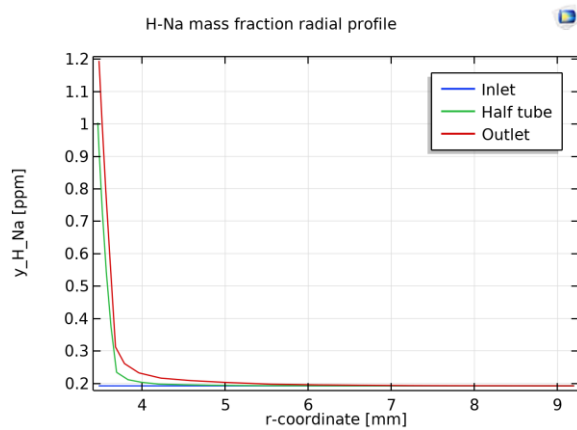
Finally, we can conclude that the sodium flowrate effect on the permeation is negligible.

Table 5-6 Sodium flowrate sensitivity study: simulated cases with related values of sodium flowrate, velocity, Re and hydrogen permeation flow

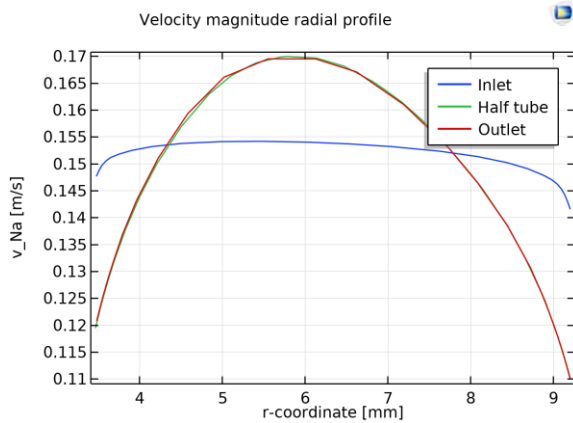
Case	Ref Figure 5-9	\dot{V}_{Na}	v_{Na} - average	Re_{Na} - average	$\frac{C_{H,Na}^*}{k_{s,Na}}$	$Q_{H2,p}$
		$m^3 h^{-1}$	$m s^{-1}$	-	$Pd^{0.5}$	$mol s^{-1}$
T7-0.375	e, f	0.375	0.45	18000	1.42	1.573×10^{-7}
T7	na	0.25	0.3	12000	1.61	1.570×10^{-7}
T7-0.125	c, d	0.125	0.15	6000	2.03	1.565×10^{-7}
T7-0.075	a, b	0.075	0.09	3600	2.40	1.560×10^{-7}



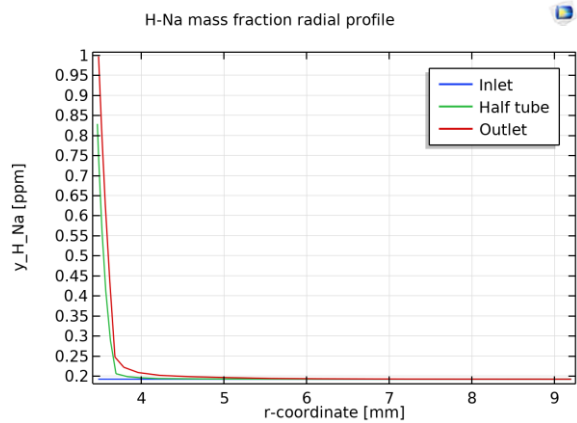
(a)



(b)



(c)



(d)

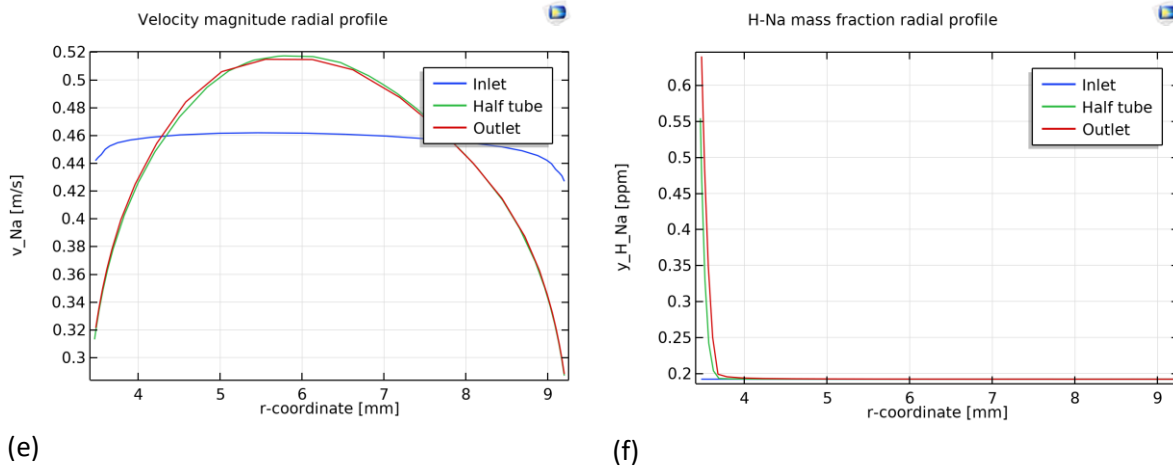


Figure 5-9 Sodium flowrate sensitivity study - Na velocity and mass fraction radial profiles for three Q_{Na} [m^3h^{-1}]: 0.075 (a, b), 0.125 (c, d), 0.375 (e, f).

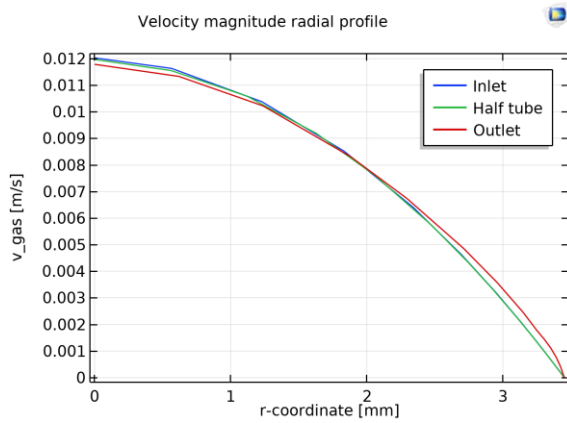
5.5.3.3 Gas flowrate

A sensitivity study for the gas phase flowrate is provided as well; even if in the experimental test a fixed gas flowrate is tested (i.e. 200 Nml/min for the 4 tubes), it is interesting to see which impact it has on the permeation. Taking the case T7 as reference, three additional gas flowrates are tested: data on velocity, Reynolds number, hydrogen retentate concentration, mean partial pressure and permeation are reported in Table 5-7. Unlike the sodium flowrate, the gas flowrate can have a non negligible impact on the permeation: in fact, all the other parameters unchanged, the hydrogen permeation flowrate variation is of around 7% between the T7-25 and the T7-200 case. This effect is essentially due to the higher axial convective transport of the hydrogen in the gas phase: as a result, the hydrogen concentration in the retentate (i.e. gas outlet) is higher and, since the inlet concentration and the gas pressure are the same, the mean hydrogen partial pressure in the gas phase is higher. This is demonstrated by the gas phase mean partial pressure values ($\sqrt{C_{H_2,gas}^* RT}$) reported in Table 5-7, increasing with the gas flowrate. Moreover, this is confirmed by the axial profile of the hydrogen permeation flux on the membrane (Figure 5-10- b, d and f): for the same permeation flux $J_{H_2,p}$ at the inlet ($z=0$), the higher is the gas flowrate, the lower is the reduction of the flux along the z -coordinate, thus giving a higher global permeation flowrate $Q_{H_2,p}$ (i.e. the surface integral of $J_{H_2,p}$ along the membrane's length).

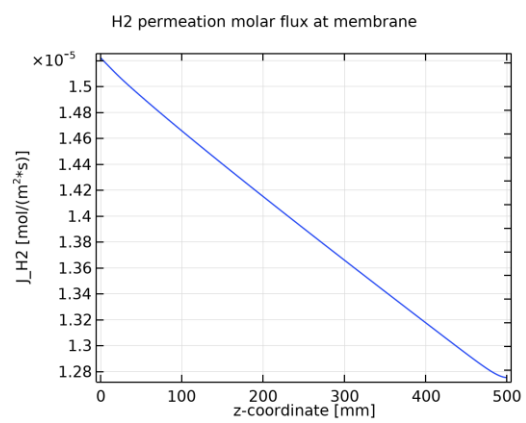
Finally, it is worth noting that this permeation increase is not linear with the gas flowrate over the observed range: in particular, a much higher increase of $Q_{H_2,p}$ is found between 25 and 50 Nml/min (+4.6%), than between 100 and 200 Nml/min (+1%). This is because, at higher flowrates, $X_{H_2,r}$ approaches more and more to the inlet molar fraction of 2.926%; theoretically, for an infinite gas flowrate, $X_{H_2,r}$ will be equal to 2.926%. In practical terms, the more the gas flowrate is augmented, the more $X_{H_2,r}$ tends to the asymptotic value of 2.926% and, consequently, the hydrogen permeation increases asymptotically as well. In this practical case, we can state that increasing the gas flowrate above 200 Nml/min, would not produce any significant permeation increase.

Table 5-7 Gas flowrate sensitivity study: simulated cases with related values of gas flowrate, velocity, Re ; hydrogen partial pressure and permeation flow

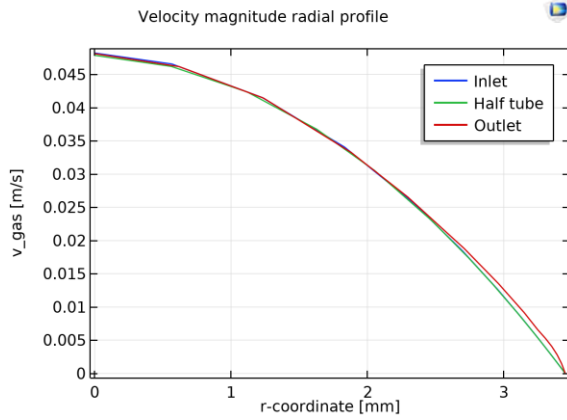
Case	Ref Figure 5-10	Q_{gas}	v_{gas} -average	Re_{gas} -average	$X_{H2,r}$	$\sqrt{C_{H2,gas}^*RT}$	$Q_{H2,p}$
		$Nml\ min^{-1}$	$m\ s^{-1}$	-	%mol	$Pq^{0.5}$	$mol\ s^{-1}$
T7-200	e, f	200	0.052	17	2.82	119.8	1.617×10^{-7}
T7-100	na	100	0.026	8	2.71	118.6	1.601×10^{-7}
T7	c, d	50	0.012	4	2.50	116.3	1.570×10^{-7}
T7-25	a, b	25	0.006	2	2.12	111.8	1.508×10^{-7}



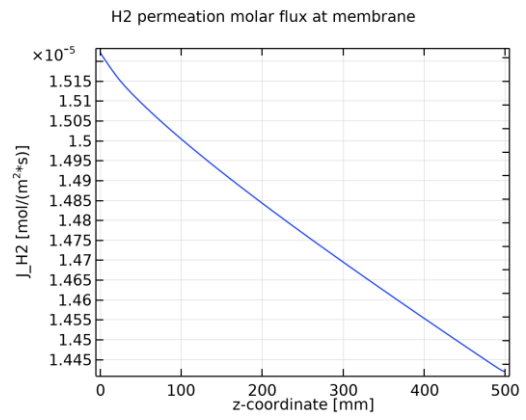
(a)



(b)



(c)



(d)

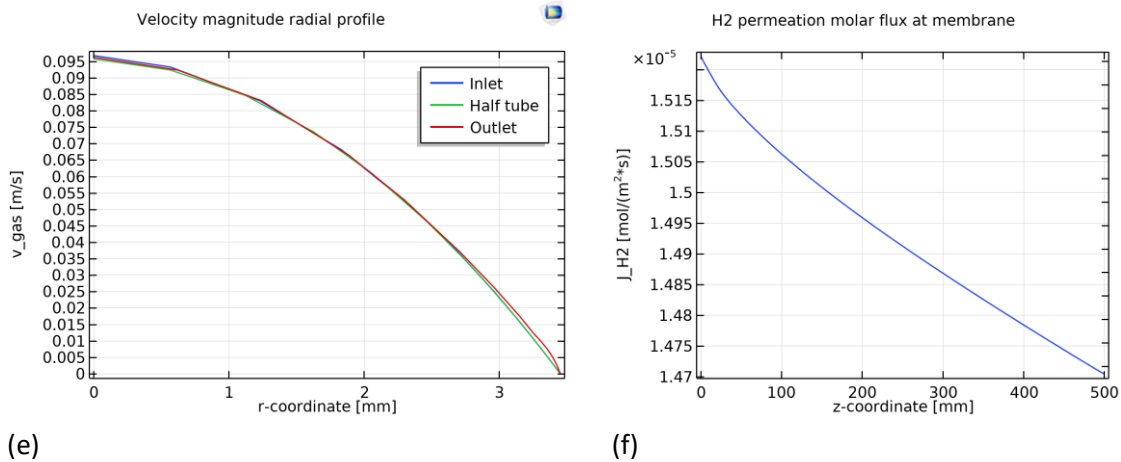


Figure 5-10 Gas flowrate sensitivity study - Na velocity and mass fraction radial profiles for three Q_{gas} [Nml min^{-1}]: 25 (a, b), 100 (c, d), 200 (e, f).

5.6 Comparison with 1-D model and experimental results

Results for all the simulated cases of Table 5-4 are reported in Figure 5-11: in particular, since we are mostly interested in comparing the hydrogen permeation, $Q_{\text{H}_2,p}$ is plotted against the hydrogen mean partial pressure square root in the gas phase. In order to have a coherent comparison with the 1D model results applied to the full permeator prototype (cf. Section 3.2.3), the $Q_{\text{H}_2,p}$ obtained with COMSOL is multiplied by four. Both for CFD simulations and 1D model the Robertson “best fit” permeability coefficient is taken as input.

It is worth noting that, for each case (corresponding to a tested experimental case), the 1D model and the CFD simulation results are in perfect agreement. This means that, for the considered assumptions, the 2D axial-symmetric modelling, does not reveal further resistance mechanisms to the hydrogen mass transport over the physical domain external to the membrane. In particular, the 2D simulations of the gas and sodium phase, including their boundary layers, corresponds to the simpler 1D analytical model. In other words, the approximations and assumptions made to develop the 1D model are acceptable to describe correctly the mass transfer resistance in the gas and sodium phase.

These results confirm the results of the analysis of the axial and radial profiles (cf 5.5.1) and the sensitivity study (par 5.5.3). In fact, the main observations regarding the gas and sodium phase can be resumed as follows:

- Gas phase: it does not provide a significant mass transfer resistance in the radial direction. It mainly affects the permeation in the axial direction, where the hydrogen concentration decreases, depending on the gas pressure, flowrate and temperature.
- Sodium phase: a significant resistance in the boundary layer is found, which actually provides a hydrogen concentration radial gradient between the bulk and the membrane boundary. However, this has a negligible effect on the permeation, since the hydrogen equivalent partial pressure at the membrane boundary in the sodium phase, is always orders of magnitude lower than the gas phase one.

Considering the two former conclusions, it is easy to understand why the CFD 2D modelling coincides with the 1D model presented in Section 3.2.3. In fact, although both the axial and radial coordinates

are considered in the CFD model, it does not add any significant effect on the permeation to the simpler 1D model, which takes into account only the radial coordinate.

Moreover, since the CFD and the 1D model coincide if the same permeability coefficient is taken as input, it is trivial to compare CFD and experimental results. In fact, it is sufficient to perform CFD simulations with the experimental coefficient of gas-sodium tests as input ($E_p = 40757 \text{ [J mol}^{-1}\text{]}$ and $p_{e_0} = 4.80 \cdot 10^{-8} \text{ [mol m}^{-1} \text{ s}^{-1} \text{ Pa}^{-0.5}\text{]}$) and to compare them with experimental results, how it was presented in section 4.6.3. In particular, the same result presented in Figure 4-23 would be found. We did not repeat the procedure here for the sake of simplicity.

Nevertheless, both 1D model and CFD 2D simulations do not take into account some additional mass transfer mechanisms inside the nickel membrane, such as dislocations transport, or at the gas-membrane's interface, such as argon competitive adsorption. Moreover, we can reasonably suppose from the experimental results analysis (cf. Sections 4.6.4 and 4.6.5) that these effects could potentially affect the gas-sodium permeation, thus producing deviations from the models represented in Figure 5-11 at $\sqrt{P_{H_2}} > 140 \text{ Pa}^{0.5}$ (i.e. $P_{\text{gas}} > 7 \text{ bar}$). Therefore, particular attention should be paid when the CFD simulations are used for predictions. As perspective, further developments of the models could be provided.

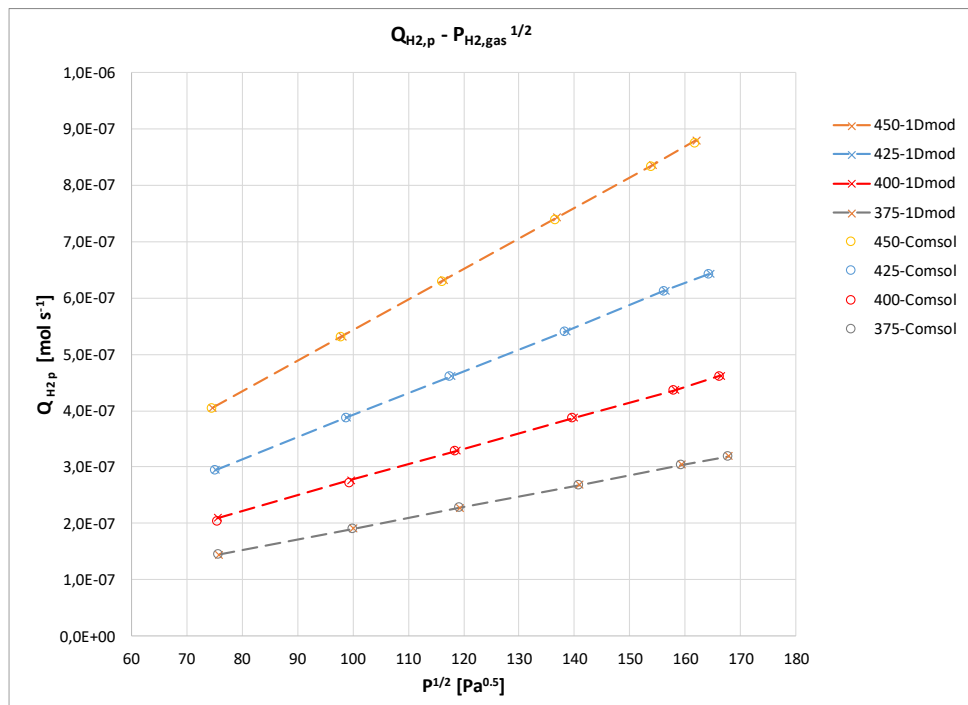


Figure 5-11 CFD study: permeation flowrate (x4 tubes) against hydrogen mean partial pressure square root in gas phase. Comparison with 1D model for all simulated cases

5.7 Conclusion

A CFD model has been developed in order to describe the hydrogen mass transfer through the gas phase, the nickel membrane and the sodium phase. The experimental prototype described in Section 3.2.5 has been simplified to a 2D axial-symmetric geometry, considering one nickel tube only, instead of four. Transport equations of mass, momentum and hydrogen as diluted species are solved for

different operating conditions, representing the gas-sodium experimental tests presented in Section 4.1.1. A sensitivity analysis on the mesh refinement, sodium and gas flowrate is reported as well. Results show details of the hydrogen radial and axial concentration profiles over the different domains; thanks to these results, a better comprehension of the mass transfer phenomenology is obtained. Nevertheless, the evaluation of the global hydrogen permeation flowrate validates what was provided by the simpler 1D model, presented in Section 3.2.3. This result confirms that the assumptions and the simplifications made to set up the 1D model are consistent, for what concerns the gas and sodium phase mass transfer resistance, in the case of a diffusion-limited permeation inside the membrane. Moreover, to obtain an estimation of the global permeation in this operating condition range, the 1D model is recommended, due to its simpler application and the lower computational cost.

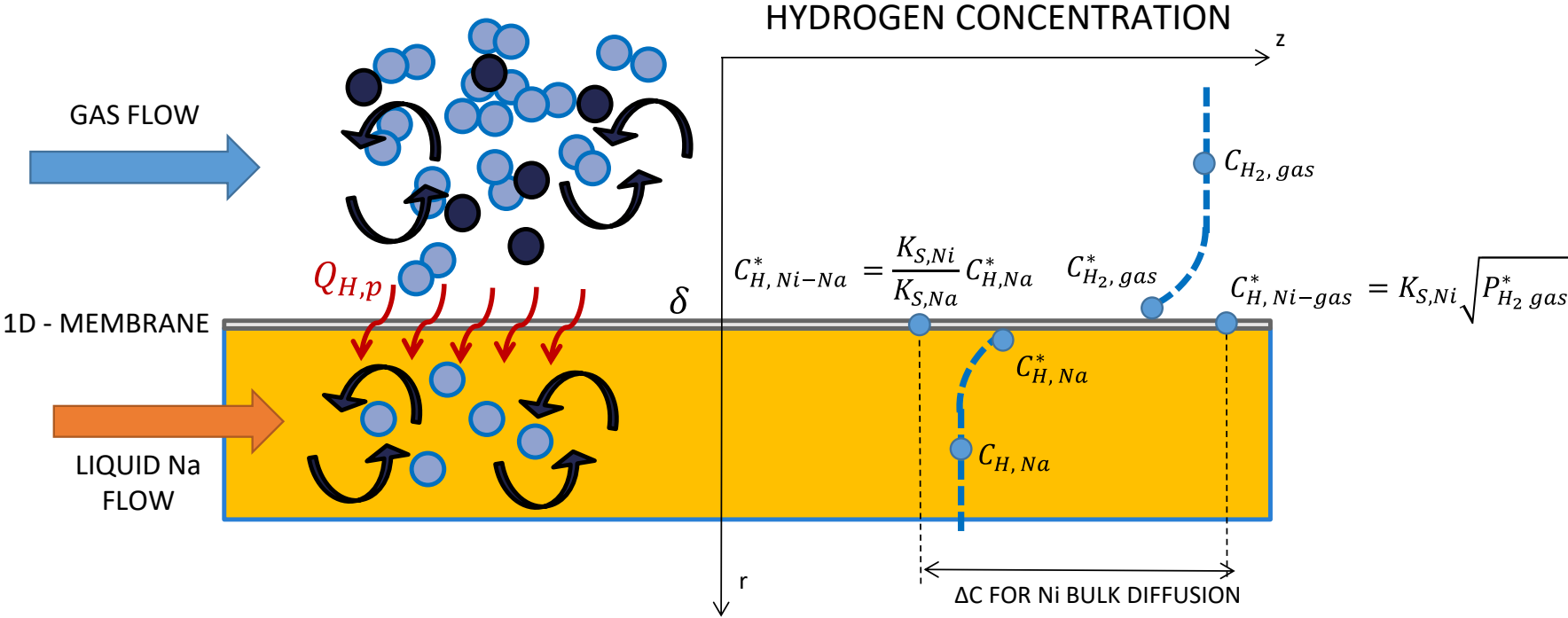
Particular attention should be paid to the application of the model and CFD simulation over the full operating conditions, since some deviations were found experimentally at $\sqrt{P_{H_2}} > 140 \text{ Pa}^{0.5}$ (i.e. $P_{\text{gas}} > 7 \text{ bar}$). They could be attributed to some additional transport mechanisms inside the membrane such as dislocations transport, or at the gas-membrane's interface, such as argon competitive adsorption, not considered in our models. Further developments of the models, taking into account these mechanisms, are recommended as a perspective.

5.8 Annex: summary of model's hypotheses, equations, parameters and variables

5.8.1 Hypotheses

In order to simplify the consultation of this Annex independently from the rest of the Chapter, the model's hypotheses presented in Section 5.2.1 and the scheme in Figure 5-1 are reported here below. The following hypotheses are considered:

- i. steady state conditions are established;
- ii. the whole system is isothermal and adiabatic;
- iii. the ideal gas law is valid;
- iv. liquid sodium density is constant over the domain;
- v. gas mixture and liquid sodium properties (viscosity, hydrogen diffusivity) are constant over the domain;
- vi. metal bulk diffusion is the rate limiting step of the permeation process through the membrane (diffusion-limited permeation) and no trapping or surface effects are considered;
- vii. chemical-physical equilibria at interfaces follow the Sieverts law;
- viii. the membrane length is much greater than its thickness, thus the hydrogen diffusion through the membrane is mainly in the radial direction r ;
- ix. the competitive adsorption of Argon at the gas-membrane interface is neglected.



5.8.2 Equations

<i>Domain</i>	<i>Dominant variable</i>		<i>Units</i>	<i>Physical-chemical parameters (explicit)</i>	<i>State variables (implicit)</i>
CONTINUITY					
Gas phase (r=0 - r _m)	ρ_{gas}	$\nabla(\rho_{gas}v) = 0$	[kg m ⁻² s ⁻²]	$v [v_z; v_r]$	na
Na phase (r=r _m - r _{sh})	ρ_{Na}	$\rho_{Na}\nabla \cdot (w) = 0$	[kg m ⁻² s ⁻²]	$w [w_z; w_r]$	na
MOMENTUM TRANSPORT					
Gas phase (r=0 - r _m)	$v [v_z; v_r]$ P_{gas}	$\rho_{gas}(v \cdot \nabla v) = -\nabla P_{gas} + \nabla \cdot \left[\mu_{gas}(\nabla v + \nabla v^T) - \frac{2}{3}\mu_{gas}(\nabla \cdot v)I \right] + F$	[kg m ⁻² s ⁻²]	$\rho_{gas}; \mu_{gas}$	T
Na phase (r= r _m - r _{sh})	$w [w_z; w_r]$	$\rho_{Na}(w \cdot \nabla w) = -\nabla P_{Na} + \nabla \cdot \left[(\mu_{Na} + \mu_{Na,T})(\nabla w + \nabla w^T) \right] + F$	[kg m ⁻² s ⁻²]	$\rho_{Na}; \mu_{Na}; \mu_{Na,T}; P_{Na}$	T, k, ε
k – ε TURBULENCE MODEL					
Na phase (r= r _m - r _{sh})	k	$\rho_{Na}(w \cdot \nabla k) = \nabla \cdot \left[\left(\mu_{Na} + \frac{\mu_{Na,T}}{\sigma_k} \right) \nabla k \right] + P_k + \rho_{Na}\varepsilon$	[kg m ⁻¹ s ⁻³]	$\rho_{Na}, \mu_{Na}, \sigma_k, P_k, \varepsilon$	
Na phase (r= r _m - r _{sh})	ε	$\rho_{Na}(w \cdot \nabla \varepsilon) = \nabla \cdot \left[\left(\mu_{Na} + \frac{\mu_{Na,T}}{\sigma_k} \right) \nabla \varepsilon \right] + C_1 \frac{\varepsilon}{k} P_k + C_2 \rho_{Na} \frac{\varepsilon^2}{k}$	[kg m ⁻¹ s ⁻⁴]	$\rho_{Na}, \mu_{Na}, \sigma_k, C_1, C_2, P_k, k$	

BOUNDARY CONDITIONS					
Gas inlet (r=0 - r _m); z=0	$v [v_z; v_r]$	$\int_{\partial\Omega} \rho_{gas}(v \cdot n) dS = \dot{m}_{gas,IN}$	[kg s ⁻¹]	$\dot{m}_{gas,IN}$	
Gas outlet (r=0 - r _m); z=L	P_{gas}	$P_{gas} = P_{gas,OUT}$	[Pa]	$P_{gas,OUT}$	
Wall (r= r _m)	$v [v_z; v_r]$	$v = 0$	[m s ⁻¹]		
Na inlet (r= r _m - r _{sh});z=0	$w [w_z; w_r]$ k, ε	$\int_{\partial\Omega} \rho_{Na}(w \cdot n) dS = \dot{m}$ $k = \frac{3}{2}(U_{ref}I_T)^2, \varepsilon = C_\mu^{3/4} \frac{k^{3/2}}{L_T}$	[kg s ⁻¹]	\dot{m}	
Na outlet (r= r _m - r _{sh});z=L	P_{Na}	$P_{Na} = P_{Na,OUT}$ $\nabla k = 0$ $\nabla \varepsilon = 0$	[Pa]	$P_{Na,OUT}$	
Wall (r= r _m)	$w [w_z; w_r]$ Wall functions	$w \cdot n = 0$ $[(\mu_{Na} + \mu_{Na,T})(\nabla w + \nabla w^T)]n = -\rho_{Na} \frac{w_\tau}{w^+} w_{tang}$ $w_{tang} = w - (w \cdot n)n$ $\nabla k \cdot n = 0, \varepsilon = \rho_{Na} \frac{C_\mu k^2}{\kappa_v \delta_w^+ \mu}$	[m s ⁻¹]		

TRANSPORT OF DILUTED SPECIES					
Gas phase ($r=0 - r_m$)	C_{H_2}	$\left(v_z \frac{\partial C_{H_2}}{\partial z} + v_r \frac{\partial C_{H_2}}{\partial r}\right) = D_{H_2,gas} \left[\frac{\partial}{\partial z} \left(\frac{\partial C_{H_2}}{\partial z}\right) + \frac{1}{r} \frac{\partial}{\partial r} \left(r \frac{\partial C_{H_2}}{\partial r}\right)\right]$	$[\text{mol}_{H_2} \text{ s}^{-1} \text{ m}^{-3}]$	$D_{H_2,gas}, v_{gas}$	T, P, gas components
Na phase ($r=r_m - r_{sh}$)	C_H	$\left(v_z \frac{\partial C_H}{\partial z} + v_r \frac{\partial C_H}{\partial r}\right) = D_{H,Na} \left[\frac{\partial}{\partial z} \left(\frac{\partial C_H}{\partial z}\right) + \frac{1}{r} \frac{\partial}{\partial r} \left(r \frac{\partial C_H}{\partial r}\right)\right]$	$[\text{mol}_H \text{ s}^{-1} \text{ m}^{-3}]$	$D_{H,Na}, v_{Na}$	T
BOUNDARY CONDITIONS					
Gas-membrane interface ($r= r_m$)	$C^*_{H_2}$	$\left(v_z \frac{\partial C^*_{H_2}}{\partial z} + v_r \frac{\partial C^*_{H_2}}{\partial r}\right) - D_{H_2,gas} \left[\frac{\partial}{\partial z} \left(\frac{\partial C^*_{H_2}}{\partial z}\right) + \frac{1}{r} \frac{\partial}{\partial r} \left(r \frac{\partial C^*_{H_2}}{\partial r}\right)\right] = -\frac{J_{H,p}}{2}$	$[\text{mol}_{H_2} \text{ s}^{-1} \text{ m}^{-3}]$	$D_{H_2,gas}, v_{gas}, J_{H,p}$	T, P, gas components, $pe_{H_2, Ni}, \delta$
Gas inlet ($r=0 - r_m$); $z=0$	C_{H_2}	$C_{H_2} = C_{H_2,IN}$	$[\text{mol}_{H_2} \text{ m}^{-3}]$	$C_{H_2,IN}$	
Na-membrane interface ($r= r_m$)	C^*_H	$\left(v_z \frac{\partial C^*_H}{\partial z} + v_r \frac{\partial C^*_H}{\partial r}\right) - D_{H,Na} \left[\frac{\partial}{\partial z} \left(\frac{\partial C^*_H}{\partial z}\right) + \frac{1}{r} \frac{\partial}{\partial r} \left(r \frac{\partial C^*_H}{\partial r}\right)\right] = J_{H,p}$	$[\text{mol}_H \text{ s}^{-1} \text{ m}^{-3}]$	$D_{H,Na}, v_{Na}, J_{H,p}$	T, $pe_{H_2, Ni}, \delta$
Na inlet ($r= r_m - r_{sh}$); $z=0$	C_H	$C_H = C_{H,IN}$	$[\text{mol}_H \text{ m}^{-3}]$	$C_{H,IN}$	

5.8.3 Variables and parameters

Symbol	Description	Definition / value	Units	Reference
MEMBRANE				
δ	Membrane thickness	3×10^{-4}	[m]	
$pe_{H2, Ni}$	Hydrogen - Nickel permeability	$pe_0 \exp \frac{-E_p}{RT}$	$[\text{mol}_{H2} \text{ m}^{-1} \text{ s}^{-1} \text{ Pa}^{-0,5}]$	
pe_0	Pe pre-exponential factor	3.33×10^{-7}	$[\text{mol}_{H2} \text{ m}^{-1} \text{ s}^{-1} \text{ Pa}^{-0,5}]$	Robertson « best fit »
E_p	Pe exponential factor – Activation energy	54598	[J mol ⁻¹]	Robertson « best fit »
$J_{H,p}$	H permeation molar flux	$J_{H,p} = \frac{1}{\delta} 2pe_{H2, Ni} \left(\sqrt{C_{H2, gas}^* RT} - \frac{C_{H, Na}^*}{k_{s, Na}} \right)$	$[\text{mol}_H \text{ m}^{-2} \text{ s}^{-1}]$	
$C_{H, Ni-gas}^*$	Molar concentration of H atoms in nickel at the membrane-gas interface		$[\text{mol}_H \text{ m}^{-3}]$	
$C_{H, Ni-Na}^*$	Molar concentration of H atoms in nickel on the membrane-Na interface		$[\text{mol}_H \text{ m}^{-3}]$	

SODIUM				
w	Na velocity		$[\text{m s}^{-1}]$	
C_H	Atomic hydrogen (H) molar concentration		$[\text{mol}_H \text{ m}^{-3}]$	
$C_{H,Na}^*$	Atomic hydrogen (H) molar concentration in Na phase at membrane-Na interface		$[\text{mol}_H \text{ m}^{-3}]$	
$y_{H,Na}$	H atoms mass fraction		$[\text{wppm}]$	
ρ_{Na}	Na density	$219 + 275.32 \left(1 - \frac{T[K]}{2503.7}\right) + 511.58 \left(1 - \frac{T[K]}{2503.7}\right)^{0.5}$	$[\text{kg m}^{-3}]$	
μ_{Na}	Na viscosity	$\ln \mu = -6.4406 - 0.3958 \ln(T[K]) + \frac{556.835}{T[K]}$	$[\text{Pa s}]$	
$\mu_{Na,T}$	Na turbulent viscosity	$\mu_{Na,T} = \rho_{Na} C_\mu \frac{k^2}{\epsilon}$		
k	Na turbulent kinetic energy		$[\text{m}^2 \text{ s}^{-2}]$	
ϵ	Na turbulent dissipation		$[\text{m}^2 \text{ s}^{-3}]$	
$K_{s,Na}$	Hydrogen-in-Na solubility constant	$10^{(0.86 - \frac{122}{T[K]})}$	$[\text{ppm Torr}^{-0.5}]$	Vissers
$k_{s,Na}$	Hydrogen-in-Na solubility constant	$K_{s,Na} \frac{\rho_{Na}}{MM_H} \frac{1}{\sqrt{133.322}} 10^{-6}$	$[\text{mol}_H \text{ m}^{-3} \text{ Pa}^{-0.5}]$	
$D_{H,Na}$	Hydrogen-in-Na diffusivity	$2 \times 10^{-5} e^{(-\frac{49053}{RT})}$	$[\text{m}^2 \text{ s}^{-1}]$	Trouve et Laplanche

GAS				
v	Gas velocity		$[\text{m s}^{-1}]$	
C_{gas}	Gas molar concentration		$[\text{mol m}^{-3}]$	
C_{H_2}	H ₂ gas molar concentration		$[\text{mol}_{H_2} \text{m}^{-3}]$	
$C_{H_2,gas}^*$	H ₂ molar concentration in gas phase at gas-membrane interface		$[\text{mol}_{H_2} \text{m}^{-3}]$	
$x_{H_2,gas}$	H ₂ gas molar fraction		[%]	
MM_{H_2}	H ₂ molar mass		$[\text{g mol}^{-1}]$	
MM_{gas}	Mass molaire gas		$[\text{g mol}^{-1}]$	
P_{gas}	Gas pressure		[Pa]	
ρ_{gas}	Gas density		$[\text{kg m}^{-3}]$	
μ_{gas}	Gas viscosity		[Pa s]	
$D_{H_2,gas}$	Hydrogen-in-gas diffusivity		$[\text{m}^2 \text{s}^{-1}]$	

5.8.4 Relationships between variables and parameters

Variables of interest	Relationship	Reference	Hypothesis
Hydrogen partial pressure in gas	$P_{H2,gas} = x_{H2,gas} P_{gas} = C_{H2,gas} RT$		Ideal gas
H ₂ -gas molar fraction	$x_{H2,gas} = \frac{C_{H2,gas}}{C_{gaz}}$		Ideal gas
H ₂ -gas molar concentration	$C_{gas} = \frac{n}{V} = \frac{P_{gas}}{RT}$		Ideal gas
H-Na molar concentration	$C_{H,Na} = y_{H,Na} [ppm] \frac{\rho_{Na} [kg m^{-3}]}{MM_H [kg mol^{-1}]} 10^{-6}$		Constant density
Hydrogen diffusivity in a gas X (X=N ₂ , Ar, etc.)	$D_{H2,gas} = D_{H2-X} = \frac{0.00266T[K]^{3/2}}{P[bar]MM^{1/2}\sigma^2\Omega_D}$	The properties of gases and liquids	Binary gas system at low pressure; Ideal gas law;
Gas viscosity	$\mu_{gas} = \frac{26.69 (MM T[K])^{1/2}}{\sigma^2\Omega_\mu}$	Chapman-Enskog	Nonpolar, spherical, monoatomic molecules
Viscosity collision integral	$\Omega_\mu = 1.604(T^*)^{-0.5}$	Kim and Ross	
Molar mass	$M = 2 \left[\left(\frac{1}{MM_{H2}} \right) + \left(\frac{1}{MM_X} \right) \right]^{-1}$		
Characteristic length	$\sigma = \frac{\sigma_{H2} + \sigma_X}{2}$	Lennard-Jones	σ_{H2}, σ_X given tabulated values
Characteristic Energy	$\varepsilon = (\varepsilon_{H2}\varepsilon_X)^{1/2}$	Lennard-Jones	$\varepsilon_{H2}, \varepsilon_X$ given tabulated values
Diffusion collision integral	$\Omega_D = \frac{A}{(T^*)^B} + \frac{C}{\exp(DT^*)} + \frac{E}{\exp(FT^*)} + \frac{G}{\exp(HT^*)}$	Neufield (1972)	A,B,C,D,E,F,G,H given constants
T*	$T^* = \frac{kT}{\varepsilon}$	Neufield (1972)	K Boltzmann Constant
Equilibrium membrane – gas (Sieverts law)	$C_{H,Ni-gas}^* = K_{s,Ni} \sqrt{P_{H2,gas}^*}$		

<p>Equilibrium membrane – Na (Sieverts law)</p>	$C_{H,Ni-Na}^* = K_{S,Ni} \sqrt{P_{H2,Na}^*}$		
<p>Hydrogen partial pressure in sodium</p>	$\sqrt{P_{H2,Na}^*} = \frac{C_{H,Na}^*}{k_{S,Na}}$	<p>Whittingham (1976)</p>	

Conclusions and perspectives

In the perspective of an hypothetical design of Sodium Fast Reactor (ASTRID-600 project), the possibility to realize a permeator at the industrial scale has to be studied, in order to transfer a continuous hydrogen flux from a gas phase to the secondary sodium circuit.

In this work, the hydrogen injection in a liquid sodium stream by permeation through a nickel membrane has been investigated, thanks to a theoretical analysis of hydrogen transfer associated with an experimental validation at the pilot scale, by means of an original permeator prototype.

A detailed state of the art review has shown that Richardson's law is the most well-known way to describe the steady state hydrogen diffusion through metals, in case of a gas-gas configuration on both sides of the membrane, when enough thick membranes are considered, leading to a diffusion-limited permeation. With this model, one can obtain the local hydrogen flux per unit surface through a membrane under steady state conditions.

In the past many authors have studied experimentally the hydrogen permeation through small size Nickel membranes, in gas-gas configuration, over high temperature range ($>300\text{ }^{\circ}\text{C}$). The Richardson's law was always followed by the experimental data, obtained in well-controlled conditions, for different membrane thicknesses, pressures, temperatures and measurement techniques.

Furthermore, various applications involving hydrogen permeation through a multi-tubes Nickel membrane, between a gaseous medium and liquid sodium, were developed in the past. The most studied and consolidated one is the hydrogen-meter technology, exploiting the hydrogen permeation from sodium towards a gaseous side. Several studies confirmed that, in this case, the hydrogen permeation flux follows the Richardson's law, within the nominal conditions of use of this device, thus confirming that diffusion across the Nickel membrane is the rate limiting step and that Sieverts' law for Sodium-Nickel interface equilibrium is valid.

Nevertheless, a gas-to-sodium hydrogen introduction method through a nickel membrane has been already developed. However, the operating conditions was very limited and no elements about modelling or theoretical calculation has been provided. Additionally, no information about the validity of the Richardson's law has been reported.

Therefore, an experimental study of a permeator prototype at the pilot scale has been developed in this work, with respect of the constraints coming from the aimed application (Sodium Fast Reactors) and from the available experimental facility. The goal was to demonstrate the feasibility of a gas-to-sodium controlled hydrogen introduction, and to identify the key parameters to properly describe the process.

First, an analytical model (called for simplicity 1D model) aiming to represent locally the permeation process in the radial direction through gas phase, nickel membrane and sodium phase has been set up as support for the prototype sizing. The hydrogen permeation through the nickel membrane is considered a diffusion-limited process and others mechanisms such as dislocation transport or surface adsorption effects are not included in the model. As main result, we found that the gas and sodium phase resistances to hydrogen mass transfer can be neglected, when a turbulent sodium flowrate is

provided and if the membrane thickness is $>50 \mu\text{m}$. Therefore, according to this model, the hydrogen diffusion across the nickel membrane could be considered as the mass transfer driving step. Under this condition, a simplified theoretical law (Equation 3-19) has been identified to describe the local hydrogen permeation through an infinitesimal membrane length. By integrating the Equation 3-19 over the real prototype geometry (multi-tube membrane), assuming a plug-flow in gas phase, the final sizing of the prototype has been defined, with respect of all the technical and practical constraints, so that the hydrogen permeation flowrate can be accurately measured during the experiments by means of mass balances in both gas and sodium phase .

The facility configuration, the measurement techniques based on gas chromatography, RGA analysis and mass spectrometry have been set up, in order to quantify the hydrogen permeation flowrate through the prototype in two different configurations: gas-vacuum and gas-sodium. A data reconciliation method has been applied to gas-vacuum tests in order to validate the different direct and indirect measurements on the retentate (μGC) and permeate (pressure gauge) side. With both techniques, a maximum relative uncertainty of the order of 10% has been assessed for hydrogen permeation flowrates in the range $Q_{H_2 p} > 4 \times 10^{-7} \text{ mol/s}$, by a detailed measurement uncertainty analysis.

A results post-treatment method have been proposed, which allows to compare the experimental results with a single-equation law (Equation 4-3), called “integrated permeation law”, which links the global hydrogen permeation flowrate to the temperature and to the square-root of the hydrogen mean partial pressure in the feed/retentate side.

For gas-vacuum tests, a good agreement is found between measurements on retentate (μGC) and permeate (pressure gauge) sides, by means of data reconciliation, thus validating the use of μGC by itself for the gas-sodium campaign. The prototype performances in gas-vacuum configuration follows the integrated permeation law for all the pressure tested up to the average temperature of 387°C , while for the two highest temperatures (410°C and 434°C) the law is followed only up to hydrogen partial pressure of $2 \times 10^4 \text{ Pa}$ ($\sqrt{P_{H_2}} = 140 \text{ Pa}^{0.5}$, obtained for a gas pressure of 7 bar). However, a non-uniform temperature is measured along the membrane length, thus not allowing to establish precisely a global permeability coefficient value for the mean temperatures between 293°C and 434°C . An overestimation of around 20°C of the effective membrane temperature probably occurs. If we consider the average temperature of the membrane during tests, the permeability law coefficients are a linear function of $1/T$, confirming the Arrhenius law of permeability. In particular, we obtain $E_p = 46309 \text{ [J mol}^{-1}\text{]}$ and $p_{e_0} = 1.08 \cdot 10^{-7} \text{ [mol m}^{-1} \text{ s}^{-1} \text{ Pa}^{-0.5}\text{]}$.

In gas-sodium configuration, a good agreement with the integrated permeation law has been found for hydrogen partial pressures up to $2 \times 10^4 \text{ Pa}$ ($\sqrt{P_{H_2}} = 140 \text{ Pa}^{0.5}$) and for temperatures from 375°C to 450°C . Permeation flowrates ($Q_{H_2 p}$) in the range $3 \times 10^{-7} - 1.1 \times 10^{-6} \text{ mol/s}$ have been measured. By a linear regression on the experimental data coherent with the theoretical Arrhenius law, the experimental permeability law coefficients have been obtained: $E_p = 40757 \text{ [J mol}^{-1}\text{]}$ and $p_{e_0} = 4.80 \cdot 10^{-8} \text{ [mol m}^{-1} \text{ s}^{-1} \text{ Pa}^{-0.5}\text{]}$.

The comparison between gas-vacuum and gas-sodium tests provides globally the same permeation features: this demonstrates the theoretical prediction stating that the sodium phase does not add a significant mass transfer resistance.

Furthermore, measurements of hydrogen concentration inside sodium have been provided during gas-sodium test, based on the well-known hydrogen-meter technology. Thanks to a dedicated estimation of the hydrogen-meter permeability, together with a transient analysis during the permeation tests, coherent results have been found. In particular, for a given hydrogen permeation rate, a coherent concentration increase is found, thus confirming that the entire hydrogen transferred by permeation is dissolved in sodium.

A comparison of the gas-sodium permeability coefficient, related to the full prototype, with previous literature values for small-size nickel membranes, showed that some non-ideal phenomena, probably linked to the membrane deformation by cold-working, could affect the hydrogen permeation in this study. In fact, quite higher permeation with a lower activation energy is found here if compared to the literature (as reference Robertson “best fit” coefficients $E_p = 54560$ [J mol⁻¹] and $pe_0 = 3.33 \cdot 10^{-7}$ [mol m⁻¹ s⁻¹ Pa^{-0.5}]). Moreover, results deviate from the linear dependence of $Q_{H_2 p}$ with $\sqrt{P_{H_2}}$, both for gas-vacuum and gas-sodium tests, when $\sqrt{P_{H_2}} > 140$ Pa^{0.5} and $P_{gas} > 7$ bar. Some hypotheses are provided for further investigations, but one reasonable explanation of this deviation could be the modification of the membrane crystalline structure (caused by the presence of dislocations), induced by the higher mechanical constraint, obtained at the higher pressures and temperatures. In addition, the competitive adsorption of Argon at the membrane surface at high pressure could also be considered.

As a perspective, further studies at a fixed total gas pressure and variable hydrogen concentrations should be carried out, in order to investigate these various mechanisms. Furthermore, test on a small-size nickel sample, before and after a cold-work induced deformation, could assess the effect of cold-working in quantitative terms, in comparison with our results.

Finally, a CFD model has been developed in order to describe the hydrogen mass transfer through the gas phase, the nickel membrane and the sodium phase. The experimental prototype has been simplified to a 2D axial-symmetric geometry, considering one nickel tube only, instead of four. Transport equations of mass, momentum and hydrogen as diluted species are solved for different operating conditions, representing the gas-sodium experimental tests. Results show details of the hydrogen radial and axial concentration profiles over the different domains, with particular regard to the boundary layers at both the membrane’s sides; a better comprehension of the mass transfer phenomenology is provided. Nevertheless, the evaluation of the global hydrogen permeation flowrate over all the tested conditions validates what was provided by the simpler 1D model. This result confirms that the assumptions and the simplifications made to set up the 1D model are consistent, for what concerns the gas and sodium phase mass transfer resistance, in the case of a diffusion-limited permeation inside the membrane.

In summary, different numerical or analytical methods have been assessed to provide, at the pilot scale, an estimation of the hydrogen permeation rate in a gas-sodium configuration, depending on the operating conditions considered. We can resume these methods here below:

1. The analytical 1D-model (chapter 3).
2. The integrated permeation law (chapter 4).
3. The CFD simulations (Chapter 5).

These three methods have been compared with each other and with the experimental results: it has been found that they are substantially equivalent and that, if the experimental permeability coefficient

obtained for gas-sodium test ($E_p = 40757 \text{ [J mol}^{-1}]$ and $pe_0 = 4.80 \cdot 10^{-8} \text{ [mol m}^{-1} \text{ s}^{-1} \text{ Pa}^{-0.5}]$) is used as a model input parameter, the numerical results are in good agreement with the experimental results, for temperatures from 375°C to 450°C and up to $\sqrt{P_{H_2}} > 140 \text{ Pa}^{0.5}$ and $P_{\text{gas}} > 7 \text{ bar}$

One of the above-cited methods can be used for the prototype scale-up, for what concern the hydrogen mass transfer performance. In particular, the required H input from ASTRID-600 is around 20 to 60 times higher than the performance obtained by our experimental prototype (20 for the highest and 60 for the lowest prototype operational points, in terms of hydrogen permeation flowrate). Since the three methods above listed give the same results for the same input parameters, in a first attempt it is advisable to employ the less computational and time consuming one, i.e. the integrated permeation law. It can be applied to different physical parameters in the range of validity proved by this study (i.e. $\approx 375^\circ\text{C} < T < 450^\circ\text{C}$, gas pressure up to 7 bar) and geometry combinations, in order to quickly compare different solutions. The CFD simulations could be used only in a second step, if one wants for example to study some particular thermal-hydraulics features of the permeator, always in the same validity range. Nevertheless, it is not recommended to employ any of the three methods listed above for design purpose out of the validity range, in particular at higher gas pressures. In fact, they do not take into account the effect of the dislocations induced by a potential membrane's deformation and of the gas competitive adsorption at the surface, which could be sources of degradation in the permeation performances at high gas pressures, as revealed by our experimental results. Particular attention should be paid as well to the membrane design pressure and temperature which, combined with the dislocation transport mechanisms, could affect its mechanical resistance with an aging process. If possible, gas mixtures with higher hydrogen concentrations ($> 3\% \text{ mol}$) and a lower operating pressure could be recommended, instead of low concentrations and high pressures.

In particular, the scale-up approach should consider a combination between a full compact and a modular solution, playing on the module's size and on the number of modules, in order to give more flexibility and reliability to the entire system.

Moreover, a periodical calibration of the measuring devices and of the permeator should be carried out in order to support the performances assessment of the system and guarantee the hydrogen mass balance in the system.

In order to limit the number of modules, a strategy could consist in using a single module (if possible) and pure hydrogen, the permeator being inserted into a vessel under vacuum or inert gas (to avoid any explosion hazard). This option, which could reduce significantly the complexity of the system, could be investigated, after checking the limited impact of pure hydrogen, into the Nickel membrane. This option could also prevent from any poisoning effect due to the inert gas ("competitive" adsorption on the surface) if this phenomenon is confirmed in a certain range of operating conditions.

Bibliography

- [1] N. Khatcheressian, 'Développement d'un modèle de transferts couplés pour l'aide à la conception et à la conduite des systèmes de purification du sodium des réacteurs à neutrons rapides', These de doctorat, Toulouse, INPT, 2013.
- [2] A. C. Whittingham, 'An equilibrium and kinetic study of the liquid sodium-hydrogen reaction and its relevance to sodium-water leak detection in LMFBR systems', *J. Nucl. Mater.*, vol. 60, no. 2, pp. 119–131, May 1976, doi: 10.1016/0022-3115(76)90157-4.
- [3] CEA, *Les réacteurs nucléaires à caloporteur sodium*, Le Moniteur Editions. 2014.
- [4] A. Chassery, 'Analyse préliminaire de procédés d'apport d'hydrogène dissous dans le sodium secondaire pour limiter les rejets tritium', CEA Centre d'Etudes Nucleaires de Cadarache, Private Communication, 2016.
- [5] T. Gilardi, 'Etude du procédé d'introduction d'hydrogène dans le sodium secondaire d'ASTRID', CEA Centre d'Etudes Nucleaires de Cadarache, Private Communication, 2017.
- [6] C. Latge, 'A new process for the removal of impurities in the cold traps of liquid metal fast reactors', 1997, [Online]. Available: http://inis.iaea.org/Search/search.aspx?orig_q=RN:31040841.
- [7] D. R. Vissers, J. T. Holmes, L. G. Bartholme, and P. A. Nelson, 'A Hydrogen-Activity Meter for Liquid Sodium and Its Application to Hydrogen Solubility Measurements', *Nucl. Technol.*, vol. 21, no. 3, pp. 235–244, Mar. 1974, doi: 10.13182/NT74-A31394.
- [8] O. W. Richardson, J. Nicol, and T. Parnell, 'I. The diffusion of hydrogen through hot platinum', *Lond. Edinb. Dublin Philos. Mag. J. Sci.*, vol. 8, no. 43, pp. 1–29, Jul. 1904, doi: 10.1080/14786440409463168.
- [9] R. W. Webb, 'HYDROGEN PERMEATION THROUGH METALS', *Other Information: Orig. Receipt Date: 31-DEC-64*, Apr. 27, 1964. <https://digital.library.unt.edu/ark:/67531/metadc865810/>.
- [10] J. Desreumaux and G. Laplanche, 'Mesure de perméabilité à l'hydrogène des membranes de Nickel', CEA Centre d'Etudes Nucleaires de Cadarache, Private Communication, 1984.
- [11] J. Mascarade, 'Étude phénoménologique et modélisation d'un réacteur catalytique à membrane pour la valorisation d'eau tritiée', These de doctorat, Toulouse, INPT, 2015.
- [12] B. Garcinuño, D. Rapisarda, C. Moreno, J. Sanz, and Á. Ibarra, 'Design of a System for Hydrogen isotopes Injection into Lead-Lithium', *Fusion Eng. Des.*, vol. 137, pp. 427–434, Dec. 2018, doi: 10.1016/j.fusengdes.2018.10.006.
- [13] J.-S. Wang, 'On the Diffusion of Gases through Metals', *Math. Proc. Camb. Philos. Soc.*, vol. 32, no. 4, pp. 657–662, 1936, doi: 10.1017/S030500410001940X.
- [14] J. K. Gorman and W. R. Nardella, 'Hydrogen permeation through metals', *Vacuum*, vol. 12, no. 1, pp. 19–24, Jan. 1962, doi: 10.1016/0042-207X(62)90821-7.
- [15] M. A. Pick and K. Sonnenberg, 'A model for atomic hydrogen-metal interactions — application to recycling, recombination and permeation', *J. Nucl. Mater.*, vol. 131, no. 2, pp. 208–220, Apr. 1985, doi: 10.1016/0022-3115(85)90459-3.
- [16] P. L. Andrew and A. A. Haasz, 'Models for hydrogen permeation in metals', *J. Appl. Phys.*, vol. 72, no. 7, pp. 2749–2757, 1992, doi: 10.1063/1.351526.
- [17] T. L. Ward and T. Dao, 'Model of hydrogen permeation behavior in palladium membranes', *J. Membr. Sci.*, vol. 153, no. 2, pp. 211–231, Feb. 1999, doi: 10.1016/S0376-7388(98)00256-7.
- [18] N. D. Deveau, Y. H. Ma, and R. Datta, 'Beyond Sieverts' law: A comprehensive microkinetic model of hydrogen permeation in dense metal membranes', *J. Membr. Sci.*, vol. 437, pp. 298–311, Jun. 2013, doi: 10.1016/j.memsci.2013.02.047.
- [19] N. W. Ockwig and T. M. Nenoff, 'Membranes for Hydrogen Separation', *Chem. Rev.*, vol. 107, no. 10, pp. 4078–4110, Oct. 2007, doi: 10.1021/cr0501792.
- [20] H. Wipf, 'Solubility and diffusion of hydrogen in pure metals and alloys', *Phys. Scr.*, vol. 2001, no. T94, p. 43, 2001, doi: 10.1238/Physica.Topical.094a00043.
- [21] A. Sieverts, 'The Absorption of Gases by Metals', *Zeitschrift für Metallkunde*, pp. 37–46, 1929.

- [22] A. Ciampichetti, 'Analisi del trasporto del trizio nei sistemi SFR', ENEA, Private Communication, Sep. 2011. Accessed: Mar. 26, 2018. [Online]. Available: <http://openarchive.enea.it/handle/10840/3726>.
- [23] C. Latge, S. Sellier, TH. Pelletier, J. Bressieux, Ph. Boucquey, and P. Giroux, 'FUEL-CLEAN-UP SYSTEM Experimental study and modeling of a palladium-silver permeator', in *Fusion Technology 1990*, B. E. Keen, M. Huguet, and R. Hemsworth, Eds. Oxford: Elsevier, 1991, pp. 699–703.
- [24] C. J. Smithells and C. E. Ransley, 'The diffusion of gases through metals', *Proc R Soc Lond A*, vol. 150, no. 869, pp. 172–197, May 1935, doi: 10.1098/rspa.1935.0095.
- [25] D. L. Cummings and D. A. Blackburn, 'The effect of pressure modulation on the flow of gas through a solid membrane: Surface inhibition and internal traps', *Metall. Trans. A*, vol. 16, no. 6, pp. 1013–1024, Jun. 1985, doi: 10.1007/BF02811671.
- [26] J. PLUSQUELLEC, 'Gaz dans le fer et les aciers', *Ref : TIP551WEB - 'Étude et propriétés des métaux'*, Jan. 10, 1981. <https://www.techniques-ingenieur.fr/base-documentaire/archives-th12/archives-etudes-et-proprietes-des-metaux-tiamb/archive-1/gaz-dans-le-fer-et-les-aciers-m210/> (accessed Dec. 12, 2017).
- [27] A. Santucci, S. Tosti, and A. Basile, '4 - Alternatives to palladium in membranes for hydrogen separation: nickel, niobium and vanadium alloys, ceramic supports for metal alloys and porous glass membranes', in *Handbook of Membrane Reactors*, vol. 1, A. Basile, Ed. Woodhead Publishing, 2013, pp. 183–217.
- [28] B. Baranowski, S. Majchrzak, and T. B. Flanagan, 'The volume increase of fcc metals and alloys due to interstitial hydrogen over a wide range of hydrogen contents', *J. Phys. F Met. Phys.*, vol. 1, no. 3, p. 258, 1971, doi: 10.1088/0305-4608/1/3/307.
- [29] A. Altunoglu, 'Hydrogen Permeation Through Nickel And Nickel Alloys. Surface reactions and trapping', PhD Thesis, The Open University, 1994.
- [30] D. K. Kuhn and H. H. Johnson, 'Transient analysis of hydrogen permeation through nickel membranes', *Acta Metall. Mater.*, vol. 39, no. 11, pp. 2901–2908, Nov. 1991, doi: 10.1016/0956-7151(91)90106-B.
- [31] R. C. Frank, D. E. Swets, and D. L. Fry, 'Mass Spectrometer Measurements of the Diffusion Coefficient of Hydrogen in Steel in the Temperature Range of 25°–90°C', *J. Appl. Phys.*, vol. 29, no. 6, pp. 892–898, Jun. 1958, doi: 10.1063/1.1723324.
- [32] K. S. Forcey, D. K. Ross, J. C. B. Simpson, and D. S. Evans, 'Hydrogen transport and solubility in 316L and 1.4914 steels for fusion reactor applications', *J. Nucl. Mater.*, vol. 160, no. 2, pp. 117–124, Dec. 1988, doi: 10.1016/0022-3115(88)90038-4.
- [33] J. Crank, *The Mathematics of Diffusion*. Clarendon Press, 1979.
- [34] S. K. Lee, Y. G. Ohn, and S. J. Noh, 'Measurement of hydrogen permeation through nickel in the elevated temperature range of 450 - 850 °C', *J. Korean Phys. Soc.*, vol. 63, no. 10, pp. 1955–1961, 2013, doi: 10.3938/jkps.63.1955.
- [35] B. Zajec and V. Nemanič, 'Determination of parameters in surface limited hydrogen permeation through metal membrane', *J. Membr. Sci.*, vol. 280, no. 1, pp. 335–342, Sep. 2006, doi: 10.1016/j.memsci.2006.01.037.
- [36] K. Kizu and T. Tanabe, 'Deuterium permeation through metals under hydrogen counter flow', *J. Nucl. Mater.*, vol. 266–269, pp. 561–565, Mar. 1999, doi: 10.1016/S0022-3115(98)00589-3.
- [37] S. Tosti, 'Supported and laminated Pd-based metallic membranes', *Int. J. Hydrog. Energy*, vol. 28, no. 12, pp. 1445–1454, Dec. 2003, doi: 10.1016/S0360-3199(03)00028-4.
- [38] J. M. Leimert and J. Karl, 'Nickel membranes for in-situ hydrogen separation in high-temperature fluidized bed gasification processes', *Int. J. Hydrog. Energy*, vol. 41, no. 22, pp. 9355–9366, Jun. 2016, doi: 10.1016/j.ijhydene.2016.04.073.
- [39] B. Predel, 'Na-Pd (Sodium-Palladium)', in *Li-Mg – Nd-Zr*, O. Madelung, Ed. Berlin, Heidelberg: Springer Berlin Heidelberg, 1997, pp. 1–1.
- [40] M. L. Wayman and G. C. Weatherly, 'The H-Ni (Hydrogen-Nickel) system', *Bull. Alloy Phase Diagr.*, vol. 10, no. 5, pp. 569–580, Oct. 1989, doi: 10.1007/BF02882416.

- [41] Y. Sakamoto, 'Nickel-Hydrogen System', *Solid State Phenomena, Vols. 73-75*, pp. 137-206, 2000, 2000.
- [42] Y. Fukai, S. Yamamoto, S. Harada, and M. Kanazawa, 'The phase diagram of the Ni-H system revisited', *J. Alloys Compd.*, vol. 372, no. 1, pp. L4-L5, Jun. 2004, doi: 10.1016/j.jallcom.2003.09.134.
- [43] N. Bourgeois, J.-C. Crivello, A. Saengdeejing, Y. Chen, P. Cenedese, and J.-M. Joubert, 'Thermodynamic Modeling of the Ni-H System', Oct. 14, 2015. <https://pubs.acs.org/doi/abs/10.1021/acs.jpcc.5b06393> (accessed Oct. 03, 2018).
- [44] W. M. Robertson, 'Hydrogen permeation, diffusion and solution in nickel', *Z. Fuer Met. Res. Adv. Tech.*, vol. 64, no. 6, pp. 436-443, 1973.
- [45] Y. Ebisuzaki, W. J. Kass, and M. O'Keeffe, 'Diffusion and Solubility of Hydrogen in Single Crystals of Nickel and Nickel-Vanadium Alloy', *J. Chem. Phys.*, vol. 46, no. 4, pp. 1378-1381, Feb. 1967, doi: 10.1063/1.1840860.
- [46] M. R. Louthan, J. A. Donovan, and G. R. Caskey, 'Hydrogen diffusion and trapping in nickel', *Acta Metall.*, vol. 23, no. 6, pp. 745-749, Jun. 1975, doi: 10.1016/0001-6160(75)90057-7.
- [47] S.-M. Lee and J.-Y. Lee, 'The trapping and transport phenomena of hydrogen in nickel', *Metall. Trans. A*, vol. 17, no. 2, pp. 181-187, Feb. 1986, doi: 10.1007/BF02643893.
- [48] A. K. Altunoglu, D. A. Blackburn, N. St. J. Braithwaite, and D. M. Grant, 'Permeation of hydrogen through nickel foils: surface reaction rates at low temperatures', *J. Common Met.*, vol. 172-174, pp. 718-726, Aug. 1991, doi: 10.1016/0022-5088(91)90195-A.
- [49] A. D. Le Claire, 'Permeation of gases through solids', UKAEA Atomic Energy Research Establishment, AERE-R-10846, 1983. Accessed: Dec. 19, 2017. [Online]. Available: http://inis.iaea.org/Search/search.aspx?orig_q=RN:14786384.
- [50] T. Kiyoshi, T. Namba, K. Yamaguchi, and M. Yamawaki, 'Effect of surface impurities and argon sputtering on deuterium permeation of nickel', *J. Nucl. Mater.*, vol. 141-143, pp. 249-252, Nov. 1986, doi: 10.1016/S0022-3115(86)80045-9.
- [51] D. L. Cummings and D. A. Blackburn, 'Pressure modulated absorption-desorption: Permeation, diffusion and surface rate coefficients for hydrogen in nickel and palladium', *J. Nucl. Mater.*, vol. 144, no. 1, pp. 81-93, Jan. 1987, doi: 10.1016/0022-3115(87)90283-2.
- [52] A. K. Altunoglu and N. S. J. Braithwaite, 'Hydrogen trapping and permeation in nickel thoria', *Metall. Mater. Trans. A*, vol. 27, no. 9, pp. 2495-2503, Sep. 1996, doi: 10.1007/BF02652343.
- [53] K. Yamakawa, M. Ege, B. Ludescher, M. Hirscher, and H. Kronmüller, 'Hydrogen permeability measurement through Pd, Ni and Fe membranes', *J. Alloys Compd.*, vol. 321, no. 1, pp. 17-23, May 2001, doi: 10.1016/S0925-8388(01)00948-3.
- [54] S. W. Stafford and R. B. McLellan, 'The solubility of hydrogen in nickel and cobalt', *Acta Metall.*, vol. 22, no. 12, pp. 1463-1468, Dec. 1974, doi: 10.1016/0001-6160(74)90107-2.
- [55] D. Tseng, Q. Y. Long, and K. Tangri, 'Detection of hydrogen permeation on the microscopic scale in nickel', *Scr. Metall.*, vol. 22, no. 5, pp. 649-652, Jan. 1988, doi: 10.1016/S0036-9748(88)80176-5.
- [56] A. Oudriss, 'Influence des hétérogénéités métallurgiques sur les processus de diffusion et de piégeage de l'hydrogène dans le nickel', These de doctorat, La Rochelle, 2012.
- [57] A. Oudriss *et al.*, 'Grain size and grain-boundary effects on diffusion and trapping of hydrogen in pure nickel', *Acta Mater.*, vol. 60, no. 19, pp. 6814-6828, Nov. 2012, doi: 10.1016/j.actamat.2012.09.004.
- [58] A. Oudriss, J. Creus, J. Bouhattate, C. Savall, B. Peraudeau, and X. Feaugas, 'The diffusion and trapping of hydrogen along the grain boundaries in polycrystalline nickel', *Scr. Mater.*, vol. 66, no. 1, pp. 37-40, Jan. 2012, doi: 10.1016/j.scriptamat.2011.09.036.
- [59] T. Gnanasekaran, 'Thermochemistry of binary Na-NaH and ternary Na-O-H systems and the kinetics of reaction of hydrogen/water with liquid sodium - a review', *J. Nucl. Mater.*, vol. 274, no. 3, pp. 252-272, Sep. 1999, doi: 10.1016/S0022-3115(99)00072-0.
- [60] J.-P. Maupre, 'Study of the Na-C-O and Na-H-O ternary systems in the sodium rich corner', PhD Thesis, Université de Provence - Centre Saint Charles, 1978.

- [61] R. Thompson, 'A solvation model for non-metals in liquid alkali metals', *J. Inorg. Nucl. Chem.*, vol. 34, no. 8, pp. 2513–2522, Aug. 1972, doi: 10.1016/0022-1902(72)80198-2.
- [62] S. A. Meacham, E. F. Hill, and A. A. Gordus, 'SOLUBILITY OF HYDROGEN IN SODIUM.', Atomic Power Development Associates, Inc., Detroit, Mich., APDA-241, Jan. 1970. Accessed: Feb. 04, 2019. [Online]. Available: <https://www.osti.gov/biblio/4156845>.
- [63] J. Trouve and G. Laplanche, 'Hydrogen diffusion and permeation in sodium', presented at the International conference on liquid metal engineering and technology in energy production, Oxford (UK), 1984, [Online]. Available: http://inis.iaea.org/Search/search.aspx?orig_q=RN:16075402.
- [64] P. Roy and D. N. Rodgers, 'Characterization of a Diffusion Tube Hydrogen Detector in a Dynamic Sodium System', *Nucl. Technol.*, vol. 12, no. 4, pp. 388–392, Dec. 1971, doi: 10.13182/NT71-A30989.
- [65] D. R. Vissers, J. T. Holmes, P. A. Nelson, and L. G. Bartholme, 'A Hydrogen Monitor for Detection of Leaks in LMFBR Steam Generators', *Nucl. Technol.*, vol. 12, no. 2, pp. 218–225, Oct. 1971, doi: 10.13182/NT71-A31029.
- [66] K. Paumel, 'Comparative tests of two hydrogen-meter technologies in the Phenix reactor', presented at the NPIC&HMIT, San Diego, CA, Jul. 2012.
- [67] M. Girard, 'Testing of an IGCAR Electrochemical hydrogen Meter (ECHM) on a Sodium facility in Cadarache', CEA Centre d'Etudes Nucleaires de Cadarache, Private Communication, 2017.
- [68] T. Gnanasekaran, K. H. Mahendran, R. Sridharan, V. Ganesan, G. Periaswami, and C. K. Mathews, 'An Electrochemical Hydrogen Meter for Measurement of Dissolved Hydrogen in Liquid Sodium', *Nucl. Technol.*, vol. 90, no. 3, pp. 408–416, Jun. 1990, doi: 10.13182/NT90-A34404.
- [69] Morliere and Courouau, 'Validation de l'unité de perméation du procédé PRIAM: résultats et interprétation de la campagne d'essais réalisée sur le premier prototype', CEA Centre d'Etudes Nucleaires de Cadarache, Private Communication, Sep. 2000.
- [70] McKee, 'A calibration system for hydrogen meters in sodium'. *Trans. Amer. Nuc. Soc.* 27, p. 253, 1977, 1977.
- [71] J. M. McKee, F. A. Smith, and E. R. Koehl, 'Evaluation of hydrogen and oxygen meters in sodium as steam generator leak detectors', *Int. Conf. Liq. Met. Technol. Energy Prod. Proc. 2nd 1980*, 1980, Accessed: Feb. 12, 2019. [Online]. Available: http://inis.iaea.org/Search/search.aspx?orig_q=RN:14729021.
- [72] E. L. Cussler, 'DIFFUSION: MASS TRANSFER IN FLUID SYSTEMS, THIRD EDITION', p. 655.
- [73] F. Waelbroeck, P. Wienhold, J. Winter, E. Rota, and T. Bauno, 'Influence of bulk and surface phenomena on the hydrogen permeation through metals', Kernforschungsanlage Juelich G.m.b.H. (Germany, JUEL--1966, 1984. Accessed: Jun. 06, 2019. [Online]. Available: http://inis.iaea.org/Search/search.aspx?orig_q=RN:16053332.
- [74] J. Catalano, M. Giacinti Baschetti, and G. C. Sarti, 'Influence of the gas phase resistance on hydrogen flux through thin palladium–silver membranes', *J. Membr. Sci.*, vol. 339, no. 1, pp. 57–67, Sep. 2009, doi: 10.1016/j.memsci.2009.04.032.
- [75] A. Mourgues and J. Sanchez, 'Theoretical analysis of concentration polarization in membrane modules for gas separation with feed inside the hollow-fibers', *J. Membr. Sci.*, vol. 252, no. 1, pp. 133–144, Apr. 2005, doi: 10.1016/j.memsci.2004.11.024.
- [76] F. Gallucci, F. Chiaravalloti, S. Tosti, E. Drioli, and A. Basile, 'The effect of mixture gas on hydrogen permeation through a palladium membrane: Experimental study and theoretical approach', *Int. J. Hydrog. Energy*, vol. 32, no. 12, pp. 1837–1845, Aug. 2007, doi: 10.1016/j.ijhydene.2006.09.034.
- [77] W.-H. Chen and J. Escalante, 'Influence of vacuum degree on hydrogen permeation through a Pd membrane in different H₂/N₂ gas mixtures', *Renew. Energy*, vol. 155, pp. 1245–1263, Aug. 2020, doi: 10.1016/j.renene.2020.04.048.
- [78] B. E. Poling, J. M. Prausnitz, and J. P. O'Connell, *The properties of gases and liquids*. McGraw-Hill, 2001.
- [79] IAEA, *Sodium Coolant Handbook: Physical and Chemical Properties*. 2018.
- [80] BIPM, 'Guide to the Expression of Uncertainty in Measurement (GUM)', JCGM 100:2008, 2008.

Annexes

I. Analytical resolution of the 1D model on the radial direction

The analytical resolution of the model presented in 3.2.3.1 follows the below described steps:

1. by equalizing Eq. 3-14 and 3-16, $C_{H,Na}^*$ can be expressed as function of $C_{H_2,gas}^*$;
2. equalize Equations 3-14 and 3-15;
3. substitute in b) the expression of $C_{H,Na}^*$ obtained in a);
4. resolve the 2nd grade equation to obtain the unknown $C_{H_2,gas}^*$;
5. calculate $C_{H,Na}^*$ with the expression obtained in a);
6. obtain $C_{H,Ni-Na}^*$ and $C_{H,Ni-gas}^*$ by substituting $C_{H,Na}^*$ and $C_{H_2,gas}^*$ in Equations 3-11 and 3-13;

By fixing the geometry and physical parameters, the system can be solved: hydrogen concentrations and hydrogen mass transfer rate per unit length dQ_H/dz are calculated analytically.

III. Residual gas analysis (RGA) technique

Before to start permeation tests, the system is continuously pumped off until a very low pressure is obtained, typically 1×10^{-8} to 5×10^{-7} mbar (pressure indicated by the BA Pressure Gauge), depending on the pumping time (1 night, 2 days during weekend, etc). The spectrometry analysis reveals the presence of hydrogen in the system (which is progressively outgassed by the piping surface), and of small traces of water (residual humidity) and nitrogen (residual air).

At this pressure levels (High Vacuum), a molecular flow is established in the system, which means that single molecules flow independently with very few interactions between them, depending on the value of their "mean free path and the geometry of the system.

A. Pumping speed and throughput

The turbomolecular pump continues to evacuate the system according to its operational curve: in particular we can see that for pressures $\leq 10^{-4}$ mbar the pumping speed (volumetric flow expressed in l/s) is constant at its maximum value, then it decrease with increasing pressure; for pressures between 10^{-4} and 10^{-3} mbar the pumping speed is reduced of only 10% approximately (see pump curve in attachment).

During system conditioning (2-3 days of pumping or 1 night of pumping between permeation tests), the pressure continues to slowly decrease towards to a minimum value, which represents the maximum pump capacity (ultimate pressure). For our system we reach pressures of 1×10^{-8} to 5×10^{-7} mbar.

During permeation test the system pressure reaches a maximum of 1×10^{-5} to 5×10^{-4} mbar; so we can approximate that pump speed is constant at his maximum value all along the pressure range of our interest. This is confirmed also by the rotational frequency of the pump, visualized on the screen during tests, which is always at his maximum value of 1350 Hz.

The given pumping speed for H_2 is of 50 l/s. This is a mean value given by constructor; the uncertainty is not given.

According to perfect gas law, if the temperature inside the UHV piping is maintained constant, for a given pumping speed we can calculate the molar flow rate of the pump (also called "throughput" in vacuum system) as:

$$Q = \frac{n}{t} \left[\frac{mol}{s} \right] = \frac{P[Pa] \frac{V}{t} \left[\frac{m^3}{s} \right]}{RT} \quad 0-1$$

So, for a fixed pumping speed V/s, at a fixed temperature, the molar flux evacuated by the pump increase with the pressure established in the system.

B. Pressure measurement : QMS vs Pressure Gauge Bayard-Alpert

As “system pressure” we shall consider the total pressure of the system, given by all the gases present in it; in our particular case, with or without hydrogen permeation, the main gas present in the system is hydrogen, since we have only small traces of other gases. This is constantly verified by the mass spectrometry analysis. Therefore, we can approximate that the system “total” pressure corresponds to the hydrogen pressure.

To measure this pressure, two instruments are installed in the RGA system, directly in contact with the flow coming from the permeator: the Quadrupole Mass Spectrometer (QMS) and the Bayard-Alpert (BA) Pressure Gauge. Both are based on the ionization of molecules flowing through an ionization chamber: electrons emitted by a hot cathode ionize a number of molecules proportional to the pressure in the measuring chamber. The ion collector collects the thus generated ion current and feeds it to the electrometer amplifier of the measurement instrument.

The main difference between QMS and BA Gauge is that the QMS filters the ionized molecules in the quadrupole filter according to their mass, before sending them to the collector (Figure 0-1). In fact, as a molecular flow is established at high vacuum, each single ionized molecule passes through the filter with a trajectory depending on its mass, and then impacts on the ion collector, which detects the ion current.

For the proper functioning of QMS, a maximum pressure of 1×10^{-4} mbar is accepted; over this value, in fact, the mean free path of molecules decreases. Depending on the filter geometry, the ionized molecules flowing through it can have more probability to collide with one another, rather than flow across the filter directly to the ion collector. For this reason, the QMS signal loses its linearity with increasing pressure and for pressures above 1×10^{-4} mbar the signal can be inverted (decreasing instead of increasing).

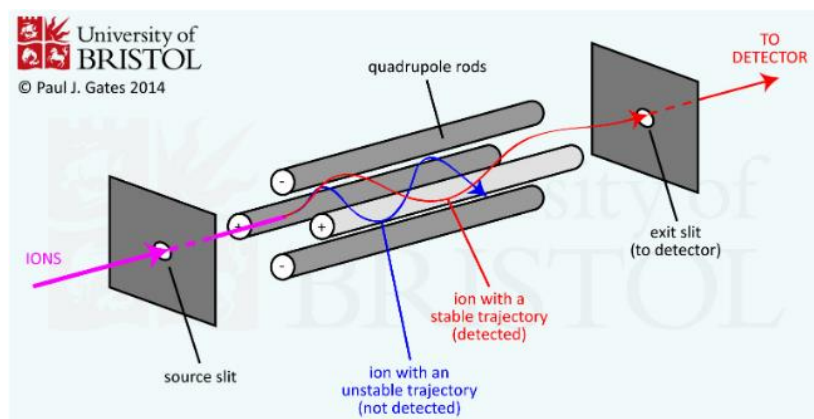


Figure 0-1 QMS principle

The BA Gauge instead counts directly all the ionized molecules in the chamber, since no filter is used to separate molecules (Figure 0-2). For this reason, its maximum allowable pressure is higher than the QMS's one. In particular, it can measure up to 2.7×10^{-2} mbar.

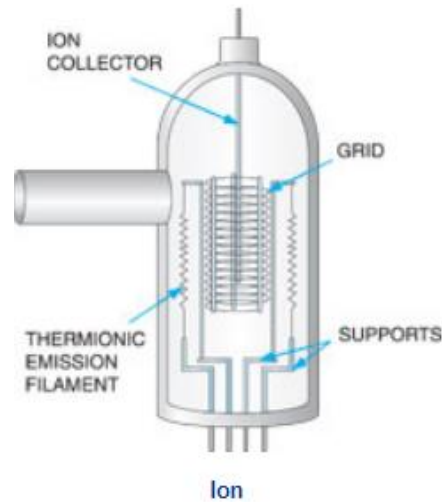


Figure 0-2 Pressure Gauge Bayard-Alpert principle

C. System behavior during hydrogen permeation

When permeation take place, a hydrogen flux starts ($Q_{H_2 p}$ [mol/s]) flowing into the vacuum system from the permeator membranes. As the pressure of vacuum side is extremely lower than H_2 partial pressure on feed side, we can consider that, after an initial transitory time, the hydrogen permeation incoming flow is constant as long as the feed side is maintained stable (gas Pressure, gas flowrate and membrane T).

Considering $Q_{H_2 TP}$ as the molar flow evacuated by the turbo-pump, according to mass conservation we can say that:

- If $Q_{H_2 p} > Q_{H_2 TP} \rightarrow$ P system increases
- If $Q_{H_2 p} < Q_{H_2 TP} \rightarrow$ P system decreases
- If $Q_{H_2 p} = Q_{H_2 TP} \rightarrow$ P system is stable

As the hydrogen flow starts coming into the system:

1. the pressure increases;
2. as a consequence, the pump, which turns at constant speed, evacuates a higher molar flux;
3. if the molar flux evacuated is not enough ($Q_{H in} > Q_{H out}$), the pressure continues increasing;
4. as pressure increases, molar flux evacuated increases;

This process continues as long as an equilibrium is reached: in particular, the system pressure will increase until the pump evacuates the same flux coming into the system; at this moment, the pressure is stable at an equilibrium value. This is confirmed by the experimental measurements effectuated.

As conclusion, we can say that the “*equilibrium pressure*” value depends from the hydrogen permeation flow; namely, it is the pressure value that allows the pump to maintain the system in equilibrium.

D. Hydrogen permeation flow calculation

Therefore, from the “*equilibrium pressure*” measurement, we can calculate indirectly the value of the hydrogen permeation flux by means of two methods:

1. By leak calibration and pressure measurement. In particular, we introduce into the system a known hydrogen molar flow (opening the calibrated leak) and we measure its equilibrium pressure. Assuming the linearity between the hydrogen molar flow and the equilibrium pressure in the system we have the following proportionality :

$$\frac{P_{leak}}{Q_{leak}} = \frac{P_x}{Q_x} \quad 0-2$$

Where P_x and Q_x correspond to the x condition tested.

2. By estimation from the pumping speed (V/t) and the system pressure/temperature, as follows:

$$Q_x = \frac{P_x}{RT_x} \left[\frac{V}{t} \right] \left[\frac{mol}{s} \right] \quad 0-3$$

The method 2, without precise information on the pump speed uncertainty, and involving the temperature, is to be considered an approximation.

The method 1, by means of calibration leak, is normally used in literature to extrapolate results of hydrogen flux. This method is the only used in this work, as presented in par. 3.4.2.2.

Anyway, it is interesting to compare the two calculation methods for each tested condition, in order to verify the coherence with the physic of the system. In Table 0-1, we report two different calculation for two operational cases (T1 and T7 of gas-vacuum test) and for the leak calibration. For the method 2 we consider a pumps speed of 50 l/s and a temperature of 150°C, since the vacuum system was maintained at this constant temperature along all tests. Since the only variable is the pressure measured by the gauge in both methods, we have a constant ratio between the flow calculated with method 1 and 2. In particular, we find a molar flow 1.47 times higher with method 2. This difference can be reasonable if we consider high uncertainties on pump speed and on the effective temperature of the gas inside piping.

Table 0-1 Hydrogen molar flowrate calculation methods in the RGA system

Molar flow comparison					
Test	T	P gas	P gauge	H2 flow	
				method 1	method 2
	°C	bar a	mbar	mol/s	mol/s
T1	300	5	5,20E-05	1,20E-07	1,77E-07
T7	450	5	3,27E-04	7,54E-07	1,12E-06
Calibrated leak	na	na	9,50E-05	2,19E-07	3,24E-07

E. HIDEN – HAL 201-RC Mass spectrometer technical data

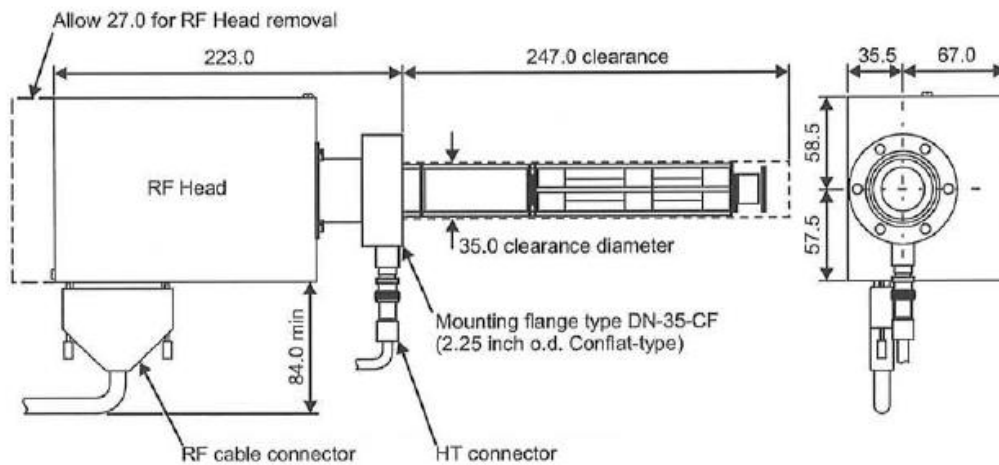


Figure 2.6 HAL 201/301 Probe and RF Head

	Residual Gas Analysers	
HAL0 100 RC	RGA sytem 100 amu Faraday Detector Minimum detectable partial pressure 2×10^{-11} mbar Maximum operating pressure 1×10^{-4} mbar	141100
HAL 201 RC	RGA sytem 200 amu Faraday and Electron Multiplier Detector Minimum detectable partial pressure 5×10^{-14} mbar Maximum operating pressure 1×10^{-4} mbar	144100

F. INFICON - BPG400 (Bayard-Alpert Pressure Gauge) technical data



2 Technical Data

Measurement	Measuring range (air, N ₂ , O ₂)	5 × 10 ⁻¹⁰ ... 1000 mbar, continuous
	Accuracy	15% of reading in the range of 10 ⁻⁸ ... 10 ⁻² mbar (after 5 min stabilization)
	Repeatability	5% of reading in the range of 10 ⁻⁸ ... 10 ⁻² mbar (after 5 min stabilization)
	Gas type dependence	→ Appendix B
Emission	Switching on threshold	2.4 × 10 ⁻² mbar
	Switching off threshold	3.2 × 10 ⁻² mbar
	Emission current	
	p ≤ 7.2 × 10 ⁻⁵ mbar	5 mA
	7.2 × 10 ⁻⁵ mbar < p < 3.2 × 10 ⁻² mbar	25 μA
Emission current switching		
25 μA ⇒ 5 mA	7.2 × 10 ⁻⁵ mbar	
5 mA ⇒ 25 μA	3.2 × 10 ⁻⁵ mbar	

Calibration in pressure range
10^{-3} mbar

The gas type dependence in the pressure range 10^{-3} mbar can be compensated by means of the following formula (gauge adjusted for air):

$$p_{\text{eff}} = C \times \text{indicated pressure}$$

where

Gas type	Calibration factor C
Air, O ₂ , CO, N ₂	1.0
N ₂	1.0
He	5.9
Ne	4.1
H ₂	2.4
Ar	0.8
Kr	0.5
Xe	0.4

(The above calibration factors are mean values.)

IV. Experimental uncertainties and data reconciliation

A. Generalities

A physical system can be theoretically described by a mathematical model, namely a certain number of equation combining different variables and parameters. When all or part of these variables are experimentally measured, being affected by uncertainties, the system of equations is not necessarily satisfied by the measured variables, because of the errors that affect them. Therefore, a data reconciliation method can be applied, in order to find the best estimation of the variable's "true" value, which normally will satisfy the physical system model. Data reconciliation is the estimation of process variables based on information contained in the process measurements and models.

When experiments take place, raw measurements of some variables are recorded. For each condition tested, we will have then datasets randomly dispersed around mean values of X_i . The experimental mean of each dataset will be taken as the measured value of the i -variable, here called \bar{X}_i . Moreover, an instrument rarely directly measures a physical variable, but their measurement comes from the application of conversion laws to the instrument signal. Therefore, they can be affected by further uncertainties coming from the instrument calibration procedure, constant determination and so on.

Hypothesis: only random errors exist, no systematic errors affect measurements. The measured variables X_i follow a Normal distribution

For an observed system, we define the following parameters:

Table 0-2 Data reconciliation parameters

n	Number of measured variables
X_i	Measured variable i
\bar{X}_i	Experimental mean of measured variable i
X_i^*	Reconciled value of measured variable i
$\sigma^2(X_i)$	Variance of the mean measured variable i

According to data reconciliation theory, the reconciled values X_i^* of each measured variable can be obtained by the following system:

$$\min \sum_{i=1}^n \sqrt{\frac{(\bar{X}_i - X_i^*)^2}{\sigma^2(X_i)}} \quad 0-4$$

$$f(X_i^*) = 0 \quad 0-5$$

Where $f(X_i^*)$ constitutes the system constraints, i.e. the model's equations involving the measured variables. The constraints can both contain measured variables only or measured and unmeasured variables. In both cases, to be allowed to apply data reconciliation, the system must have two characteristics:

- Observability : all variables can be measured or estimated from the physical model
- Redundancy : measured variable can be estimated by other measured variables via process models, in addition to its measurement

To apply data reconciliation, it is necessary to correctly estimate the variance $\sigma^2(X_i)$, indicating the uncertainty of the measured variable. According to GUM [80], an experimental variance estimation defined $u^2(X_i)$ can be done by two different methods, according to the available information :

- TYPE A STANDARD UNCERTAINTY

*“The estimated variance u^2 characterizing an uncertainty component obtained from a Type A evaluation is **calculated from series of repeated observations** and is the familiar statistically estimated variance s^2 . The estimated standard deviation u , the positive square root of u^2 , is thus $u = s$ and for convenience is sometimes called a Type A standard uncertainty”.*

Where the experimental variance of the mean or Type A variance is :

$$u_A^2(X_i) = s^2(\bar{X}_i) = \frac{1}{N(N-1)} \sum_{j=1}^N (X_{i,j} - \bar{X}_i)^2 \quad 0-6$$

Where N is the number of independent repeated observation of the variable X_i .

And the Type A standard uncertainty is :

$$u_A(X_i) = \sqrt{u^2(X_i)} \quad 0-7$$

It is evident that Type A standard uncertainty can be evaluated only when repeated observations of the variable X_i are available; therefore it represent the random variation during repeated tests in the same conditions, linked to the variable observation. In our case, this type of evaluation will be applied to all the directly measured variables.

- TYPE B STANDARD UNCERTAINTY

When a quantity X_i has not been obtained from repeated observations, GUM introduce the TYPE B evaluation, stating that *“the associated estimated variance $u^2(X_i)$ or the standard uncertainty $u(X_i)$ is evaluated by scientific judgement based on all of the available information on the possible variability of X_i ”*. Such information may include:

- Previous measurements data
- Experience or general knowledge of the instrument behavior
- Manufacturer’s specifications
- Data provided in calibration and other certificates
- Uncertainties assigned to reference data taken from handbooks or literature

This type of evaluation is applied to measured variables for which information are available about the instrument accuracy, to calibration constants and to non-measured physical parameters affecting indirectly some variable measurement.

- COMBINED STANDARD UNCERTAINTY

When a variable Y is obtained by combining through a function f more variables X_i , for which the standard uncertainties $u(X_i)$ are known, the combined standard uncertainty $u_C(Y)$ is given by :

$$u_C(Y) = \sqrt{\sum_{i=1}^n \left(\frac{\partial f}{\partial x_i}\right)^2 u^2(X_i)} \quad 0-8$$

When f is composed by only multiplications and rapports :

$$\frac{u_c(Y)}{Y} = \sqrt{\sum_{i=1}^n \left(\frac{u(X_i)}{X_i}\right)^2} \quad 0-9$$

Where $\frac{u(X_i)}{X_i}$ is called the “relative” standard uncertainty of the variable X_i .

The combined uncertainty is typically applied to indirectly measured variables and to model parameters depending from a measured physical variable (for example the Temperature), affecting the parameter with its uncertainty.

In conclusion, different types of uncertainty can be estimated for a certain variable, according to the variable nature. If more uncertainties are affecting a variable, their combination will be considered to establish the global uncertainty.

For a directly measured variable, a type A uncertainty is estimated as well as the type B when information are available. Combination of type A and type B gives its global standard uncertainty.

For physical parameters, a type B uncertainty is estimated when information are available.

For indirectly measured variables, a combined uncertainty is calculated by combining the uncertainties of directly measured variables and parameters from which it depends.

B. Uncertainty of measured variables

For each measured variable X_i listed in Table 0-3 a global standard uncertainty is evaluated by combining the effect of different sources.

- GAS FLOWRATE

TYPE A : As for all the directly measured variables, we obtain during the experiments a certain number of repeated observations. Thus, we can calculate a Type A standard uncertainty according to equation 0-6.

TYPE B : The gas molar flow is measured in Nml/min by a Gas Mass Flowmeter - Brooks SLA 5850, which has a precision of 0.9% of measured value, declared by the constructor. Without an indication by the constructor, according to GUM-2008 we consider for this precision a confidence interval at 95% (1.96 of coverage factor); we obtain a relative standard uncertainty of $u_B(Q_{\text{gas}})/Q_{\text{gas}} = 0.045\% = 0.0045$.

- GAS RETENTATE HYDROGEN CONCENTRATION

The Micro-GC is able to give a measurement of hydrogen concentration inside the gas flow coming from the sampling lines at the permeator inlet and outlet. Basically it gives a spectrum where a peak reveals the abundancy of the detected molecule. To give a consistent value of H_2 concentration, it has to be calibrated with a standard leak of known hydrogen concentration. Thus the measured H_2 peaks, compared with the calibration peak value, can give an absolute value of H_2 concentration.

The Ar-H₂ 2,926% gas bottle from Air Liquide (Crystal mixture) has a relative uncertainty of 2%, calculated with a 2-sigma confidence interval. This means that its corresponding type B standard uncertainty is $u(X_{H_2,in}) = 1\%$.

Actually, for the data reconciliation procedure, we do not consider $X_{H_2,in}$ as an unknown variable of the system, since its value is not measured for each experiment, but we consider it as a constant value of 2,926% given by the gas bottle, which actually never changes during experiments. It is of course affected by its uncertainty, but if we consider an uncertainty for it, the data reconciliation would treat it as a variable of the system giving it a different value for each tested condition, which is not physical.

The gas chromatograph is calibrated by multiple measurements of a known mixture; in our case we used the Ar-H₂ 2,926% bottle as calibration mixture. The μ GC signal is then automatically calibrated at this given concentration, for which we consider the bottle uncertainty of 1%. Additionally we consider the type A uncertainty obtained experimentally on multiple observations, estimated at 0,5% of measured value.

Therefore we have $\frac{u_A(X_{H_2,r})}{X_{H_2,r}} = 0,5\%$ and $\frac{u_B(X_{H_2,r})}{X_{H_2,r}} = 1\%$.

- QMS SIGNAL

The mass spectrometer gives a spectrum of peaks, whose amplitude is proportional to the abundance of the corresponding molecular mass. Here we consider only the analysis of the mass $m/z=2$, corresponding to H₂ molecules. The corresponding H₂ signal given by MS, here called S_{MS} [Torr], can be considered proportional to hydrogen flowrate coming into the MS chamber.

We consider for the measured S_{MS} a Type A standard uncertainty only, resulting from its observations during the experiments: the considered value is of $\frac{u_A(S_{MS})}{S_{MS}} = 0,5\%$. No information are available about the sensibility of the signal, so a Type B estimation is not possible.

- PRESSURE GAUGE BAYARD-ALPERT

The Bayard-Alpert pressure gauge measures the pressure of an ultra-vacuum system. If in the system there is only hydrogen (and this can be verified by the mass spectroscopy), the pressure increase linearly with the hydrogen flowrate coming into the system, i.e. the permeation flowrate. The TYPE A relative standard uncertainty of pressure measurement is of $\frac{u_A(P_p)}{P_p} = 0,5\%$.

- MASS SPECTROMETER/ PRESSURE GAUGE CALIBRATION CONSTANT

In order to obtain a flowrate measurement, it is necessary to calibrate the MS and the pressure gauge with a hydrogen standard leak, giving a known H₂ flowrate and then calculate the linearity constant, which links the hydrogen flowrate to the measured signals, as follows:

$$K_{MS} = \frac{Q_{leak}}{S_{S,leak}} \quad 0-10$$

$$K_P = \frac{Q_{leak}}{P_{p,leak}} \quad 0-11$$

Where K_{MS} [(mol/s)/Torr] and K_P [(mol/s)/mbar] are the linearity constant for mass spectrometer and Gauge BA respectively, Q_{leak} [mol/s] is the standard leak hydrogen flowrate, $S_{S,leak}$ [Torr] and $P_{p,leak}$ [mbar] are the output signals corresponding to the standard leak analysis.

We calculate for the signals $S_{S,leak}$ and $P_{p,leak}$ a type A uncertainty, resulting from its observations during the calibration procedure.

While on the value of Q_{leak} we have a Type B uncertainty, coming from constructor certificate, corresponding to 10%.

Therefore, for K_{MS} and K_P a combined uncertainty is calculated as follows:

$$\frac{u(K_{MS})}{K_{MS}} = \sqrt{\left(\frac{u(Q_{leak})}{Q_{leak}}\right)^2 + \left(\frac{u(S_{S,leak})}{S_{S,leak}}\right)^2} \quad 0-12$$

$$\frac{u(K_P)}{K_P} = \sqrt{\left(\frac{u(Q_{leak})}{Q_{leak}}\right)^2 + \left(\frac{u(P_{p,leak})}{P_{p,leak}}\right)^2} \quad 0-13$$

- GAS-VACUUM TEST : PERMEATE HYDROGEN MOLAR FLOWRATE

Once the calibration is set up, the permeate hydrogen flowrate under different conditions can be obtained pressure gauge measurements as:

$$Q_{H2,p} = K_P P_p \quad [\text{mol/s}] \quad 0-14$$

For the $Q_{H2,p}$ uncertainty evaluation we can use the combined uncertainty formula:

$$\frac{u(Q_{H2,p})}{Q_{H2,p}} = \sqrt{\left(\frac{u(K_P)}{K_P}\right)^2 + \left(\frac{u(P_p)}{P_p}\right)^2} \quad 0-15$$

The so obtained relative uncertainty is about 10%.

NOTE : it is important to remark that this combined uncertainty affecting $Q_{H2,p}$ includes both the calibration procedure uncertainties, defined before the experimental campaign on the basis of available information (Type B estimation), and the uncertainty of P_p (Type A), which is calculated for every experimental condition analyzed by means of repeated measurements.

GAS-SODIUM TEST

- SODIUM TEMPERATURE

The Type B relative standard uncertainty for K-type thermocouples in our temperature range is $u(T)/T=0.004$.

- SODIUM LOOP VOLUME

It represents the total volume of sodium circulating inside the circuit during the permeation test. With reference to Figure 3-11, It includes the test section, pump, piping, plugging indicator and heating tank. The volume is calculated for each test according to the sodium level measured in the heating tank; in fact, due to temperature variations and to operation activities, the sodium volume circulating is not always the same. During sodium tests we measured volumes varying from 32 to 36 liters. However, uncertainties still exist on the part of piping which are isolated from the closed loop during the

permeation test (i.e. cold trap branches, plugging indicator). It is really difficult to give an estimation of this uncertainty: for this study, we take as a reasonable value 5%.

- SODIUM DENSITY

The sodium density standard uncertainty is calculated with the combined uncertainty formula, considering the effect of temperature uncertainty. The so obtained relative standard uncertainty is around 2%.

- SODIUM SIEVERTS CONSTANT

As for sodium density, a combined uncertainty is estimated due to the effect of temperature uncertainty on its calculation. The so obtained relative standard uncertainty is around 0.2%.

- DH NICKEL MEMBRANE PERMEABILITY

In this case the DH permeability is estimated by means of experimental measurements (cf. par 4.5.2). Many parameters are used for this analysis and also in this case is not possible to calculate an uncertainty value. For this study we take as a reasonable value 5%.

- HYDROGEN CONCENTRATION IN SODIUM $y_{H,Na}$

The combined relative standard uncertainty on $y_{H,Na}$, calculated according to Equation 3.31, can be expressed as :

$$\frac{u(y_{H,Na})}{y_{H,Na}} = \sqrt{\left(\frac{u(K_{S,Na})}{K_{S,Na}}\right)^2 + \left(\frac{u(pe)}{pe}\right)^2 + \left(\frac{u(K_{MS})}{K_{MS}}\right)^2} \quad 0-16$$

Its value is about 10%-15%.

- HYDROGEN PERMEATION FLOWRATE

Finally, the combined relative standard uncertainty on $Q_{H_2 p}$, calculated according to Equation 4-12, can be expressed as :

$$\frac{u(Q_{H_2 p})}{Q_{H_2 p}} = \sqrt{\left(\frac{u(y_{H,Na})}{y_{H,Na}}\right)^2 + \left(\frac{u(V_{Na})}{V_{Na}}\right)^2 + \left(\frac{u(\rho_{Na})}{\rho_{Na}}\right)^2} \quad 0-17$$

Its value is about 15%.

C. Gas-vacuum test data reconciliation

Hypothesis 1: stationary conditions

We consider that the initial transitory phase of permeation is very small if compared to the permeation test duration. Furthermore, we can consider that the imposed stable conditions (i.e. constant gas flowrate, gas pressure and membrane temperature) will give a constant hydrogen permeation rate during the test duration, so that stationary condition hypothesis is respected.

Therefore, we can write the instantaneous molar balance equations as follows:

- Equation 1 – total molar balance : $Q_{in} - Q_r - Q_p = 0$ [mol/s]
- Equation 2 – hydrogen molar balance : $Q_{in}X_{H_2,in} - Q_rX_{H_2,r} - Q_pX_{H_2,p} = 0$ [mol/s]
- Equation 3 – argon molar balance : $Q_{in}X_{Ar,in} - Q_rX_{Ar,r} - Q_pX_{Ar,p} = 0$ [mol/s]
- Equation 4 – gas inlet composition : $X_{H_2,in} + X_{Ar,in} = 1$
- Equation 5 – gas outlet composition : $X_{H_2,r} + X_{Ar,r} = 1$
- Equation 6 – gas permeate composition : $X_{H_2,p} + X_{Ar,p} = 1$

Where Q_i are the gas mix molar flux expressed in [mol/s] and X_i are the molar fractions [mol_i/mol_{mix}] of hydrogen and argon.

Hypothesis 2: $X_{Ar,p} = 0$

We consider that only hydrogen can permeate through Nickel walls, due to the non permeability of Argon through metals.

Equation 6 and 2 reduces to:

- Equation 6 : $X_{H_2,p} = 1$
- Equation 2 : $Q_{in}X_{H_2,in} - Q_rX_{H_2,r} - Q_p = 0$

Practically Q_p coincides with the permeate hydrogen molar flow, here defined $Q_{H_2,p}$.

By considering the here-above hypothesis, the system reduces to 5 equations:

- Equation 1 : $Q_{in} - Q_r - Q_{H_2,p} = 0$ [mol/s]
- Equation 2 : $Q_{in}X_{H_2,in} - Q_rX_{H_2,r} - Q_{H_2,p} = 0$ [mol/s]
- Equation 3 : $Q_{in}X_{Ar,in} - Q_rX_{Ar,r} = 0$ [mol/s]
- Equation 4 : $X_{H_2,in} + X_{Ar,in} = 1$
- Equation 5 : $X_{H_2,r} + X_{Ar,r} = 1$

The total number of variables is 7. Four of them are measured (directly or indirectly), while the remaining three are non-measured, as listed in the below table:

Table 0-3 List of measured and non-measured variables for gas test

Measured variable (X_i)		Units	Instrument
Q_{in}	Gas molar flow inlet	mol/s	Gas Mass Flowmeter
$X_{H_2,in}$	Hydrogen molar concentration inlet	mol _{H2} /mol _{mix}	Gas Chromatograph (μGC)
$X_{H_2,r}$	Hydrogen molar concentration retentate	mol _{H2} /mol _{mix}	Gas Chromatograph (μGC)
$Q_{H_2,p}$	Hydrogen molar flow permeate	mol/s	Bayard-Alpert Pressure Gauge
Non Measured variable (X_i)		Units	
Q_r	Gas molar flow retentate	mol/s	
$X_{Ar,in}$	Argon molar concentration inlet	mol _{Ar} /mol _{mix}	
$X_{Ar,r}$	Argon molar concentration retentate	mol _{Ar} /mol _{mix}	

In conclusion, all variables are observable: the measured for definition and the non-measured can be obtained from the 5 equations describing the system. Moreover, the system is redundant, since for 3 non-measured variables we dispose of 5 equations. Therefore, data reconciliation can be applied to the system.

For the gas-vacuum test, the constraint $f(X_i^*)$ is given by the equations 1,2,3 and 5 simultaneously.

It depends from reconciled values of both measured and non-measured variables.

This optimization problem is solved with the Excel Solver. In order to have an easier convergence, the gas flowrates are expressed in Nml/min and not in mol/s (conversion factor Nml/min to mol/s 7.43625×10^{-7}).

V. Integrated permeation law demonstration

Demonstration of the correlation given in Equation 4-3, developed from the analogy with heat transfer LMTD.

1. Hydrogen axial mass transfer in the gas phase – integrated form:

$$Q_{H2,p} = Q_{gas\ in}(X_{H2\ in} - X_{H2\ r})$$

2. Hydrogen axial mass transfer in the gas phase – discretized form:

$$dX_{H2} = -\frac{dQ_{H2,p}}{Q_{gas\ in}}$$

3. Hydrogen permeation at the axial coordinate z – discretized form:

$$dQ_{H2,p}(z) = \left[\frac{1}{\delta} \left(p e_0 e^{-\frac{E_{pe}}{RT}} \right) \sqrt{P_{gas}} \right] dA \sqrt{X_{H2}(z)}$$

4. Define U:

$$\frac{1}{\delta} \left(p e_0 e^{-\frac{E_{pe}}{RT}} \right) \sqrt{P_{gas}} = U$$

5. Combine (2)+(3)+(4) :

$$\frac{dX_{H2}}{\sqrt{X_{H2}(x)}} = -\frac{U dA}{Q_{gas\ in}}$$

6. Integration of (5) between “in”- gas inlet and “r”-gas retentate + (1):

$$2(\sqrt{X_{H2\ r}} - \sqrt{X_{H2\ in}}) = -UA \frac{(X_{H2\ in} - X_{H2\ r})}{Q_{H2,p}}$$

From this expression, we obtain the form presented in equation 4-3, where:

$$\sqrt{\overline{P_{H2}}} = \sqrt{P_{gas}} \sqrt{\overline{X_{H2}}} = \sqrt{P_{gas}} \frac{X_{H2\ r} - X_{H2\ in}}{2(\sqrt{X_{H2\ r}} - \sqrt{X_{H2\ in}})} \quad [Pa^{0.5}] \quad 0-18$$

It corresponds to a mean partial pressure difference between inlet/retentate and permeate side, in analogy with the heat transfer LMTD, where the permeate contribution is neglected; in particular, $\sqrt{\overline{P_{H2}}}$ is a combination of the gas total pressure, which is uniform during a permeation test, and the hydrogen concentration which varies along the permeator between inlet and retentate side. However, this expression obtained analytically as, can be replaced by the following simplified form:

$$\sqrt{\overline{P_{H2}}} = \sqrt{P_{gas} \overline{X_{H2}}} = \sqrt{P_{gas} \frac{X_{H2\ r} + X_{H2\ in}}{2}} \quad [Pa^{0.5}] \quad 0-19$$

Where the mean hydrogen concentration $\overline{X_{H2}}$ is calculated as the arithmetic mean between inlet and retentate side. This expression has not an analytical basis, but it is mathematically equivalent to the previous one if the hydrogen concentration varies linearly along the permeator. In fact, for our experimental conditions, a negligible difference is found in calculating $\sqrt{\overline{P_{H2}}}$ according to equation 0-18 or equation 0-19. The practical advantage in using the second expression is that a lower uncertainty is associated to $\sqrt{\overline{P_{H2}}}$ (around 10 times lower), since a simpler expression is employed and, as a consequence, a lower combined uncertainty is produced.

VI. Hydrogen equilibrium at the sodium-cover gas interface

This calculation has been performed in order to demonstrate that, consequently to the hydrogen injected inside sodium during gas-sodium test, any possible hydrogen dispersion in the circuit cover gas (Argon) can be neglected in our mass balance. The calculation is based on Sieverts' equilibrium for a Na-Ar system, constituted by the sodium circulating in the circuit and the heating tank and the Ar cover gas contained in the heating tank upper part.

The example reported in Figure 0-3 done at 450°C, considering a variation of 200 ppb of hydrogen concentration between the start (t_0) and the end (t_{eq}) of the test. These are typical values obtained during gas-sodium tests. Equilibrium hydrogen partial pressures in the Argon cover gas are calculated, according to the Sieverts law.

Both in sodium and in gas phase, there is an obvious increase of hydrogen mass during the test. However, the hydrogen mass dissolved inside sodium, is 0.007% and 0.02% of the mass dissolved inside argon, at the test beginning and end respectively. This shows that, despite a certain amount of injected hydrogen diffuses to the cover gas, this quantity is absolutely negligible if compared to the hydrogen mass dissolved inside sodium. Therefore, we are allowed to not consider it in the global hydrogen-sodium mass balance.

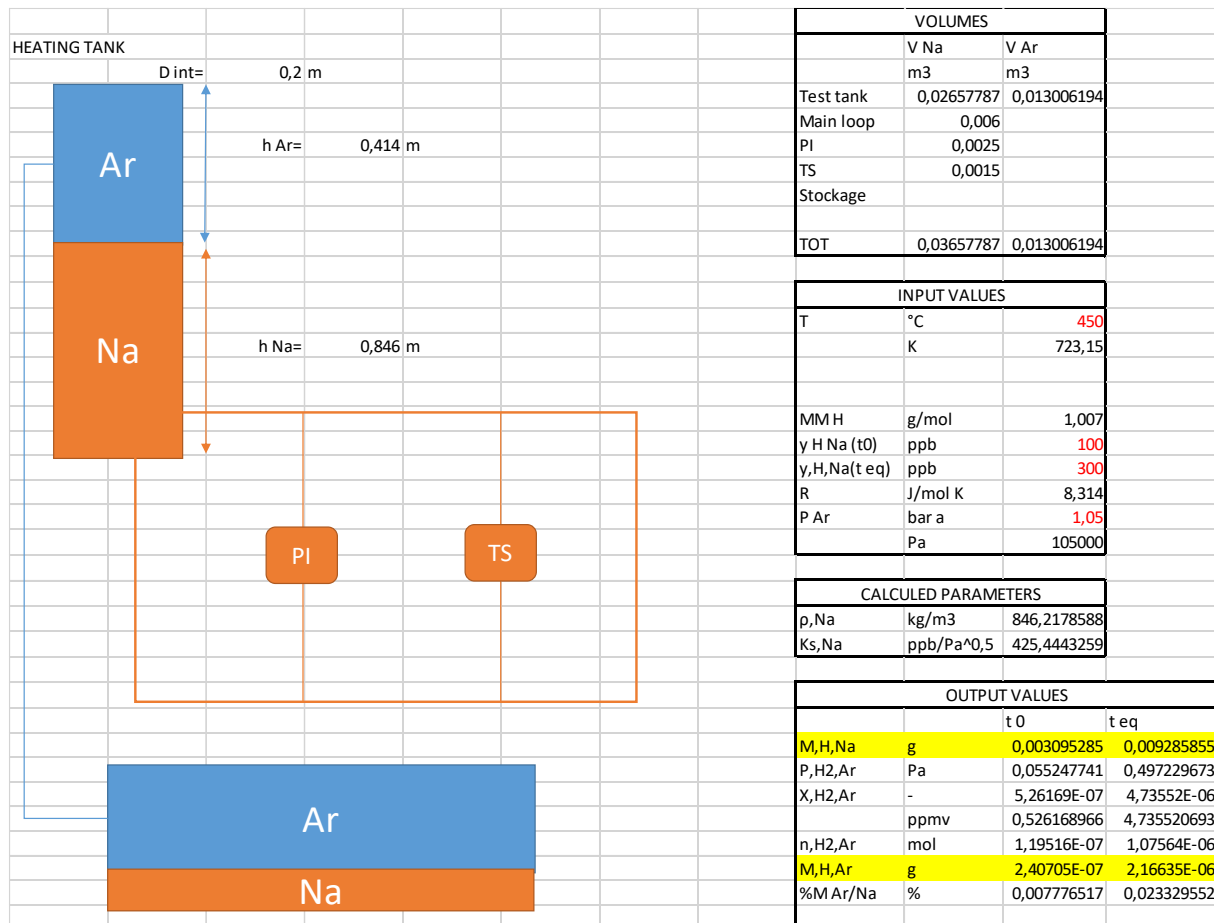


Figure 0-3 Hydrogen equilibrium at the Na-Ar interface, calculated at 450°C for a hydrogen injection of 200 ppb

Numerical and experimental study at the pilot scale of the hydrogen injection into liquid sodium by permeation through nickel membrane

Abstract

In the framework of the SFR, in order to control tritium contamination in sodium circuits, it is fundamental to maintain a certain amount of hydrogen dissolved in the liquid sodium stream. To do this, the hydrogen injection by permeation through nickel dense membranes has been proposed. In this study, an original permeator prototype has been designed and an experimental activity at pilot-scale has been carried out on an experimental sodium loop, up to 450°C. The measured hydrogen permeation flowrate depends linearly on the square root of the hydrogen partial pressure in the feed side up to 20 kPa, thus demonstrating that the process in this range is limited by the hydrogen diffusion inside the nickel membrane. In particular, the presence of sodium in the permeate side does not affect significantly the whole mass transfer process. A comparison with literature results for small nickel samples, showed that some metal-lattice phenomenon could affect the hydrogen permeation in this study. Nevertheless, the experimental process has been successfully validated, thus demonstrating the feasibility of this application at the pilot-scale. An analytical 1D model has been set up with a multi-physics approach, in order to assess the radial hydrogen mass transfer in steady conditions over three physical domains, as support of the design activity. CFD simulations, performed in a 2D axial-symmetric geometry with the software Comsol Multi-physics, have provided a better comprehension of the transport phenomena taking place and have confirmed the results of the straightforward 1D model under certain conditions. Finally, the experimental results have shown a good agreement with both the 1D model and CFD simulations in the whole temperature interval and up to a hydrogen partial pressure of 20 kPa. By resuming all the elements provided by this study, a single equation law has been defined to describe the prototype performance and to enhance the industrial scale-up design activity.

Keywords: *Hydrogen, Permeation, Nickel membrane, Sodium Fast Reactor, Tritium*

Etude numérique et expérimentale à l'échelle pilote de l'injection d'hydrogène dans le sodium liquide par perméation à travers une membrane de nickel

Résumé

Dans le cadre des RNR-Na, pour le contrôle de la contamination du tritium dans les circuits sodium, il est fondamental de maintenir une quantité minimale d'hydrogène dissous dans le sodium liquide. Pour cela, l'injection d'hydrogène par perméation à travers une membrane dense de nickel a été proposée. Dans cette étude, un nouveau prototype de perméateur a été conçu et testé expérimentalement à l'échelle pilote dans un circuit sodium expérimental, jusqu'à 450°C. Le flux de perméation mesuré dépend linéairement de la racine carrée de la pression partielle d'hydrogène en alimentation jusqu'à 20 kPa, démontrant ainsi que, dans cet intervalle, le processus est limité par la diffusion de l'hydrogène à travers la membrane de nickel. En particulier, la présence du sodium dans le côté perméat ne semble pas avoir d'influence significative sur le transfert de masse de l'hydrogène. La comparaison avec les résultats de la littérature, concernant des petits échantillons de nickel, révèle que des phénomènes ayant lieu dans le réticule cristallin de la membrane, probablement liés à la déformation à froid subie lors de sa fabrication, pourraient avoir un impact sur la perméation. Globalement, le processus expérimental a été validé avec succès tout en démontrant la faisabilité de cette application à l'échelle pilote. Un modèle analytique 1D a été développé avec une approche multi-physique, afin d'établir le transfert de masse radial de l'hydrogène à travers les trois domaines physiques. Des simulations CFD, réalisées dans une géométrie 2D axisymétrique avec Comsol-Multi-physics, ont fourni une meilleure compréhension des phénomènes de transport ayant lieu et ont confirmé les résultats obtenus par le plus simple modèle 1D sous certaines conditions. En conclusion, l'activité expérimentale a montré un bon accord avec le modèle 1D et les simulations CFD tout au long de l'intervalle de température et jusqu'à des pressions partielles d'hydrogène de 20 kPa. En rassemblant les éléments expérimentaux et numériques obtenus par cette étude, une loi constituée d'une simple équation a été définie pour décrire les performances du prototype afin d'aider l'activité de conception de cette application à l'échelle industrielle.

Mots clefs : *Hydrogène, Perméation, Membrane de nickel, Réacteurs à Neutrons Rapides refroidis à Sodium, Tritium*